

Switchable Nanoparticle Systems Enabled by Bioorthogonal Inverse Electron-Demand Diels-Alder Reactions

Dissertation to obtain the Degree of Doctor of Natural Sciences

(Dr. rer. nat)

From the Faculty of Chemistry and Pharmacy

University of Regensburg



Presented by

Johannes Lang

from Wertheim

2025

Johannes Lang

**Switchable Nanoparticle Systems Enabled by
Bioorthogonal Inverse Electron-Demand Diels-
Alder Reactions**

This work was carried out from February 2021 to January 2025 at the Department of Pharmaceutical Technology at the University of Regensburg.

The thesis was prepared under the supervision of Prof. Dr. Achim Göpferich.

Doctoral application submitted on: December 1, 2025

Examination board:

Chair:	Prof. Dr. Jens Schlossmann
1 st Expert:	Prof. Dr. Achim Göpferich
2 nd Expert:	Prof. Dr. Miriam Breunig
3 rd Expert:	Prof. Dr. Joachim Wegener

“Hypothesen sind Netze, nur der wird fangen, der auswirft.”

Novalis (1772-1801)

Table of contents

Chapter 1	Introduction Exploring New Opportunities for Diagnostic and Therapeutic Applications by Combining Nanoparticles with the Bioorthogonal Inverse Electron-Demand Diels–Alder Reaction.....	1
Chapter 2	Goals of the Thesis	59
Chapter 3	Using a Fluorogenic Tetrazine-Coumarin Probe to Explore the Potential of the Inverse Electron-Demand Diels–Alder Reaction for Nanoparticle Functionalization in Biological Environments	69
Chapter 4	Towards a Switchable Nanoparticle Behavior Using Inverse Electron-Demand Diels-Alder Chemistry and Ectoenzyme-Based Ligand Activation	129
Chapter 5	Ligand-Switchable Nanoparticles for Increased Target Cell Specificity and Steerable Nanoparticle Uptake	189
Chapter 6	Summary and Conclusion	239
Appendix	245

Chapter 1

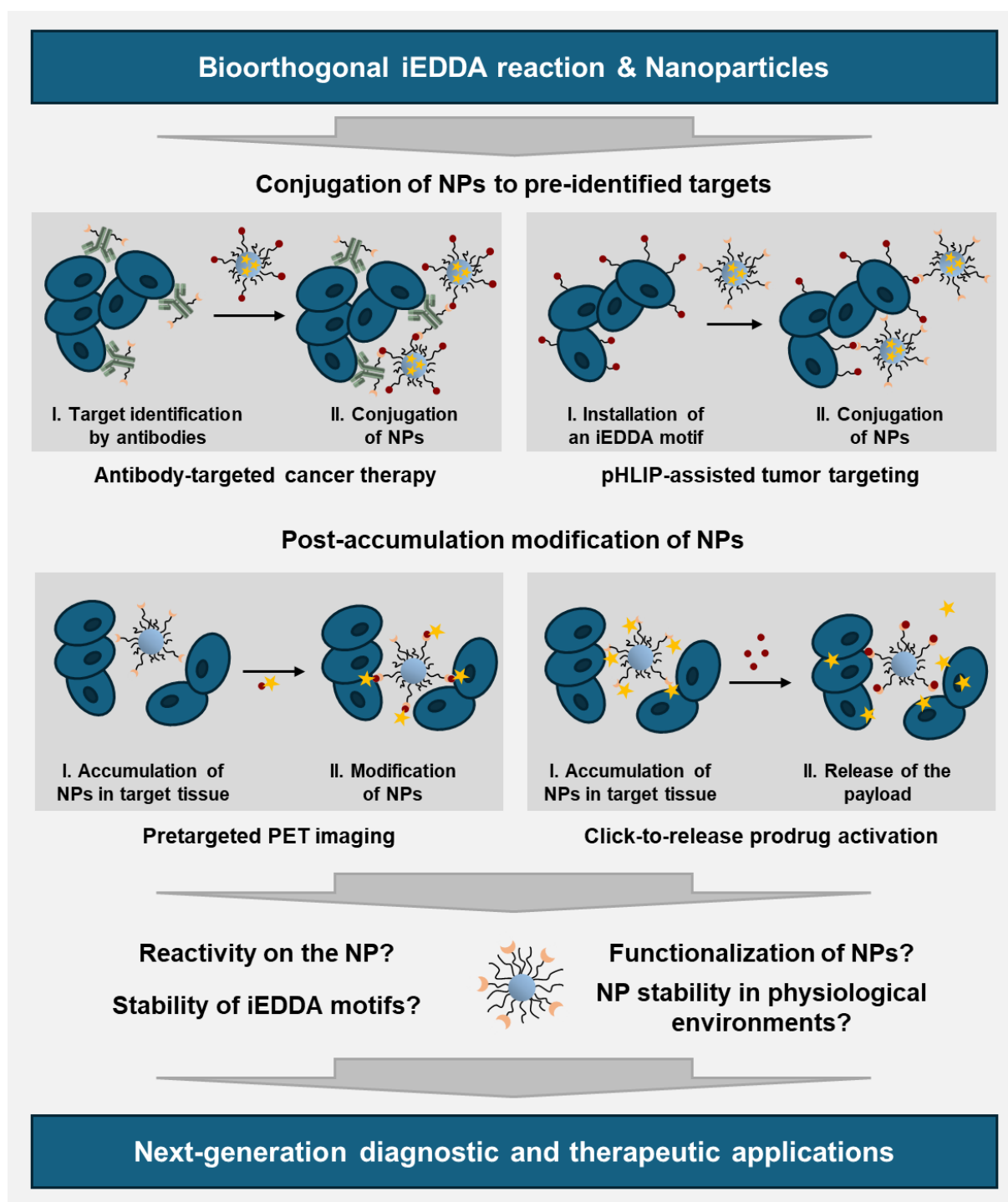
Introduction - Exploring New Opportunities for
Diagnostic and Therapeutic Applications by Combining
Nanoparticles with the Bioorthogonal Inverse Electron-
Demand Diels–Alder Reaction

Chapter 1

Abstract

Recent research has begun to explore the synergy between the two powerful concepts of bioorthogonal chemistry and nanotechnology. The bioorthogonal inverse electron-demand Diels–Alder (iEDDA) reaction offers rapid, selective conjugation under physiological conditions, enabling two-step targeting approaches that enhance specificity and minimize off-target effects. When combined with the unique properties of nanoparticles (NPs), such as multimodal imaging capabilities and multifunctional drug delivery, this synergy unlocks new opportunities for advanced imaging, targeted drug release, and, in combination, theranostics. Recent advances highlight the promise of iEDDA-functionalized NPs in pretargeted PET imaging and click-to-release prodrug activation. However, in the future, the two concepts must be considered increasingly in conjunction investigating how functionalizing NPs with iEDDA motifs affects the stability and biodistribution of the particles, and conversely, how attaching iEDDA motifs to NPs influences their reactivity and stability in biological environments. This review discusses in detail the current state of the literature on concepts for the effective interplay between the iEDDA reaction and NPs and identifies key aspects that require closer examination. Future directions for exploiting the full potential of iEDDA-based NP platforms are outlined, paving the way for next-generation, personalized diagnostic and therapeutic applications.

Graphical Abstract



Visualization of key concepts linking bioorthogonal iEDDA reaction chemistry with nanoparticle-based applications in next-generation medicine.

Chapter 1

1. Introduction

The development of bioorthogonal reactions has fundamentally transformed the way chemists manipulate biomolecules within living systems. Whereas the formation of covalent bonds was previously restricted to controlled conditions *in vitro*, bioorthogonal chemistry now enables selective chemical transformations within living organisms without interfering with natural biochemical processes. [1] The significance of this field was highlighted by the awarding of the Nobel Prize in Chemistry in 2022 to Carolyn Bertozzi, Morten Meldal, and K. Barry Sharpless, bringing click chemistry and bioorthogonal reactions into the broader public spotlight. [2] Among the various bioorthogonal reactions developed to date, the inverse electron-demand Diels–Alder (iEDDA) reaction between tetrazines and strained alkenes or alkynes stands out. It offers exceptional reaction kinetics combined with excellent biocompatibility, making it possible to form covalent bonds even at low reactant concentrations and on timescales relevant for *in vivo* applications. [3] While bioorthogonal chemistry has already demonstrated immense potential in chemical biology and molecular imaging, recent research has begun to explore its synergy with nanotechnology. [4] Nanoparticles (NPs) possess unique physicochemical properties that have been intensively explored in biomedicine over the past decades in the search for advanced diagnostic and therapeutic tools. [5] The combination of bioorthogonal iEDDA chemistry with NPs represents a promising strategy to overcome several limitations of conventional NP-based approaches, particularly in the context of targeted drug delivery and precision diagnostics. The iEDDA reaction enables two-step targeting concepts, in which one component is first used to identify the target and then another component is administered to enable imaging or to deliver drugs. [6] The iEDDA reaction allows rapid and selective coupling of the two components *in vivo* alongside a variety of other functional groups. Importantly, the NP can serve as either the first or the second component in the two-step strategy, resulting in different requirements and possibilities. If the NP is administered as the first component, the enhanced permeability and retention (EPR) effect of the particles in the tumor tissue is often exploited. [7] The interaction of the NPs with the biological environment plays a decisive role here. If the NP is used as the second component, the target labeling usually takes place beforehand using antibodies or iEDDA motifs are artificially installed on the target cells. In this case, the intrinsic properties of NPs are leveraged, such as the possibility of integrating several imaging modalities or therapeutic substances into them, enabling multifunctional applications. [8]

In this work, we explore the potential of combining the iEDDA reaction with NPs for advanced diagnostic and therapeutic applications. We begin with a brief introduction to the field of bioorthogonal chemistry, followed by a more detailed overview of the two key components: the bioorthogonal iEDDA reaction and NPs. The main part of this review focuses on how the synergy between the bioorthogonal iEDDA reaction and NPs can be leveraged to improve biomedical applications. Subsequently critical

factors for the successful interplay of these two concepts are identified and discussed in depth. By summarizing recent developments, highlighting knowledge gaps, and outlining key opportunities, we aim to contribute to the ongoing development of innovative nanomedicine strategies that fully exploit the potential of bioorthogonal chemistry.

2. A brief introduction to bioorthogonal reactions

The history of bioorthogonal reactions began with the rediscovery of the Staudinger reaction [9] and its subsequent development into the Staudinger ligation, which utilizes azides as chemical reporters in combination with phosphines. [10] In its initial form, the organophosphorus compound remains incorporated into the final product. However, in 2000, Raines et al. [11] and Bertozzi et al. [12] independently introduced the so-called traceless Staudinger ligation. In this variant, an amide bond is formed, while the organophosphorus moiety dissociates, yielding a phosphorus-free conjugate (see **Figure 1**). This click reaction demonstrates sufficient biocompatibility for applications in living systems; however, its use is limited by slow reaction kinetics and the oxidation of phosphines. [13] Bertozzi was also the first to coin the term bioorthogonal reaction and played a pivotal role in advancing the development of such reactions. [14] Azide groups remained at the center of attention due to their absence in biological environments, making them ideal candidates for bioorthogonal chemistry. [1] Among the classical click reactions the Cu(I)-catalyzed [3+2] azide–alkyne cycloaddition (CuAAC) is particularly well known. [15] This reaction is based on the azide–alkyne cycloaddition originally described by Huisgen in 1963, which, however, requires elevated temperatures and produces a mixture of 1,4- and 1,5-disubstituted adducts. [16] In 2002, Sharpless et al. [17] and Meldal et al. [18] independently discovered that the reaction could be catalyzed by Cu(I), allowing it to proceed at room temperature with the exclusive formation of a 1,4-disubstituted 1,2,3-triazole product (see **Figure 1**). The CuAAC reaction has been widely applied to biomolecules and bioconjugates, including nucleic acids [19], proteins [20], and glycans [21]. However, its use in living systems is limited by the toxicity of copper. [22] Efforts have been made to enhance the biocompatibility of CuAAC by employing water-soluble Cu(I) ligands to stabilize the oxidation state of the metal. This strategy aims to reduce the presence of free copper ions, which are responsible for generating cytotoxic reactive oxygen species. [23, 24] While some of these approaches have proven highly effective, they ultimately represent attempts to mitigate rather than eliminate the intrinsic toxicity of Cu(I). A fundamentally different and highly promising approach was introduced by Bertozzi et al. in 2004. [25] They demonstrated that ring strain could be exploited to drive the reaction without requiring a copper catalyst.

Chapter 1

In the strain-promoted and thus copper-free azide–alkyne [3+2] cycloaddition (SPAAC), the alkyne is incorporated within an eight-membered ring (see **Figure 1**). This structural constraint induces a ring strain of approximately 18 kcal/mol, which enables the reaction to proceed without a copper catalyst - something that would be unfeasible for linear alkynes. [25] Compared to the CuAAC reaction, the initial reaction rates observed for SPAAC with simple cyclooctynes were relatively slow, with second-order rate constants in the range of $10^{-3} \text{ M}^{-1} \text{ s}^{-1}$, similar to those of the Staudinger ligation. [26] Consequently, various strategies were explored to enhance the reactivity of the alkyne component and increase the reaction rate. Since the reaction is presumed to occur between the lowest unoccupied molecular orbital (LUMO) of the alkyne and the highest occupied molecular orbital (HOMO) of the azide, efforts were made to withdraw electron density from the alkyne through strongly electronegative substituents, particularly fluorine, thereby lowering its LUMO energy level. [27] The introduction of two fluorine atoms into the cyclooctyne ring resulted in a 60-fold increase in the reaction rate constant. [28] Another strategy to accelerate the reaction involved further increasing ring strain. This was achieved by incorporating additional structural constraints, such as the introduction of a cyclopropane ring opposite to the triple bond, leading to the bicyclo[6.1.0]non-4-yne (BCN) scaffold [29], as well as the development of fused azadibenzocyclooctyne (ADIBO or DBCO) derivatives. [30, 31] The most significant enhancement in reaction rate was achieved with the biarylazacyclooctynone (BARAC) derivative, which exhibited a ~400-fold increase in reactivity compared to the parent compound, with a second-order rate constant of $k = 0.96 \text{ M}^{-1} \text{ s}^{-1}$. [32] However, it is important to note that higher reaction rates are often accompanied by significantly reduced stability and shelf life of the alkyne reagent. For instance, BARAC requires storage at 0°C , protected from light and oxygen, to maintain its reactivity. [32] Additionally, the synthesis of cyclooctyne derivatives is often labor-intensive and characterized by low yields. [29] Therefore, for practical applications, a balance must be struck between achieving a high reaction rate, ensuring sufficient stability of the reactants, and maintaining a feasible synthetic route for the cyclooctyne component.

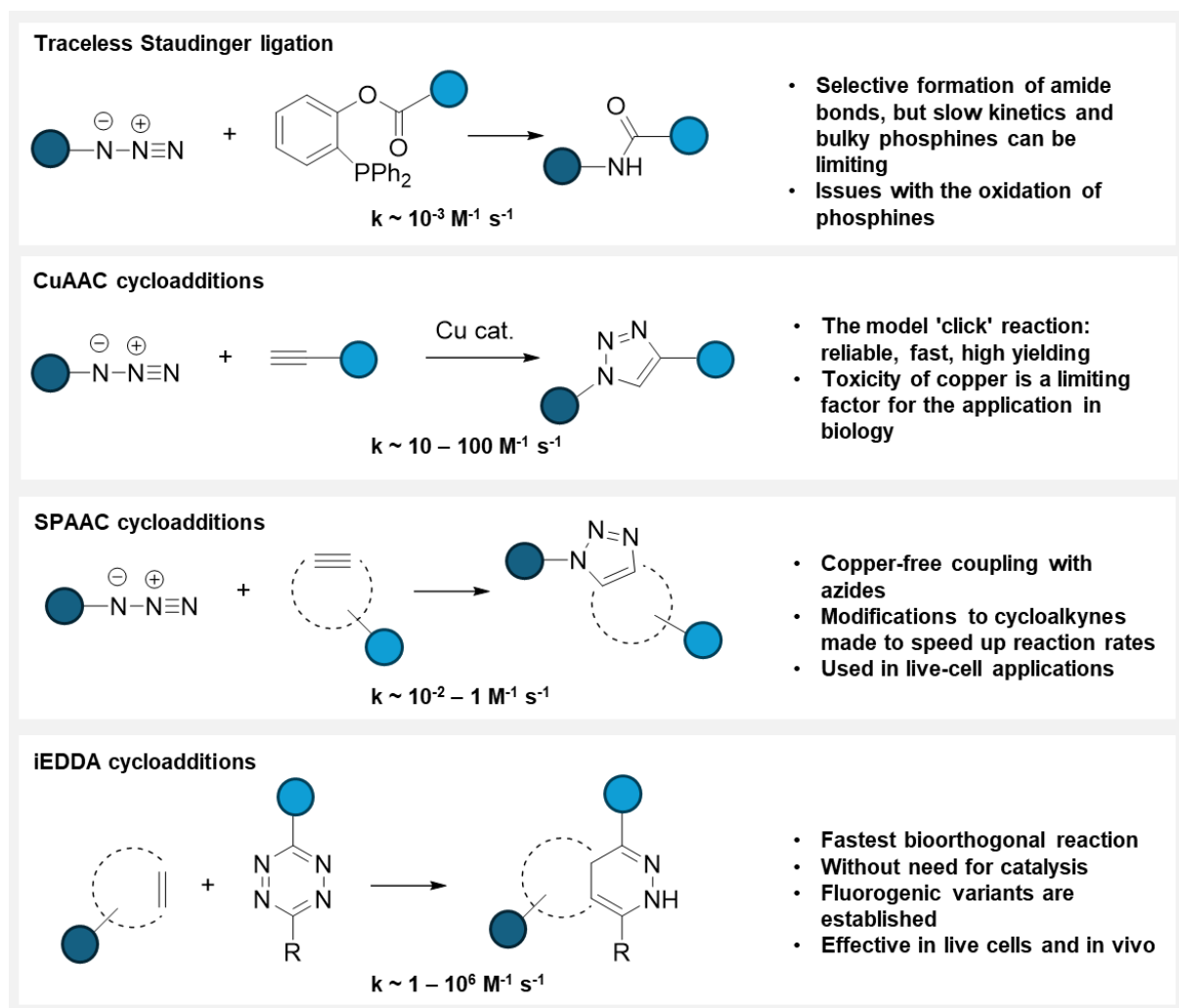


Figure 1. Overview of the most important bioorthogonal reactions. Schematic reactions and general comments about their utility and challenges. (Adapted from Scinto, Bilodeau et al. [1] and Oliveira, Guo et al. [3])

3. Meeting the candidates

3.1 Inverse electron-demand Diels–Alder (iEDDA) reaction

The iEDDA reaction can be regarded as a major breakthrough in the field of bioorthogonal chemistry. Discovered in 2008 by the groups of Fox [33] and Weissleder [34], it offers a significantly enhanced reaction rate, with kinetics reaching up to $10^6 \text{ M}^{-1} \text{ s}^{-1}$ compared to approximately $1 \text{ M}^{-1} \text{ s}^{-1}$ for SPAAC. [3] This high reaction rate enables the direct observation and manipulation of biological processes, as the iEDDA reaction remains sufficiently fast even at the low concentrations typical of biologically relevant molecules. [35] The iEDDA reaction currently best fulfills the criteria for bioorthogonality, including selectivity, biocompatibility, and rapid kinetics. In contrast to the conventional Diels–Alder

Chapter 1

reaction, the iEDDA reaction involves an electron-deficient diene and an electron-rich dienophile (see **Figure 2 A**). [3] The diene is almost exclusively tetrazine, which is why this reaction is sometimes referred to in the literature as the tetrazine ligation. The most commonly used dienophile is trans-cyclooctene (TCO) [36]; however, norbornene derivatives [37] and other dienophiles, such as cyclopropene [38] and cyclooctyne derivatives (e.g., BCN, DBCO) [39], are also employed (see **Figure 2 B**). Unlike the conventional Diels–Alder reaction, the iEDDA reaction is irreversible. In the initial step, a 1,4-addition occurs between the $-C=N-N=C-$ diene system of the tetrazine and the alkene. The resulting highly strained bicyclic intermediate undergoes a retro-Diels-Alder reaction, leading to the release of one equivalent of nitrogen and the formation of the corresponding 4,5-dihydropyridazine. This 4,5-dihydropyridazine then isomerizes to its 1,4-dihydro-isomers and is subsequently oxidized to form a pyridazine. [40] When an alkyne, such as BCN, is used instead of an alkene, the reaction directly yields an aromatic pyridazine without the need for an oxidation step. The primary drawback of this highly reactive and widely applicable bioorthogonal reaction is the stability of its reaction partners, tetrazine and TCO. Trans-cyclooctene can isomerize to its nearly unreactive cis form [41], and tetrazine is also known to degrade in biological environments. [42] Consequently, efforts have been made to develop more stable and reactive partners for the iEDDA reaction.

Tetrazines are typically synthesized by reacting aromatic or aliphatic nitriles or imidoesters with hydrazine. The first synthesis of tetrazines via imidoesters was reported by Pinner in 1893. [43] Under Pinner conditions, an amidrazone intermediate is initially formed, which subsequently reacts with additional hydrazine to yield the dihydrotetrazine. Currently, the more commonly employed synthetic approach involves the reaction of nitriles with hydrazine. [3] This reaction can be catalyzed by sulfur [44], thiols [45], or Lewis acids. [46] As in the imidoester-based synthesis, dihydrotetrazines are initially formed and must be oxidized to yield the final tetrazine product. Nitrous gas, generated by the reaction of sodium nitrate with an acid, is commonly used for this oxidation; however, alternative oxidants have been tested with varying success. [47] Additionally, methods have been developed to introduce preformed tetrazine moieties onto target structures under mild conditions using palladium-catalyzed coupling reactions of aryl halides or aryl boronic acids. [48, 49] The second reaction partner in the iEDDA reaction, TCO, is produced via photoisomerization. The corresponding cis-cyclooctene is first synthesized and then subjected to a closed-loop flow system in which it is repeatedly exposed to a light source (254 nm) to induce photoisomerization. AgNO₃-impregnated silica selectively enriches the desired TCO component within this cycle. [50] Thus, while sufficient synthetic methodologies exist for both iEDDA reaction partners, specialized laboratory equipment is particularly required for TCO production.

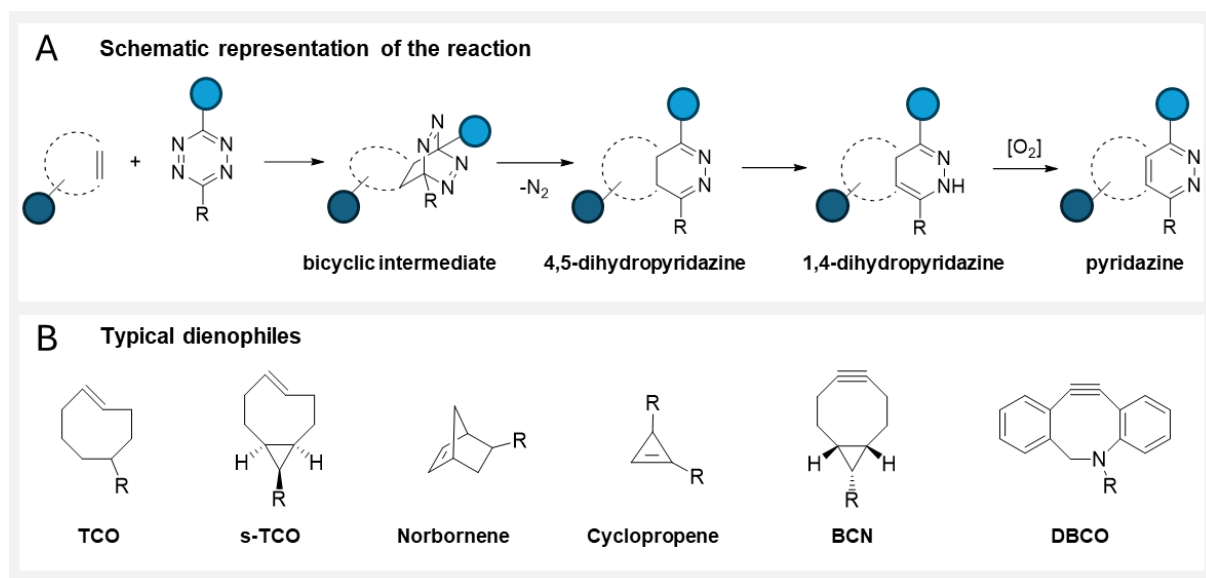


Figure 2. Mechanism of the iEDDA reaction. (A) Schematic representation of the reaction between tetrazine and a dienophile. (B) Illustration of typical dienophiles, foremost trans-cyclooctene (TCO). BCN stands for bicyclo[6.1.0]nonyne; DBCO for dibenzocyclooctyne. (Adapted from Scinto, Bilodeau et al. [1] and Oliveira, Guo et al. [3])

Beyond its application in the modification of NPs for improved therapeutic and diagnostic applications, the iEDDA reaction has been utilized in numerous other fields due to its advantageous properties. [3] Its exceptionally rapid reaction kinetics make it particularly well suited for tracking and imaging fast biological processes. [51] Additional applications include fluorescent labeling of low-abundance proteins within living cells for super-resolution imaging [52], identification of the targets of bioactive small molecules and proteins in living cells [53], protein profiling in living systems [54], and sequence-specific detection of DNA and mRNA. [55] Owing to its high specificity, biocompatibility, and versatility, the iEDDA reaction is poised to play an important role in the development of biorthogonal technologies for both fundamental research and clinical applications.

3.2 Nanoparticles for biomedical applications

NPs have been developed over recent decades as advanced tools for the diagnosis and therapy of various diseases. [56] One of the earliest biomedical applications of NPs was the development of liposomal drug delivery systems in the 1970s. A key milestone in this context was the approval of Doxil®, a PEGylated liposomal formulation of the anticancer drug doxorubicin, by the FDA in 1995. [57] This paved the way for the development of further nanotherapeutic approaches. As particles typically ranging in size from a few to several hundred nanometers, they exhibit unique physicochemical properties, including a high surface-to-volume ratio, tunable surface chemistry, and especially in the case of inorganic NPs size-dependent optical, magnetic, or electronic effects that clearly distinguish them from their macroscopic counterparts. [58] To provide an overview of the relatively broad range of NPs available for biomedical

Chapter 1

applications today, NPs can be classified based on their composition (see **Figure 3 A**). [59] The group of organic NPs includes, lipid-based NPs and polymeric NPs. These are generally well biocompatible and often biodegradable, whereas this is typically not the case for inorganic NPs. However, inorganic NPs, such as gold NPs, iron oxide NPs, silica NPs, and quantum dots, offer robust structural properties and high functional versatility. They can be employed for biosensing [60], photodynamic therapy [61], magnetic and optical hyperthermia [62], or as contrast agents in magnetic resonance [63], photoacoustic [64], or photoluminescence [65] imaging. Organic NPs, in contrast, are particularly suitable as nanocarriers for the controlled delivery of therapeutic molecules. [66] Compared to conventional systemic drug delivery, NP-mediated drug administration offers several advantages. Since the active pharmaceutical ingredient is not freely distributed throughout the body but instead accumulates at the target site via the NP-based delivery system, the overall burden on healthy tissues is reduced. As a result, NPs are associated with lower systemic toxicity. Additionally, their high drug loading capacity, protection of therapeutic cargo, and the improved bioavailability of the drug are particularly advantageous. [4] Moreover, NPs can be engineered to respond to specific biological stimuli (e.g., pH value, redox conditions), enabling precise and site-specific drug release. [67] By combining suitable NP materials, it is often possible to integrate diagnostic and therapeutic functions into a single multifunctional nanoplatform, a concept known as “theranostics”. [68]

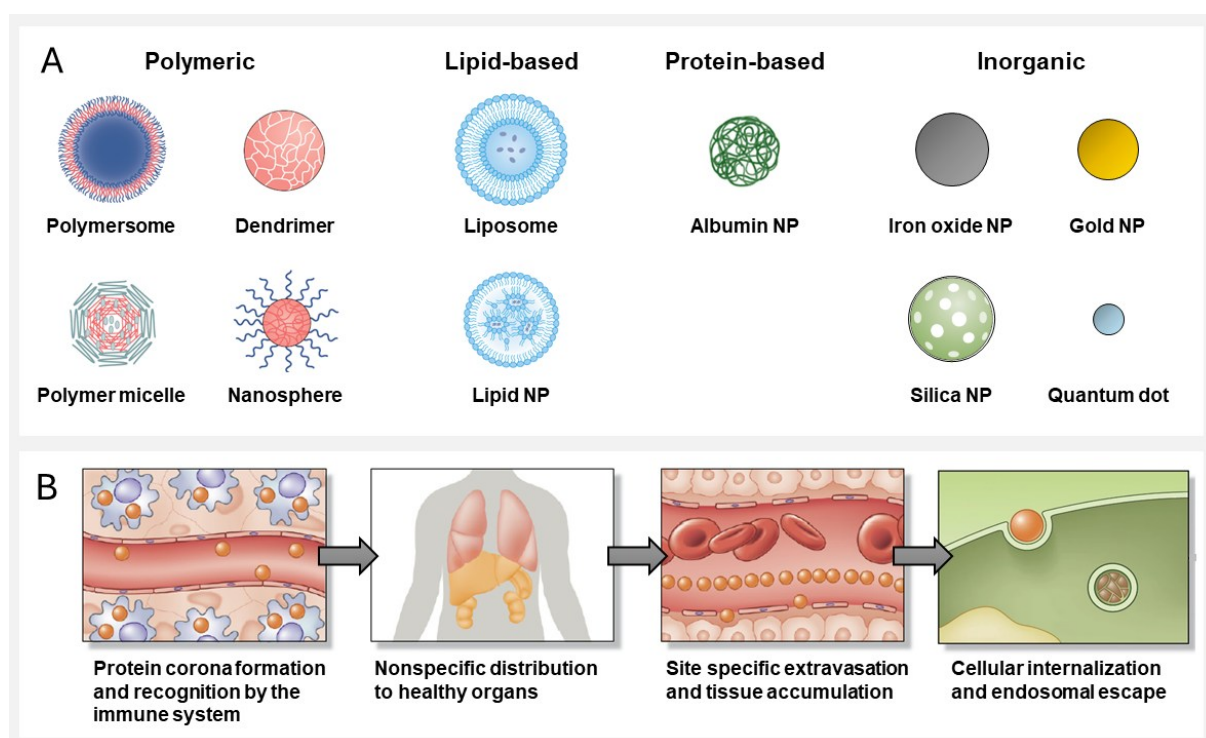


Figure 3. Overview of NP classes and biological barriers encountered by intravenously administered NPs. (A) Classification of NPs by composition into organic NPs including polymeric, lipid-based and protein-based particles and inorganic NPs. (Adapted from Mitchell, Billingsley et al. [69]) (B) Obstacles of intravenously administered NPs on the way to the target site. (Adapted from Blanco, Shen et al. [70])

NPs are applied in numerous medical fields, with cancer therapy and diagnostics representing a particular focus. [71] Due to increased vascular permeability and dysfunctional lymphatic drainage in tumor tissues, NPs passively accumulate in tumors via the so-called enhanced permeability and retention (EPR) effect. [7] Beyond oncology, NPs are also being explored as carriers for antiviral agents or RNA-based therapeutics in the treatment of infectious diseases. [72] Certain NPs are also capable of crossing the blood-brain barrier (BBB), making them promising candidates for the treatment of neurological disorders such as Alzheimer's and Parkinson's disease, where conventional drug delivery systems are often inadequate. [73] Additionally, NPs are utilized in the treatment of cardiovascular diseases, where they enable targeted delivery of anti-inflammatory or antithrombotic agents, as well as real-time imaging of vascular inflammation. [74] Despite their significant potential, several challenges remain for the successful application of NPs as advanced diagnostic and therapeutic tools. Following intravenous administration, NPs encounter a multitude of biological barriers (see **Figure 3 B**). [70] Initially, a protein corona forms around the NPs, and they must evade recognition and clearance by the immune system. [75] Further challenges arise during site-specific extravasation and tissue accumulation. Upon reaching the target cell, additional barriers hinder effective drug delivery. Unlike small hydrophobic molecules, NPs require active cellular uptake mechanisms. [76] Once internalized, NPs are typically sequestered in endosomes, from which either the NP or at least the therapeutic payload must be released. [77] Throughout the entire journey from administration to the target site, NP properties such as size, shape, charge, and surface coating play a crucial role. [5] Due to this complexity, predicting the *in vivo* fate of NPs remains challenging, and unexpected effects may occur. Moreover, certain inorganic NPs, especially those containing heavy metals such as cadmium (e.g., in some quantum dots), raise concerns regarding long-term safety and bioaccumulation. [78]

When moving from research to large-scale applications, it is important to note that the reproducible mass production of NPs with consistent quality remains technically challenging. [79] In addition, there are significant regulatory hurdles. As nanomedicine often ventures into uncharted territory, approval processes can be lengthy and complex. [80] Nevertheless, NPs offer intriguing opportunities, and the integration of NPs with other innovative technologies, such as CRISPR gene editing [81], immunotherapy [82], or personalized medicine [69], opens up new horizons. Overall, developments from the first liposomal drugs to current advances demonstrate that NP research is both highly promising and exceedingly complex. With a growing understanding of nano-bio interactions and through interdisciplinary collaboration between the material and life sciences, NPs have the potential to usher in a new era, fundamentally transforming the ways in which diseases are diagnosed, monitored, and treated.

4. Concepts for the combination of iEDDA reaction and NPs and resulting advanced biomedical applications

This section illustrates how the bioorthogonal iEDDA reaction can be synergistically combined with NPs to improve biomedical applications. The iEDDA reaction can be employed at two stages: during NP preparation and modification or post-synthetically during the application in biological environments, such as cell culture or *in vivo* systems. In the NP fabrication process, the iEDDA reaction is frequently utilized to conjugate antibodies or other complex biomolecules to the NP surface [83–85] or to introduce radioactive labels for imaging purposes. [86–88] For example, Han, Niemeyer et al. used the iEDDA reaction to covalently attach antibodies to quantum dots, facilitating straightforward bioconjugation. [85] Using these QD/antibody conjugates, the authors were able to target a rare cell population in bone marrow at the single-cell level in live animals. Van Onzen, Rossin et al. demonstrated the use of the iEDDA reaction between a tetrazine-tagged radiolabel and a TCO-tagged fluorescent small molecule building block as an efficient radiolabeling strategy. [86] Here, the rapid kinetics of the iEDDA reaction are particularly advantageous, enabling swift and efficient generation of radiolabeled NPs. While the application of the iEDDA reaction in NP modification during synthesis is well-established and justified, it is generally not considered to yield highly innovative concepts. Therefore, the focus of this work is on the post-synthetic application of the iEDDA reaction in biological environments. In this context, the iEDDA reaction enables two-step targeting strategies. Initially, one component is administered to identify and bind the biological target, followed by a second component that facilitates imaging or delivers therapeutic agents. This approach fully exploits the iEDDA reaction's potential, allowing for rapid and selective *in vivo* coupling of two components in the presence of a myriad of other functional groups. The synergy between bioorthogonal chemistry and NPs thus offers significant promise for the development of advanced diagnostic and therapeutic modalities in biomedicine. [89] To systematically review the literature on iEDDA chemistry in conjunction with NPs for pretargeted strategies, studies were categorized based on whether the NP serves as the primary or secondary component within the respective conceptual framework.

4.1 Conjugation of NPs to pre-identified targets

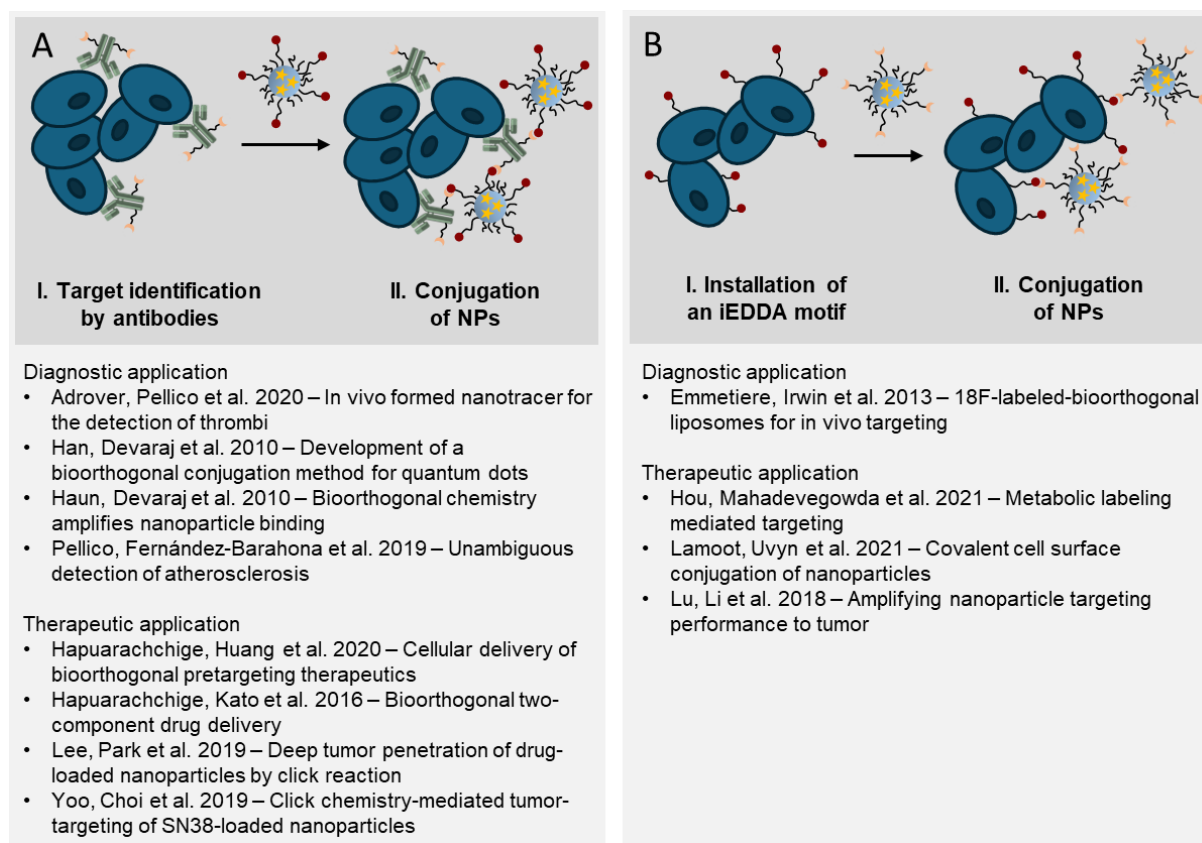


Figure 4. Schematic representation and literature references for pretargeted strategies with NPs and bioorthogonal iEDDA reaction in which the NP is the secondary component. (A) Strategies in which the target is labeled by a corresponding antibody. (B) Strategies in which iEDDA motifs are directly installed on the target cell.

4.1.1 Target identification by antibodies

The combination of iEDDA chemistry with NPs was first implemented by the Weissleder group in 2010. [90] They modified antibodies targeting biomarkers of interest with TCO and subsequently conjugated tetrazine-functionalized magneto-fluorescent NPs (MFNPs) to these antibodies. The authors referred to this technique as ‘bioorthogonal nanoparticle detection’ (BOND). In an approach termed BOND-1, a NP was pre-conjugated with a TCO-modified antibody prior to use, whereas in the BOND-2 approach, the antibody was first used for target cell recognition and only then were tetrazine-functionalized NPs added. The authors were able to demonstrate that the BOND-2 strategy led to higher NP binding to mammalian cells compared to other standard techniques. Due to the large number of TCO moieties attached to the antibody and the relatively small size of the NPs, a multitude of NPs could bind to a single antibody scaffold, thereby significantly amplifying the signal per marker. In contrast, in direct NP immuno-conjugates, typically only one NP binds per antibody. BOND-2 also generated a substantially higher signal than a similar two-step targeting strategy utilizing avidin/biotin. Because of

Chapter 1

the size of avidin, fewer avidin molecules could be attached per NP. Furthermore, biotin must associate within a deep cleft inside the avidin protein, which may physically or spatially constrain certain binding configurations. In contrast, tetrazine as a small molecule can react with TCOs on the antibody without significant steric hindrance. Haun, Devaraj et al. concluded that the increased detection sensitivity resulting from amplification, together with the modular nature of the BOND-2 technique, make it ideally suited for clinically oriented molecular profiling applications. [90]

Pellico, Fernández-Barahona et al. also used a two-step approach with an antibody in their study, which focused on the unambiguous detection of atherosclerosis. [91] Initially, a TCO-modified antibody targeting oxidized LDL was administered. Subsequently, a tetrazine (Tz)-functionalized iron oxide nano-radiomaterial doped with gallium-68 ($^{68}\text{Ga-NRM-Tz}$) was injected, which selectively binds to the antibody. This innovative method combines positron emission tomography (PET) and T1-weighted magnetic resonance imaging (T1-MRI, with positive contrast) to simultaneously provide both structural and functional information about atherosclerotic plaques. Among other advantages, the authors point out that their approach allows the use of short half-life radioisotopes, as the NPs are administered only after the antibodies have localized the target, thereby reducing radiation exposure to healthy tissue. The synergistic combination of NPs and iEDDA reaction expanded for the first time the range of applications of pretargeted imaging to cardiovascular diseases. [91] A follow-up study by the same research group describes the development of "Thrombo-tag," an *in vivo*-generated nanotracer for the rapid detection of thrombi using pretargeted molecular imaging. [92] Based on bioorthogonal chemistry, the system utilizes a combination of a TCO-modified anti-CD41 antibody, which targets the integrin alpha-chain IIb on the platelet membrane of thrombocytes accumulating in thrombi, together with, as in the previous study, a tetrazine (Tz)-functionalized ^{68}Ga -doped iron oxide NP. Whereas previous studies on pretargeted strategies employed a waiting period between antibody administration and radiotracer injection, here the two components are administered simultaneously, allowing the reaction to occur directly in the bloodstream. This enabled rapid and specific labeling of thrombi, which could be visualized by PET imaging within minutes. The presented Thrombo-tag specifically detected thrombi in mouse models of acute lung injury and myocardial infarction, thus demonstrating potential for clinical application in emergency situations. [92]

The concepts outlined here share the common feature of a two-step approach, in which the target is first identified by an antibody, after which NPs are covalently bound to these TCO-modified antibodies via the bioorthogonal iEDDA reaction. NPs are particularly advantageous in this context because multiple imaging modalities can be integrated into them. The combination of two imaging techniques, such as hybrid PET/MRI, could allow the complementary strengths of both modalities to be harnessed. [93] In contrast, it is generally more challenging to incorporate multiple imaging modalities into small molecular probes. Furthermore, NPs could be equipped with additional therapeutic molecules, facilitating future applications in theranostic approaches. [94] It should be noted, however, that the

advantages of NPs come at the cost of losing the rapid excretion due to the size of the material. Nevertheless, in some applications, the overall benefits of NPs may outweigh these drawbacks. The main advantage of the iEDDA reaction lies in enabling the pretargeted strategy by ensuring that NPs are rapidly and selectively bound to the TCO-modified antibodies. [6]

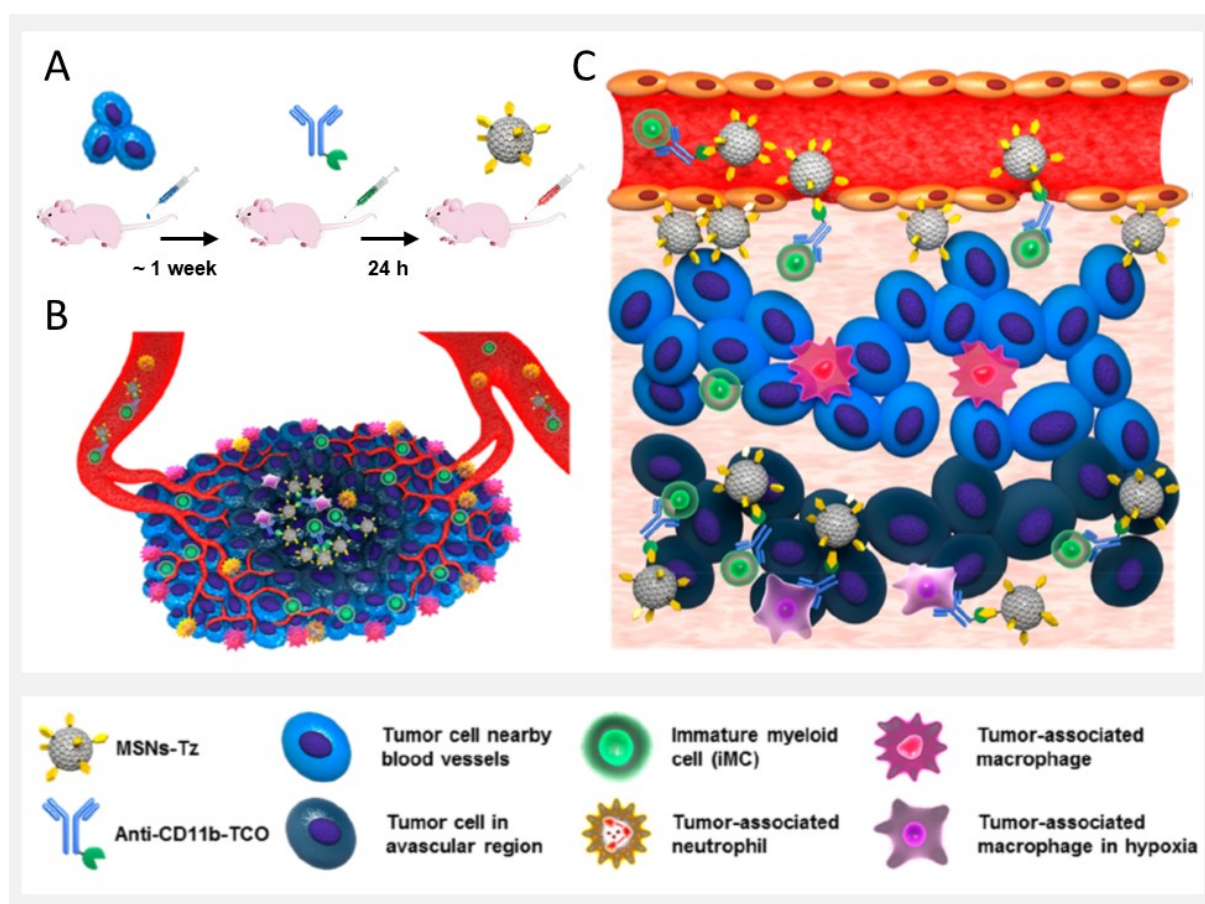


Figure 5. Schematic representation of the click reaction assisted immune cell targeting (CRAIT) strategy to enhance tumor penetration of drug-loaded NPs. (A) In the orthotopic 4T1 tumor mouse model, CD11b antibodies functionalized with TCO and NIR dye are intravenously administered to label CD11b⁺ cells in blood vessels and the tumor microenvironment. Subsequently, mesoporous silica NPs functionalized with tetrazines (MSNs-Tz) are injected and selectively bind to these cells via iEDDA click chemistry. (B) The tumor microenvironment consists of heterogeneous CD11b⁺ inflammatory cells such as immature myeloid cells (iMCs), tumor-associated macrophages (TAMs), and neutrophils; many tumor regions are poorly vascularized and thus difficult to access. (C) The labeled CD11b⁺ cells transport the chemotherapeutic agent-loaded MSNs deep into avascular tumor regions, thereby improving drug penetration. (Adapted from Lee, Park et al. [98])

When moving from diagnostic to therapeutic applications of this concept, it becomes evident that it is employed almost exclusively for cancer treatment. The general procedure remains largely unchanged. [95–97] An antibody targeting a specific cancer marker is modified with TCO and administered first. Subsequently, a tetrazine-functionalized, drug-loaded NP is injected. These NPs react via the iEDDA

Chapter 1

reaction with the TCO-modified antibodies directly on the target cell. Each antibody typically presents multiple TCO groups, allowing several NPs to bind per antibody. Hapuarachchige, Kato et al. discussed that cross-linking can also occur when a NP reacts with two adjacent antibodies. [96] The authors reported that nanoclusters can form on the cell surface, which enables more efficient internalization. Studies in this area mainly differ with respect to the choice of antibody, NP material, and therapeutic agent. While most previous studies have focused primarily on the direct targeting of tumor cells, Lee, Park et al. utilized immune cells as carrier vehicles to achieve deeper tumor penetration. In general, the penetration of NPs into tumors is typically limited. Thus, this approach represents an interesting new strategy to achieve better distribution of therapeutics within the tumor. CD11b-positive immune cells were labeled with TCO-modified antibodies, after which tetrazine-functionalized mesoporous silica NPs loaded with doxorubicin were administered. [98] The labeled immune cells infiltrated the tumor tissue and transported the drug carriers deep into avascular tumor regions (see **Figure 5**). The "Trojan horse" approach resulted in a significant reduction in tumor burden, whereas free doxorubicin and doxorubicin-loaded MSNs alone were ineffective.

In general, these concepts raise the question of what advantages they offer over conventional antibody-drug conjugates. One possible benefit may be that nanoparticles are capable of transporting larger amounts of therapeutic agents. The two-step approach described here, also allows for the binding of multiple NPs per antibody as well as potential cross-linking events, resulting in the formation of nanoclusters on the target cell surface. Another potential advantage of the two-component strategy lies in the ability to combine different therapeutic agents with the same antibody, without the need to optimize a new antibody-drug conjugate for each combination. This may allow for more rapid adaptation to different cancer types or the emergence of drug resistance.

4.1.2 Installation of an iEDDA motif

In addition to the possibility of identifying the target through an antibody, another approach is to directly attach one of the iEDDA reaction partners to the target structure. The NP, administered as the second component, can then covalently bind to the target. A straightforward strategy to install an iEDDA motif on the target cell would be metabolic glycoengineering. [99] This approach is relatively simple and widely implemented for azides as bioorthogonal motifs. [100] Through the use of azido sugars, a large number of azide groups can be introduced as artificial low molecular weight cell surface receptors with a reported minimal influence on cellular functionality. [101] Azides primarily enable the reaction with strained cycloalkynes as complementary reaction partners in the strain-promoted azide-alkyne cycloaddition (SPAAC) reaction. [25] However, the SPAAC reaction is significantly slower than the iEDDA reaction, thus limiting its applicability. For the iEDDA reaction, either tetrazine or TCO would need to be metabolically installed on the target. Both reactants, however, are considerably larger and

notably more apolar compared to azides as small bioorthogonal markers, making their metabolic installation more challenging. [3] Lamoot, Uvyn et al. therefore proposed a concept that takes advantage of the fact that azides are relatively easy to introduce. [102] In their concept, cells were first metabolically labeled with azides, followed by reaction with a DBCO-Tz linker via SPAAC. The tetrazine thus attached can subsequently react with TCO functionalized NPs in an iEDDA reaction. The authors emphasized that, in contrast to the direct attachment of DBCO-NPs via SPAAC, their two-step approach enables highly specific cell surface conjugation of the lipid NPs with very low non-specific background binding. However, despite the apparent success of the method, it is noted that the requirement for two consecutive steps makes the process somewhat cumbersome.

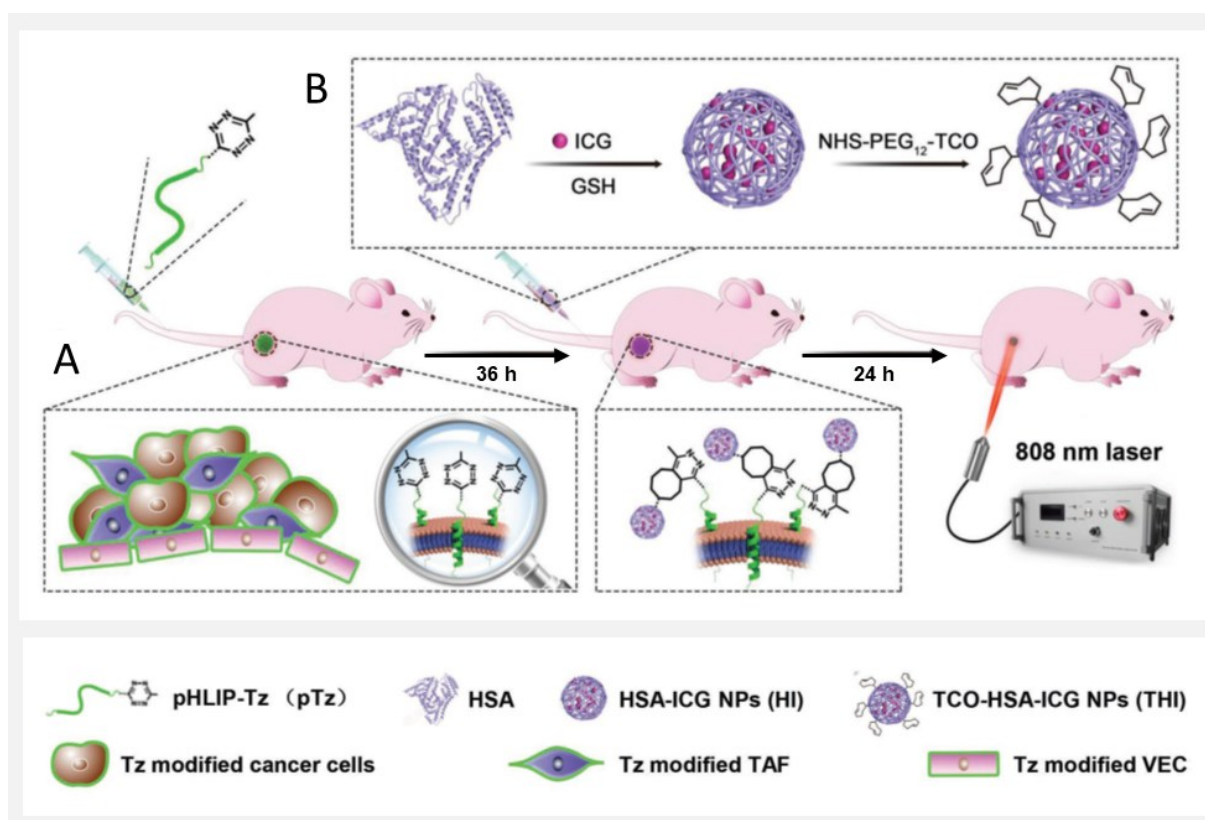


Figure 6. Schematic illustration of the two-step tumor targeting strategy using pHLIP-Tz and TCO-HSA-ICG NPs. (a) Tetrazine (Tz) was conjugated to the pH (low) insertion peptide (pHLIP), enabling selective incorporation into various cells within the acidic tumor microenvironment after intravenous injection. (b) Indocyanine green (ICG)-loaded, trans-cyclooctene (TCO)-conjugated human serum albumin NPs (TCO-HSA-ICG NPs, denoted as THI) were prepared as carriers for secondary administration. Subsequent to the EPR effect, these particles efficiently bind to the pre-anchored Tz groups via iEDDA click chemistry, enhancing both targeting precision and photothermal therapeutic efficacy. (Adapted from Lu, Li et al. [106])

Another option, besides metabolic labeling, to install a reactive partner for the iEDDA reaction on target cells is the use of pH (low) insertion peptides (pHLIP). These are peptides that exclusively adopt an α -

Chapter 1

helical conformation and insert into the cell membrane under acidic conditions. [103] Primarily, this takes advantage of the acidic tumor microenvironment, so that corresponding concepts are mainly found in cancer detection or therapy. [104] Emmetiere, Irwin et al. utilized this concept for cancer detection by covalently binding TCO-functionalized ^{18}F -liposomes to pHLIP-Tz in tumor tissue. As a result, there was an accumulation of radioactivity in the tumor, which could be detected by PET. [105] Lu, Li et al. focused more on the therapeutic application of the concept. After installing numerous tetrazine moieties in the tumor tissue via pHLIP, they administered indocyanine green (ICG)-loaded and TCO-conjugated human serum albumin (HSA) NPs (TCO-HSA-ICG NPs). [106] These can react via the iEDDA reaction, resulting in a greatly improved targeting performance and photothermal therapeutic effect based on the two-step strategy (see **Figure 6**). In particular, when compared to NPs that accumulated solely via the EPR effect but also to NPs modified with folic acid as an example of classical active targeting, a marked difference was observed. Since the acidic environment is characteristic of solid tumors, the pHLIP-based approach could be a promising option for advanced NP-based antitumor therapy. This approach also allows for addressing the problem of tumor heterogeneity, as, in contrast to classical targeting concepts, it does not rely on the presence of specific tumor markers.

The advantage of NPs in this context lies in their ability to transport large amounts of therapeutic agents, to protect their cargo, and to accommodate multiple imaging modalities within a single NP for imaging purposes. Furthermore, NPs can enable a combination of diagnostic and therapeutic functions, thus advancing theranostic applications. The iEDDA reaction allows for rapid and selective conjugation of NPs *in vivo* to the sites marked by pHLIP, making it an indispensable and valuable tool.

4.2 Post-accumulation modification of NPs

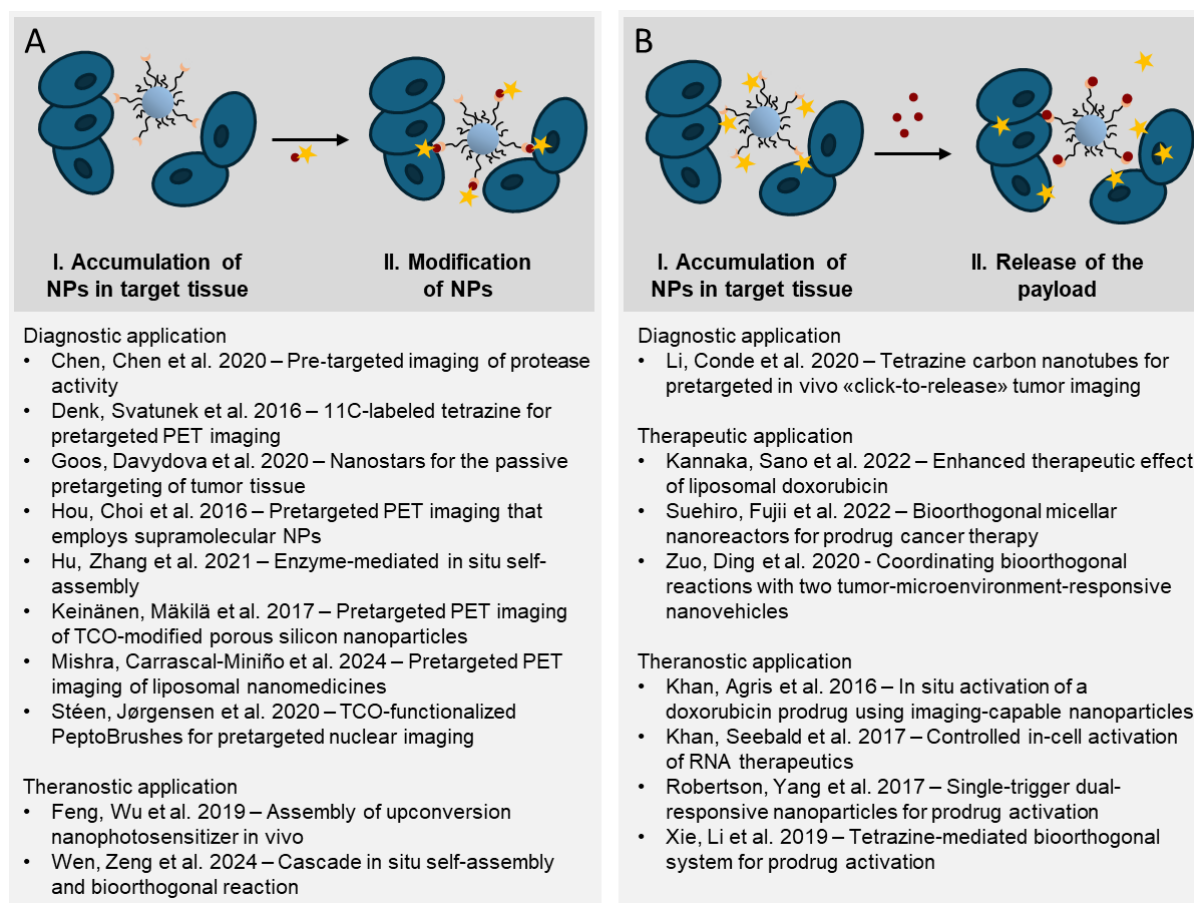


Figure 7. Schematic representation and literature references for pretargeted strategies with NPs and bioorthogonal iEDDA reaction in which the NP is the primary component. (A) Strategies in which the NP is functionalized via the iEDDA reaction after accumulation. Mainly used for the attachment of short-lived radioisotopes for PET imaging. (B) Strategies in which, after NP accumulation, cargo is selectively released via click-to-release iEDDA reaction. Mainly used for switchable prodrug activation.

4.2.1 Modification of NPs

The major advantage of the iEDDA reaction lies in its ability to enable two-step targeting concepts. In such strategies, the NP does not have to be the second component conjugating to pre-identified targets. Indeed, potentially even more intriguing applications arise when the particle is administered as the first component. NPs can accumulate in tumor tissue via the EPR effect. [7] If a radioisotope functionalized with the corresponding partner for the iEDDA reaction is subsequently administered, tumors can be precisely localized by PET imaging. Several publications have leveraged and further developed this concept. For example, Hou, Choi et al. utilized supramolecular chemistry to produce tumor-targeting NPs functionalized with TCO. [107] After intravenous administration, these NPs accumulated in tumors of living mice via the EPR effect. Owing to the dynamic nature of their supramolecular structure, the NPs can partially disassemble to release a TCO-grafted molecular building block. As the second

Chapter 1

component, a positron-emitting radioisotope (^{64}Cu) modified with tetrazine was injected. Thanks to the tetrazine modification, the radioisotope could bind selectively and irreversibly to the TCO. Following rapid clearance of the unreacted ^{64}Cu -Tz probe, high-contrast PET images of the tumor could be acquired. A similar approach was taken by Goos, Davydova et al., who, instead of supramolecular NPs with dynamic structure, used polymeric nanostars for the passive pretargeting of tumor tissue. [108] Maximal accumulation of the nanostars in tumor tissue was reached three days post-injection and ^{18}F -modified tetrazine was then administered. The authors evaluated various strategies to enhance the tumor-to-background ratio, including the use of masking strategies, comparison of tetrazines with different pharmacokinetic properties, and adjustment of the molecular distance between the TCOs and the polymer backbone. The work of Stéen, Jørgensen et al. also falls into this category. Here, so-called PeptoBrushes, single-molecule polymer NPs, were used as targeting agents, while a ^{111}In -labeled tetrazine derivative served as the imaging agent. [109] An important advantage of these concepts is that the targeting step can be temporally separated from the imaging step. This allows the use of radioisotopes with short half-lives, even though the NPs may accumulate in the tumor tissue only slowly, and thereby reduces the overall radiation burden for the patient. Denk, Svatunek et al. demonstrated that even a low-molecular-weight tetrazine labeled with the short-lived positron emitter carbon-11 (half-life of ^{11}C : 20.4 min) can be successfully employed for pretargeted imaging with NPs. [110] The pretargeting concepts with NPs are therefore of particular interest for single-photon emission computed tomography (SPECT) or positron emission tomography (PET). Other medical imaging modalities have not been extensively explored. Compared to antibody-based pretargeting approaches, the NP-based strategy, by exploiting the EPR effect covers a broader spectrum of tumor types.

It is also interesting when not an already assembled NP accumulates in the target tissue, but rather, NPs are generated *in situ* through specific enzymatic activity. Chen, Chen et al. monitored the activity of an enzymatic target, in their case, caspase-3/7 activity. [111] Initially, a small substrate probe was employed, which contained a peptide sequence cleavable by caspase-3/7. Upon enzymatic cleavage, a reactive aminothioliol group was released, which subsequently reacted with an aromatic nitrile group, thereby triggering macrocyclization. [112] The resulting molecules then aggregated *in situ*, driven by hydrophobic and π - π interactions, to form NPs. [113] Due to their size and interactions with the local environment, these nanoaggregates cannot simply diffuse away and thus remain at the target site, leading to local accumulation. In a second step, imaging was enabled by a bioorthogonal labeling. The nanoaggregates contained TCO as the reactive site. Injection of a tetrazine-labeled imaging tag, such as Tz-BDP for fluorescence or Tz- ^{64}Cu for PET, resulted in a rapid and highly selective iEDDA reaction between tetrazine and TCO. This led to the formation of a stable imaging complex, allowing for precise visualization of enzymatic activity. Since enzymatic activation and imaging are separated in time, the probe can first accumulate at the target site before labeling, which improves the signal-to-noise ratio. Moreover, the substrate probe can be repeatedly injected to generate more TCO-modified

nanoaggregates and further enrich them at the target site. In summary, the authors demonstrated that this approach allows for precise and specific visualization of protease activity in both cell cultures and living organisms. [111]

Hu, Zhang et al. also employed a strategy in which NPs are generated *in situ* through enzymatic activity. [114] They used a small-molecule probe with quenched NIR fluorescence and low MRI signal, which could penetrate deeply into tumor tissues. Alkaline phosphatase (ALP) on the tumor cell membrane could activate the probe, whereupon enzymatic cleavage simultaneously triggered a fluorogenic reaction and initiated *in situ* self-assembly of NPs. This process enhanced both the NIR fluorescence and, via aggregation of the nanoaggregates, the MRI signal. [115] In addition, the probe was equipped with TCO for a subsequent bioorthogonal iEDDA reaction. As a result, tetrazine-modified radiotracers, such as ^{68}Ga -Tz, could be administered and bind specifically to the TCOs. This enabled the accumulation of radioactivity in the tumor tissue and, besides NIR fluorescence and MR imaging, also advanced PET imaging. Thus, pretargeted multimodal imaging resulted in a powerful method for non-invasive imaging of ALP-positive tumors with high sensitivity, deep tissue penetration, and excellent spatial resolution. [114] A particular advantage compared to the strategy of Chen, Chen et al. is that the formation of nanoaggregates can be directly monitored in real time, as it is associated with an increase in fluorescence intensity. This also facilitates the determination of the optimal time point for subsequent injection of the tetrazine-labeled radioisotope.

In a subsequent study, Wen, Zeng et al. further expanded the promising concept developed by this research group by incorporating a therapeutic approach. [116] They again employed the small-molecule probe, which can be similarly activated and converted into NPs via alkaline phosphatase (ALP)-mediated fluorogenic reaction and *in situ* self-assembly within tumors. However, instead of conjugating a radioisotope for PET imaging through the iEDDA reaction, a photosensitizer for photodynamic therapy (PDT) was attached. In addition, a tetrazine-labeled small-molecule carbonic anhydrase (CA) inhibitor was co-administered to effectively alleviate the hypoxic tumor microenvironment. The authors reported that the iEDDA reaction between the nanoaggregates, the near-infrared (NIR) nanophotosensitizer, and the carbonic anhydrase inhibitor led to the formation of nanoclusters, resulting in substantially enhanced retention within tumor tissues (see **Figure 8**). They demonstrated that subcutaneous HeLa tumors could be completely eradicated and no tumor recurrence was observed in treated mice following irradiation with an 808 nm laser. [116] This two-step strategy, combining enzyme-mediated *in situ* self-assembly of NPs and bioorthogonal conjugation, advances tumor photodynamic therapy in living mice with high sensitivity and spatial resolution.

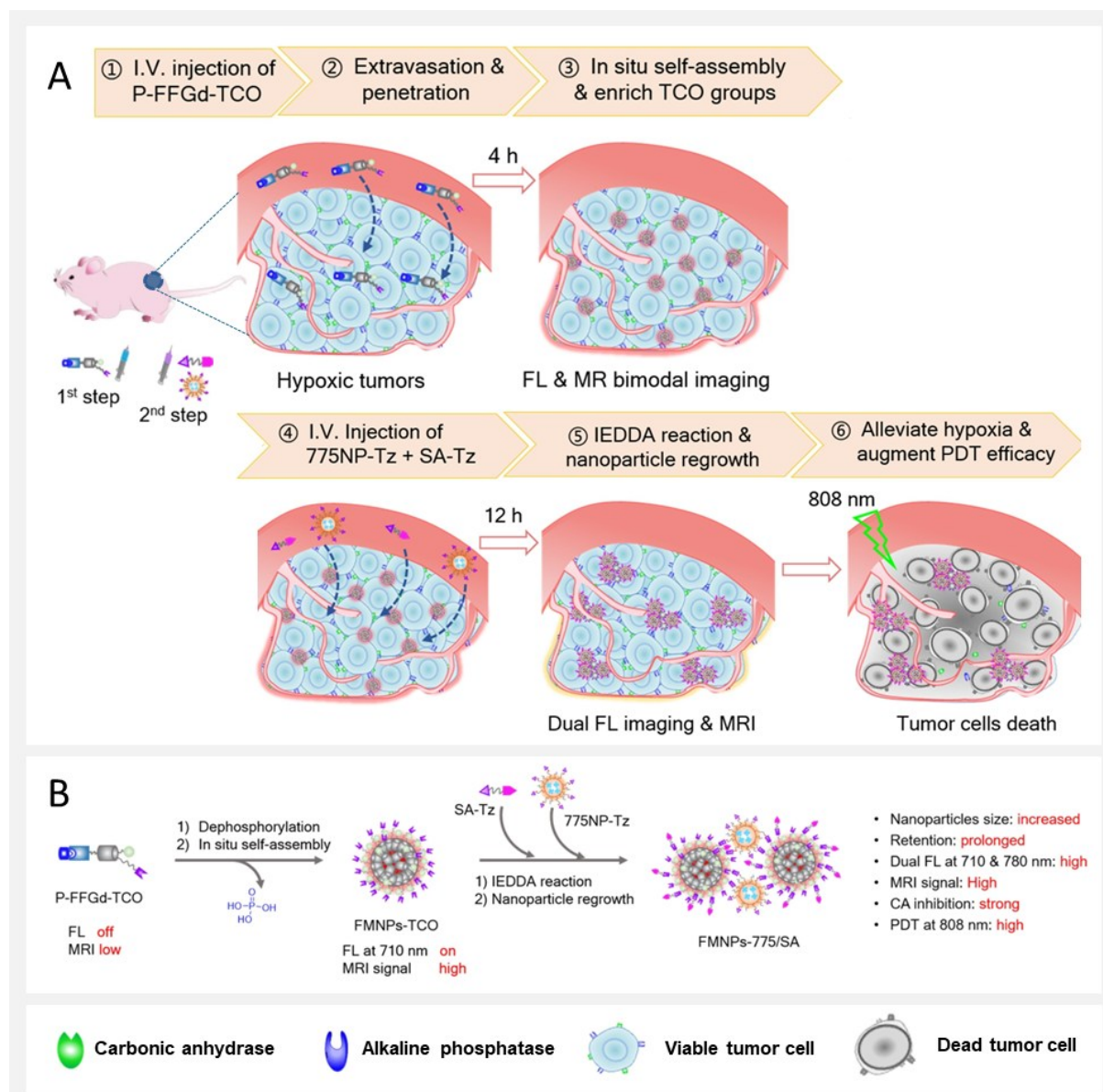


Figure 8. Schematic illustration of pretargeted multimodal cancer theranostics via cascade ALP-mediated *in situ* self-assembly and bioorthogonal iEDDA reaction. (a) Mechanism of the two-step pretargeting strategy: After intravenous injection, P-FFGd-TCO extravasates into s.c. HeLa tumors, where membrane-bound ALP catalyzes its dephosphorylation and *in situ* self-assembly into fluorescent and magnetic TCO-containing NPs (FMNPs-TCO). These FMNPs-TCO on tumor cell membranes serve as artificial antigens to capture subsequently injected 775NP-Tz and SA-Tz via rapid iEDDA click chemistry, leading to crosslinking and formation of FMNPs-775/SA microparticles. FMNPs-775/SA enable prolonged retention in tumor tissue, supporting sustained CA inhibition, hypoxia alleviation, and enhanced photodynamic therapy (PDT) efficacy, guided by dual NIR fluorescence and MRI signals. (b) Schematic process of ALP-mediated self-assembly and subsequent binding of 775NP-Tz and SA-Tz to form FMNPs-775/SA. (Adapted from Wen, Zeng et al. [116])

In contrast to the aforementioned concept, Feng, Wu et al. employed fully assembled NPs relying on their accumulation in tumor tissue via the enhanced permeability and retention (EPR) effect combined with folic acid-mediated active targeting. [117] They similarly utilized the bioorthogonal inverse

electron-demand Diels–Alder (iEDDA) reaction for the rapid and selective conjugation of a photosensitizer onto the NPs for photodynamic therapy (PDT). Prior to photosensitizer administration, the NPs could be employed solely as contrast agents under near-infrared (NIR) light irradiation for imaging purposes. Following the iEDDA reaction, efficient energy transfer occurs between the upconversion NPs (UCNPs) and rose bengal as the photosensitizer, enabling PDT with high efficacy. Compared to “all-in-one” strategies [118, 119], in which photosensitizers are covalently anchored to the UCNPs, the advantage of this approach may lie in the practical benefit of spatially and temporally separating imaging and therapeutic functionalities. For example, during surgery, localization of the tumor margin via UCNP-mediated imaging may suffice, while PDT can subsequently be applied postoperatively to prevent tumor recurrence.

In summary, NPs as primary targeting vectors present compelling opportunities. When used as secondary components, emphasis is mainly placed on the intrinsic NP properties such as multimodal imaging capability or high cargo loading capacity. Conversely, when employed as primary components, the biological interactions of NPs *in vivo* assume greater significance. The EPR effect is frequently exploited for passive tumor accumulation of NPs, and ligands can be incorporated for active targeting. The temporal decoupling of accumulation and imaging enabled by the iEDDA reaction makes the combination of bioorthogonal chemistry and NPs particularly attractive for PET imaging, allowing the use of short-lived radioisotopes and resulting in reduced radiation exposure for patients alongside improved tumor-to-background signal ratios. Moreover, the in-situ generation of NPs via enzymatic activity followed by self-assembly of smaller probes into NPs represents an additional promising avenue warranting further exploration.

4.2.2 Release of the payload

While the previous section discussed that NPs can be administered as the primary component and subsequently functionalized via the bioorthogonal iEDDA reaction after their accumulation, there is also the possibility of employing the iEDDA reaction to deliberately cleave a component from the NP. These so-called click-to-release strategies have been applied in a variety of ways in conjunction with NPs. Fundamentally, there are two main approaches: A drug substance can be conjugated to the NPs via a TCO linker that is cleavable through the iEDDA reaction. In this case, the drug is inactivated and can be released upon addition of tetrazine as a trigger. Alternatively, the iEDDA-releasable TCO moiety can be attached to the drug molecule itself, thereby generating a prodrug that can be activated by the reaction with tetrazine-functionalized NPs to unleash its therapeutic effect.

Khan, Agris et al. were the first, in 2016, to utilize the click-to-release capability of the iEDDA reaction in combination with NPs. [120] They conjugated cleavable TCO to doxorubicin, which led to a significant reduction in the potency of the drug. The Dox-TCO prodrug can then react with tetrazine-

Chapter 1

functionalized NPs that have previously accumulated in tumor tissue, releasing the biologically active chemotherapeutic doxorubicin form. An advantage of this concept is that the fluorescently-labeled magnetic iron oxide NPs (MNPs) enable tracking of accumulation via fluorescence microscopy, thereby allowing for image-guided prodrug activation. Suehiro, Fujii et al. also employed Dox-TCO as a prodrug. [121] In their case, the release of the active compound doxorubicin occurred in polymer micelles equipped with tetrazine. Unlike the NIRF-labeled MNPs, this approach loses the imaging capability. However, the authors observed that the iEDDA reaction can be accelerated in the micellar system compared to the free tetrazine. Thus, they described their polymer micelles as bioorthogonal micellar nanoreactors for *in vivo* chemotherapeutic prodrug activation. It was demonstrated that this concept led to inhibition of tumor growth without significant systemic toxicity. Importantly, the click-to-release capability of the iEDDA reaction can be utilized not only for therapeutic applications in conjunction with NPs, but also for diagnostic purposes. Li, Conde et al. developed a NIR fluorophore whose fluorescence could be substantially quenched by conjugating TCO to its amine group. [122] Upon reaction with tetrazine-modified single-walled carbon nanotubes (TZ@SWCNTs), which accumulate in tumor tissue via the EPR effect, fluorescence is restored upon tetrazine-triggered ligation and liberation of the fluorophore. This concept enabled real-time, non-destructive tumor fluorescence imaging with a high target-to-background ratio.

Another interesting approach utilizing the click-to-release concept was presented by Zuo, Ding et al. They also employed doxorubicin in the form of a Dox-TCO prodrug, in which doxorubicin is caged by a cleavable TCO group. In contrast to previous studies, they encapsulated the prodrug in stimuli-responsive polymeric micelles. [123] The tetrazine counterpart required for drug release via the iEDDA reaction was, in turn, encapsulated in a different type of polymeric micelle. Only within the tumor tissue can both nanovehicles dissociate by responding to two distinct tumor microenvironmental stimuli. The Dox-TCO prodrug was released from low pH-sensitive polymeric micelles, while tetrazine was liberated from matrix metalloproteinase 2 (MMP-2)-sensitive polymeric micelles. Immediate iEDDA reaction took place, resulting in the cleavage of the TCO group from doxorubicin. This precisely regulated doxorubicin delivery led to reduced side effects compared to the clinical Doxorubicin hydrochloride liposomal injection (Doxil), while the antitumor therapeutic efficacy remained potent. It should be noted at this point that not only prodrugs inactivated via cleavable TCO have been used. Xie, Li et al. utilized an alternative approach in their study, where the drug camptothecin was caged via a vinyl ether. [124] The bioorthogonal camptothecin prodrug was further encapsulated within a liposome. Through the iEDDA reaction with tetrazine, which was conjugated to gold nanorods, camptothecin could be released for chemotherapy. The gold nanorods additionally exhibited high photothermal capability for photothermal therapy, and the combination of chemo- and photothermal therapy resulted in greatly inhibited tumor growth in mice.

As previously discussed, the concept can also be applied in reverse, such that the drug is not administered as a prodrug with TCO, but rather is directly attached to the NP. Khan, Seebald et al. conjugated siRNA to the surface of iron oxide NPs via the TCO linker that is cleavable through the iEDDA reaction. [125] By immobilizing the siRNA on the NP, its activity was completely suppressed. The polydextran coating of the NPs appears to prevent the siRNA from accessing the RNA interference specificity complex (RISC) and thus from silencing its target gene. As the siRNA was labeled with a NIR fluorophore, the cellular uptake of the siRNA-loaded NPs could be monitored by fluorescence microscopy. Once uptake was complete and the NPs had accumulated at the target site, tetrazine was added as a cell-permeable small molecule chemical trigger to release the siRNA from the NPs. The activated siRNAs, targeting GFP and the CDK8 gene as examples, exhibited the expected and desired activity against their respective target genes. The siRNA targeting the CDK8 gene was able to silence the oncogene, thereby reducing the proliferation of breast cancer cells. In principle, this strategy should be applicable for the activation of any siRNA, and thus holds great potential. The same research group further advanced the concept and utilized, in a follow-up study, the fact that axially substituted TCO reacts faster than equatorially substituted TCO. They conjugated to the same NP one drug via a di-axial fast-release TCO linker and another drug via a di-equatorial slow-release TCO linker. [126] However, in this study, they did not use siRNA as a drug but, to validate the system, initially employed fluorophores and subsequently the small molecule drugs doxorubicin and PAC-1. Upon addition of tetrazine as a biologically inert small molecule trigger, the component linked via the fast-reacting TCO linker is released within minutes, whereas the component attached via the slow-reacting TCO linker is released over several days. Thus, the addition of a single trigger enables controlled and temporally staggered release of two drugs. The authors demonstrated that this concept was successfully applied for the treatment of triple-negative BT-20 breast cancer cells, wherein the NP with fast-releasing PAC-1 and slow-releasing doxorubicin showed superior therapeutic efficacy compared to a NP releasing both drugs simultaneously. This approach opens new possibilities for various combination therapies where two drugs are intended to be released in a temporally controlled manner.

Kannaka, Sano et al. presented a concept that does not rely on the classical click-to-release iEDDA reaction. In their work, no cleavage of covalent bonds occurs as in the previously discussed examples in this section. Instead, they employ the iEDDA reaction to transiently and selectively destabilize the liposomal membrane, resulting in the release of the drug payload from the liposome. [127] Thus, in a broader sense, this also constitutes release of payload via the iEDDA reaction. In the two-step therapeutic strategy, the liposomes first accumulate in tumor tissue via the EPR effect. The administration of a norbornene derivative initiates the bioorthogonal iEDDA reaction with tetrazine embedded in the liposomal membrane (see **Figure 9**). This leads to increased membrane fluidity and a reduction of the repulsive forces between liposomal components, thereby resulting in significant drug release. The authors demonstrated that the combination of liposomes encapsulating doxorubicin and

Chapter 1

tetrazine in the membrane with norbornene suppressed tumor growth more effectively compared to conventional doxorubicin-encapsulated liposomes. The iEDDA reaction in the liposomal membrane enabled a switchable, accelerated drug release, rendering this concept a promising approach for effective cancer therapy.

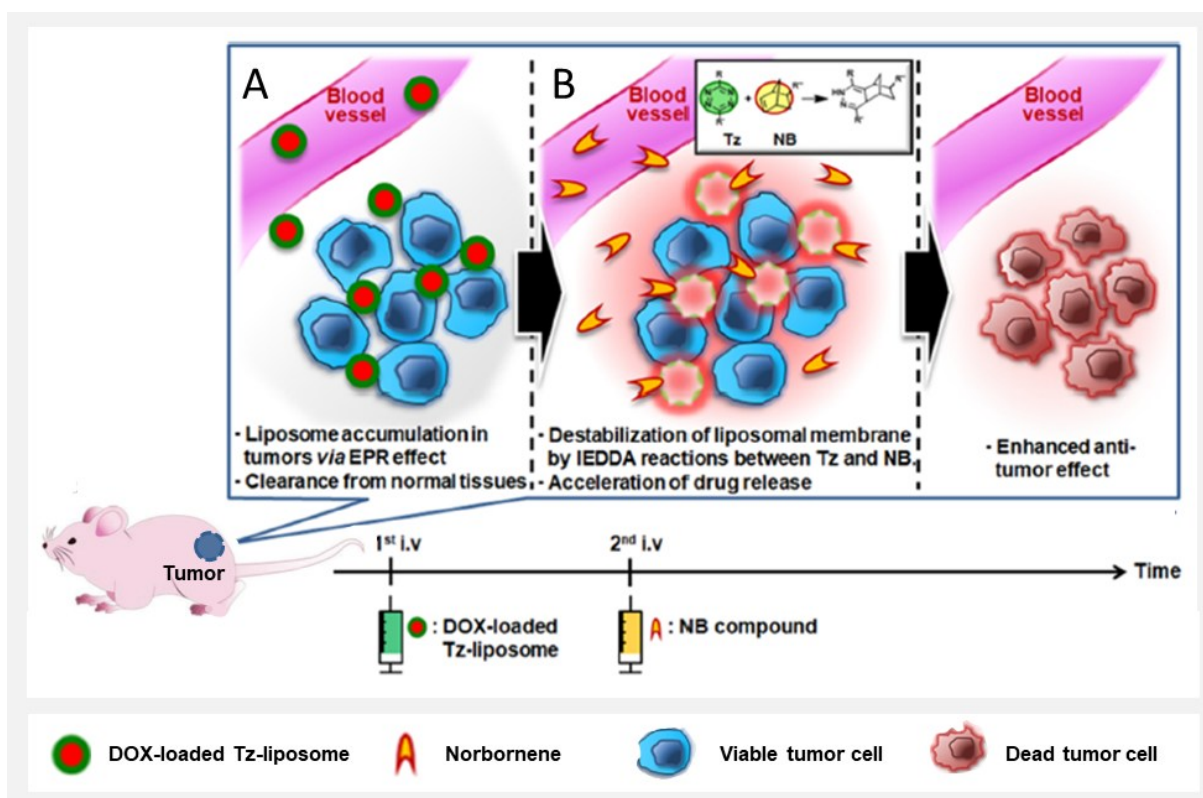


Figure 9. Schematic illustration of the strategy for cancer therapy using a liposomal formulation and accelerated drug release via the iEDDA reaction in the liposomal membrane. (a) In the first step, tetrazine (Tz)-bearing liposomes accumulate selectively in the tumor tissue after injection via the enhanced permeability and retention (EPR) effect. (b) In the second step, a norbornene derivative is administered, which triggers a bioorthogonal iEDDA reaction with Tz in the liposomal membrane. This leads to a transient destabilization of the membrane and accelerated release of the encapsulated drug within the tumor. (Adapted from Kannaka, Sano et al. [127])

In general, it can be stated that the click-to-release iEDDA reaction utilizing TCO containing a carbamate-linked payload at the allylic position represents a highly valuable tool, particularly for therapeutic applications. This strategy enables the targeted activation of prodrugs on NPs or the on-demand release of drugs bound to NPs. The combination with NPs offers the additional advantage that NPs can be employed with appropriate imaging modalities. This allows for monitoring of NP accumulation and facilitates image-guided prodrug activation, which can contribute to improved therapeutic outcomes. Beyond imaging capabilities, other NP properties can also be exploited, such as the potential for photothermal therapy. The click-to-release iEDDA reaction on NPs opens numerous

opportunities to develop novel and enhanced therapies, and particularly the synergy between the iEDDA reaction and various NP materials provides significant advantages for future developments.

5. Key factors for a successful combination of iEDDA reaction and NPs

5.1 Kinetics of the iEDDA reaction on the nanoparticle

A rapid reaction on the NP surface is particularly important for the *in vivo* modification of NPs via the iEDDA reaction. In living systems, only low concentrations of the two reactants are likely to be present, and the iEDDA reaction must proceed sufficiently fast even at these low concentrations. In general, electron-withdrawing groups on the tetrazine increase the reaction rate. The electron-withdrawing effect lowers the LUMO of the diene and reduces the gap between the LUMO of the diene and the HOMO of the dienophile, thereby accelerating the reaction (see **Figure 10 A**). [39] Furthermore, it should be noted that hydrogen-substituted tetrazines result in faster kinetics than would be predicted based on frontier molecular orbital (FMO) considerations. For example, hydrogen-substituted tetrazines react significantly faster than methyl-substituted tetrazines, suggesting that steric effects may also play an important role in the rate of the reaction (see **Figure 10 B**). [42] These general principles are likely to apply to iEDDA reactions on NPs as well. For the combination of NPs with the bioorthogonal iEDDA reaction, a variety of tetrazine substitution patterns have been employed to date. Most commonly, tetrazines on one side phenyl-substituted and on the other hydrogen-substituted are used, likely due to the good balance of stability and fast reaction kinetics reported by Karver, Weissleder et al. [42] Phenyl/methyl-substituted tetrazines are also frequently encountered. In contrast, dipyritydyl-, diisopropyl- or diphenyl-substituted tetrazines are rarely used in studies combining iEDDA reactions and NPs.

As the counterpart to tetrazine in the iEDDA reaction on NPs, the standard TCO is used almost exclusively. For click-to-release applications, TCOs containing a carbamate-linked payload at the allylic position are also used, enabling the release of the cargo upon the iEDDA reaction. [128] In general, the axial isomer of TCO reacts faster than the equatorial isomer. [41] Robertson, Yang et al. exploited this property and developed a NP concept in which TCO was substituted both axially and equatorially for click-to-release applications. A drug was attached to the axially substituted TCO for rapid release upon addition of tetrazine, while a drug attached to the equatorially substituted TCO was intended for slow release. [126] Notably, strategies aimed at further increasing the reaction rate of the iEDDA reaction by modifying the dienophile TCO have received little attention in combination with NPs. Only Denk,

Chapter 1

Svatunek et al. have employed s-TCO on their mesoporous silica NPs. [110] The s-TCO was developed by Taylor, Blackman et al. to accelerate the iEDDA reaction further by increasing ring strain through fusing a cis-cyclopropane onto the cyclooctene moiety. [129] It can be speculated that the use of advanced TCO derivatives is limited by their commercial availability. In a few cases, norbornene has been used as a dienophile instead of TCO. However, it should be noted that the reaction between tetrazine and norbornene is significantly slower ($1\text{--}10\text{ M}^{-1}\text{ s}^{-1}$). [40]

It is also of fundamental interest whether the interplay between NPs and the bioorthogonal iEDDA reaction leads to unique features regarding reaction kinetics. One might expect that anchoring one of the iEDDA reaction partners on the NP surface would result in fewer collisions between the reactants and thus a slower reaction rate. Surprisingly, studies employing the iEDDA reaction on NPs have almost never investigated the reaction kinetics of the iEDDA reaction on the particle itself. Stéen, Jørgensen et al. are among the few groups who compared the reaction rate on NPs with that in solution and obtained the remarkable result that the measured reaction rates per TCO on their single-chain polymer NPs far exceeded those of a PEG derivative with a short PEG linker. [109] The second-order rate constant was increased up to 45-fold on the NP. They attributed this to a hydrophobic effect, discussing that the side chains of the polymer could arrange themselves to form hydrophobic TCO patches consisting of 2–3 TCO moieties, which could serve as high-affinity binding sites for lipophilic tetrazines. Furthermore, Steen, Jørgensen et al. demonstrated that more lipophilic tetrazines clearly accelerate the iEDDA reaction on their polymer NPs. Similar observations were made by Suehiro, Fujii et al. for their click-to-release system. [121] They used tetrazine in block copolymer micelles for targeted uncaging of doxorubicin-TCO and reported that the reaction in the micellar system proceeded faster than with free tetrazine. They postulated that TCO-functionalized prodrugs could diffuse into the interior of the block copolymer micelle. The hydrophobic Dox-TCO would accumulate in the hydrophobic core, leading to a locally increased concentration of Dox-TCO, which in turn would result in a faster iEDDA reaction and thus more rapid cargo release. The authors went so far in their conclusion as to suggest that polymer micelles could be used as nanoreactors for prodrug activation. Thus, the literature provides evidence that, in particular, polymer NPs can promote significantly faster iEDDA reactions than in solution, driven by the hydrophobic effect (see **Figure 10 C**). This effect has also been observed with carbon nanotubes during the uncaging of prodrugs. Li, Conde et al. reported that tetrazine-functionalized carbon nanotubes exhibited increased decaging reactivity compared to the small-molecule tetrazine counterpart. [122]

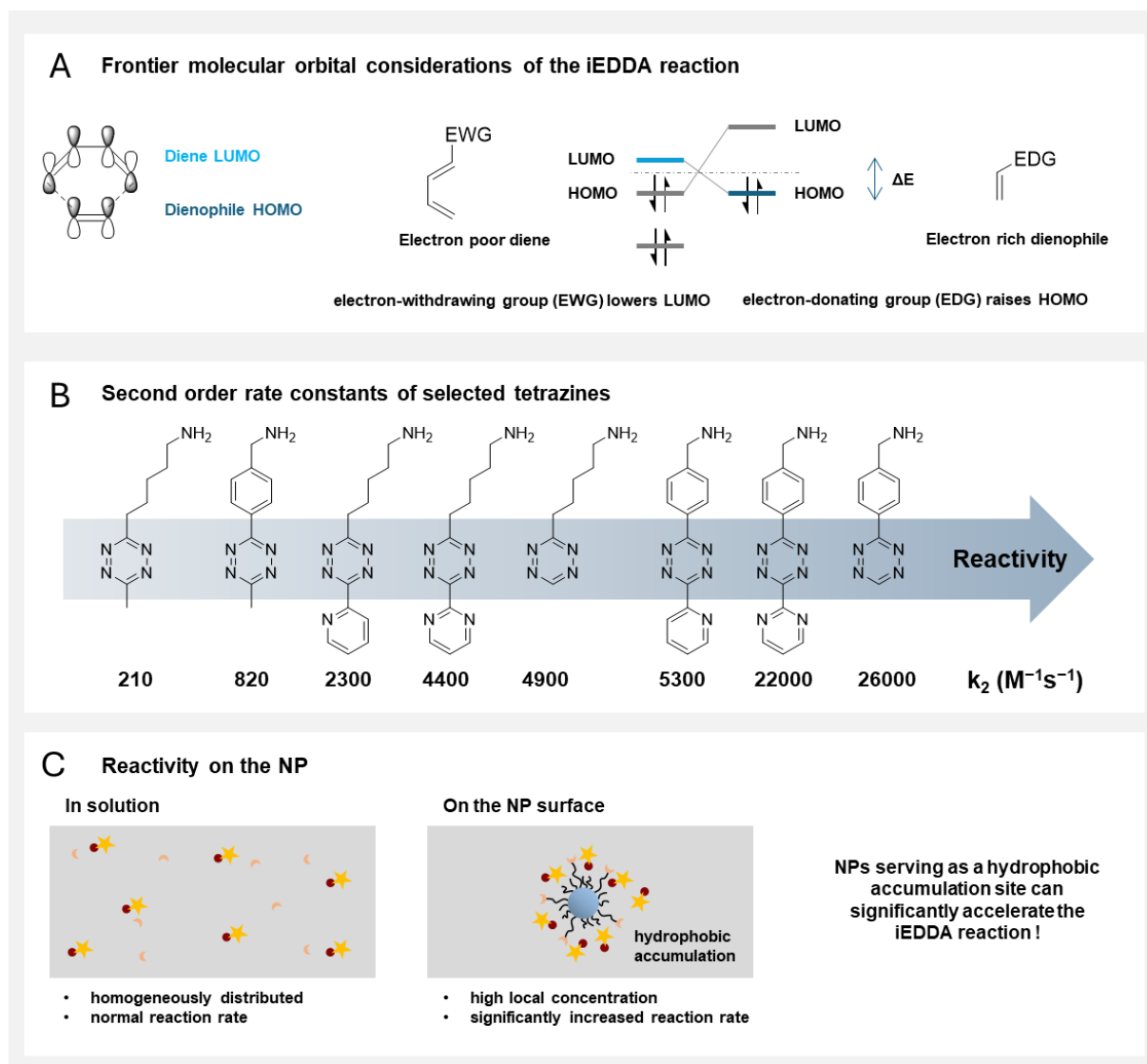


Figure 10. Kinetics of the iEDDA reaction on nanoparticles. (A) Frontier molecular orbital considerations for the iEDDA reaction, which proceeds between the HOMO of the dienophile and the LUMO of the diene. Pairs with a smaller energy difference react faster in iEDDA reactions. (Adapted from Oliveira, Guo et al. [3]) (B) Second order [4 + 2] cycloaddition rate constants of selected tetrazines with TCO in PBS at 37°C. (Adapted from Karver, Weissleder et al. [42]) (C) Comparison of reactivity in solution and on the NP surface.

These findings raise intriguing questions about how other NP materials might influence the rate of the iEDDA reaction. To date, the choice of iEDDA reaction partners does not appear to have been considered in conjunction with the choice of NP, even though it is likely that the combination itself significantly affects reaction kinetics. To facilitate the selection of iEDDA reaction partners and NP materials for future applications, a systematic investigation of factors such as NP size, material, linker, etc., on reaction rate would be highly beneficial. This would enable the targeted selection of iEDDA and NP combinations that promise rapid reactions. Exploiting NP-induced acceleration of the iEDDA

Chapter 1

reaction could be particularly advantageous, as a fast reaction is generally desirable for *in vivo* applications.

5.2 Stability of iEDDA motifs in biological systems

In addition to rapid reaction kinetics, sufficient stability of the reaction partners is also crucial for the combination of the iEDDA reaction and NPs in *in vivo* applications. In a way, this is a weak point of the otherwise so advantageous iEDDA reaction. Tetrazines can be attacked by nucleophiles, which are abundant in biological environments (see **Figure 11 A**). [130] Electron-withdrawing groups on the tetrazine, which accelerate the iEDDA reaction, simultaneously increase the likelihood of nucleophilic attack and thus lead to decomposition. [42] For a long time, it was therefore assumed that a suitable compromise between rapid reaction and sufficient stability had to be found. [3] Recently, Svatunek, Wilkovitsch et al. demonstrated that a solution to this reactivity versus stability dilemma exists. The iEDDA reaction can be accelerated not only by electron-withdrawing substituents on the tetrazine, but also by intramolecular repulsion, which does not result in increased degradation in biological environments. [130] The authors suggest the use of 3,4-dihydro-2H-pyran (DHP) substitution instead of 2-pyridyl substitution on the tetrazine. To date, such a tetrazine has not been employed in combination with NPs and, due to limited commercial availability, its application may be delayed. For the commonly used phenyl/hydrogen-substituted tetrazine, Emmetiere, Irwin et al. reported a half-life of approximately 29 hours in human serum. However, in this study the tetrazine was not conjugated to the NP but was free in serum. [105] The half-life of more than one day should provide a sufficient time window for biomedical applications.

The situation appears more challenging on the side of the dienophile TCO. Rossin, van den Bosch et al. showed that in fresh mouse serum at 37 °C, the TCO isomerizes to cis-cyclooctene with a half-life of approximately 3 hours (3.26 h for equatorially substituted TCO and 3.36 h for axially substituted TCO). [41] The resulting cis-cyclooctene is several orders of magnitude less reactive than trans-cyclooctene, so this isomerization effectively results in deactivation. The authors attribute the rapid loss of reactivity *in vivo* to interactions with copper-containing proteins (see **Figure 11 B**). Chen, Chen et al. confirmed this finding and reported a half-life of approximately 4 hours in mouse serum for TCO on their molecule, which is designed to undergo macrocyclization and *in situ* self-assembly into NPs. [111] Using HPLC and MS analysis, they demonstrated a clean conversion from trans- to cis-cyclooctene. Norbornene, as an alternative dienophile, exhibits good stability but is generally too slow for *in vivo* applications. [34]

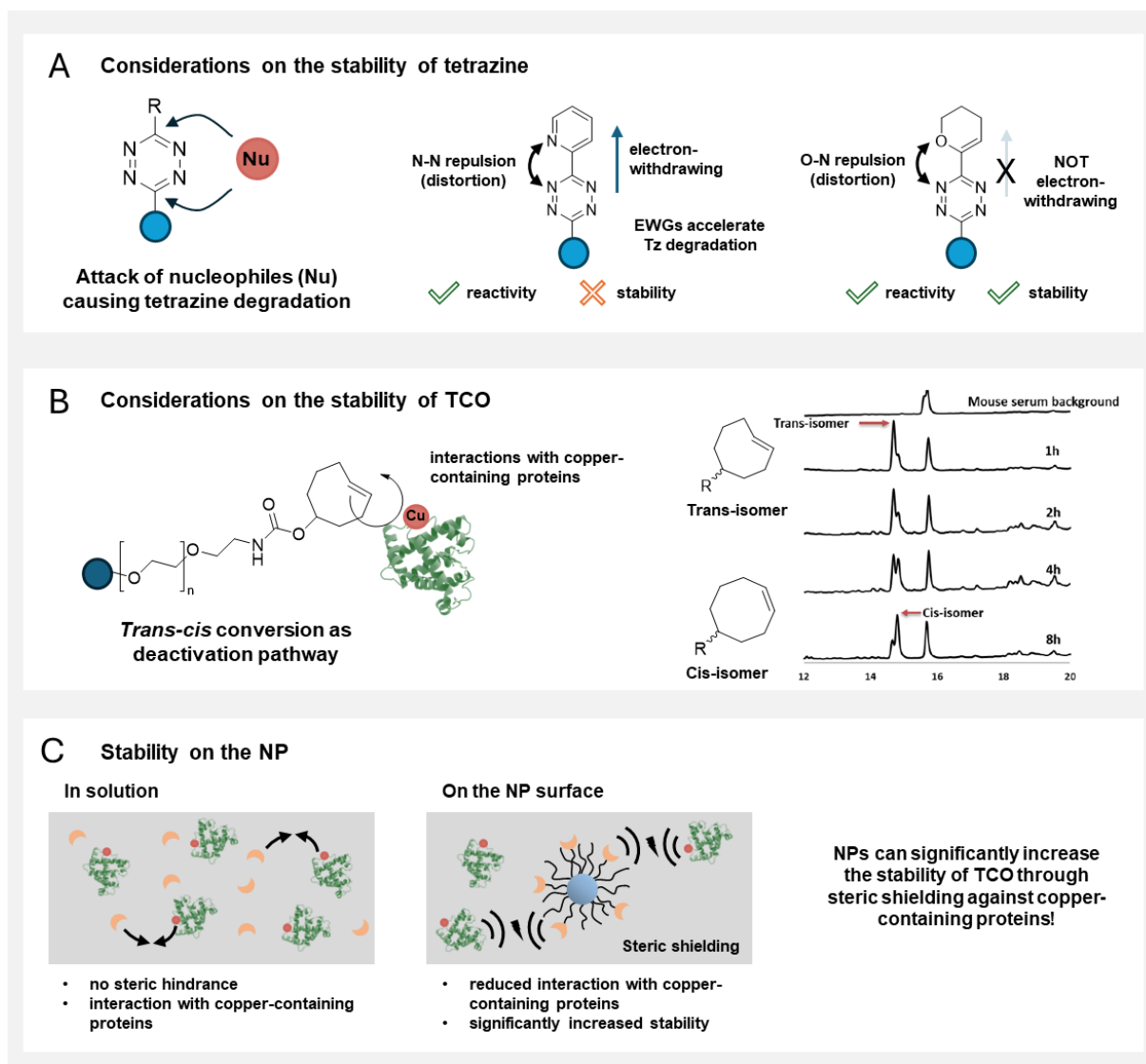


Figure 11. Stability of iEDDA motifs in biological systems. (A) Considerations on the stability of tetrazine. Tetrazines can be attacked by nucleophiles, with electron-withdrawing substituents on the tetrazine accelerating degradation. (Adapted from Svatunek, Wilkovitsch et al. [130]) (B) Considerations on the stability of TCO. TCO can be deactivated by trans-cis isomerization. Conversion can be monitored by HPLC profiles. (Adapted from Rossin, van den Bosch et al. [41] and Chen, Chen et al. [113]) (C) Comparison of stability in solution and on the NP.

This raises the question of how TCO, despite its short half-life in serum, could be successfully employed in combination with NPs. Rossin, van den Bosch et al. have already demonstrated potential strategies in this context. They observed that TCO, when attached to an antibody via a linker, exhibited significantly greater stability. The *in vivo* stability half-life was 2.62 days for equatorially substituted TCO and 1.12 days for axially substituted TCO, in contrast to the few hours observed for TCO in serum. [41] It appears that steric hindrance provided by the antibody reduces the interaction of TCO with serum protein-bound copper, thereby suppressing trans–cis isomerization. For TCO-functionalized antibodies, this results in a time window of approximately two days due to the increased TCO stability. In approaches where

Chapter 1

target cells are first identified by an antibody and subsequently tetrazine-functionalized NPs are administered to “click” onto the already labeled targets, an interval of 12 or 24 hours between the injection of the TCO-antibody and the tetrazine-functionalized NPs has typically been chosen. [96–98] Steen, Jørgensen et al. investigated the plasma half-life of TCO moieties in single-chain polymer NPs and found it to be approximately 1.9 days, which is comparable to the half-lives observed for TCOs attached to antibodies. [109] Thus, NPs, like antibodies, seem to provide steric shielding, making TCO less accessible to copper-containing serum proteins (see **Figure 11 C**). The publication emphasized that, compared to free TCO moieties, the plasma half-life on the NP increased approximately 14-fold. Therefore, the combination of the iEDDA reaction with NPs can compensate for one of the drawbacks of the iEDDA reaction - namely, the sometimes poor stability of the reaction partners in biological environments.

Rossin, van den Bosch et al. also demonstrated with antibodies that shortening or omitting the linker between TCO and the antibody can further increase TCO stability. They observed an increase in TCO half-life from 2.62 to 6.19 days for equatorially substituted TCO. [41] It is of interest to evaluate whether shortening the linker on NPs would also increase TCO stability, and consequently, whether TCO should ideally be coupled directly to the NP surface. Goos, Davydova et al. varied the PEG linker length between the polymer backbone and TCO on polymer nanostars. [108] They found that *in vivo* radioligand binding at the tumor site was highest when nanostars were directly functionalized with TCO without a linker. Since the TCO-functionalized nanostars were administered three days prior to the tetrazine radioligand, it can be concluded that the improved TCO stability in the absence of a PEG linker may have contributed to the higher efficiency of the iEDDA reaction. Thus, literature evidence suggests that, analogous to observations with antibodies, shortening the linker on NPs could further enhance TCO stability. For mesoporous silica NPs, Keinänen, Mäkilä et al. observed a reaction with a tetrazine radioligand when TCO-functionalized NPs were administered 15 minutes in advance, but not when administration occurred 24 hours prior. [131] They speculated that the PEG12 linker used may not have provided sufficient steric shielding to mask the TCO group and prevent trans–cis isomerization *in vivo*. Alternatively, it is possible that the NPs were largely internalized after 24 hours, rendering the TCO moieties inaccessible to the ¹⁸F-tetrazine tracer.

In summary, current literature suggests that the stability of TCO is increased when it is conjugated to NPs. This improved stability is likely due to steric shielding from copper-containing serum proteins, which could otherwise promote trans–cis isomerization. There is also evidence indicating that TCO stability may benefit from positioning the TCO moiety as close as possible to the NP surface, using a very short linker. However, this has not been thoroughly investigated. Overall, more studies are needed that specifically examine the stability of TCO on NPs. In particular, a systematic evaluation of linker length on different NP materials and its impact on both the stability and reactivity of TCO would be highly desirable. Such investigations would enable more rational decisions in the selection process of

iEDDA reaction partners and NP materials. Given that the stability of the reaction partners is critical for successful *in vivo* applications, it is important to elucidate how and to what extent NPs enhance TCO stability. Notably, the stability of tetrazine on NPs has not yet been investigated, presumably because tetrazine is generally considered the less problematic partner in terms of stability. This gap should also be addressed in future studies to determine whether and how conjugation of tetrazine to NPs affects its stability.

5.3 Functionalization of nanoparticle surfaces

For the successful combination of the bioorthogonal iEDDA reaction with NPs for advanced biomedical applications, the NPs must be adequately functionalized with one partner of the iEDDA reaction. In general, the choice of conjugation strategy is dictated by a combination of factors on the NP side, including NP material, surface chemistry, and structure, as well as factors determined by the molecule to be attached. Here, the nature of the molecule, its size, and the desired utility in the final application must be considered. Conjugation can generally proceed either covalently or non-covalently, the latter encompassing electrostatic attachment, other forms of adsorption, and encapsulation. [132] Since proteins are comparable to NPs in terms of size and protein labeling is well-developed, techniques from this field were among the first to be applied for attaching molecules of interest to NPs. The most common chemistries here are the formation of amide bonds using NHS and EDC, and maleimide conjugation to thiols. [133] Furthermore, reactions from the click chemistry toolbox, such as the copper-catalyzed azide-alkyne cycloaddition (CuAAC), are also available for covalent anchoring of molecules to the NP surface. [134] Thus, several options exist for the targeted attachment of molecules to the NP surface. In the case of the iEDDA motif, non-covalent attachment is generally unsuitable, as it cannot be ensured that the motif remains associated with the NP. Covalent binding renders the process more precise and manageable. This is also reflected in the fact that all papers considered opted for covalent attachment. Specifically, for attaching iEDDA reaction partners, thiol-maleimide conjugation is likely less suitable, as both tetrazine and TCO can be adversely affected by high thiol concentrations. [3]

Regardless of the NP material and any linkers used, in nearly all analyzed papers, the iEDDA reaction partner was anchored to the NP via an amide bond. This approach is advantageous because amide bonds are highly stable against hydrolysis and can be formed using straightforward and established chemistry under mild reaction conditions. [135] When a pre-assembled NP was modified with the iEDDA reaction partner in a final step, as is especially common for inorganic and protein-based NPs, the particle was typically amine-functionalized. The amine-functionalized NP then reacted with the NHS ester-activated carboxylic acid of the iEDDA motif to be attached. Alternative strategies were employed for lipid-based and polymeric NPs. In these cases, individual phospholipids or polymers can be modified with an iEDDA reaction partner prior to final NP assembly (see **Figure 12 A**). Both variants are reported in the

Chapter 1

literature: either the PEGylated phospholipid or polymer is amine-terminated and reacts with an NHS ester of the iEDDA motif, or vice versa. Interestingly, only one study in the literature utilized a different chemistry for attaching the iEDDA motif. Keinänen, Mäkilä et al. used the SPAAC reaction between azide-functionalized mesoporous silica NPs and DBCO-PEG₁₂-TCO, thus utilizing the bioorthogonal click chemistry toolbox. [131] The SPAAC reaction is rapid, efficient, and compatible with biological systems. However, since NP functionalization with iEDDA motifs is typically performed in advance under well-defined conditions, rather than in a biological milieu, the SPAAC reaction offers no significant advantages. In fact, the relatively bulky DBCO increases the steric demand of the coupling components compared to the more compact amide bond, which could be disadvantageous. Overall, it can be concluded that classical peptide coupling chemistry via NHS esters provides sufficient possibilities for NP modification by simply attaching ready-synthesized iEDDA motifs.

In addition to a suitable conjugation chemistry, an appropriate number of iEDDA motifs on the NP is also required. Here, a distinction emerges between NPs that are fully assembled and subsequently equipped with iEDDA motifs, and those for which the NP-forming lipids or polymers are functionalized in advance. In the latter case, there is the elegant possibility of varying the ratio of functionalized to non-functionalized lipids or polymers during NP preparation. This allows for straightforward adjustment of the density of iEDDA reaction partners on the NP. For example, Yoo, Choi et al. used different ratios of DSPE-PEG/DSPE-PEG-Tz in the preparation of their lipid NPs. [97] For already fully assembled NPs that are subsequently functionalized with the iEDDA reaction partner, the possible number and thus the density of iEDDA motifs on the NP is directly determined by the number of pre-existing amine groups. For example, Khan, Agris et al. reported 180 amine termini on the surface of their iron oxide NPs. [120] In this respect, there are certain limitations. However, a lower degree of NP functionalization with the iEDDA motif can still be achieved by using a sub-stoichiometric amount relative to the available amines on the NP. The methods used to quantify the attached iEDDA reaction partners vary considerably depending on the NP material (see **Figure 12 B**). For polymeric NPs, ¹H NMR spectroscopy is commonly employed. For instance, Goos, Davydova et al. estimated the number of TCOs per nanostar by analyzing the proton ratio between the methyl group in the RAFT chain transfer agent and the alkene moiety of the TCO. [108] Denk, Svatunek et al. determined the number of TCO moieties on their mesoporous silica NPs by measuring the decrease in tetrazine concentration due to the iEDDA reaction, which they quantified via HPLC. [110] Alternatively, Keinänen, Mäkilä et al. used the increase in nitrogen content, determined by elemental analysis, to quantify the number of TCO motifs on silica NPs. [131] A widespread approach for quantifying tetrazines on inorganic NPs involves reacting the NPs with Cy5-TCO and, following appropriate separation of unreacted material, measuring the fluorescence. [92, 98] As diverse as the methods for quantifying iEDDA reaction partners on NPs are, so are the ways in which the results are reported. In addition to the number of iEDDA motifs per NP, values are also reported as μmol of iEDDA motifs per gram of NP, or as nmol per mmol of iron as

the main component of inorganic NPs. For improved comparability and to make the data from individual publications more accessible for potential meta-analyses, it would be desirable to report results according to a certain standard. In summary, it appears that a sufficient number of iEDDA motifs can be attached to various NPs, with the optimal number being largely determined by the intended application. Polymeric or lipid-based NPs may offer somewhat greater flexibility in tailoring the number of iEDDA reaction partners, as they are typically assembled after functionalization with the iEDDA motif.

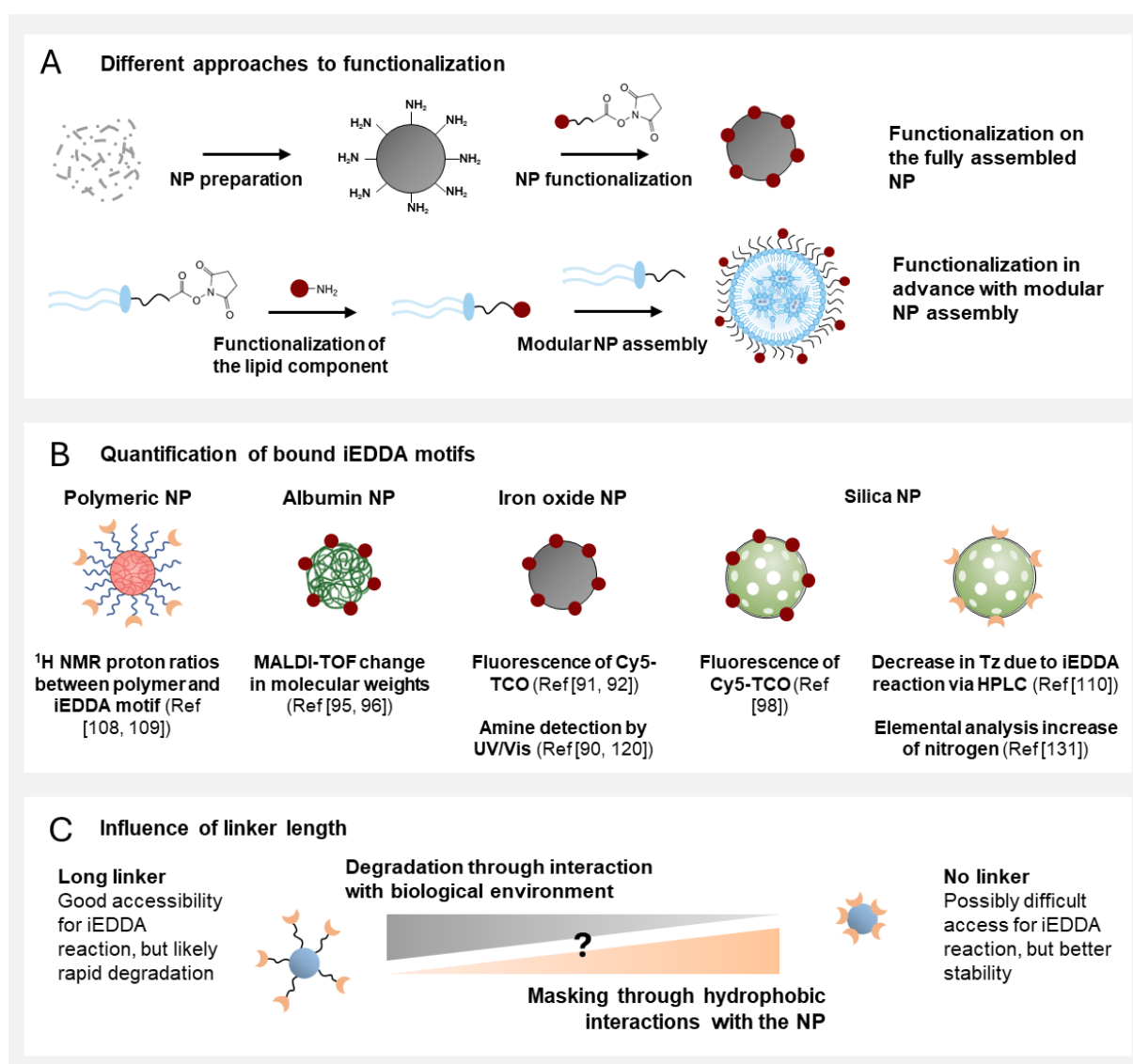


Figure 12. Functionalization of NP surfaces. (A) Different approaches to functionalization: Either the NP is first prepared and the iEDDA motifs are directly attached to the ready-made NP (shown here exemplarily for Khan, Agris et al. [120]), or individual components that will later be assembled into the NP are pre-functionalized with the iEDDA motif and the particle is then assembled in a modular fashion (shown here exemplarily for Yoo, Choi et al. [97]). (B) Approaches described in the literature for the quantification of iEDDA motifs per NP. (C) Illustration of the influence of linker length.

Chapter 1

The iEDDA motifs, introduced in sufficient numbers using appropriate chemistry, must also remain accessible. Depending on the NP material, the iEDDA motifs were therefore attached to the NP via a linker. In most cases, PEG is encountered as the linker due to its water solubility, lack of toxicity, and low immunogenicity. [136] The PEG spacer extends the iEDDA reaction partner away from the NP surface, potentially improving its accessibility for the reaction. However, this improved accessibility, particularly for TCO, can also accelerate deactivation. Nevertheless, simply omitting the linker does not appear to be a universal solution. Rahim, Kota et al. demonstrated that, in their case, antibody-bound TCOs are not inactivated by trans-cis isomerization. Instead, TCOs are likely masked by hydrophobic interactions with the antibody. [137] A similar scenario can be assumed for NPs instead of antibodies. Thus, the choice of an appropriate linker length is a balance between sufficient length to minimize hydrophobic interactions with the NP and being short enough to prevent excessive exposure of the iEDDA motif, which would promote rapid degradation (see **Figure 12 C**). Approximately half of the reviewed publications do not use a linker in their approach. With the corresponding NP materials, hydrophobic interactions do not appear to be pronounced enough to interfere with the successful interplay between NP and the iEDDA reaction. Keinänen, Mäkilä et al. are among the few who discussed their choice of linker length. They used PEG12 as a linker, arguing that this could reduce possible deactivation of the TCO on the thermally hydrocarbonized silicon surface and that the TCO moiety would be more sterically accessible for the ^{18}F -tetrazine tracer. [131] Overall, there are very few studies that discuss the rationale behind their choice of linker length, let alone studies that systematically vary the linker length and examine its effects on reactivity and stability. It appears that the choice of linker length is often based more on intuition than on rational design criteria, highlighting significant potential for improvement.

5.4 Nanoparticle stability in physiological environments

In the reviewed papers on the combination of NPs with the bioorthogonal iEDDA reaction, a wide range of NP materials were utilized. Approximately half of the studies use inorganic NPs, including iron oxide, silica, and gold particles. Inorganic NPs are followed by polymeric NPs, whereas lipid-based NPs are found less frequently. Protein-based NPs, which are exclusively albumin particles, also constitute a minor proportion. Each of these NP materials offers intriguing possibilities for future applications but also presents challenges, particularly with respect to colloidal stability. One of the earliest and most fundamental approaches for describing colloidal stability is the well-known DLVO theory, named after Derjaguin, Landau, Verwey, and Overbeek. [138] It describes the total interaction between colloidal particles as the sum of a repulsive electrostatic interaction and an attractive van der Waals interaction. NPs with surface charge can be stably dispersed in water because the repulsive electrostatic interaction overwhelms the attractive van der Waals interaction. [139] However, since many NPs are neutral or

only weakly charged, the classical DLVO theory was later extended by an additional steric stabilization contribution. Steric stabilization arises, for example, from polymer shells, as in block or graft copolymers, whose hydrophilic segments protrude into the aqueous medium and form a barrier against aggregation. [140] Overall, both electrostatic and steric repulsive forces are nowadays regarded as the source of colloidal stability in water. However, for the intended biomedical application of the NPs, it is not sufficient to consider colloidal stability solely in water. [141] To serve as an effective platform in combination with the bioorthogonal iEDDA reaction, NPs must also possess sufficient stability in physiological environments (see **Figure 13 A**). It must be taken into account that high ionic strengths in physiological media can shield the electrostatic repulsive forces between particles, leading to aggregation and ultimately sedimentation. [142] Furthermore, upon contact with physiological fluids, NPs will interface with a wide range of biomacromolecules. Thus, a so-called protein corona is rapidly formed around the NPs. This may determine the biological fate of NPs as well as their colloidal properties. [143]

For the NPs used in conjunction with the iEDDA reaction, the same stabilization strategies are employed as for other NPs in biomedical applications. [144] Typically, polymers are installed on the particle surface, providing a certain steric barrier and increasing biocompatibility. For example, Khan, Seebald et al. coated their iron oxide NPs for the click-to-release application of the iEDDA reaction with a dextran polymer coating to improve dispersity, bioavailability, and circulation half-life for *in vivo* studies. [125] By far the most commonly used strategy to enhance NP stability in biological environments is polyethylene glycol (PEG) functionalization, often referred to as PEGylation. [145] Like the installation of other polymers, PEGylation enhances colloidal stability by forming a hydrophilic, neutrally charged shell that repels other particles via steric hindrance. In addition, PEG is quite effective at reducing protein adsorption and limits recognition by the mononuclear phagocyte system (MPS), thereby increasing circulation time. [146] Depending on the NP material, PEG grafting was thus applied to the NPs employed in conjunction with the iEDDA reaction. The PEG density and, directly related to this, the conformation of PEG on the NP surface plays an important role here (see **Figure 13 B**). The literature discusses two conformations, termed “mushroom” and “brush”. [147] If the PEG density on the NP surface is low, the mushroom conformation is predominant. However, for higher values of density, PEG chains are closer and acquire a more straight (brush-like) conformation, thus forming a thicker hydrophilic barrier. [136] The brush conformation is especially advantageous, as it reduces protein adsorption. [148] Focusing on the requirements arising from the combination of iEDDA reaction and NPs, the brush conformation is also beneficial here. It can be assumed that iEDDA motifs attached to PEG arms in the brush conformation are accessible on the exterior of the NP. Backfolding of the rather hydrophobic iEDDA motifs, such as TCO and tetrazine, towards the particle core becomes less likely due to the high PEG density of the brush conformation. The PEG coating for NP stabilization can also be well integrated with linker strategies. If the accessibility of iEDDA motifs

Chapter 1

needs to be further improved, longer PEG arms can be utilized, ensuring that the iEDDA reactive groups extend further out from the PEG brush on the particle surface.

Among all types of NPs, lipid-based NPs are particularly noteworthy for their pronounced PEG coating and long PEG linkers. In this case, there is another reason for this besides the excellent properties of the PEG. If the iEDDA reaction partner were directly attached to the phospholipids, membrane destabilization could occur. Kannaka, Sano et al. deliberately utilized this effect by attaching the tetrazine without a linker, resulting in its direct incorporation into the liposomal membrane. Due to the iEDDA reaction, the physicochemical properties are altered, for example, membrane fluidity is increased, which, in turn, promotes drug release. [127] For lipid-based NPs, the linker thus also serves the essential function of ensuring an adequate distance from the NP core, preventing any adverse effects on the NP itself. The PEG linker is crucial for maintaining lipid membrane integrity. Such an effect is generally not relevant for other NP materials. No further specific effects of the iEDDA reaction partners on NP stability have been addressed in the literature. However, both iEDDA motifs are relatively hydrophobic. If a large number of them are introduced onto the surface of a NP, the overall surface may become highly hydrophobic. Colloidal stability could be compromised if such hydrophobic particles aggregate to avoid interactions with water. [149] The maximum number of iEDDA motifs that can be installed on a single NP needs to be considered in this context, even though this has not yet been systematically evaluated. Moreover, it can be assumed that the hydrophobic regions introduced by the iEDDA reaction partners on the NP will interact with serum components differently than similar NPs without iEDDA functionalities. [150] The presence of iEDDA motifs may induce a different protein corona composition through hydrophobic interactions, potentially altering the biological fate of the NPs (see **Figure 13 C**). This aspect has also not been experimentally investigated or discussed in the literature. Furthermore, in the examined publications concerning the interplay between bioorthogonal iEDDA reactions and NPs, the question of whether the iEDDA motifs remain accessible and reactive under the protein corona has received no attention. This is rather surprising, as it determines the successful implementation of the concept to a significant extent. At best, it may be inferred from the reported results that accessibility of the iEDDA reaction partners was at least partly retained, despite the presence of a protein corona.

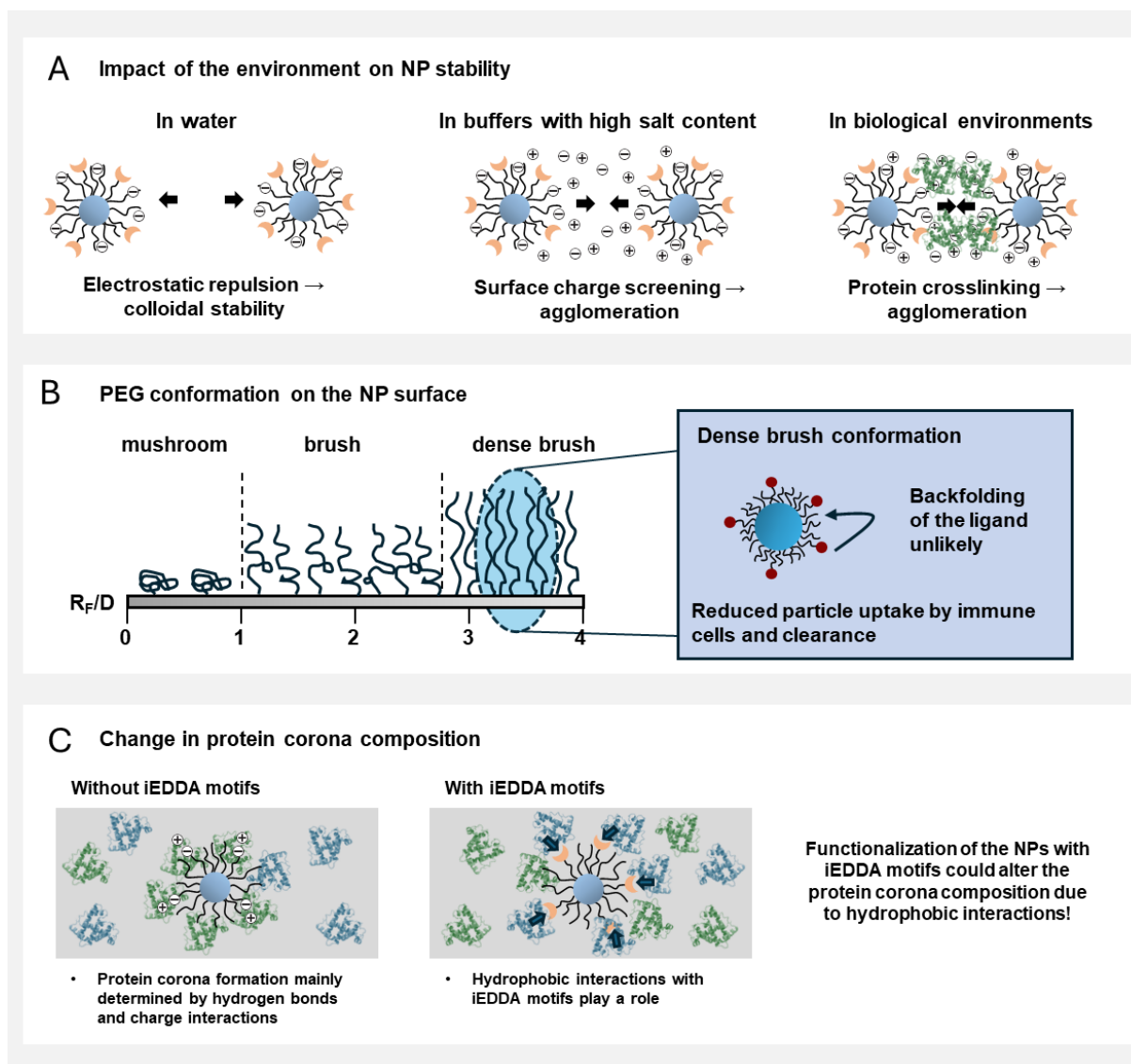


Figure 13. Nanoparticle stability in physiological environments. (A) Impact of the environment on NP stability. In water, electrostatic repulsion usually ensures sufficient colloidal stability, whereas at high ionic strength, the surface charge can be screened, and in biological environments, protein crosslinking can also occur, leading to agglomeration. (Adapted from Nienhaus, Nienhaus [75]) (B) PEG conformation on the NP surface. The conformation of bound PEG is determined by the Flory radius R_F of the PEG coils (directly dependent on the PEG molecular weight) as well as by the distance between anchoring points D (inversely proportional to the grafting density). (Adapted from Yang, Jones et al. [148]) (C) Possible change in the composition of the protein corona through the introduction of hydrophobic iEDDA motifs.

The NP sizes reported in the analyzed papers vary widely. Some NPs are relatively small, exhibiting hydrodynamic diameters around 20 nm, a range in which many inorganic and polymeric NPs are found, while others are considerably larger, with hydrodynamic diameters on the order of 200 nm, especially in the case of *in situ* self-assembled NPs. A common feature among these studies is that NP size is typically determined only in water or simple buffer solutions. However, as previously discussed, NPs encounter a multitude of biological macromolecules in physiological environments, leading to the

Chapter 1

formation of a corona around the NPs. [75] Consequently, measurements conducted in water have only limited relevance. As is the case for other NPs intended for biomedical applications, it is crucial to investigate NP size and behaviors, such as aggregation, in biologically relevant environments. [151] Only two of the considered studies evaluated NP stability in biological media. Lee, Park et al. utilized fluorescence correlation spectroscopy (FCS) for this purpose. [152] They incubated mesoporous silica NPs with tetrazine functionalization for 24 hours in 10% FBS cell media or PBS, observing that the resulting FCS curves appeared nearly identical, demonstrating excellent colloidal stability. [98] Stéen, Jørgensen et al. employed a specialized DLS approach to study the behavior of their PeptoBrush in human serum. [153] They observed no aggregation between human serum proteins and PeptoBrush at a concentration of 50 mg/L, a typical concentration for pretargeting approaches *in vivo*. [109]

In summary, for NPs utilized in combination with the iEDDA reaction, the same strategies are applied to ensure sufficient stability in biological environments as for all other NPs intended for biomedical applications. The specific consequences of introducing hydrophobic iEDDA motifs for NP stability have not been further considered in the literature. Neither the possible limitation in the number of installable iEDDA motifs nor the influence of iEDDA motifs on the protein corona has been discussed to date. To gain a better understanding of NP applications in biological environments, it is recommended, as is increasingly common in the field of NPs for biomedical applications, to also consider NP size and behavior in physiological media.

6. Challenges and future perspectives

The preceding discussion has demonstrated that the interplay between bioorthogonal iEDDA reactions and NPs can enable a wide range of advanced applications. However, it must be emphasized that this combination significantly increases the complexity of drug delivery or imaging strategies. Even predicting the *in vivo* fate of fully functionalized NPs alone is challenging, with numerous hurdles to overcome before successful biomedical application can be achieved. [70] The addition of the iEDDA reaction introduces yet another dimension of complexity. The component intended to react with the NP via the iEDDA reaction must initially be considered separately, before the two building blocks are finally joined through the bioorthogonal reaction. Several key factors have been identified for the successful integration of bioorthogonal iEDDA reactions with NPs. On the side of the iEDDA reaction, the reactivity and stability of the iEDDA motifs are of primary importance. Regarding the NPs, functionalization and NP stability under physiological conditions warrant particular attention. While both iEDDA reactions and NPs have been extensively studied individually, significant knowledge gaps remain regarding their combined use. [3] In the future, the selection of iEDDA reaction partners should

be considered in conjunction with the choice of the NP, as the reaction kinetics may differ substantially from those observed in solution. Furthermore, a deeper understanding is needed of how NPs may enhance the stability of TCO, in order to design NP/TCO combinations with improved stability of the iEDDA reaction partner. [109] To fully harness the synergistic potential of NPs and bioorthogonal iEDDA reactions, a systematic investigation of factors such as NP size, material, linker length, and their effects on iEDDA reaction kinetics and stability is required. Such studies would enable a more rational selection process, thereby accelerating and improving the success of projects and advancing the field as a whole.

On the NP side, it would be valuable to determine how many hydrophobic iEDDA motifs can be installed on a single NP before colloidal stability becomes compromised, a point that has not yet been sufficiently addressed. Additionally, the establishment of standardized methods for quantifying iEDDA reaction partners on NPs and for reporting results would be highly beneficial. The influence of hydrophobic iEDDA motifs on the protein corona of NPs, as well as the accessibility of these motifs within the corona, also remains largely unexplored. As is generally the case in the field of NPs for biomedical applications, future studies combining NPs and iEDDA reactions should move beyond characterizing NP size solely in water or simple buffers, and instead assess NP size and behavior, such as aggregation, in biological media. [75] In conclusion, many aspects of the interplay between iEDDA reactions and NPs require further elucidation. The authors encourage others to contribute to the fundamental understanding of these systems alongside the development of specific applications. With deeper insight, the successful realization of advanced concepts should be within reach, allowing the synergistic benefits of NPs and bioorthogonal reactions to be fully exploited.

Recent publications highlight the considerable potential of this field. The iEDDA reaction enables two-step strategies, allowing the targeting step to be separated from the imaging or drug delivery step, with all the associated advantages. [154] Initial developments involved NPs as the secondary component, where the target was marked by an antibody modified with an iEDDA reaction partner. [155] The advantage of NPs in this context lies in their ability to integrate multiple imaging modalities, which is challenging to achieve with small molecular probes. However, it should be noted that the benefits of NPs come at the cost of losing rapid tracer excretion due to the size of the nanomaterial. [91] When antibodies modified with an iEDDA reaction partner are used for therapeutic purposes, a potential advantage is that cross-linking can occur through the reaction of an NP with two adjacent antibodies. This can lead to the formation of nanoclusters on the cell surface, which may facilitate improved internalization. [95] In addition to antibody-based targeting, iEDDA motifs could also be introduced artificially onto the cell surface via metabolic engineering. Despite recent advances in this field, metabolic glyocalyx labeling with bulky unnatural motifs still lags far behind the use of azido sugars, which, however, enable only SPAAC but not iEDDA reactions. [102] Advances in metabolic

Chapter 1

engineering for the introduction of the relatively hydrophobic iEDDA motifs could directly accelerate the integration of iEDDA chemistry with NPs.

More innovative concepts arise when the NP serves as the primary component. The combination of bioorthogonal iEDDA reactions and NPs has already been successfully established for imaging within pretargeting strategies as well as for the targeted release of therapeutics. The authors expect continued fruitful synergy in these areas. For imaging applications, NPs functionalized with one of the iEDDA reaction partners are first administered, allowing accumulation in the target tissue. After sufficient clearance from the bloodstream, the complementary reaction partner labeled, for example, with a radioactive isotope for positron emission tomography (PET) is administered. [109] The high reaction rate and selectivity of the iEDDA reaction ensure efficient conjugation exclusively at the target site, leading to a significant reduction in nonspecific background signals and thus improving the sensitivity and resolution of imaging. [108] Particularly in the context of PET imaging, a further advantage is that by decoupling the target detection and imaging steps, radioisotopes with a rather short half-life can be used, thus reducing the radiation exposure for the patient. [110] The combination of iEDDA reactions and NPs has become established in the field of pretargeted PET imaging and is likely to continue to flourish, as evidenced by a growing number of publications in this area. Beyond diagnostic applications, iEDDA chemistry in combination with NPs also opens new avenues for targeted drug release. The development of inactive prodrugs that are activated only at the target site via a bioorthogonal click-to-release reaction is a promising concept for reducing systemic side effects. [120] NPs can serve both as carriers for the prodrug and as platforms for its activation. In more advanced designs, multiple functionalities can be combined on a single nanoplatform, enabling the integration of diagnosis (e.g., imaging) and therapy (e.g., chemotherapy, photothermal therapy) in a single system (“theranostics”). [124] In this field, numerous novel concepts are expected to emerge in the coming years.

If fundamental research succeeds in providing a deeper understanding and thereby managing the additional complexity arising from the interplay between iEDDA reactions and NPs, a wide range of opportunities will open up. It should be emphasized that the combination of these two promising concepts, bioorthogonal chemistry and NPs for biomedical applications, is not inherently a breakthrough on its own. Rather, it is the broad spectrum of possibilities that makes this approach particularly noteworthy, offering a versatile platform for the successful realization of both diagnostic and therapeutic applications. A key challenge lies in exploiting this synergy in a targeted manner for specific applications. Overall, the combination of iEDDA-based bioorthogonal reactions with NP systems represents a modular and highly adaptable strategy for the development of precise and effective approaches, particularly in the context of increasingly personalized medicine.

7. Conclusion

The fusion of bioorthogonal iEDDA chemistry with NP technology has emerged as a powerful and versatile platform for both diagnostic and therapeutic applications in biomedicine. On one hand, the iEDDA reaction enables rapid and selective conjugation of components to NPs *in vivo*, thereby facilitating two-step targeting strategies. On the other hand, NPs, with their capacity for multimodal imaging and multifunctional payloads, further expand the potential of this approach. To date, the synergy between iEDDA chemistry and NPs has been particularly prominent in the context of pretargeted PET imaging and targeted drug release via click-to-release mechanisms. Despite these advances, several challenges must still be addressed. The increased complexity arising from the interplay between iEDDA chemistry and NP behavior in biological systems requires a deeper mechanistic understanding. Furthermore, issues such as biodistribution, clearance, and potential immunogenicity must be resolved to ensure safe and effective clinical translation. Looking forward, the modularity and adaptability of iEDDA-based NP systems position them as highly promising tools for precision medicine, enabling the integration of diagnostic and therapeutic functions within a single platform. Continued interdisciplinary research will be essential to overcome current limitations and to fully realize the broad spectrum of opportunities offered by this innovative field. Ultimately, the synergy of bioorthogonal chemistry and nanotechnology holds great promise for the realization of next-generation, patient-tailored medical solutions.

Chapter 1

References

1. Scinto SL, Bilodeau DA, Hincapie R, Lee W, Nguyen SS, Xu M, Ende CW am, Finn MG, Lang K, Lin Q, Pezacki JP, Prescher JA, Robillard MS, Fox JM (2021) Bioorthogonal chemistry. *Nat Rev Methods Primers* 1(1), 1–23. 10.1038/s43586-021-00028-z.
2. Nobel Prize (2025) Press release: The Nobel Prize in Chemistry 2022. <https://www.nobelprize.org/prizes/chemistry/2022/press-release/>. Accessed 14 June 2025.
3. Oliveira BL, Guo Z, Bernardes GJL (2017) Inverse electron demand Diels-Alder reactions in chemical biology. *Chem. Soc. Rev.* 46(16), 4895–4950. 10.1039/C7CS00184C.
4. Idiago-López J, Moreno-Antolín E, La Fuente JM de, Fratila RM (2021) Nanoparticles and bioorthogonal chemistry joining forces for improved biomedical applications. *Nanoscale Adv.* 3(5), 1261–1292. 10.1039/D0NA00873G.
5. Zhao Z, Ukidve A, Krishnan V, Mitragotri S (2019) Effect of physicochemical and surface properties on in vivo fate of drug nanocarriers. *Advanced Drug Delivery Reviews* 143, 3–21. 10.1016/j.addr.2019.01.002.
6. Liao A, Du W, Yang H (2024) The Inverse Electron Demand Diels-Alder Reaction Between Tetrazine and Trans-Cyclooctene for Pretargeted Bioimaging Applications. *Analysis & Sensing* 4(2), e202300053. 10.1002/anse.202300053.
7. Wu J (2021) The Enhanced Permeability and Retention (EPR) Effect: The Significance of the Concept and Methods to Enhance Its Application. *Journal of Personalized Medicine* 11(8), 771. 10.3390/jpm11080771.
8. Cole JT, Holland NB (2015) Multifunctional nanoparticles for use in theranostic applications. *Drug Deliv. and Transl. Res.* 5(3), 295–309. 10.1007/s13346-015-0218-2.
9. Staudinger H, Meyer J (1919) Über neue organische Phosphorverbindungen III. Phosphinmethylderivate und Phosphinimine. *HCA* 2(1), 635–646. 10.1002/hlca.19190020164.
10. Saxon E, Bertozzi CR (2000) Cell surface engineering by a modified Staudinger reaction. *Science* 287(5460), 2007–2010. 10.1126/science.287.5460.2007.
11. Nilsson BL, Kiessling LL, Raines RT (2000) Staudinger ligation: a peptide from a thioester and azide. *Organic Letters* 2(13), 1939–1941. 10.1021/ol0060174.
12. Saxon E, Armstrong JI, Bertozzi CR (2000) A “traceless” Staudinger ligation for the chemoselective synthesis of amide bonds. *Organic Letters* 2(14), 2141–2143. 10.1021/ol006054v.
13. Bednarek C, Wehl I, Jung N, Schepers U, Bräse S (2020) The Staudinger Ligation. *Chemical Reviews* 120(10), 4301–4354. 10.1021/acs.chemrev.9b00665.
14. Sletten EM, Bertozzi CR (2011) From mechanism to mouse: a tale of two bioorthogonal reactions. *Accounts of Chemical Research* 44(9), 666–676. 10.1021/ar200148z.
15. Meldal M, Tornøe CW (2008) Cu-catalyzed azide-alkyne cycloaddition. *Chemical Reviews* 108(8), 2952–3015. 10.1021/cr0783479.

16. Huisgen R (1961) 1,3-Dipolar Cycloadditions: Proceedings of the Chemical Society. October 1961. Proc. Chem. Soc.(October), 357. 10.1039/ps9610000357.
17. Rostovtsev VV, Green LG, Fokin VV, Sharpless KB (2002) A Stepwise Huisgen Cycloaddition Process: Copper(I)-Catalyzed Regioselective “Ligation” of Azides and Terminal Alkynes. *Angewandte Chemie International Edition* 41(14), 2596–2599. 10.1002/1521-3773(20020715)41:14<2596:AID-ANIE2596>3.0.CO;2-4.
18. Tornøe CW, Christensen C, Meldal M (2002) Peptidotriazoles on solid phase: 1,2,3-triazoles by regiospecific copper(i)-catalyzed 1,3-dipolar cycloadditions of terminal alkynes to azides. *The Journal of organic chemistry* 67(9), 3057–3064. 10.1021/jo011148j.
19. El-Sagheer AH, Brown T (2012) Click nucleic acid ligation: applications in biology and nanotechnology. *Accounts of Chemical Research* 45(8), 1258–1267. 10.1021/ar200321n.
20. Dirks AJ, Cornelissen JJLM, van Delft FL, van Hest JCM, Nolte RJM, Rowan AE, Rutjes FPJT (2007) From (bio)Molecules to Biohybrid Materials with the Click Chemistry Approach. *QSAR & Combinatorial Science* 26(11-12), 1200–1210. 10.1002/qsar.200740085.
21. Hanson SR, Greenberg WA, Wong C-H (2007) Probing Glycans With the Copper(I)-Catalyzed [3+2] Azide-Alkyne Cycloaddition. *QSAR Comb. Sci.* 26(11-12), 1243–1252. 10.1002/qsar.200740112.
22. Hong V, Steinmetz NF, Manchester M, Finn MG (2010) Labeling live cells by copper-catalyzed alkyne—azide click chemistry. *Bioconjugate Chemistry* 21(10), 1912–1916. 10.1021/bc100272z.
23. Presolski SI, Hong V, Cho S-H, Finn MG (2010) Tailored ligand acceleration of the Cu-catalyzed azide-alkyne cycloaddition reaction: practical and mechanistic implications. *Journal of the American Chemical Society* 132(41), 14570–14576. 10.1021/ja105743g.
24. Soriano Del Amo D, Wang W, Jiang H, Besanceney C, Yan AC, Levy M, Liu Y, Marlow FL, Wu P (2010) Biocompatible copper(I) catalysts for in vivo imaging of glycans. *Journal of the American Chemical Society* 132(47), 16893–16899. 10.1021/ja106553e.
25. Agard NJ, Prescher JA, Bertozzi CR (2004) A strain-promoted 3 + 2 azide-alkyne cycloaddition for covalent modification of biomolecules in living systems. *Journal of the American Chemical Society* 126(46), 15046–15047. 10.1021/ja044996f.
26. Jewett JC, Bertozzi CR (2010) Cu-free click cycloaddition reactions in chemical biology. *Chem. Soc. Rev.* 39(4), 1272–1279. 10.1039/B901970G.
27. Agard NJ, Baskin JM, Prescher JA, Lo A, Bertozzi CR (2006) A comparative study of bioorthogonal reactions with azides. *ACS Chemical Biology* 1(10), 644–648. 10.1021/cb6003228.
28. Baskin JM, Prescher JA, Laughlin ST, Agard NJ, Chang PV, Miller IA, Lo A, Codelli JA, Bertozzi CR (2007) Copper-free click chemistry for dynamic in vivo imaging. *Proceedings of the National Academy of Sciences of the United States of America* 104(43), 16793–16797. 10.1073/pnas.0707090104.

Chapter 1

29. Dommerholt J, Schmidt S, Temming R, Hendriks LJA, Rutjes FPJT, van Hest JCM, Lefeber DJ, Friedl P, van Delft FL (2010) Readily accessible bicyclononynes for bioorthogonal labeling and three-dimensional imaging of living cells. *Angewandte Chemie International Edition* 49(49), 9422–9425. 10.1002/anie.201003761.
30. Ning X, Guo J, Wolfert MA, Boons G-J (2008) Visualizing metabolically labeled glycoconjugates of living cells by copper-free and fast huisgen cycloadditions. *Angewandte Chemie International Edition* 47(12), 2253–2255. 10.1002/anie.200705456.
31. Debets MF, van Berkel SS, Schoffelen S, Rutjes FPJT, van Hest JCM, van Delft FL (2010) Aza-dibenzocyclooctynes for fast and efficient enzyme PEGylation via copper-free (3+2) cycloaddition. *Chem. Commun.* 46(1), 97–99. 10.1039/B917797C.
32. Jewett JC, Sletten EM, Bertozzi CR (2010) Rapid Cu-free click chemistry with readily synthesized biarylazacyclooctynones. *Journal of the American Chemical Society* 132(11), 3688–3690. 10.1021/ja100014q.
33. Blackman ML, Royzen M, Fox JM (2008) Tetrazine ligation: fast bioconjugation based on inverse-electron-demand Diels-Alder reactivity. *Journal of the American Chemical Society* 130(41), 13518–13519. 10.1021/ja8053805.
34. Devaraj NK, Weissleder R, Hilderbrand SA (2008) Tetrazine-based cycloadditions: application to pretargeted live cell imaging. *Bioconjugate Chemistry* 19(12), 2297–2299. 10.1021/bc8004446.
35. Blizzard RJ, Backus DR, Brown W, Bazewicz CG, Li Y, Mehl RA (2015) Ideal Bioorthogonal Reactions Using A Site-Specifically Encoded Tetrazine Amino Acid. *Journal of the American Chemical Society* 137(32), 10044–10047. 10.1021/jacs.5b03275.
36. Darko A, Wallace S, Dmitrenko O, Machovina MM, Mehl RA, Chin JW, Fox JM (2014) Conformationally Strained trans-Cyclooctene with Improved Stability and Excellent Reactivity in Tetrazine Ligation. *Chemical science* 5(10), 3770–3776. 10.1039/C4SC01348D.
37. Knall A-C, Hollauf M, Slugovc C (2014) Kinetic studies of inverse electron demand Diels-Alder reactions (iEDDA) of norbornenes and 3,6-dipyridin-2-yl-1,2,4,5-tetrazine. *Tetrahedron Letters* 55(34), 4763–4766. 10.1016/j.tetlet.2014.07.002.
38. Yang J, Šečkutė J, Cole CM, Devaraj NK (2012) Live-cell imaging of cyclopropene tags with fluorogenic tetrazine cycloadditions. *Angewandte Chemie International Edition* 51(30), 7476–7479. 10.1002/anie.201202122.
39. Chen W, Wang D, Dai C, Hamelberg D, Wang B (2012) Clicking 1,2,4,5-tetrazine and cyclooctynes with tunable reaction rates. *Chem. Commun.* 48(12), 1736–1738. 10.1039/C2CC16716F.
40. Knall A-C, Slugovc C (2013) Inverse electron demand Diels-Alder (iEDDA)-initiated conjugation: a (high) potential click chemistry scheme. *Chem. Soc. Rev.* 42(12), 5131–5142. 10.1039/C3CS60049A.

41. Rossin R, van den Bosch SM, Hoeve W ten, Carvelli M, Versteegen RM, Lub J, Robillard MS (2013) Highly reactive trans-cyclooctene tags with improved stability for Diels-Alder chemistry in living systems. *Bioconjugate Chemistry* 24(7), 1210–1217. 10.1021/bc400153y.
42. Karver MR, Weissleder R, Hilderbrand SA (2011) Synthesis and evaluation of a series of 1,2,4,5-tetrazines for bioorthogonal conjugation. *Bioconjugate Chemistry* 22(11), 2263–2270. 10.1021/bc200295y.
43. Pinner A (1893) Ueber die Einwirkung von Hydrazin auf Imidoäther. *Ber. Dtsch. Chem. Ges.* 26(2), 2126–2135. 10.1002/cber.189302602188.
44. Qu Y, Sauvage F-X, Clavier G, Miomandre F, Audebert P (2018) Metal-Free Synthetic Approach to 3-Monosubstituted Unsymmetrical 1,2,4,5-Tetrazines Useful for Bioorthogonal Reactions. *Angewandte Chemie International Edition* 57(37), 12057–12061. 10.1002/anie.201804878.
45. Mao W, Shi W, Li J, Su D, Wang X, Zhang L, Pan L, Wu X, Wu H (2019) Organocatalytic and Scalable Syntheses of Unsymmetrical 1,2,4,5-Tetrazines by Thiol-Containing Promoters. *Angewandte Chemie International Edition* 58(4), 1106–1109. 10.1002/anie.201812550.
46. Yang J, Karver MR, Li W, Sahu S, Devaraj NK (2012) Metal-catalyzed one-pot synthesis of tetrazines directly from aliphatic nitriles and hydrazine. *Angewandte Chemie (International ed. in English)* 51(21), 5222–5225. 10.1002/anie.201201117.
47. Selvaraj R, Fox JM (2014) An efficient and mild oxidant for the synthesis of s-tetrazines. *Tetrahedron Letters* 55(34), 4795–4797. 10.1016/j.tetlet.2014.07.012.
48. Wu H, Yang J, Šečková J, Devaraj NK (2014) In Situ Synthesis of Alkenyl Tetrazines for Highly Fluorogenic Bioorthogonal Live-Cell Imaging Probes. *Angew. Chem.* 126(23), 5915–5919. 10.1002/ange.201400135.
49. Lambert WD, Fang Y, Mahapatra S, Huang Z, Ende CW am, Fox JM (2019) Installation of Minimal Tetrazines through Silver-Mediated Liebeskind-Srogl Coupling with Arylboronic Acids. *Journal of the American Chemical Society* 141(43), 17068–17074. 10.1021/jacs.9b08677.
50. Royzen M, Yap GPA, Fox JM (2008) A photochemical synthesis of functionalized trans-cyclooctenes driven by metal complexation. *Journal of the American Chemical Society* 130(12), 3760–3761. 10.1021/ja8001919.
51. Peng T, Hang HC (2016) Site-Specific Bioorthogonal Labeling for Fluorescence Imaging of Intracellular Proteins in Living Cells. *Journal of the American Chemical Society* 138(43), 14423–14433. 10.1021/jacs.6b08733.
52. Uttamapinant C, Howe JD, Lang K, Beránek V, Davis L, Mahesh M, Barry NP, Chin JW (2015) Genetic code expansion enables live-cell and super-resolution imaging of site-specifically labeled cellular proteins. *Journal of the American Chemical Society* 137(14), 4602–4605. 10.1021/ja512838z.

Chapter 1

53. Li Z, Wang D, Li L, Pan S, Na Z, Tan CYJ, Yao SQ (2014) “Minimalist” cyclopropene-containing photo-cross-linkers suitable for live-cell imaging and affinity-based protein labeling. *Journal of the American Chemical Society* 136(28), 9990–9998. 10.1021/ja502780z.
54. Elliott TS, Townsley FM, Bianco A, Ernst RJ, Sachdeva A, Elsässer SJ, Davis L, Lang K, Pisa R, Greiss S, Lilley KS, Chin JW (2014) Proteome labeling and protein identification in specific tissues and at specific developmental stages in an animal. *Nat Biotechnol* 32(5), 465–472. 10.1038/nbt.2860.
55. Seckute J, Yang J, Devaraj NK (2013) Rapid oligonucleotide-templated fluorogenic tetrazine ligations. *Nucleic acids research* 41(15), e148. 10.1093/nar/gkt540.
56. Parveen S, Misra R, Sahoo SK (2012) Nanoparticles: a boon to drug delivery, therapeutics, diagnostics and imaging. *Nanomedicine nanotechnology, biology, and medicine* 8(2), 147–166. 10.1016/j.nano.2011.05.016.
57. Barenholz Y (2012) Doxil®--the first FDA-approved nano-drug: lessons learned. *Journal of controlled release official journal of the Controlled Release Society* 160(2), 117–134. 10.1016/j.jconrel.2012.03.020.
58. Auffan M, Rose J, Bottero J-Y, Lowry GV, Jolivet J-P, Wiesner MR (2009) Towards a definition of inorganic nanoparticles from an environmental, health and safety perspective. *Nat. Nanotechnol.* 4(10), 634–641. 10.1038/nnano.2009.242.
59. Eker F, Duman H, Akdaşçi E, Bolat E, Sarıtaş S, Karav S, Witkowska AM (2024) A Comprehensive Review of Nanoparticles: From Classification to Application and Toxicity. *Molecules (Basel, Switzerland)* 29(15), 3482. 10.3390/molecules29153482.
60. Malik S, Singh J, Goyat R, Saharan Y, Chaudhry V, Umar A, Ibrahim AA, Akbar S, Ameen S, Baskoutas S (2023) Nanomaterials-based biosensor and their applications: A review. *Heliyon* 9(9), e19929. 10.1016/j.heliyon.2023.e19929.
61. Lucky SS, Soo KC, Zhang Y (2015) Nanoparticles in photodynamic therapy. *Chemical Reviews* 115(4), 1990–2042. 10.1021/cr5004198.
62. Sharma SK, Shrivastava N, Rossi F, Le Tung D, Thanh NTK (2019) Nanoparticles-based magnetic and photo induced hyperthermia for cancer treatment. *Nano Today* 29, 100795. 10.1016/j.nantod.2019.100795.
63. Lapusan R, Borlan R, Focsan M (2024) Advancing MRI with magnetic nanoparticles: a comprehensive review of translational research and clinical trials. *Nanoscale Adv.* 6(9), 2234–2259. 10.1039/D3NA01064C.
64. Lemaster JE, Jokerst JV (2017) What is new in nanoparticle-based photoacoustic imaging? *Wiley interdisciplinary reviews. Nanomedicine and nanobiotechnology* 9(1). 10.1002/wnan.1404.
65. Algar WR, Massey M, Rees K, Higgins R, Krause KD, Darwish GH, Peveler WJ, Xiao Z, Tsai H-Y, Gupta R, Lix K, Tran MV, Kim H (2021) Photoluminescent Nanoparticles for Chemical and

- Biological Analysis and Imaging. *Chemical Reviews* 121(15), 9243–9358. 10.1021/acs.chemrev.0c01176.
66. Kim M, Shin M, Zhao Y, Ghosh M, Son Y-O (2024) Transformative Impact of Nanocarrier-Mediated Drug Delivery: Overcoming Biological Barriers and Expanding Therapeutic Horizons. *Small science* 4(11), 2400280. 10.1002/smsc.202400280.
67. Majumder J, Minko T (2021) Multifunctional and stimuli-responsive nanocarriers for targeted therapeutic delivery. *Expert Opinion on Drug Delivery* 18(2), 205–227. 10.1080/17425247.2021.1828339.
68. Yasir M, Mishra R, Tripathi AS, Maurya RK, shahi A, Zaki MEA, Al Hussain SA, Masand VH (2024) Theranostics: a multifaceted approach utilizing nano-biomaterials. *Discover Nano* 19(1), 35. 10.1186/s11671-024-03979-w.
69. Mitchell MJ, Billingsley MM, Haley RM, Wechsler ME, Peppas NA, Langer R (2021) Engineering precision nanoparticles for drug delivery. *Nat Rev Drug Discov* 20(2), 101–124. 10.1038/s41573-020-0090-8.
70. Blanco E, Shen H, Ferrari M (2015) Principles of nanoparticle design for overcoming biological barriers to drug delivery. *Nat Biotechnol* 33(9), 941–951. 10.1038/nbt.3330.
71. Wang B, Hu S, Teng Y, Chen J, Wang H, Xu Y, Wang K, Xu J, Cheng Y, Gao X (2024) Current advance of nanotechnology in diagnosis and treatment for malignant tumors. *Sig Transduct Target Ther* 9(1), 200. 10.1038/s41392-024-01889-y.
72. Kirtane AR, Verma M, Karandikar P, Furin J, Langer R, Traverso G (2021) Nanotechnology approaches for global infectious diseases. *Nat. Nanotechnol.* 16(4), 369–384. 10.1038/s41565-021-00866-8.
73. Saraiva C, Praça C, Ferreira R, Santos T, Ferreira L, Bernardino L (2016) Nanoparticle-mediated brain drug delivery: Overcoming blood-brain barrier to treat neurodegenerative diseases. *Journal of controlled release official journal of the Controlled Release Society* 235, 34–47. 10.1016/j.jconrel.2016.05.044.
74. Soumya RS, Raghu KG (2023) Recent advances on nanoparticle-based therapies for cardiovascular diseases. *Journal of Cardiology* 81(1), 10–18. 10.1016/j.jjcc.2022.02.009.
75. Nienhaus K, Nienhaus GU (2023) Mechanistic Understanding of Protein Corona Formation around Nanoparticles: Old Puzzles and New Insights. *Small* 19(28), e2301663. 10.1002/sml.202301663.
76. Rennick JJ, Johnston APR, Parton RG (2021) Key principles and methods for studying the endocytosis of biological and nanoparticle therapeutics. *Nat. Nanotechnol.* 16(3), 266–276. 10.1038/s41565-021-00858-8.
77. Smith SA, Selby LI, Johnston APR, Such GK (2019) The Endosomal Escape of Nanoparticles: Toward More Efficient Cellular Delivery. *Bioconjugate Chemistry* 30(2), 263–272. 10.1021/acs.bioconjchem.8b00732.

Chapter 1

78. Oh E, Liu R, Nel A, Gemill KB, Bilal M, Cohen Y, Medintz IL (2016) Meta-analysis of cellular toxicity for cadmium-containing quantum dots. *Nat. Nanotechnol.* 11(5), 479–486. 10.1038/nnano.2015.338.
79. Patel DM, Patel NN, Patel JK (2021) Nanomedicine Scale-Up Technologies: Feasibilities and Challenges, in: Patel JK (ed.) *Emerging Technologies for Nanoparticle Manufacturing*, pp. 511–539. Cham: Springer International Publishing AG.
80. Sainz V, Conriot J, Matos AI, Peres C, Zupancic E, Moura L, Silva LC, Florindo HF, Gaspar RS (2015) Regulatory aspects on nanomedicines. *Biochemical and Biophysical Research Communications* 468(3), 504–510. 10.1016/j.bbrc.2015.08.023.
81. Li T, Yang Y, Qi H, Cui W, Zhang L, Fu X, He X, Liu M, Li P-f, Yu T (2023) CRISPR/Cas9 therapeutics: progress and prospects. *Sig Transduct Target Ther* 8(1), 36. 10.1038/s41392-023-01309-7.
82. Farooq MU, Lawrie CH, Deng N-N (2024) Engineering nanoparticles for cancer immunotherapy: Current achievements, key considerations and future perspectives. *Chemical Engineering Journal* 486, 150356. 10.1016/j.cej.2024.150356.
83. Kramer S, Svatunek D, Alberg I, Gräfen B, Schmitt S, Braun L, van Onzen AHAM, Rossin R, Koynov K, Mikula H, Zentel R (2019) HPMA-Based Nanoparticles for Fast, Bioorthogonal iEDDA Ligation. *Biomacromolecules* 20(10), 3786–3797. 10.1021/acs.biomac.9b00868.
84. Go EB, Lee JH, Cho JH, Kwon NH, Choi J-i, Kwon I (2024) Enhanced therapeutic potential of antibody fragment via IEDDA-mediated site-specific albumin conjugation. *J Biol Eng* 18(1), 23. 10.1186/s13036-024-00418-3.
85. Han H-S, Niemeyer E, Huang Y, Kamoun WS, Martin JD, Bhaumik J, Chen Y, Roberge S, Cui J, Martin MR, Fukumura D, Jain RK, Bawendi MG, Duda DG (2015) Quantum dot/antibody conjugates for in vivo cytometric imaging in mice. *Proceedings of the National Academy of Sciences of the United States of America* 112(5), 1350–1355. 10.1073/pnas.1421632111.
86. van Onzen AHAM, Rossin R, Schenning APHJ, Nicolay K, Milroy L-G, Robillard MS, Brunsveld L (2019) Tetrazine- trans-Cyclooctene Chemistry Applied to Fabricate Self-Assembled Fluorescent and Radioactive Nanoparticles for in Vivo Dual Mode Imaging. *Bioconjugate Chemistry* 30(3), 547–551. 10.1021/acs.bioconjchem.9b00038.
87. Lumen D, Näkki S, Imlimthan S, Lambidis E, Sarparanta M, Xu W, Lehto V-P, Airaksinen AJ (2019) Site-Specific ¹¹¹In-Radiolabeling of Dual-PEGylated Porous Silicon Nanoparticles and Their In Vivo Evaluation in Murine 4T1 Breast Cancer Model. *Pharmaceutics* 11(12). 10.3390/pharmaceutics11120686.
88. Lambidis E, Lumén D, Koskipahta E, Imlimthan S, Lopez BB, Sánchez AIF, Sarparanta M, Cheng RH, Airaksinen AJ (2022) Synthesis and ex vivo biodistribution of two ⁶⁸Ga-labeled tetrazine

- tracers: Comparison of pharmacokinetics. *Nuclear Medicine and Biology* 114-115, 151–161. 10.1016/j.nucmedbio.2022.05.004.
89. Zhang R, Gao J, Zhao G, Zhou L, Kong F, Jiang T, Jiang H (2023) Tetrazine bioorthogonal chemistry makes nanotechnology a powerful toolbox for biological applications. *Nanoscale* 15(2), 461–469. 10.1039/d2nr06056f.
90. Haun JB, Devaraj NK, Hilderbrand SA, Lee H, Weissleder R (2010) Bioorthogonal chemistry amplifies nanoparticle binding and enhances the sensitivity of cell detection. *Nat. Nanotechnol.* 5(9), 660–665. 10.1038/nnano.2010.148.
91. Pellico J, Fernández-Barahona I, Benito M, Gaitán-Simón Á, Gutiérrez L, Ruiz-Cabello J, Herranz F (2019) Unambiguous detection of atherosclerosis using bioorthogonal nanomaterials. *Nanomedicine nanotechnology, biology, and medicine* 17, 26–35. 10.1016/j.nano.2018.12.015.
92. Adrover JM, Pellico J, Fernández-Barahona I, Martín-Salamanca S, Ruiz-Cabello J, Hidalgo A, Herranz F (2020) Thrombo-tag, an in vivo formed nanotracer for the detection of thrombi in mice by fast pre-targeted molecular imaging. *Nanoscale* 12(45), 22978–22987. 10.1039/d0nr04538a.
93. Pellico J, Ruiz-Cabello J, Saiz-Alía M, Del Rosario G, Caja S, Montoya M, Fernández de Manuel L, Morales MP, Gutiérrez L, Galiana B, Enríquez JA, Herranz F (2016) Fast synthesis and bioconjugation of (68) Ga core-doped extremely small iron oxide nanoparticles for PET/MR imaging. *Contrast media & molecular imaging* 11(3), 203–210. 10.1002/cmimi.1681.
94. Wu Y, Vazquez-Prada KX, Liu Y, Whittaker AK, Zhang R, Ta HT (2021) Recent Advances in the Development of Theranostic Nanoparticles for Cardiovascular Diseases. *Nanotheranostics* 5(4), 499–514. 10.7150/ntno.62730.
95. Hapuarachchige S, Huang CT, Donnelly MC, Bařinka C, Lupold SE, Pomper MG, Artemov D (2020) Cellular Delivery of Bioorthogonal Pretargeting Therapeutics in PSMA-Positive Prostate Cancer. *Molecular pharmaceutics* 17(1), 98–108. 10.1021/acs.molpharmaceut.9b00788.
96. Hapuarachchige S, Kato Y, Artemov D (2016) Bioorthogonal two-component drug delivery in HER2(+) breast cancer mouse models. *Sci Rep* 6(1), 24298. 10.1038/srep24298.
97. Yoo J, Choi S, Son J, Yi G, Kim E, Koo H (2019) Click chemistry-mediated tumor-targeting of SN38-loaded nanoparticles using trastuzumab. *Biochemical and Biophysical Research Communications* 515(1), 207–213. 10.1016/j.bbrc.2019.05.128.
98. Lee SH, Park OK, Kim J, Shin K, Pack CG, Kim K, Ko G, Lee N, Kwon S-H, Hyeon T (2019) Deep Tumor Penetration of Drug-Loaded Nanoparticles by Click Reaction-Assisted Immune Cell Targeting Strategy. *Journal of the American Chemical Society* 141(35), 13829–13840. 10.1021/jacs.9b04621.
99. Kufleitner M, Haiber LM, Wittmann V (2023) Metabolic glycoengineering - exploring glycosylation with bioorthogonal chemistry. *Chem. Soc. Rev.* 52(2), 510–535. 10.1039/D2CS00764A.

Chapter 1

100. Agatemor C, Buettner MJ, Ariss R, Muthiah K, Saeui CT, Yarema KJ (2019) Exploiting metabolic glycoengineering to advance healthcare. *Nat Rev Chem* 3(10), 605–620. 10.1038/s41570-019-0126-y.
101. Wang H, Mooney DJ (2020) Metabolic glycan labelling for cancer-targeted therapy. *Nat. Chem.* 12(12), 1102–1114. 10.1038/s41557-020-00587-w.
102. Lamoot A, Uvyn A, Kasmi S, Geest BG de (2021) Covalent Cell Surface Conjugation of Nanoparticles by a Combination of Metabolic Labeling and Click Chemistry. *Angewandte Chemie International Edition* 60(12), 6320–6325. 10.1002/anie.202015625.
103. Andreev OA, Dupuy AD, Segala M, Sandugu S, Serra DA, Chichester CO, Engelman DM, Reshetnyak YK (2007) Mechanism and uses of a membrane peptide that targets tumors and other acidic tissues in vivo. *Proceedings of the National Academy of Sciences of the United States of America* 104(19), 7893–7898. 10.1073/pnas.0702439104.
104. Wyatt LC, Lewis JS, Andreev OA, Reshetnyak YK, Engelman DM (2017) Applications of pHLIP Technology for Cancer Imaging and Therapy. *Trends in biotechnology* 35(7), 653–664. 10.1016/j.tibtech.2017.03.014.
105. Emmetiere F, Irwin C, Viola-Villegas NT, Longo V, Cheal SM, Zanzonico P, Pillarsetty N, Weber WA, Lewis JS, Reiner T (2013) (18)F-labeled-bioorthogonal liposomes for in vivo targeting. *Bioconjugate Chemistry* 24(11), 1784–1789. 10.1021/bc400322h.
106. Lu G, Li F, Zhang F, Huang L-L, Zhang L, Lv Y, Wei W, Xie H-Y (2018) Amplifying Nanoparticle Targeting Performance to Tumor via Diels-Alder Cycloaddition. *Adv. Funct. Mater.* 28(30), 1707596. 10.1002/adfm.201707596.
107. Hou S, Choi J-S, Garcia MA, Xing Y, Chen K-J, Chen Y-M, Jiang ZK, Ro T, Wu L, Stout DB, Tomlinson JS, Wang H, Chen K, Tseng H-R, Lin W-Y (2016) Pretargeted Positron Emission Tomography Imaging That Employs Supramolecular Nanoparticles with in Vivo Bioorthogonal Chemistry. *ACS nano* 10(1), 1417–1424. 10.1021/acsnano.5b06860.
108. Goos JACM, Davydova M, Dilling TR, Cho A, Cornejo MA, Gupta A, Price WS, Puttick S, Whittaker MR, Quinn JF, Davis TP, Lewis JS (2020) Design and preclinical evaluation of nanostars for the passive pretargeting of tumor tissue. *Nuclear Medicine and Biology* 84-85, 63–72. 10.1016/j.nucmedbio.2020.02.012.
109. Stéen EJJ, Jørgensen JT, Johann K, Nørregaard K, Sohr B, Svatunek D, Birke A, Shalgunov V, Edem PE, Rossin R, Seidl C, Schmid F, Robillard MS, Kristensen JL, Mikula H, Barz M, Kjær A, Herth MM (2020) Trans-Cyclooctene-Functionalized PeptoBrushes with Improved Reaction Kinetics of the Tetrazine Ligation for Pretargeted Nuclear Imaging. *ACS nano* 14(1), 568–584. 10.1021/acsnano.9b06905.
110. Denk C, Svatunek D, Mairinger S, Stanek J, Filip T, Matscheko D, Kuntner C, Wanek T, Mikula H (2016) Design, Synthesis, and Evaluation of a Low-Molecular-Weight (11)C-Labeled Tetrazine

- for Pretargeted PET Imaging Applying Bioorthogonal in Vivo Click Chemistry. *Bioconjugate Chemistry* 27(7), 1707–1712. 10.1021/acs.bioconjchem.6b00234.
111. Chen Z, Chen M, Zhou K, Rao J (2020) Pre-targeted Imaging of Protease Activity through In Situ Assembly of Nanoparticles. *Angew. Chem.* 132(20), 7938–7944. 10.1002/ange.201916352.
112. Ren H, Xiao F, Zhan K, Kim Y-P, Xie H, Xia Z, Rao J (2009) A biocompatible condensation reaction for the labeling of terminal cysteine residues on proteins. *Angewandte Chemie International Edition* 48(51), 9658–9662. 10.1002/anie.200903627.
113. Chen Z, Chen M, Cheng Y, Kowada T, Xie J, Zheng X, Rao J (2020) Exploring the Condensation Reaction between Aromatic Nitriles and Amino Thiols To Optimize In Situ Nanoparticle Formation for the Imaging of Proteases and Glycosidases in Cells. *Angewandte Chemie International Edition* 59(8), 3272–3279. 10.1002/anie.201913314.
114. Hu Y, Zhang J, Miao Y, Wen X, Wang J, Sun Y, Chen Y, Lin J, Qiu L, Guo K, Chen H-Y, Ye D (2021) Enzyme-Mediated In Situ Self-Assembly Promotes In Vivo Bioorthogonal Reaction for Pretargeted Multimodality Imaging. *Angewandte Chemie International Edition* 60(33), 18082–18093. 10.1002/anie.202103307.
115. Yan R, Hu Y, Liu F, Wei S, Fang D, Shuhendler AJ, Liu H, Chen H-Y, Ye D (2019) Activatable NIR Fluorescence/MRI Bimodal Probes for in Vivo Imaging by Enzyme-Mediated Fluorogenic Reaction and Self-Assembly. *Journal of the American Chemical Society* 141(26), 10331–10341. 10.1021/jacs.9b03649.
116. Wen X, Zeng W, Zhang J, Liu Y, Miao Y, Liu S, Yang Y, Xu J-J, Ye D (2024) Cascade In Situ Self-Assembly and Bioorthogonal Reaction Enable the Enrichment of Photosensitizers and Carbonic Anhydrase Inhibitors for Pretargeted Cancer Theranostics. *Angewandte Chemie International Edition* 63(4), e202314039. 10.1002/anie.202314039.
117. Feng Y, Wu Y, Zuo J, Tu L, Que I, Chang Y, Cruz LJ, Chan A, Zhang H (2019) Assembly of upconversion nanophotosensitizer in vivo to achieve scatheless real-time imaging and selective photodynamic therapy. *Biomaterials* 201, 33–41. 10.1016/j.biomaterials.2019.02.015.
118. Idris NM, Gnanasammandhan MK, Zhang J, Ho PC, Mahendran R, Zhang Y (2012) In vivo photodynamic therapy using upconversion nanoparticles as remote-controlled nanotransducers. *Nat Med* 18(10), 1580–1585. 10.1038/nm.2933.
119. Park YI, Kim HM, Kim JH, Moon KC, Yoo B, Lee KT, Lee N, Choi Y, Park W, Ling D, Na K, Moon WK, Choi SH, Park HS, Yoon S-Y, Suh YD, Lee SH, Hyeon T (2012) Theranostic probe based on lanthanide-doped nanoparticles for simultaneous in vivo dual-modal imaging and photodynamic therapy. *Advanced Materials* 24(42), 5755–5761. 10.1002/adma.201202433.
120. Khan I, Agris PF, Yigit MV, Royzen M (2016) In situ activation of a doxorubicin prodrug using imaging-capable nanoparticles. *Chem. Commun.* 52(36), 6174–6177. 10.1039/c6cc01024e.

Chapter 1

121. Suehiro F, Fujii S, Nishimura T (2022) Bioorthogonal micellar nanoreactors for prodrug cancer therapy using an inverse-electron-demand Diels-Alder reaction. *Chem. Commun.* 58(50), 7026–7029. 10.1039/D2CC02121H.
122. Li H, Conde J, Guerreiro A, Bernardes GJL (2020) Tetrazine Carbon Nanotubes for Pretargeted In Vivo “Click-to-Release” Bioorthogonal Tumour Imaging. *Angewandte Chemie International Edition* 59(37), 16023–16032. 10.1002/anie.202008012.
123. Zuo L, Ding J, Li C, Lin F, Chen PR, Wang P, Lu G, Zhang J, Huang L-L, Xie H-Y (2020) Coordinating bioorthogonal reactions with two tumor-microenvironment-responsive nanovehicles for spatiotemporally controlled prodrug activation. *Chemical science* 11(8), 2155–2160. 10.1039/c9sc05036a.
124. Xie X, Li B, Wang J, Zhan C, Huang Y, Zeng F, Wu S (2019) Tetrazine-Mediated Bioorthogonal System for Prodrug Activation, Photothermal Therapy, and Optoacoustic Imaging. *ACS Appl. Mater. Interfaces* 11(45), 41875–41888. 10.1021/acsami.9b13374.
125. Khan I, Seebald LM, Robertson NM, Yigit MV, Royzen M (2017) Controlled in-cell activation of RNA therapeutics using bond-cleaving bio-orthogonal chemistry. *Chemical science* 8(8), 5705–5712. 10.1039/C7SC01380A.
126. Robertson NM, Yang Y, Khan I, LaMantia VE, Royzen M, Yigit MV (2017) Single-trigger dual-responsive nanoparticles for controllable and sequential prodrug activation. *Nanoscale* 9(28), 10020–10030. 10.1039/C7NR04138A.
127. Kannaka K, Sano K, Munekane M, Yamasaki T, Hagimori M, Mukai T (2022) Enhanced Therapeutic Effect of Liposomal Doxorubicin via Bio-Orthogonal Chemical Reactions in Tumors. *Molecular pharmaceutics* 19(5), 1400–1409. 10.1021/acs.molpharmaceut.1c00936.
128. Versteegen RM, Rossin R, Hoeve W ten, Janssen HM, Robillard MS (2013) Click to release: instantaneous doxorubicin elimination upon tetrazine ligation. *Angewandte Chemie International Edition* 52(52), 14112–14116. 10.1002/anie.201305969.
129. Taylor MT, Blackman ML, Dmitrenko O, Fox JM (2011) Design and synthesis of highly reactive dienophiles for the tetrazine-trans-cyclooctene ligation. *Journal of the American Chemical Society* 133(25), 9646–9649. 10.1021/ja201844c.
130. Svatunek D, Wilkovitsch M, Hartmann L, Houk KN, Mikula H (2022) Uncovering the Key Role of Distortion in Bioorthogonal Tetrazine Tools That Defy the Reactivity/Stability Trade-Off. *Journal of the American Chemical Society* 144(18), 8171–8177. 10.1021/jacs.2c01056.
131. Keinänen O, Mäkilä EM, Lindgren R, Virtanen H, Liljenbäck H, Oikonen V, Sarparanta M, Molthoff C, Windhorst AD, Roivainen A, Salonen JJ, Airaksinen AJ (2017) Pretargeted PET Imaging of trans-Cyclooctene-Modified Porous Silicon Nanoparticles. *ACS omega* 2(1), 62–69. 10.1021/acsomega.6b00269.

132. Sapsford KE, Algar WR, Berti L, Gemmill KB, Casey BJ, Oh E, Stewart MH, Medintz IL (2013) Functionalizing nanoparticles with biological molecules: developing chemistries that facilitate nanotechnology. *Chemical Reviews* 113(3), 1904–2074. 10.1021/cr300143v.
133. Kaymaz SV, Nobar HM, Sargül H, Soylukan C, Akyüz L, Yüce M (2023) Nanomaterial surface modification toolkit: Principles, components, recipes, and applications. *Advances in Colloid and Interface Science* 322, 103035. 10.1016/j.cis.2023.103035.
134. Li N, Binder WH (2011) Click-chemistry for nanoparticle-modification. *J. Mater. Chem.* 21(42), 16717. 10.1039/c1jm11558h.
135. Montalbetti CAGN, Falque V (2005) Amide bond formation and peptide coupling. *Tetrahedron* 61(46), 10827–10852. 10.1016/j.tet.2005.08.031.
136. Padín-González E, Lancaster P, Bottini M, Gasco P, Tran L, Fadeel B, Wilkins T, Monopoli MP (2022) Understanding the Role and Impact of Poly (Ethylene Glycol) (PEG) on Nanoparticle Formulation: Implications for COVID-19 Vaccines. *Frontiers in Bioengineering and Biotechnology* 10, 882363. 10.3389/fbioe.2022.882363.
137. Rahim MK, Kota R, Haun JB (2015) Enhancing reactivity for bioorthogonal pretargeting by unmasking antibody-conjugated trans-cyclooctenes. *Bioconjugate Chemistry* 26(2), 352–360. 10.1021/bc500605g.
138. Derjaguin B, Landau L (1993) Theory of the stability of strongly charged lyophobic sols and of the adhesion of strongly charged particles in solutions of electrolytes. *Progress in Surface Science* 43(1-4), 30–59. 10.1016/0079-6816(93)90013-L.
139. Agmo Hernández V (2023) An overview of surface forces and the DLVO theory. *ChemTexts* 9(4). 10.1007/s40828-023-00182-9.
140. Witten TA, Pincus PA (1986) Colloid stabilization by long grafted polymers. *Macromolecules* 19(10), 2509–2513. 10.1021/ma00164a009.
141. Lazzari S, Moscatelli D, Codari F, Salmona M, Morbidelli M, Diomede L (2012) Colloidal stability of polymeric nanoparticles in biological fluids. *J Nanopart Res* 14(6), 920. 10.1007/s11051-012-0920-7.
142. Guerrini L, Alvarez-Puebla RA, Pazos-Perez N (2018) Surface Modifications of Nanoparticles for Stability in Biological Fluids. *Materials (Basel, Switzerland)* 11(7). 10.3390/ma11071154.
143. Martínez R, Navarro Poupard MF, Álvarez A, Soprano E, Migliavacca M, Carrillo-Carrión C, Polo E, Pelaz B, Pino Pd (2020) Chapter 2 - Nanoparticle behavior and stability in biological environments, in: Chung EJ, Leon L, Rinaldi C (eds.) *Nanoparticles for biomedical applications: Fundamental concepts, biological interactions and clinical applications*, pp. 5–18. Oxford: Elsevier.
144. Schubert J, Chanana M (2018) Coating Matters: Review on Colloidal Stability of Nanoparticles with Biocompatible Coatings in Biological Media, Living Cells and Organisms. *Current medicinal chemistry* 25(35), 4553–4586. 10.2174/0929867325666180601101859.

Chapter 1

145. Suk JS, Xu Q, Kim N, Hanes J, Ensign LM (2016) PEGylation as a strategy for improving nanoparticle-based drug and gene delivery. *Advanced Drug Delivery Reviews* 99(Pt A), 28–51. 10.1016/j.addr.2015.09.012.
146. Owens DE, Peppas NA (2006) Opsonization, biodistribution, and pharmacokinetics of polymeric nanoparticles. *International Journal of Pharmaceutics* 307(1), 93–102. 10.1016/j.ijpharm.2005.10.010.
147. Li M, Jiang S, Simon J, Paßlick D, Frey M-L, Wagner M, Mailänder V, Crespy D, Landfester K (2021) Brush Conformation of Polyethylene Glycol Determines the Stealth Effect of Nanocarriers in the Low Protein Adsorption Regime. *Nano letters* 21(4), 1591–1598. 10.1021/acs.nanolett.0c03756.
148. Yang Q, Jones SW, Parker CL, Zamboni WC, Bear JE, Lai SK (2014) Evading immune cell uptake and clearance requires PEG grafting at densities substantially exceeding the minimum for brush conformation. *Molecular pharmaceutics* 11(4), 1250–1258. 10.1021/mp400703d.
149. Chen C-Y, Hsieh M-J, Raj A, Peng W-C, Hamaguchi H-O, Chuang W-T, Wang X, Wang C-L (2023) Missing Piece in Colloidal Stability—Morphological Factor of Hydrophobic Nanoparticles. *Langmuir the ACS journal of surfaces and colloids* 39(8), 2922–2931. 10.1021/acs.langmuir.2c02582.
150. Yu Q, Zhao L, Guo C, Yan B, Su G (2020) Regulating Protein Corona Formation and Dynamic Protein Exchange by Controlling Nanoparticle Hydrophobicity. *Frontiers in Bioengineering and Biotechnology* 8, 210. 10.3389/fbioe.2020.00210.
151. Moore TL, Rodriguez-Lorenzo L, Hirsch V, Balog S, Urban D, Jud C, Rothen-Rutishauser B, Lattuada M, Petri-Fink A (2015) Nanoparticle colloidal stability in cell culture media and impact on cellular interactions. *Chem. Soc. Rev.* 44(17), 6287–6305. 10.1039/c4cs00487f.
152. Pack CG, Song MR, Tae EL, Hiroshima M, Byun KH, Kim JS, Sako Y (2012) Microenvironments and different nanoparticle dynamics in living cells revealed by a standard nanoparticle. *Journal of controlled release official journal of the Controlled Release Society* 163(3), 315–321. 10.1016/j.jconrel.2012.07.036.
153. Fischer K, Schmidt M (2016) Pitfalls and novel applications of particle sizing by dynamic light scattering. *Biomaterials* 98, 79–91. 10.1016/j.biomaterials.2016.05.003.
154. Handula M, Chen K-T, Seimbille Y (2021) IEDDA: An Attractive Bioorthogonal Reaction for Biomedical Applications. *Molecules (Basel, Switzerland)* 26(15), 4640. 10.3390/molecules26154640.
155. Han H-S, Devaraj NK, Lee J, Hilderbrand SA, Weissleder R, Bawendi MG (2010) Development of a bioorthogonal and highly efficient conjugation method for quantum dots using tetrazine-norbornene cycloaddition. *Journal of the American Chemical Society* 132(23), 7838–7839. 10.1021/ja101677r.

Chapter 1

Chapter 2
Goals of the Thesis

Chapter 2

Nanoparticles (NPs) have emerged as versatile platforms for biomedical applications over the past two decades. [1] Their unique physicochemical properties allow for the encapsulation of therapeutic agents, thereby protecting them from degradation, and enable targeted delivery to specific tissues or cells. At the same time, NPs can serve as contrast agents in imaging or even as theranostic systems that combine diagnosis and therapy within a single platform. The ability to finely tune their size, shape, and surface chemistry provides a broad design space. [2] Despite these advantages, NPs face numerous challenges within the living organism. Following intravenous administration, they must first withstand the dynamics of the bloodstream and rapid clearance by the mononuclear phagocyte system (MPS). Subsequently, processes such as extravasation into the target tissue, cellular uptake, and intracellular trafficking impose additional barriers. [3] At each of these stages, the physicochemical properties of NPs play a decisive role. However, a major challenge lies in the fact that different stages often require contradictory properties: while “stealth” characteristics reduce MPS-mediated clearance, they can simultaneously impair uptake by target cells. [4] To address these obstacles, the concept of stimuli-responsive NPs has been developed. These systems are designed to alter their properties in response to specific stimuli. [5] Endogenous stimuli such as the acidic pH and hypoxia of tumor tissues [6], elevated levels of particular enzymes [7], or reactive oxygen species [8] have been widely employed to induce NP transformations in proximity to disease sites. Similarly, exogenous stimuli including light [9], heat [10], or ultrasound [11] may be utilized. Stimuli-responsive designs enable modulation of particle size, surface charge, and even particle morphology in a controlled manner.

Moreover, many NP systems are functionalized with ligands that specifically recognize receptors on target cells. [12] However, since such receptors are often also expressed on healthy cells, unspecific binding can increase side effects and diminish therapeutic efficacy. Stimuli-responsive NP design also offers an elegant strategy to overcome this limitation. In so-called ligand-switchable NPs, the ability of ligands to bind receptors is activated only at the target site, resulting in improved selectivity and temporally controlled cellular uptake. [13] Strategies pursued so far typically rely on reversible covalent bonds [14] or electrostatic interactions to block ligands. [15] Alternatively, ligands can be inactivated by steric shielding, for example with long polymer chains such as PEG, which can be removed upon specific stimulation. [16] Another concept involves ligands on long linker polymers which were initially folded towards the particle core. Upon stimulation the polymers extend beyond the PEG brush on the NP surface, uncovering the cell uptake-promoting ligand (see **Figure 1**). [17] While these approaches highlight the potential of spatially and temporally controlled ligand exposure, they are often constrained by the risk of premature ligand unmasking, limited precision or incomplete switchability.

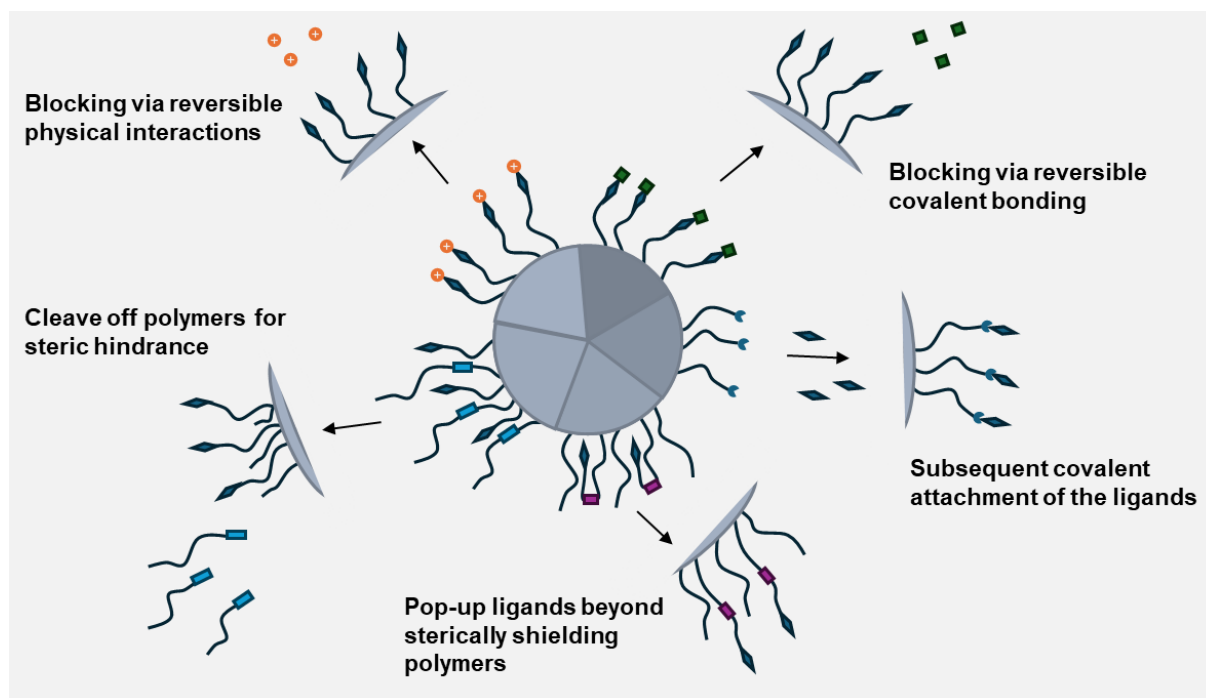


Figure 1. Schematic representation of different strategies to realize ligand-switchable NPs. Mechanisms to control ligand exposure include: (i) blocking via reversible physical interactions, (ii) blocking via reversible covalent bonding, (iii) subsequent covalent attachment of ligands, (iv) “pop-up” ligands extending beyond sterically shielding polymers, and (v) cleavage of polymers to reduce steric hindrance. (Adapted from Li, Montague et al. [13])

In this context, the question arises whether NPs can also be functionalized in a targeted and chemically precise manner during their circulation within the organism. Bioorthogonal reactions provide a promising pathway towards this goal. These reactions are characterized by the ability to proceed with high selectivity in complex biological environments without interfering with endogenous processes. [18] Thus, they could provide the foundation for novel strategies in which NPs are not rigidly preconfigured but are adaptively modified within the biological context. One of the most powerful bioorthogonal reactions is the inverse electron-demand Diels–Alder (iEDDA) reaction. It typically proceeds between a strained, electron-rich trans-cyclooctene (TCO) as the dienophile and an electron-deficient tetrazine as the diene which is why the iEDDA reaction is sometimes also referred to as tetrazine ligation. [19] The iEDDA reaction is characterized by exceptionally high reaction rates, allowing it to occur efficiently even at low concentrations and under physiological conditions. [20] In combination with NPs, iEDDA chemistry provides outstanding opportunities for innovation, as outlined in **Chapter 1**. The multivalency of NPs, together with the tunability of their surface architecture, allows for the precise spatial arrangement of multiple iEDDA-reactive motifs. Moreover, the robustness of the iEDDA chemistry ensures that these reactive groups can be effectively addressed *in vivo*.

Chapter 2

The aim of this work was to combine the iEDDA reaction with the concept of ligand-switchable NPs. Such an approach would allow NPs to circulate initially in a “stealth” mode within the organism, thereby evading premature recognition and clearance, and to be selectively activated for target cell recognition only when required through a precisely triggered chemical switching reaction. In addition, the use of pro-ligands, which can be converted into their active form by biological factors such as enzymes present on the target cell surface, offers an additional level of specificity. Taken together, the interplay between bioorthogonal iEDDA chemistry and nanoparticulate carrier systems offers a novel strategy for the development of highly specific, switchable NPs designed for advanced biomedical applications. These concepts directly address the fundamental challenges of NP design: ensuring stability during circulation, overcoming biological barriers, and achieving controlled functionality at the target site. In this context, the present work pursues the goal of systematically evaluating the applicability of the iEDDA reaction for the development of switchable NP systems.

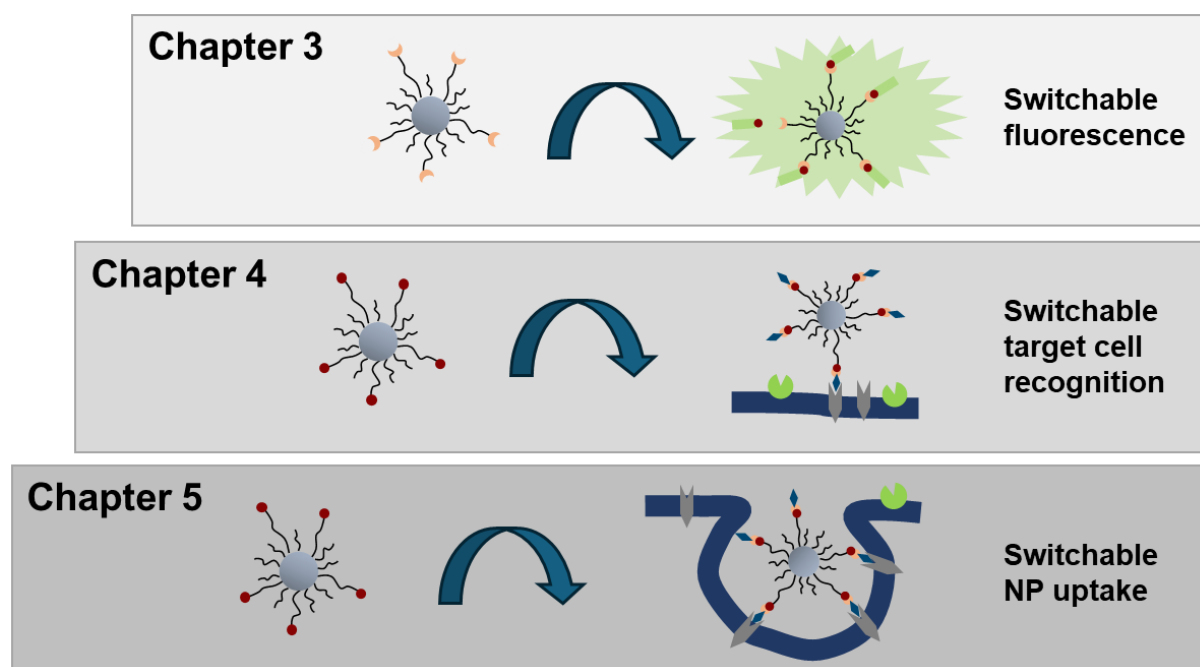


Figure 2. Schematic overview of the thesis chapters. Chapter 3 describes the development of NPs with switchable fluorescence properties. Chapter 4 focuses on the design and implementation of NPs enabling switchable target cell recognition. Chapter 5 evaluates switchable NP uptake. Collectively, these chapters illustrate the potential of combining bioorthogonal iEDDA reactions and NPs to design switchable NP systems for advanced biomedical applications.

Chapter 3 aimed to evaluate the potential of the iEDDA reaction for the selective and efficient functionalization of polymeric NPs in complex biological environments. The NPs were designed with a poly(lactic-co-glycolic acid) (PLGA) core and a modularly adjustable surface composition comprising

trans-cyclooctene (TCO)-functionalized and non-functionalized poly(lactide)-poly(ethylene glycol) (PLA-PEG) block copolymers, enabling precise control over the density of reactive surface groups. To enable real-time monitoring of the iEDDA reaction, a fluorogenic tetrazine-coumarin probe was employed, whose fluorescence turn-on directly reflects the progress of the reaction. [21] Within the scope of this study, the reaction kinetics on the NP surface were investigated and compared with the corresponding reaction in solution. Furthermore, the iEDDA-mediated functionalization in biological media as well as the stability of the reaction partners under such conditions were assessed. In addition, the potential of the probe for direct visualization of NP functionalization on the membranes of potential target cells was explored. The use of this fluorogenic approach enabled the creation of NPs with switchable fluorescence and demonstrated that the iEDDA reaction provides a viable and efficient route for the functionalization of polymeric NPs, even under challenging biological conditions, thereby supporting its suitability for future *in vivo* applications.

Chapter 4 built upon these promising results, shifting the focus from fluorescence switching to the development of NPs capable of switchable target cell recognition. The goal was to demonstrate that the iEDDA reaction can be employed as an external chemical trigger to introduce ligands required for receptor interaction onto the NP surface. In this way, initially ligand-free NPs could benefit from a pronounced stealth effect before enabling temporally controlled recognition of the desired target cells. The concept was further advanced by incorporating an additional activation step. To minimize potential biological side effects of the ligand, an inactive proligand was first conjugated to the NP surface via the iEDDA reaction. This proligand was then intended to be processed by an ectoenzyme expressed on the surface of the target cell, thereby forming the active, receptor-binding ligand. Such a two-step recognition process involving the activation by an ectoenzyme and the subsequent interaction with the receptor was expected to further enhance specificity for the target cell. The feasibility of this approach was investigated *in vitro* using angiotensin as a model ligand targeting the angiotensin II type 1 (AT1) receptor on mesangial cells. [22] Following an initial evaluation of the affinity of free angiotensin for the AT1R, tetrazine-functionalized NPs were post-modified with angiotensin I as a proligand via the iEDDA reaction. Subsequent enzymatic conversion of NP-bound angiotensin I to angiotensin II by angiotensin-converting enzyme (ACE) was assessed, followed by the avidity of the activated NPs towards AT1R. This strategy enabled the generation of NPs with switchable avidity towards a target cell receptor.

Chapter 5 then aimed to extend these findings by investigating whether switchable target cell recognition also translates into switchable cellular uptake. The concept established in Chapter 4 was adopted here, in which angiotensin I was first conjugated to the NP as a proligand via the iEDDA reaction and subsequently activated by the ectoenzyme ACE to form angiotensin II, the ligand responsible for mediating cellular internalization. NP internalization was assessed by flow cytometry, while confocal laser scanning microscopy (CLSM) was employed to evaluate the cellular localization

Chapter 2

of the NPs and to corroborate the flow cytometry results. By evaluating whether temporally controlled ligand presentation not only enables receptor binding but also governs the subsequent internalization of NPs, this chapter sought to further validate the potential of bioorthogonal chemistry for engineering dynamically controllable NPs suitable for advanced biomedical applications.

References

1. Mitchell MJ, Billingsley MM, Haley RM, Wechsler ME, Peppas NA, Langer R (2021) Engineering precision nanoparticles for drug delivery. *Nat Rev Drug Discov* 20(2), 101–124. 10.1038/s41573-020-0090-8.
2. Zhao Z, Ukidve A, Krishnan V, Mitragotri S (2019) Effect of physicochemical and surface properties on in vivo fate of drug nanocarriers. *Advanced Drug Delivery Reviews* 143, 3–21. 10.1016/j.addr.2019.01.002.
3. Blanco E, Shen H, Ferrari M (2015) Principles of nanoparticle design for overcoming biological barriers to drug delivery. *Nat Biotechnol* 33(9), 941–951. 10.1038/nbt.3330.
4. Jin Q, Deng Y, Chen X, Ji J (2019) Rational Design of Cancer Nanomedicine for Simultaneous Stealth Surface and Enhanced Cellular Uptake. *ACS nano* 13(2), 954–977. 10.1021/acsnano.8b07746.
5. Lu Q, Yu H, Zhao T, Zhu G, Li X (2023) Nanoparticles with transformable physicochemical properties for overcoming biological barriers. *Nanoscale* 15(32), 13202–13223. 10.1039/D3NR01332D.
6. Su Y, Jin G, Zhou H, Yang Z, Wang L, Mei Z, Jin Q, Lv S, Chen X (2023) Development of stimuli responsive polymeric nanomedicines modulating tumor microenvironment for improved cancer therapy. *Medical Review* 3(1), 4–30. 10.1515/mr-2022-0048.
7. He Y, Lei L, Cao J, Yang X, Cai S, Tong F, Huang D, Mei H, Luo K, Gao H, He B, Peppas NA (2021) A combinational chemo-immune therapy using an enzyme-sensitive nanoplatform for dual-drug delivery to specific sites by cascade targeting. *Science advances* 7(6). 10.1126/sciadv.aba0776.
8. Cao Z, Li D, Wang J, Yang X (2021) Reactive oxygen species-sensitive polymeric nanocarriers for synergistic cancer therapy. *Acta Biomaterialia* 130, 17–31. 10.1016/j.actbio.2021.05.023.
9. Tao Y, Chan HF, Shi B, Li M, Leong KW (2020) Light: A Magical Tool for Controlled Drug Delivery. *Adv. Funct. Mater.* 30(49), 2005029. 10.1002/adfm.202005029.
10. Sponchioni M, Capasso Palmiero U, Moscatelli D (2019) Thermo-responsive polymers: Applications of smart materials in drug delivery and tissue engineering. *Materials science & engineering. C, Materials for biological applications* 102, 589–605. 10.1016/j.msec.2019.04.069.
11. Tu L, Liao Z, Luo Z, Wu Y-L, Herrmann A, Huo S (2021) Ultrasound-controlled drug release and drug activation for cancer therapy. *Exploration* 1(3), 20210023. 10.1002/EXP.20210023.
12. Yoo J, Park C, Yi G, Lee D, Koo H (2019) Active Targeting Strategies Using Biological Ligands for Nanoparticle Drug Delivery Systems. *Cancers* 11(5), 640. 10.3390/cancers11050640.
13. Li X, Montague EC, Pollinzi A, Lofts A, Hoare T (2022) Design of Smart Size-, Surface-, and Shape-Switching Nanoparticles to Improve Therapeutic Efficacy. *Small* 18(6), e2104632. 10.1002/smll.202104632.

Chapter 2

14. Jin E, Zhang B, Sun X, Zhou Z, Ma X, Sun Q, Tang J, Shen Y, van Kirk E, Murdoch WJ, Radosz M (2013) Acid-active cell-penetrating peptides for in vivo tumor-targeted drug delivery. *Journal of the American Chemical Society* 135(2), 933–940. 10.1021/ja311180x.
15. Sethuraman VA, Bae YH (2007) TAT peptide-based micelle system for potential active targeting of anti-cancer agents to acidic solid tumors. *Journal of Controlled Release* 118(2), 216–224. 10.1016/j.jconrel.2006.12.008.
16. Li H, Miteva M, Kirkbride KC, Cheng MJ, Nelson CE, Simpson EM, Gupta MK, Duvall CL, Giorgio TD (2015) Dual MMP7-proximity-activated and folate receptor-targeted nanoparticles for siRNA delivery. *Biomacromolecules* 16(1), 192–201. 10.1021/bm501394m.
17. Ding Y, Liu J, Zhang Y, Li X, Ou H, Cheng T, Ma L, An Y, Liu J, Huang F, Liu Y, Shi L (2019) A novel strategy based on a ligand-switchable nanoparticle delivery system for deep tumor penetration. *Nanoscale Horiz.* 4(3), 658–666. 10.1039/C8NH00415C.
18. Scinto SL, Bilodeau DA, Hincapie R, Lee W, Nguyen SS, Xu M, Ende CW am, Finn MG, Lang K, Lin Q, Pezacki JP, Prescher JA, Robillard MS, Fox JM (2021) Bioorthogonal chemistry. *Nat Rev Methods Primers* 1(1), 1–23. 10.1038/s43586-021-00028-z.
19. Blackman ML, Royzen M, Fox JM (2008) Tetrazine ligation: fast bioconjugation based on inverse-electron-demand Diels-Alder reactivity. *Journal of the American Chemical Society* 130(41), 13518–13519. 10.1021/ja8053805.
20. Oliveira BL, Guo Z, Bernardes GJL (2017) Inverse electron demand Diels-Alder reactions in chemical biology. *Chem. Soc. Rev.* 46(16), 4895–4950. 10.1039/C7CS00184C.
21. Meimetis LG, Carlson JCT, Giedt RJ, Kohler RH, Weissleder R (2014) Ultrafluorogenic coumarin-tetrazine probes for real-time biological imaging. *Angewandte Chemie (International ed. in English)* 53(29), 7531–7534. 10.1002/anie.201403890.
22. Maslanka Figueroa S, Veser A, Abstiens K, Fleischmann D, Beck S, Goepferich A (2019) Influenza A virus mimetic nanoparticles trigger selective cell uptake. *Proceedings of the National Academy of Sciences of the United States of America* 116(20), 9831–9836. 10.1073/pnas.1902563116.

Goals of the Thesis

Chapter 2

Chapter 3

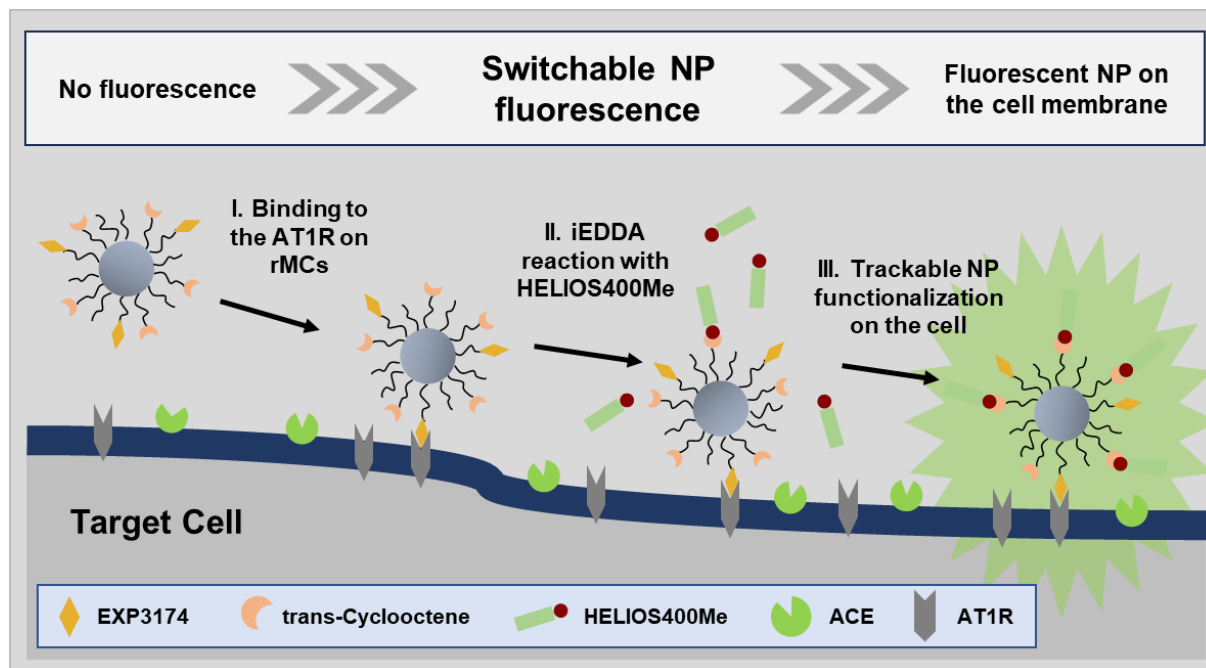
Using a Fluorogenic Tetrazine-Coumarin Probe to
Explore the Potential of the Inverse Electron-Demand
Diels–Alder Reaction for Nanoparticle
Functionalization in Biological Environments

Chapter 3

Abstract

Bioorthogonal reactions have revolutionized biomedical research by enabling selective chemical modifications in complex biological environments. The inverse electron-demand Diels-Alder (iEDDA) reaction, characterized by its rapid kinetics and bioorthogonality, is particularly promising for nanoparticle (NP) functionalization. In this study, we developed iEDDA-reactive polymer NPs with a poly(lactic-co-glycolic acid) (PLGA) core and a tunable surface composition of trans-cyclooctene (TCO)-functionalized and unmodified polylactide-polyethylene glycol (PLA-PEG) block copolymers. Using a fluorogenic tetrazine-coumarin HELIOS probe, we monitored the functionalization reaction in real time. Our kinetic studies revealed an exceptionally rapid iEDDA reaction on NP surfaces, likely driven by hydrophobic interactions. Furthermore, the iEDDA reaction was highly efficient in biological media, underscoring its potential for *in vivo* applications. Stability studies of the iEDDA reaction partners further demonstrated sufficient robustness under biological conditions, highlighting the suitability of this chemistry for the development of switchable NPs for advanced drug delivery and imaging applications.

Graphical Abstract



Schematic illustrating the investigation of the iEDDA reaction in a biological environment with a tetrazine-coumarin fluorophore. The NPs initially bind to the AT1 receptor on the target cell mediated by EXP3174. Additionally added tetrazine coumarin fluorophore HELIOS400Me reacts in the iEDDA reaction with the TCO functionalities on the NP and results in a fluorescent NP on the cell membrane.

Chapter 3

1. Introduction

Selective chemical reactions in a biological environment are challenging to achieve, but highly interesting for targeted intervention in biological processes. [1] Due to their unique ability to proceed in living systems alongside a large number of other functional groups, bioorthogonal reactions have attracted significant attention since their initial conceptualization by Bertozzi in 2003. [2] Among the selection of bioorthogonal reactions available today, the inverse electron-demand Diels-Alder (iEDDA) reaction stands out due to its exceptional kinetics. [3] The reaction takes place between an electron-deficient tetrazine derivative as the diene and a strained, electron-rich trans-cyclooctene (TCO) as the dienophile. [4] The rapid reaction rate, even at low concentrations, makes the iEDDA reaction particularly suitable for manipulating biological processes on physiologically relevant timescales. [5] The iEDDA reaction has therefore been successfully applied in numerous biological and biomedical contexts. [6–9] Combining iEDDA chemistry with nanoparticles (NPs) opens up exciting new possibilities. By making the most of the unique features of both components - namely, the multivalency of NPs, their capability to transport therapeutic agents and function as imaging probes, and the rapid and robust nature of the iEDDA reaction even in complex environments - it may be possible to design more sensitive bioimaging and detection tools as well as more efficient therapeutic systems. [10] So far, the iEDDA reaction has primarily been used for NP functionalization in the manufacturing process. For instance, antibodies have been conjugated to NPs via the iEDDA reaction [11], or NPs have been modified with radioligands prior to administration. [12] *In vivo*, iEDDA-based NP functionalization has been employed for pre-targeted imaging strategies. In this approach, NPs accumulate in tumor tissue via the enhanced permeability and retention (EPR) effect, followed by administration of a radiotracer for positron emission tomography (PET) imaging. [13] This strategy enables the use of short-lived isotopes, reducing radiation exposure to healthy tissues. [14] Beyond diagnostic applications, the potential of *in vivo* iEDDA-mediated NP functionalization for therapeutic purposes remains to be further explored. Feng, Wu et al. took an initial step in this direction by introducing a NP that can be activated via the iEDDA reaction for photodynamic therapy of cancer. [15] However, there remains significant potential for the development of additional concepts.

The aim of this study was to evaluate whether the iEDDA reaction is suitable to selectively functionalize polymer NPs in a biological environment paving the way towards *in vivo* switchable NPs for advanced drug delivery. To facilitate real-time tracking of the iEDDA reaction on NPs, we employed a fluorogenic tetrazine-based probe. Tetrazines absorb light around 520 nm and efficiently quench various fluorophores. [16] Undergoing the iEDDA reaction, the tetrazine moiety is converted into a dihydropyridazine, leading to the loss of fluorescence quenching and resulting in a turn-on fluorescence signal dependent on the fluorophore and its spatial arrangement relative to the tetrazine. [17] In this work, we prepared iEDDA-reactive NPs with a modular design. The core of the NPs was composed of

poly(lactic-co-glycolic acid) (PLGA), while surface functionalization was achieved using tunable ratios of TCO-functionalized and unmodified block copolymers of polylactide-polyethylene glycol (PLA-PEG). As a fluorogenic probe, we synthesized a tetrazine-coumarin HELIOS probe, reported to exhibit an extraordinary turn-on fluorescence enhancement of up to 4000-fold. [18] The fluorescence behavior of this probe was analyzed, and an equation was derived to fit the fluorescence intensity over time. Kinetic studies of the iEDDA reaction on NPs revealed an exceptionally fast reaction rate, likely attributed to the hydrophobic nature of the tetrazine-coumarin probe, which promotes accumulation on the NP. Additionally, the functionalization of NPs in biological environments was assessed, as well as the stability of the reactants of the iEDDA reaction in biological media. Finally, the fluorogenic probe was used to observe NP functionalization via iEDDA reaction directly on the cell membrane of the target cell.

2. Materials and Methods

2.1 Materials

The PEG derivatives HOOC-PEG2k-OH and tBoc-NH-PEG2k-OH were purchased from JenKem Technology USA Inc. (Allen, TX, USA). TCO-NHS ester was obtained from Jena Bioscience GmbH (Jena, Germany). The losartan metabolite EXP3174 was kindly provided by Kathrin Schorr. [19] Cellulose dialysis membranes were sourced from Spectrum Laboratories Inc. (Rancho Dominguez, CA, USA). Millipore ultrapure water was generated using a Milli-Q water purification system (Millipore, Schwalbach, Germany). Coumarin 102, as the core structure, and 3-cyanophenylboronic acid, required for the synthesis of the HELIOS fluorophore, were obtained from TCI Deutschland GmbH (Eschborn, Germany). TCO-PEG₄-NHS (axial isomer) was acquired from Sirius Fine Chemicals SiChem GmbH (Bremen, Germany). Fetal bovine serum (FBS) of South American origin (0.2 µm sterile filtered, Lot No.: P201004) was supplied by PAN Biotech GmbH (Aidenbach, Germany). TAMRA-labeled PLGA was generously provided by Melanie Bresinsky. [20] The ratiometric Ca²⁺ indicator Fura-2 AM and the nuclear stain DRAQ5™ (fluorescent probe solution 5 mM), used for CLSM experiments, were ordered from Thermo Fisher Scientific (Waltham, MA, USA). NP suspensions were concentrated using centrifugal filtration devices from Pall Life Sciences (Portsmouth, UK). Rat mesangial cells (rMCs) were kindly provided by Professor Dr. Armin Kurtz from the Institute of Physiology at the University of Regensburg (Regensburg, Germany). All other chemicals used in this study were of analytical grade and obtained from Sigma Aldrich (Taufkirchen, Germany).

Chapter 3

2.2 Block copolymer synthesis and ligand coupling

The block copolymers were synthesized following the protocol previously reported by our research group [21], based on the method described by Qian, Wohl et al. [22] In brief, cyclic lactide was purified via recrystallization in ethyl acetate and subsequently dried under vacuum at 40°C overnight. The PEG derivatives, either tBoc-NH-PEG2k-OH or HOOC-PEG2k-OH, were also dried under vacuum at 40°C overnight. The ring-opening polymerization of cyclic lactide was initiated using the PEG derivative as a macroinitiator in anhydrous DCM, with 1,8-diazabicyclo[5.4.0]undec-7-ene (DBU) as the catalyst. After 1 h of stirring at room temperature, the reaction was quenched, and the polymer was precipitated into at least tenfold excess of ice-cold diethyl ether. Following centrifugation, the supernatant was discarded, and the polymer pellet was dried and redissolved in acetonitrile. The precipitation–centrifugation–dissolution cycle was repeated to ensure thorough purification. For the amino-terminated block copolymer, the tBoc protecting group was subsequently removed. The protected polymer was dissolved in DCM and incubated with trifluoroacetic acid (TFA) for 30 min. Purification was performed through additional precipitation–centrifugation–dissolution cycles. Finally, the block copolymers were dried under vacuum and analyzed by ¹H NMR (approximately 10 mg of block copolymer dissolved in 0.7 mL CDCl₃), using a Bruker Avance III HD 400 spectrometer (Bruker BioSpin GmbH, Rheinstetten, Germany). The number-average molar mass of the polymers was determined based on the known molecular weight of the PEG derivative by integrating the respective signals in the ¹H NMR spectrum and considering the corresponding ratios.

While the carboxy-terminated block copolymer PLA10k-PEG2k-COOH was used as a filler polymer in NP preparation, the amine-terminated block copolymer PLA10k-PEG2k-NH₂ was used for the conjugation of carboxyl-functionalized ligands. TCO-NHS ester was added to the amine-terminated block copolymer dissolved in DMF with triethylamine (TEA). The reaction mixture was stirred at room temperature for 4 h. For the conjugation of EXP3174 to the amine-terminated block copolymer, HBTU was used as the coupling reagent. This reaction was also conducted in DMF with TEA and stirred at room temperature for 8 h. Purification was performed using multiple precipitation–centrifugation–dissolution cycles, as previously described for the synthesis of the block copolymers. Finally, the polymer solutions were added dropwise into Millipore water, forming polymer micelles, which were stirred for 2 h and subsequently dialyzed against 4 L of Millipore water using a regenerated cellulose membrane (3.5 kDa MWCO). After freeze-drying using a Christ freeze dryer Alpha 2-4 LSCplus (Martin Christ Gefriertrocknungsanlagen GmbH, Osterode am Harz, Germany), the ligand-conjugated block copolymers were obtained, and analyzed by ¹H NMR spectroscopy.

2.3 NP preparation and characterization

The polymer NPs were produced using the nanoprecipitation method. [23] Polymers used in each formulation were first dissolved in acetonitrile, maintaining a 70:30 mass ratio between PLA-PEG block copolymers forming the NP shell and the particle-core-forming PLGA (ester-terminated, 13.4 kDa). The proportion of unfunctionalized PLA10k-PEG2k-COOH block copolymer and TCO-functionalized PLA10k-PEG2k-TCO block copolymer was varied to achieve different TCO functionalization degrees on the NPs. The percentage functionalization (ranging from 0% to 80% TCO) refers to the mass fraction of PLA-PEG block copolymer with TCO attached compared to the total shell polymer used for particle preparation. A 10 mg/mL polymer solution was added dropwise to a tenfold volume of Millipore water under rapid stirring to ensure efficient mixing of acetonitrile and water, leading to the precipitation of polymers as nanoparticles. [24] To remove the organic solvent, the suspension was stirred under a fume hood at room temperature for 3 h.

The particle size and polydispersity index (PDI) were measured immediately after preparation, without further dilution, using a Malvern Zetasizer Nano ZS (Malvern Instruments GmbH, Kassel, Germany) equipped with a 633 nm He-Ne laser and operating at a detection angle of 173°. [25] Measurements were conducted at 25°C in semi-micro disposable cuvettes (Brand, Wertheim, Germany). The same instrument was used to determine the zeta potential of the NPs in Millipore water using folded capillary zeta potential cells (Malvern Instruments GmbH, Kassel, Germany). Data collection and analysis were performed using Malvern Zetasizer software version 7.11 (Malvern Instruments, Worcestershire, United Kingdom). Additionally, NP size distribution and concentration were assessed via nanoparticle tracking analysis (NTA) using a NanoSight NS300 (Malvern Panalytical GmbH, Kassel, Germany) at 25°C. [26] Samples were diluted in Millipore water (typically by a factor of 2000 or 4000) to achieve a detection range of 20–80 particles per frame. Measurements were performed at a camera level of 16 and a screen gain of 4. The analysis was conducted with a threshold setting of 3 in the NTA 3.4 software (Malvern Panalytical GmbH, Kassel, Germany). The particle concentration provided by the instrument was converted to molar concentration by division by the Avogadro constant.

For stability studies, NP samples were stored at RT and reanalyzed using the Zetasizer at designated time points. To examine NPs after the iEDDA reaction, 10 µL of NP suspension was diluted with 140 µL of water and mixed with 50 µL of a 40 µM HELIOS fluorophore solution in water. After allowing sufficient time for complete iEDDA reaction, the particle size was measured using the Zetasizer.

Chapter 3

2.4 Quantification of ligands per NP

The number of TCO ligands per NP was determined by dissolving the NPs in DMSO and reacting them with an excess of the HELIOS fluorophore. For this purpose, 10 μL of the NP sample was diluted with 140 μL of DMSO in a well of a 96-well plate, followed by the addition of 50 μL of a 40 μM HELIOS solution in DMSO. For calibration, 10 μL of blank NPs without TCO functionalization were used per well, and 140 μL of serially diluted TCO-NHS ester stock solution in DMSO was added. Similar to the sample preparation, 50 μL of a 40 μM HELIOS solution in DMSO was added to initiate the iEDDA reaction. This ensured at least a 10-fold molar excess of HELIOS relative to TCO. The fluorescence intensity over time was measured using a Synergy Neo2 plate reader (Excitation: 400/10 nm, Emission: 480/10 nm). For further analysis, the fluorescence intensity after 2 hours of reaction was used. The fluorescence intensity of a blank sample without TCO was subtracted as background, and a calibration curve was generated using the fluorescence intensities of the known TCO concentrations. The fluorescence of the NP samples was then converted into TCO concentrations using the calibration curve. Finally, the TCO concentration was divided by the NP concentration determined via NTA to calculate the number of TCO ligands per NP. Additionally, the NP surface area was calculated based on the NP size obtained from NTA measurements. The TCO density was determined by dividing the number of TCO ligands per NP by the NP surface area.

2.5 Investigation of iEDDA reaction kinetics

To study the kinetics of the iEDDA reaction under various conditions, 4 μL of the tetrazine coumarin fluorophore (HELIOS400Me) solution in DMSO were initially placed in a white 96-well plate. For the iEDDA reaction with free PEG₄-TCO, a final HELIOS concentration of 1 μM in a total volume of 200 μL was selected; for the iEDDA reaction on the NP, a final HELIOS concentration of 0.1 μM was chosen. Accordingly, for reactions in free solution, 4 μL of the 50 μM HELIOS solution were added, and for NP-based reactions, a 5 μM HELIOS solution (10-fold dilution) was used. Free PEG₄-TCO or NP-TCO and water were added directly before measurement via the plate reader's pump system, resulting in a TCO excess of 2- to 32-fold relative to HELIOS. The fluorescence intensity (excitation at 380 nm, emission at 485 nm) was measured immediately on a FLUOstar Omega microplate reader at 0.3 s intervals (for longer measurement times, intervals were extended). For reactions conducted in media other than water, such as DMSO, Leibovitz's L-15 medium with 0.1% BSA, RPMI 1640 cell culture medium with 10% FBS supplement, and pure FBS, 150 μL of the respective medium were added at the beginning to the HELIOS fluorophore. The change in fluorescence intensity over reaction time was fitted using the following equation (see eq. 1).

$$F(t) = F_{max} + (F_0 - F_{max}) \cdot e^{-k \cdot t} \quad (1)$$

Where F_0 is the initial fluorescence intensity, F_{max} the plateau fluorescence intensity, and $F(t)$ the fluorescence intensity at time t . The observed pseudo-first-order rate constants k from three independent experiments were averaged, the standard deviation calculated and plotted against the respective TCO concentration. The second-order rate constant was determined from the slope of the linear fit. [27]

2.6 HELIOS emission spectra and kinetics of fluorophore accumulation on the NP

TCO-OH and HELIOS were reacted in a 1:1 ratio at a concentration of 2 mM. From this solution, in which the fluorophore was no longer quenched, 1 μ L was added to a white 96-well plate, followed by 199 μ L of the respective solvent (water, NP solution, or liquid PEG400). Diluting the 2 mM solution by a factor of 200 in the well yielded a final concentration of 10 μ M (0.5% DMSO content). The emission spectrum from 425 to 600 nm was recorded using the Synergy Neo2 plate reader, with excitation at 400 nm. Spectra were smoothed using the Savitzky-Golay method and subsequently normalized. To study the kinetics of fluorophore accumulation on the NP, HELIOS and TCO-OH were first reacted in a 1:1 ratio at a concentration of 3.3 mM. After a brief incubation period to allow for a complete iEDDA reaction, the solution was diluted with DMSO to a final concentration of 5 μ M. As with the study of the iEDDA reaction kinetics, 4 μ L of the fluorophore solution were placed in a white 96-well plate; however, in this case, the unquenched fluorophore was used. Unfunctionalized NP-COOH and water were added via the plate reader's pump system, resulting in a concentration of blank particles equivalent to the TCO excess concentrations and corresponding NP-TCO concentrations in the study of the iEDDA reaction kinetics. Fluorescence intensity, with excitation at 380 nm and emissions at 485 nm and 520 nm, was measured every second on the FLUOstar Omega microplate reader. The fluorescence ratio at 485/520 nm served as an indicator of the fluorophore's localization, reflecting a shift to a less polar environment. Changes in the fluorescence ratio over time were fitted using Equation 1, and the observed rate constant was plotted against the NP concentration.

2.7 Stability assessment of tetrazine and TCO in various media

To examine the stability of tetrazine on the coumarin fluorophore, the fluorogenic tetrazine-coumarin fluorophore (1.5 μ M total concentration) was incubated at 37°C in the provided media (DMSO content

Chapter 3

adjusted for solubility to 25%). Medium + FBS denotes for cell culture medium RPMI 1640 with 10% FBS supplement, and Leibovitz + BSA for Leibovitz's L-15 medium with 0.1% BSA content. The increase in fluorescence intensity due to tetrazine decomposition was detected at different time points using a Synergy Neo2 plate reader (BioTek, Winooski, Vermont, USA). Excitation was performed at 400/10 nm, and emission was measured at 480/10 nm (Gain 100, orbital shaking for 15 s prior to measurement). For comparison, media without tetrazine-coumarin fluorophore, but also with a 25% DMSO content, were measured, and the values were subtracted as blanks. To determine the maximum possible fluorescence of 1.5 μM tetrazine-coumarin fluorophore, a 100-fold excess of TCO was added so that the tetrazine completely reacted off and no longer quenched the fluorophore. The fluorescence intensity at the respective time point was divided by the maximum value, providing the proportion of intact tetrazine. The measured values were fitted with an equation for exponential decay (see eq. 2) where $N(t)$ is the quantity at time t and k is a rate constant.

$$N(t) = 100 \cdot e^{-k \cdot t} \quad (2)$$

To investigate the stability of the trans-cyclooctene, 60% TCO functionalized NPs were first prepared according to the general protocol. After preparation, these were sterile-filtered through a 200 nm syringe filter to prevent bacterial growth during long incubation times. 8 μL of the 4 mg/mL NP solution were added together with 152 μL medium per well to a white 96 well plate and incubated for different periods of time at 37°C and 50 rpm. For the measurement, the plate sealer film was removed, 40 μL of the 50 μM tetrazine coumarin fluorophore solution were added per well and the fluorescence intensity (excitation 380 nm, emission 485 nm) was measured on a FLUOstar Omega microplate reader (TCO total concentration approx. 1 μM ; tetrazine coumarin fluorophore concentration 10 μM). The fluorescence intensity directly after addition of the fluorophore served as an indicator of the intact TCO. Corresponding blank values for the fluorophore in the investigated medium without NP-TCO were subtracted. The intact trans-cyclooctene after various incubation times was determined by dividing the fluorescence intensity at the respective time point by the maximum fluorescence. The measured values were also fitted with the equation given above (see eq. 2) to illustrate the exponential decrease and to determine the corresponding half-lives.

2.8 Preparation of EXP-functionalized NPs for Ca^{2+} mobilization assay and CLSM experiments

EXP-functionalized NPs for the Ca^{2+} mobilization assay and confocal laser scanning microscopy (CLSM) experiments were prepared following the general procedure (see section 2.3), with slight modifications. Instead of a 10 mg/mL polymer concentration, PLA-PEG block copolymers and PLGA

were dissolved at a 70:30 mass ratio to a final concentration of 20 mg/mL in acetonitrile. Upon dropwise addition into a tenfold volume of Millipore water, this resulted in a final NP concentration of 2 mg/mL. For CLSM experiments, PLGA was replaced with TAMRA-labeled PLGA. The block copolymer composition was adjusted such that 25% of the block copolymers were EXP-functionalized (PLA10k-PEG2k-EXP) and 40% were TCO-functionalized (PLA10k-PEG2k-TCO). Additionally, NPs with only 25% EXP-functionalized (PLA10k-PEG2k-EXP) block copolymer were prepared for comparison, with the remaining fraction consisting of unfunctionalized carboxy-terminated PLA10k-PEG2k-COOH in each case. For the Ca^{2+} mobilization assay, particles were concentrated via centrifugation using a 100-kDa molecular weight cutoff centrifugal device, while for CLSM experiments, NPs were used without further concentration. Finally, NP size distribution and concentration were determined by NTA.

2.9 Ratiometric Fura-2 AM-based Ca^{2+} mobilization assay

To investigate the avidity of the NPs for the AT1 receptor, a Fura-2 AM Ca^{2+} assay was performed as previously described by our group. [28] For the NPs decorated with the antagonist EXP3174, an inverse approach was adopted, with minor modifications made to the procedure. Briefly, AT1R-positive rMCs were cultured in a T75 flask until they reached at least 90% confluence. On the day of the experiment, the cells were harvested following standard procedures and subsequently resuspended in Fura-2 AM loading medium. The loading medium was prepared by dissolving 50 μg of Fura-2 AM in 50 μL DMSO. This stock solution was combined with 20 μL of a 20% Pluronic F127 solution and diluted to a final volume of 6 mL with Leibovitz's L-15 medium containing 2.5 mM probenecid. The cells were incubated with the loading medium for 1 hour at room temperature on a laboratory shaker set to 50 rpm. Subsequently, the cell suspension was centrifuged at $200 \times g$ for 5 minutes using a 5702 R centrifuge (Eppendorf, Germany). The supernatant was discarded, and the cell pellet was resuspended in measurement medium, which consisted of Leibovitz's L-15 medium with 2.5 mM probenecid. During resuspension, care was taken to ensure that the cells were gently dissociated and not exposed to excessive shear stress. The concentration was adjusted to 1 million rMCs per mL based on counting using a Neubauer-improved counting chamber (Marienfeld, Germany).

Dilution series were prepared for the NPs under investigation (NP-EXP and NP-EXP/TCO). A volume of 10 μL of each NP sample was added in triplicate to a white 96-well plate. Subsequently, 90 μL of the Fura-2 AM-loaded cell suspension was added and incubated with the NPs for 1 hour. Following incubation, 100 μL of a 300 nM Ang-II solution was added via the plate reader's pump system, and measurements on the FLUOstar Omega plate reader were initiated immediately upon stimulation with Ang-II. Fluorescence intensity was measured for 30 seconds per well, alternating excitation wavelengths of 340 nm and 380 nm, with an emission wavelength of 510 nm. The Grynkiewicz equation was applied

Chapter 3

to determine intracellular Ca^{2+} concentrations from the maximum recorded ratio between the different excitation wavelengths. [29] For calibration, the overall maximum ratio was obtained by lysing Fura-2 AM-loaded cells in 10 μL of 1% Triton X-100 in PBS. The minimum ratio was measured using 10 μL of 1% Triton X-100 in PBS supplemented with 45 mM EGTA in 0.5 M NaOH to chelate all available Ca^{2+} . Fluorescence values for 10% PBS were subtracted as a blank from all calculated intracellular calcium concentrations. The resulting values were normalized to the highest concentration and fitted using a four-parameter nonlinear regression model (see eq. 3) to obtain binding curves and determine IC_{50} values.

$$y = A1 + \frac{A2 - A1}{1 + 10^{(\text{LOG}x_0 - x) p}} \quad (3)$$

Here $A1$ stands for the bottom asymptote, $A2$ for the top asymptote, x_0 for the IC_{50} value and p represents the hill slope describing the steepness of the curves.

2.10 Confocal laser scanning microscopy analysis

To evaluate the functionalization of NPs directly on target cells, confocal laser scanning microscopy (CLSM) was employed. A total of 40,000 cells per well were seeded into an 8-well Ibidi slide (Ibidi, Planegg, Germany) and cultured at 37°C with a 5% CO_2 atmosphere for 24 h. The cells were washed once with 200 μL DPBS and subsequently incubated for 30 min with 200 μL of 300 pM TAMRA-labeled NP samples in Leibovitz's L-15 medium (LM). Following this, 50 μL of HELIOS solution was added, resulting in a final HELIOS concentration of 1.5 μM (corresponding to an approximate TCO/HELIOS ratio of 2:1). The cells were incubated for an additional 10 min and then washed twice with 200 μL DPBS. Subsequently, the cells were fixed with 200 μL of 4% PFA in PBS for 10 min at room temperature and washed again twice with 200 μL DPBS. Nuclei were stained with DRAQ5 by diluting a 5 mM DRAQ5 stock solution in DMSO 1:2000 in DPBS. A volume of 200 μL of the diluted solution was added to each well, incubated for 15 min at room temperature, and washed twice with 200 μL DPBS. The cells were stored covered with DPBS at 4°C until microscopy. CLSM images were acquired using a Zeiss LSM 710 (Carl Zeiss, Microscopy GmbH, Jena, Germany) and visualized with ZEN 3.10 (ZEN lite) software.

To estimate the number of NPs per cell, pixels exceeding a defined intensity threshold were counted using ImageJ. [30] The fluorescence channel corresponding to the NPs was selected, and a threshold was applied to highlight pixels above the defined intensity (threshold set to 20) excluding weak background noise. Cells were outlined as regions of interest (ROIs) using the polygon tool, and the number of pixels above the threshold within each ROI was counted. Colocalization between the NP and

Switchable Fluorescence

HELIOS channels was evaluated in ImageJ using the JaCoP plugin, with Pearson's correlation coefficient employed as a common measure of colocalization. [31] Further, the mean HELIOS fluorescence per cell was quantified by manually outlining cells as ROIs and measuring the mean fluorescence intensity. Background intensity was determined from an ROI in a cell-free area and subtracted to obtain corrected values.

2.11 Data analysis

Fits of experimental data were performed in Origin (Version 2020, OriginLab Corporation, Northampton, MA, USA).

3. Results and Discussion

3.1 Development and characterization of iEDDA-reactive TCO-functionalized NPs

We developed iEDDA-reactive NPs based on polymer particles consisting of PLA-PEG block copolymers and PLGA previously established in our research group. [24] The amphiphilic block copolymer is oriented such that the PEG segment faces outward towards the aqueous environment, while the more hydrophobic PLA segment, together with PLGA, forms the particle core. A key advantage of this modular NP design is the ability to precisely control the degree of ligand functionalization by simply adjusting the ratio of functionalized to non-functionalized block copolymer during particle preparation. [32] To generate iEDDA-reactive NPs, the PLA-PEG block copolymer was functionalized with trans-cyclooctene (TCO), a partner in the iEDDA reaction. The ratio of TCO-functionalized block copolymer (PLA10k-PEG2k-TCO) to non-functionalized block copolymer (PLA10k-PEG2k-COOH) was systematically varied, and the resulting impact on NP properties was evaluated (see **Figure 1 A**). The polymers were dissolved in acetonitrile, and NPs were subsequently prepared via nanoprecipitation in water. [33] Blank particles, composed solely of non-functionalized carboxy-terminated block copolymers with PLGA in the particle core, exhibited a size of approximately 70 nm. With increasing TCO functionalization, a slight increase in particle size was observed, reaching approximately 80 nm at 80% TCO functionalization (see **Figure 1 B**). The polydispersity index (PDI) ranged between 0.1 and 0.15 for all NPs, indicating a narrow size distribution. As TCO functionalization increased, the zeta potential of the NPs became less negative, shifting from approximately -40 mV for blank NPs to around -34 mV at 80% TCO functionalization (see **Figure 1 C**). This effect can be explained by the replacement of negatively charged carboxy-terminated block copolymers with TCO-functionalized block copolymers, which do not contribute additional charge. However, the zeta potential remained sufficiently negative to ensure good colloidal stability. During storage at room temperature, no significant changes in the hydrodynamic diameter of the NPs were observed (see **Figure 1 D**). Only at low TCO functionalization levels a minimal increase in particle size was detected after eight days. Importantly, no NP aggregation was observed over the observation period, confirming their stability.

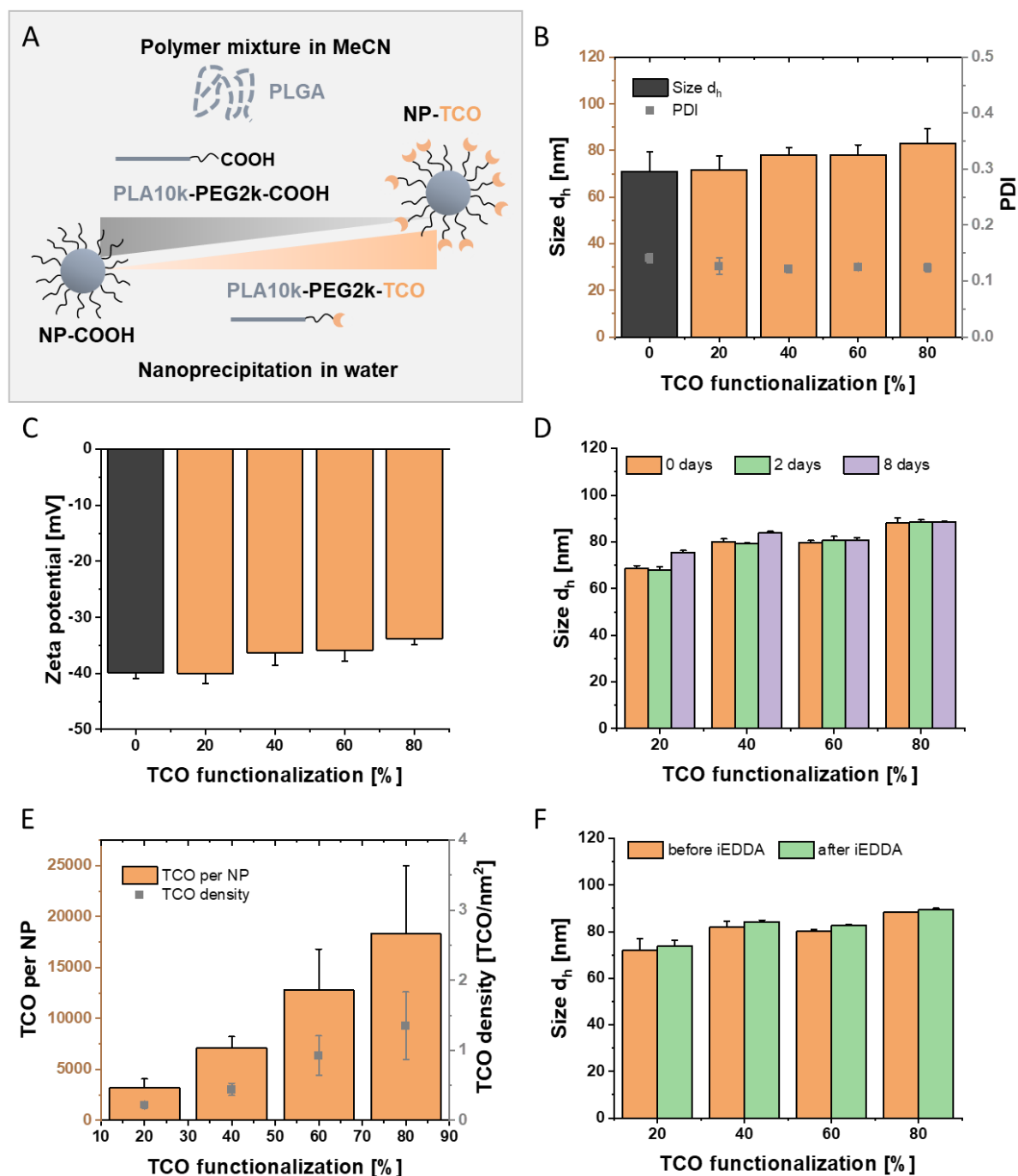


Figure 1. Preparation and characterization of NPs with increasing TCO functionalization. (A) Scheme for the production of NPs with varying TCO functionalization. (B) Size and PDI of the NPs determined via DLS on the Zetasizer. (C) Zeta potential of the NPs in Millipore water. (D) Change in NP size during storage at room temperature. (E) TCO ligands per NP and TCO density on the NP surface. (F) NP size before and after the iEDDA reaction with HELIOS400Me. Results in (B), (C) and (E) are presented as mean \pm SD of N=4 experiments, whereas the results in (D) and (F) are presented as mean \pm SD from one experiment (n=3).

Further quantification of TCO ligands on the NPs revealed a linear increase in the number of TCO units per NP with increasing incorporation of TCO-functionalized block copolymer (see **SI Figure 4**). Given the only slight increase in NP size, this also resulted in a higher TCO density on the NP surface with increasing TCO functionalization. Specifically, while NPs with 20% TCO functionalization exhibited a

Chapter 3

surface density of 0.2 TCO per nm², NPs with 80% TCO functionalization reached a density of approximately 1.4 TCO per nm² (see **Figure 1 E**). It can be noted that by using this approach and varying the ratio of unfunctionalized to TCO functionalized block copolymer, NPs with tailored number of ligands per NP can be prepared. Finally, NP size was assessed after the iEDDA reaction with the tetrazine-coumarin fluorophore HELIOS400Me. In all cases, only a minimal increase in particle size was observed. Importantly, the iEDDA reaction did not adversely affect NP properties, and no aggregation was detected (see **Figure 1 F**).

In summary, this approach enables the preparation of iEDDA-reactive TCO-functionalized NPs with tunable properties. Even at high TCO functionalization levels, the resulting NPs remained well-defined and suitable for further applications. This strategy allowed the production of NPs with precisely tailored characteristics for subsequent experiments.

3.2 Understanding the fluorescence behavior of the tetrazine coumarin probe

After successful synthesis of the tetrazine coumarin fluorophore (HELIOS400Me) (see SI section I), it was initially tested with free PEG₄-TCO in water. Contrary to the exponential fluorescence increase to saturation reported by Meimetis, Carlson et al. [18], we observed a rapid rise in fluorescence intensity followed by a decline, particularly evident at high TCO excess (see **Figure 2 A**). It was expected that the tetrazine group on the tetrazine-coumarin fluorophore would initially quench the coumarin fluorescence. As the reaction proceeded, tetrazine would be consumed in the iEDDA reaction, leading to a reduction in quenching and an increase in fluorescence intensity until saturation was reached, corresponding to complete tetrazine consumption. However, the observed decrease in fluorescence intensity after reaching a peak suggests that an additional reaction occurs, leading to a structure that again quenches the fluorophore. Other research groups also reported similar observations with fluorogenic systems during iEDDA reaction with TCO derivatives, where fluorescence intensity initially peaks, followed by a continuous decay. [34] Detailed investigations by Hild, Werther et al. revealed that the iEDDA reaction rapidly forms a fluorescent 4,5-dihydropyridazine species, which then tautomerizes into a weakly fluorescent 1,4-dihydropyridazine. [35] It appears that 1,4-dihydropyridazines can significantly quench diverse fluorophores, explaining the drop in fluorescence intensity. [36] On a much slower timescale than studied here, fluorescence intensity may recover due to oxidation of the 1,4-dihydropyridazine species to pyridazine (see **Figure 2 B**). These underlying reactions likely dictate the observed fluorescence behavior in our experiment as well. Assuming two consecutive first-order reactions, an equation to describe the fluorescence intensity curves was derived (see SI section III). The established equation fits the observed fluorescence curves very well, with a coefficient of determination of consistently above 0.96, indicating a high degree of correlation between the model and experimental

Switchable Fluorescence

observations (see SI section IV). The pseudo-first-order rate constant of the first step was then plotted against the TCO concentration (see **Figure 2 C**). From the slope of the linear fit, the second-order rate constant for the iEDDA reaction was determined. [27] For free PEG₄-TCO in water, the second-order rate constant was $7029 \pm 191 \text{ M}^{-1} \text{ s}^{-1}$. This is remarkably fast for a reaction between TCO and methyl substituted tetrazine, which is generally known to react more slowly, but provides good stability in a biological environment. [37] With a sound understanding of the observed fluorescence behavior, we next sought to investigate whether the iEDDA reaction proceeds as rapidly on the polymer NPs.

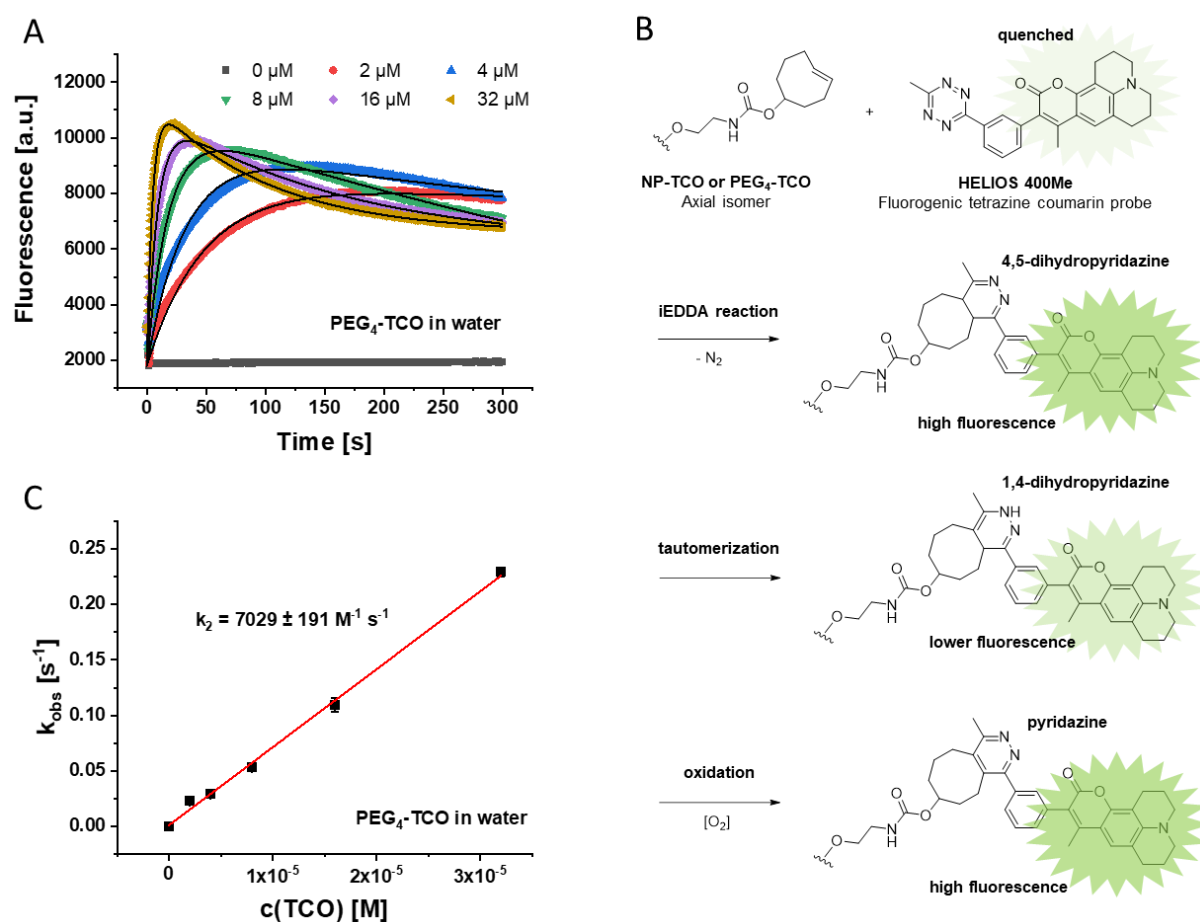


Figure 2. Evaluation of the iEDDA reaction between HELIOS400Me and free PEG₄-TCO in water. (A) Fluorescence intensity with progressing reaction time at different TCO excesses (2 to 32-fold excess). (B) Schematic illustrating the underlying reactions. (C) Plot of the pseudo-first order constants vs. the TCO concentration to determine the second order rate constant. Results in (C) are presented as mean \pm SD ($n = 3$).

3.3 Acceleration of the iEDDA reaction on polymer NPs

Testing the iEDDA reaction on NPs (NP-TCO) with $1 \mu\text{M}$ HELIOS, as performed with free TCO (PEG₄-TCO), it became immediately apparent that the iEDDA reaction on NPs was significantly faster. The fluorescence intensity peaked within seconds before gradually declining (see **Figure 3 A**). The rapid

Chapter 3

kinetics of the iEDDA reaction on the NP made it challenging to accurately track the fluorescence using the plate reader setup (see **SI Figure 6 A**). To slow down the reaction, the HELIOS concentration was reduced from 1 μM to 0.1 μM . Despite this adjustment, the reaction remained remarkably fast, requiring the analysis to focus only on the first 12 seconds (see **SI Figure 6 B**). At lower TCO excesses, reasonably resolved curves could be obtained, but at higher TCO concentrations, the reaction speed exceeded the detection capabilities of the setup. As a result, the observed pseudo-first-order rate constants no longer showed a proportional increase with increasing TCO concentration (see **SI Figure 6 D**). Therefore, only data up to an 8-fold excess of TCO were included in analysis (see **Figure 3 B**). Further diluting the reactants to achieve even slower reactions was not feasible. At 10 nM HELIOS, the fluorescence signal was too weak, even with increased gain on the plate reader (see **SI Figure 6 C**).

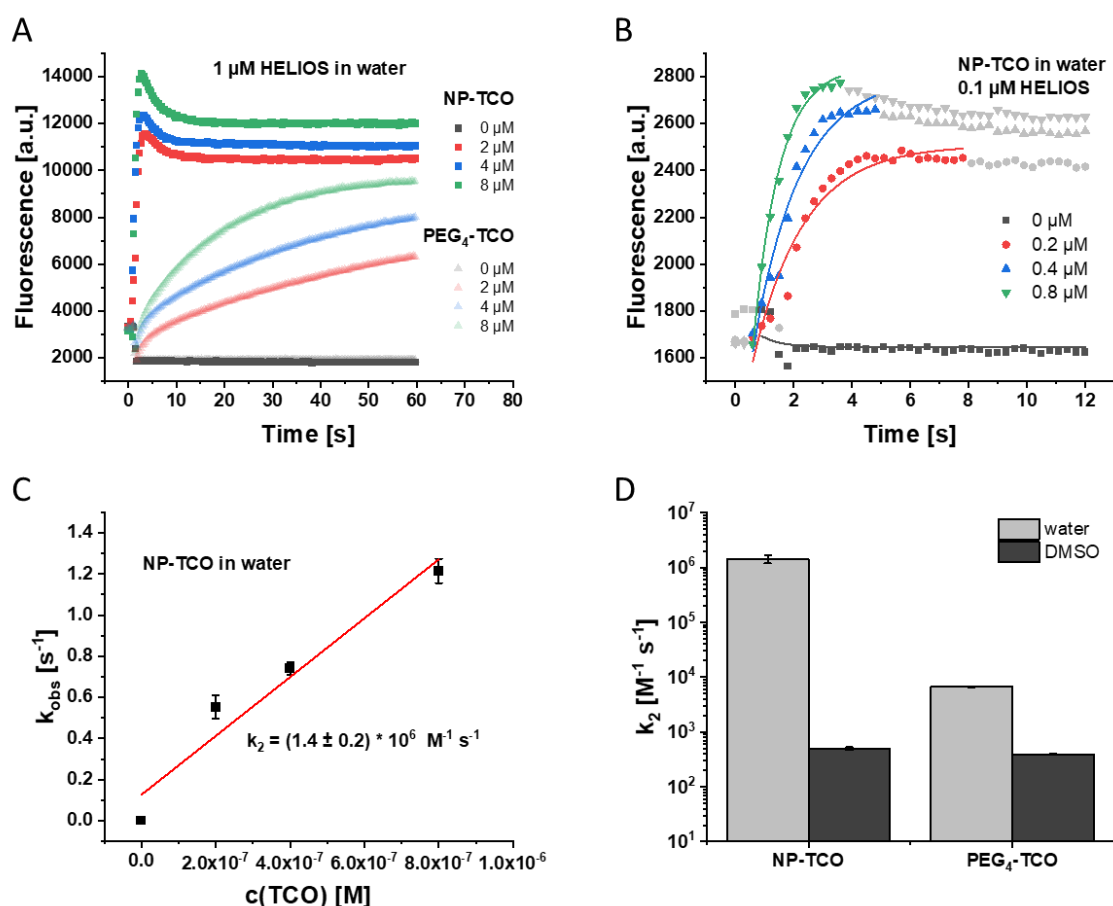


Figure 3. Kinetics of the iEDDA reaction of HELIOS400Me with NP-TCO. (A) Comparison between TCO on the NP (NP-TCO) and TCO free in solution (PEG₄-TCO) in the iEDDA reaction with 1 μM HELIOS in water. (B) Fluorescence intensity vs. reaction time for the iEDDA reaction between 0.1 μM HELIOS and TCO on the NP (various TCO excesses) in water. (C) Pseudo first-order rate constants determined from the fit, plotted against TCO concentration. (D) Comparison of the second-order rate constants on the NP and free in solution, in both water and DMSO. Results in (C) and (D) are presented as mean \pm SD ($n = 3$).

Plotting the pseudo-first-order rate constants against TCO concentration yielded a second-order rate constant for the iEDDA reaction of HELIOS with NP-TCO of $(1.4 \pm 0.2) \times 10^6 \text{ M}^{-1} \text{ s}^{-1}$ (see **Figure 3 C**). This value is several orders of magnitude higher than for HELIOS reacting with PEG₄-TCO in solution (see **Figure 3 D**), approaching the rates observed for the fastest known iEDDA reactions. [5] The NP appears to significantly accelerate the reaction, which was unexpected, as it was initially assumed that anchoring one of the iEDDA partners (in this case, the TCO) on the NP surface would restrict its mobility, thereby reducing effective collisions between TCO and tetrazine. This should have resulted in a slower reaction on the NP. [38] However, the opposite effect was observed. Notably, Stéen, Jørgensen et al. also observed a significantly faster iEDDA reaction on their TCO-functionalized PeptoBrushes, which represent unimolecular polymer NPs, compared to a water-soluble PEGylated TCO derivative. [39] To explore whether the presence of the NP itself was responsible for the accelerated reaction, the NPs were dissolved in DMSO. Here, the NPs should dissociate into individual polymer chains (see **SI Figure 7**). The kinetics of the iEDDA reaction in DMSO were studied (see **SI Figure 8 A**), and the second-order rate constant was determined (see **SI Figure 8 B**). It was found that the reaction with the NPs dissolved in DMSO was significantly slower. Additionally, the reaction of free PEG₄-TCO with HELIOS in DMSO was examined (see **SI Figure 8 C+D**). The reaction rates in DMSO were nearly similar for both the dissolved NPs and free PEG₄-TCO (see **Figure 3 D**). This suggests that the accelerated reaction is specifically associated with the intact polymer NP structure.

3.4 Hydrophobic effect as driving force behind the extraordinarily fast reaction on the NP

To learn about the localization of the fluorophore, emission spectra of the fluorophore were recorded in various environments. In water, the emission maximum was around 500 nm, consistent with the findings of Meimetis, Carlson, et al. [18] In liquid PEG, however, the emission maximum was only approximately 480 nm, as it was for the fluorophore that had reacted on the NP (see **Figure 4 A**). It is well-known in the literature that polar solvents shift the emission maximum of coumarin fluorophores to longer wavelengths (red shift). [40–42] The lower emission maximum of the fluorophore on the NP, compared to that of the fluorophore in water and similar to that in liquid PEG, can mean that the fluorophore, after the iEDDA reaction, is located in the PEG brush on the particle surface. This corresponds to a less polar environment for the coumarin, resulting in a less pronounced red shift in its emission. A fluorophore that had already reacted with TCO and was added to an NP solution exhibited an emission spectrum shifted even further towards shorter wavelengths. This suggests that, when the tetrazine-coumarin fluorophore cannot react with TCO on the particle surface and thus remains confined within the PEG brush, it seems to embed itself within the hydrophobic core of the particle made of PLA

Chapter 3

and PLGA. The accumulation of the fluorophore on or within the particle was further investigated based on Hansen solubility parameters (see SI section VIII). The tetrazine-coumarin fluorophore can clearly be considered hydrophobic. The distance between the fluorophore and water in Hansen space was very large, indicating poor solubility/miscibility of these components. Significantly lower distances, indicating better compatibility, were observed for the components of the polymer NP. According to the estimation based on the Hansen solubility parameters, the fluorophore should preferentially accumulate in the PEG brush and PLA component, and somewhat less so in the PLGA (see **Figure 4 B**). An accumulation of the fluorophore at the NP seems reasonable in light of the findings.

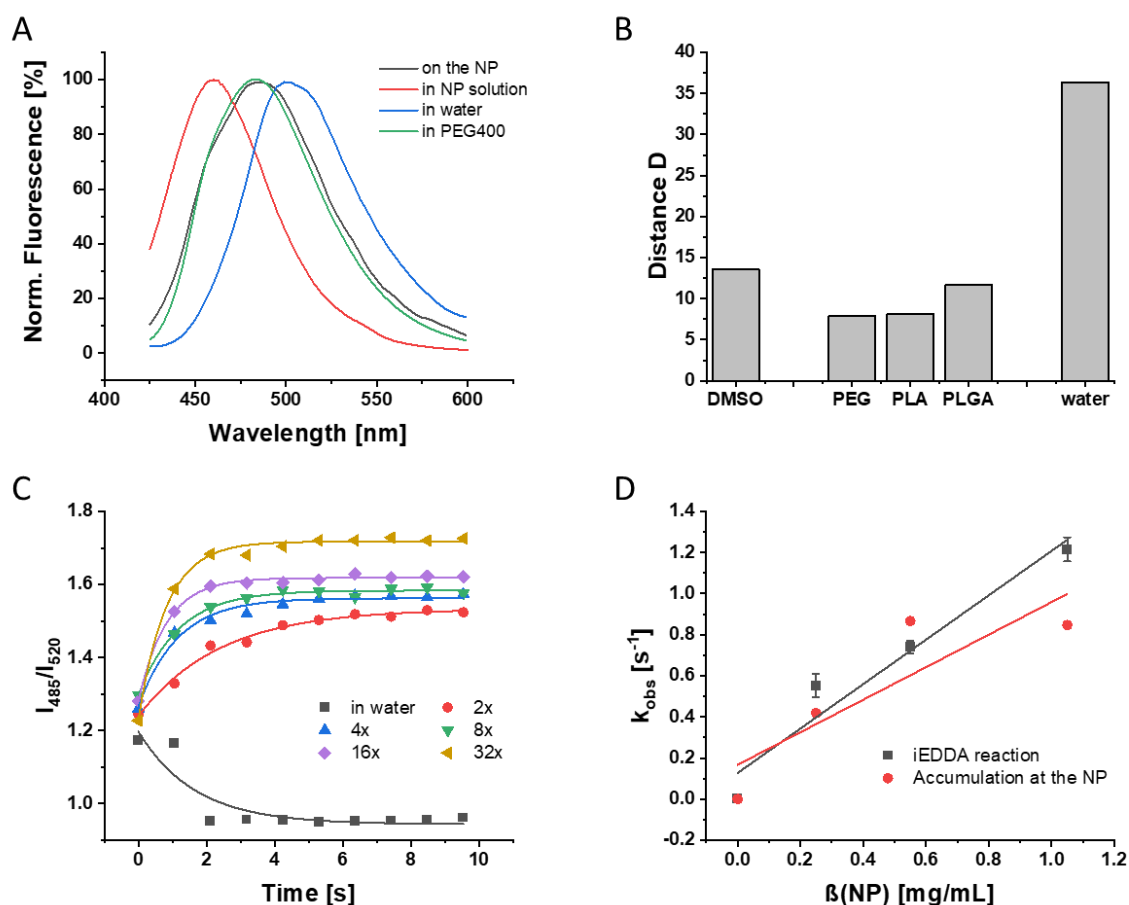


Figure 4. Studies on the accelerated reaction on the NP. (A) Emission spectra of the tetrazine coumarin fluorophore in different environments (excitation wavelength 400 nm). On the NP describes the fluorescence after the iEDDA reaction on the NP. For the other conditions (in NP solution, in water and in PEG400) the fluorophore was first reacted with PEG₄-TCO to dequench it. (B) Distance between HELIOS400Me and the listed components in Hansen's space to describe the preferred accumulation. (C) Fluorescence ratio between the emission at 485 nm to 520 nm (excitation wavelength 380 nm) to follow the kinetics of accumulation on the NP. (D) Observed pseudo first order rate constants for the iEDDA reaction and the accumulation process on the NP plotted against the NP concentration.

Further investigations focused on elucidating the kinetics of the accumulation process on the NP. For this purpose, fluorophore that had already reacted with TCO, was added to NP solutions of varying concentrations. The accumulation process was monitored by observing the emission ratio at two distinct

wavelengths: one wavelength (485 nm) indicated a less polar, more hydrophobic environment, while the other (520 nm) corresponded to a polar environment. The fluorescence ratio 485/520 nm increased within only a few seconds, suggesting an exceptionally fast accumulation of the hydrophobic fluorophore on the NP (see **Figure 4 C**). The rate of fluorophore accumulation on the NP was approximately as fast as the iEDDA reaction, as demonstrated by comparing observed pseudo-first-order rate constants at different NP concentrations (see **Figure 4 D**). This could be interpreted as indicating that the rate of accumulation on the NP also dictates the rate of the iEDDA reaction. Likely driven by the fluorophore's tendency to avoid interactions with water, it rapidly accumulates on the NP, thereby creating a locally increased concentration that accelerates the iEDDA reaction. As a result, the tetrazine-coumarin fluorophore presumably reacts with TCO on the NP surface before embedding within the particle's hydrophobic core.

In summary, the hydrophobic effect is likely the primary driving force behind the exceptionally fast reaction observed on the NP. Stéen, Jørgensen et al. reached a similar conclusion in their studies, demonstrating a strong correlation between the measured reaction rates and the calculated logarithmic distribution coefficient at physiological pH ($C \log D_{7.4}$) for all tetrazine derivatives examined. More lipophilic tetrazine derivatives appeared to facilitate higher reaction rates. [39] It is important to note that ligands designed to promote target cell recognition or uptake are expected to be significantly more polar than the highly nonpolar fluorophore used here as a surrogate. Consequently, the iEDDA reaction on the NP in such cases is expected to proceed at a slower rate, aligning more closely with the reaction kinetics observed in solution.

3.5 iEDDA reaction on NPs in biological media

The kinetics of the iEDDA reaction on NPs were studied in various biological media (see SI section IX). Pseudo-first-order rate constants were plotted against the TCO concentration to determine the second-order rate constants from the slope of the linear fit (see **Figure 5 A**). Compared to the reaction in pure water, the iEDDA reaction proceeded more slowly in all tested media. In Leibovitz's L-15 medium with 0.1% BSA (commonly used to dilute NPs for uptake experiments) the second-order rate constant was found to be $(2.7 \pm 0.3) * 10^5 \text{ M}^{-1} \text{ s}^{-1}$. Moving towards potential *in vivo* applications of the iEDDA reaction, the reaction in pure FBS was investigated and exhibited a second-order rate constant of $(1.5 \pm 0.1) * 10^4 \text{ M}^{-1} \text{ s}^{-1}$ (see **Figure 5 B**). The reaction presumably proceeded more slowly due to adsorption of the hydrophobic fluorophore onto serum components, primarily albumin present in both Leibovitz's L-15 medium with BSA and as a major constituent of FBS. The entry of coumarin fluorophores from aqueous solution into the hydrophobic domains of albumin is well-documented in the literature, typically manifesting as a blue shift in emission and fluorescence enhancement. [43] Both phenomena were also

Chapter 3

observed for the tetrazine-coumarin probe prior to the iEDDA reaction (see **SI Figure 11**). Adsorption and desorption processes involving serum components (including not only albumin but also other serum proteins, growth factors, hormones, lipids, and lipoproteins) may have hindered the iEDDA reaction in pure FBS. Additionally, a potential protein corona forming around the NP surface could have rendered the TCO functionalities less accessible. In Leibovitz's L-15 medium with 0.1% BSA, the presence of components for fluorophore adsorption is relatively limited, possibly allowing for a faster reaction compared to pure FBS, where numerous components are available for adsorption. Following this logic, the reaction rate in RPMI 1640 cell culture medium supplemented with 10% FBS fell in between these two. The second order rate constant was $(4.9 \pm 0.5) \cdot 10^4 \text{ M}^{-1} \text{ s}^{-1}$. In summary, while the iEDDA reaction proceeded more slowly in biological media compared to water, it still remained notably rapid. If the hydrophobic fluorophore is replaced by ligands intended to support active NP targeting and cell uptake, adsorption to serum components should be significantly reduced. Adsorption is likely driven by hydrophobic interactions, and thus using polar iEDDA reaction partners should not result in significant decreases in reaction speed. The iEDDA reaction appears well suited to functionalize particles in a biological environment, opening the potential to modify NPs even *in vivo*, thereby enabling precise tailoring of their properties.

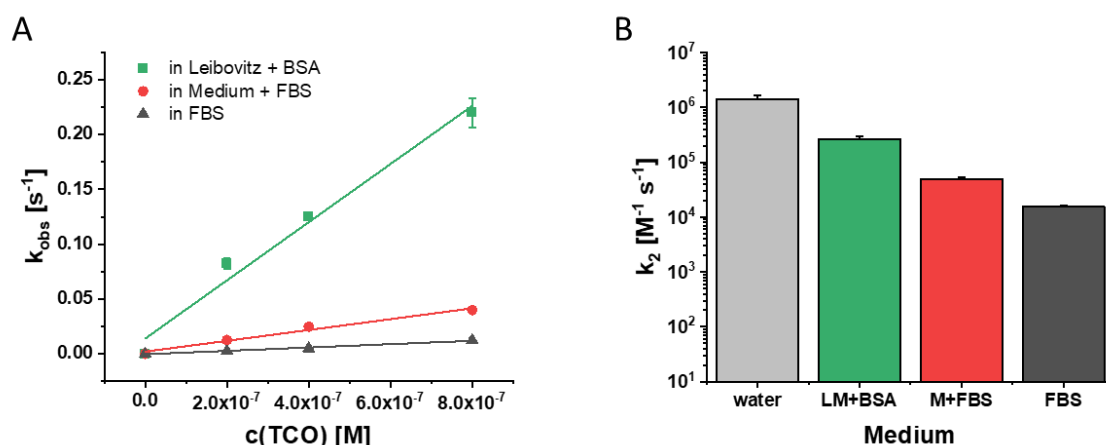


Figure 5. Kinetics of the iEDDA reaction between HELIOS400Me and NP-TCO in different biological media. (A) Observed pseudo first order rate constants plotted against TCO concentration. (B) Comparison of the second order rate constants in different biological media. In Leibovitz + BSA or LM+BSA for short means reaction in Leibovitz's L-15 medium with 0.1% BSA; in Medium + FBS or M+FBS for short means reaction in RPMI 1640 cell culture medium with 10% FBS supplement. Results are presented as mean \pm SD ($n = 3$).

3.6 Stability of iEDDA reaction partners

Tetrazine stability was investigated for tetrazine on the tetrazine coumarin fluorophore (HELIOS 400Me). [18] As the tetrazine decomposes, it no longer quenches the fluorophore and the fluorescence intensity increases, providing a straightforward way to monitor the amount of intact tetrazine. The

stability in pure fetal bovine serum (FBS) was the lowest with a half-life of 17 ± 3 h. In Leibovitz medium with 0.1% BSA supplement, a half-life of 232 ± 7 h was found. In PBS, the tetrazine hardly decomposed over the observation period of 9 days (see **Figure 6 A**). The remarkable stability of the tetrazine, e.g. also in FBS, is consistent with literature, as Karver, Weissleder et al. report nearly 95% intact tetrazine for a reasonably comparable tetrazine following a 10-hour incubation at 37°C in pure FBS. [37] Generally, it can be stated that increased stability of the employed tetrazine often comes at the expense of slower kinetics in the iEDDA reaction. This is because electron-withdrawing substituents are usually used on tetrazine to increase reactivity, but these also accelerate the attack of nucleophiles causing tetrazine degradation (see **Figure 6 D**). [44] The selection of the methyl-substituted tetrazine in this study prioritizes adequate stability within a complex biological milieu. Nevertheless, as demonstrated in section 3.5, the reaction remains sufficiently rapid to enable robust *in vitro* functionalization.

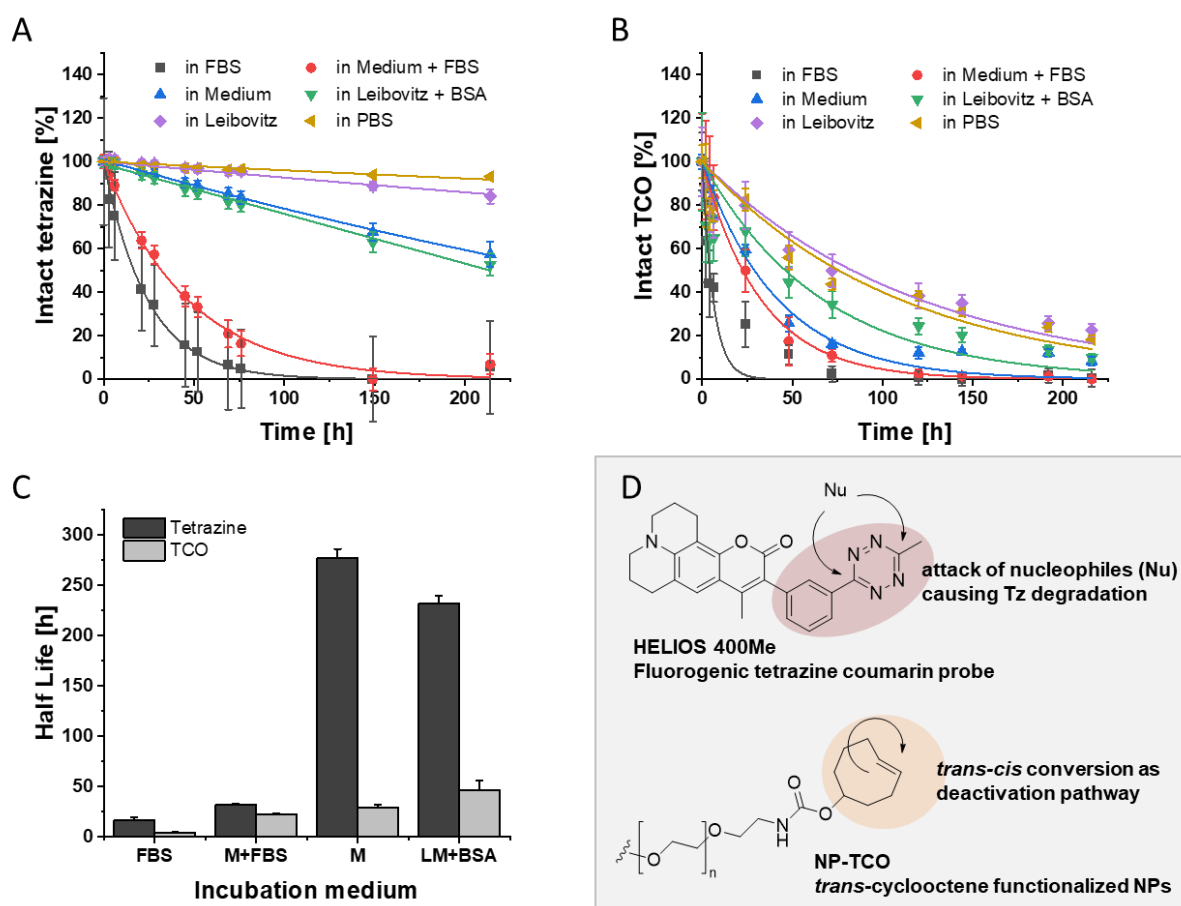


Figure 6. Stability of tetrazine and trans-cyclooctene in various media. (A) Intact tetrazine on the tetrazine coumarin fluorophore with progressing incubation time. (B) Intact trans-cyclooctene on the NP with progressing incubation time. (C) Half-lives in the different media determined by the exponential decay fit. (D) Structural formulas of the investigated components and illustration of deactivation pathways discussed in the literature. [44, 45] In Medium + FBS or M+FBS for short means incubation in RPMI 1640 cell culture medium with 10% FBS supplement; in Leibovitz + BSA or LM+BSA for short means incubation in Leibovitz's L-15 medium with 0.1% BSA. Results are presented as mean \pm SD ($n = 3$).

Chapter 3

The TCO stability on 60% TCO functionalized NPs was investigated by adding an excess of the fluorogenic tetrazine coumarin fluorophore after different incubation times. The extent to which the fluorescence intensity was increased by the iEDDA reaction was recorded and serves as a measure of how much intact TCO was still present. In contrast to tetrazine, the stability of trans-cyclooctene was considerably lower. The half-life in pure FBS was only about 4 hours. This result is consistent with a half-life of approximately 3 hours for a related TCO in fresh mouse serum reported by Rossin, van den Bosch et al. [45] The authors attribute this phenomenon to the interaction of TCO with copper-containing proteins, which may lead to the isomerization of trans-cyclooctene to cis-cyclooctene (see **Figure 6 D**), whereby the cis-cyclooctene is several orders of magnitude less reactive. The half-life in Leibovitz medium supplemented with 0.1% BSA was 46 ± 10 h. In PBS, the TCO also substantially lost its reactivity during the observation period (see **Figure 6 B**), whereby a half-life of 76 ± 9 h was determined by the fit of the exponential decrease. When stored in the refrigerator, approximately 75% of intact TCO was still detected on the NP after one month, with the particle size remaining stable (see SI section XI). The comparison of the half-lives at 37°C in different media demonstrates the higher stability of tetrazine (see **Figure 6 C**). Therefore, for further projects it seems to be the more promising strategy to attach the more stable tetrazine to the NP and the relatively short-lived TCO to the ligand, as the particles were expected to remain in a biological environment for an extended duration. Choi, Zuckerman et al. reported for example blood circulation for particles that are comparable to the polymer NPs used in this study with a half-life in the bloodstream of 13.7 hours. [46] Although the stability of TCO in biological environments has been a subject of concern due to its notably short half-life, it can be stated that the TCO used still opens a time window of several hours for subsequent NP functionalization in biological environments, rendering the NPs switchable.

3.7 EXP3174 functionalized NPs for anchoring to the target cell

Further investigations explored whether NPs can be functionalized directly on the target cell using the iEDDA reaction. For this purpose, a second ligand was integrated into the NP design. EXP3174, the active metabolite of the well-known AT1R antagonist losartan, mediates receptor attachment (see **Figure 7 A**). [47] As an antagonist of a G protein-coupled receptor (GPCR), binding to the receptor does not result in internalization of the NPs, allowing the particles to initially remain on the cell surface. [48] Subsequently, functionalization via the additional ligand using the iEDDA reaction could be achieved, enabling, for instance, the attachment of a ligand that promotes cellular uptake. The NPs were prepared through nanoprecipitation. Alongside dual-functionalized NPs containing EXP3174 for cell surface anchoring and TCO for the iEDDA reaction, NPs functionalized solely with EXP3174 were also

prepared for comparison. The dual-functionalized NPs (NP-EXP/TCO) were slightly larger (see **Figure 7 B**), with an average hydrodynamic diameter of approximately 83 nm compared to 73 nm for NP-EXP. To evaluate the anchoring of the NPs to the target cell, binding curves on the AT1 receptor were recorded. These revealed virtually no differences between the two types of particles (see **Figure 7 C**), with IC_{50} values derived from fitting being nearly identical (see **Figure 7 D**). This suggests that the second ligand, TCO, does not interfere with the binding of the NPs to the AT1 receptor via the primary ligand EXP3174. Therefore, dual-functionalized NPs can reliably bind to the target cell allowing subsequent NP functionalization directly on the target site.

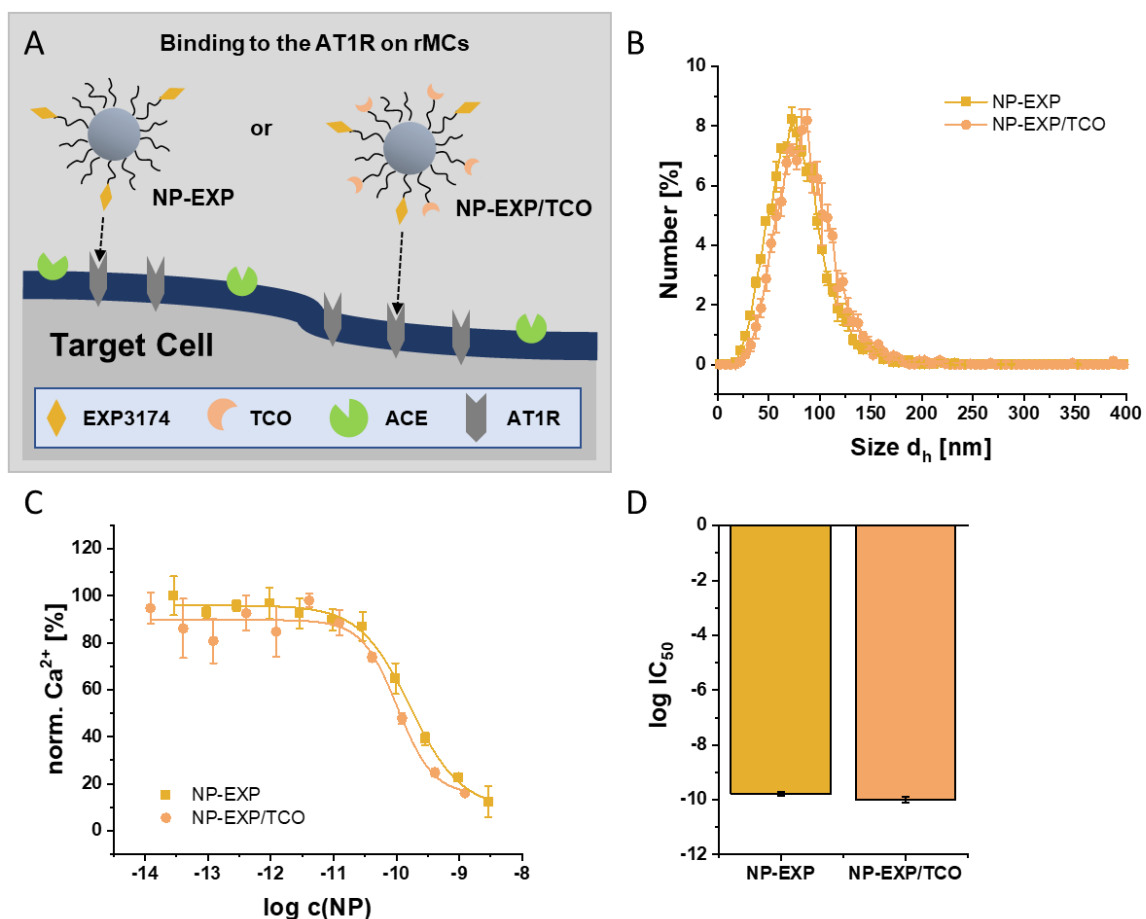


Figure 7. EXP3174 functionalized NPs for anchoring to the target cell. (A) Schematic illustrating the binding of EXP functionalized NPs to AT1 receptors on the cell surface of rMCs. (B) Size distribution of EXP-functionalized particles (NP-EXP) and dual EXP- and TCO-functionalized particles (NP-EXP/TCO) determined by NTA. (C) Binding curves to the AT1R determined by Fura-2 AM Ca^{2+} mobilization assay with rMCs using the inverse procedure. (D) $\log IC_{50}$ values determined by the fit. Results are presented as mean \pm SD (n=3).

Chapter 3

3.8 Functionalization of NPs on target cells using the HELIOS400Me fluorogenic probe

To detect the functionalization of NPs directly on the target cell, the fluorogenic tetrazine coumarin probe HELIOS400Me was employed. The primary ligand, EXP3174, was intended to mediate the binding of NPs to the AT1 receptor on the target cell. After an incubation period of 30 minutes, the fluorogenic probe was added. This probe was designed to react with the TCO-functionalized NPs, whereas no reaction would occur with NPs functionalized only with EXP3174. Consequently, if the HELIOS fluorophore attaches to the NP following a successful iEDDA reaction, a more pronounced colocalization between the NP and HELIOS channel was expected for NP-EXP/TCO compared to NP-EXP. Furthermore, the average HELIOS fluorescence per cell for NP-EXP/TCO was anticipated to increase compared to NP-EXP, as the tetrazine would be consumed in the iEDDA reaction, no longer quenching the coumarin fluorophore of the probe. CLSM images clearly confirmed that EXP3174-functionalized NPs were not directly internalized by the cells but initially remained on the cell membrane (see **Figure 8 A**). This was evidenced by a yellow outline of the cells, indicating NPs anchored on the cell surface. When the NPs were additionally functionalized with TCO for the iEDDA reaction, the membrane anchoring, and thus the staining observed in the CLSM images, was less distinct (see **Figure 8 B**). Overall, fewer particles per cell were detected for NP-EXP/TCO compared to NP-EXP (see **Figure 8 C**). It can be speculated that the second ligand, TCO, might have interfered with the multivalent binding of particles to AT1 receptors on the cell surface, contrary to the results suggested by Ca²⁺ mobilization assays (see section 3.7).

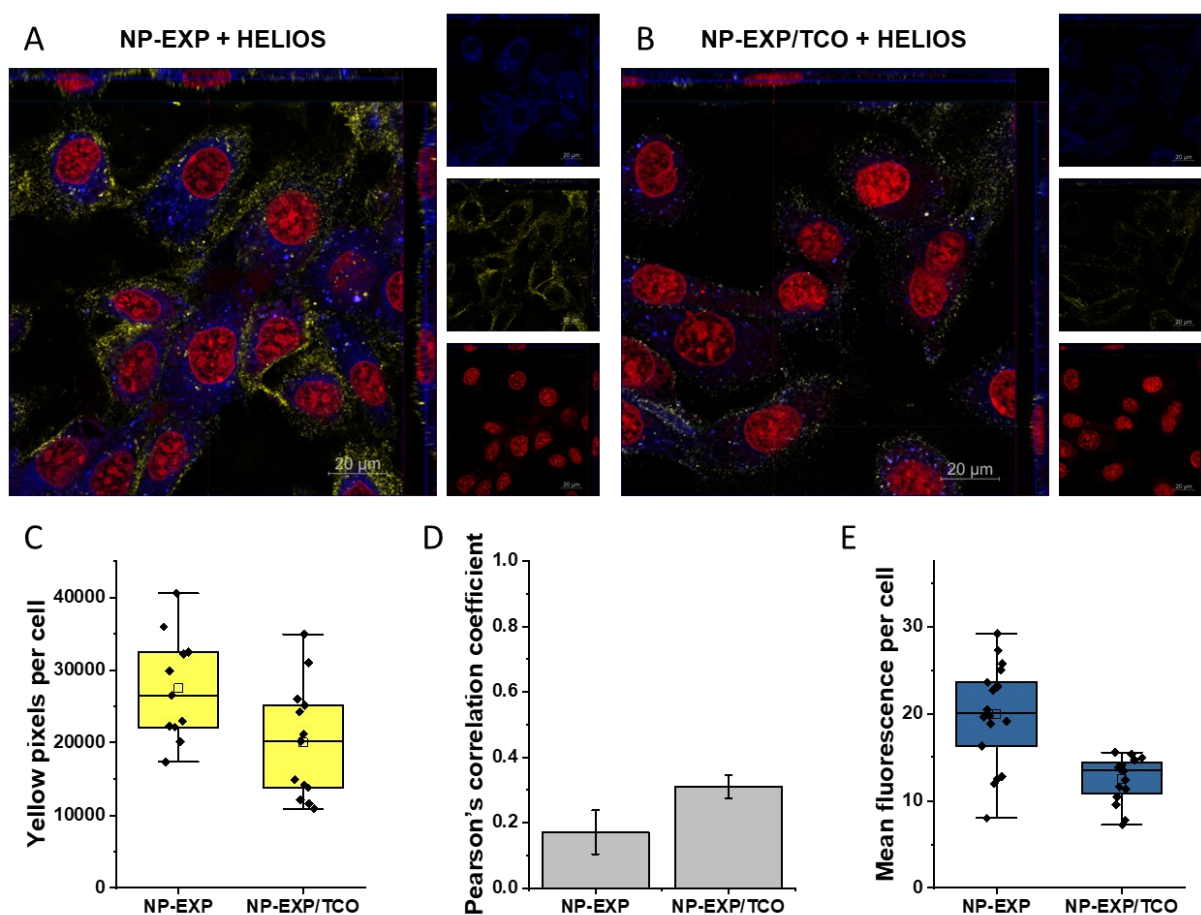


Figure 8. iEDDA reaction of NPs directly on the cell surface with HELIOS400Me. CLSM Z-stack and images of individual channels for EXP3174 functionalized NPs (A) and both EXP3174 and TCO functionalized NPs (B). The rMCs were incubated for 30 min with NPs at a concentration of 300 pM, then HELIOS solution (final total concentration 1.5 μ M) was added and incubated for another 10 min. DRAQ5 cell nuclear staining in red, TAMRA labeled NPs in yellow and HELIOS400Me in blue. (C) Box plot of yellow pixels per cell above a certain threshold as an estimate of NPs per cell. (D) Pearson's correlation coefficient for the colocalization between yellow (NP) and blue (HELIOS) channels. (E) Box plot of mean HELIOS fluorescence per cell. For (C) and (E) at least 12 cells from 3 images were included. Results in (D) are presented as mean \pm SD from $n=3$ images. The other images used for evaluation can be found in SI section XII.

The colocalization of NP with HELIOS fluorescence was generally low but slightly increased for NP-EXP/TCO compared to NPs functionalized only with EXP (see **Figure 8 D**). The cell-permeable HELIOS fluorophore primarily accumulated within the cells, while NP-EXP remained on the cell membrane. For NPs additionally functionalized with TCO, this pattern changed only marginally. HELIOS primarily stained the entire cell blue instead of predominantly marking the cell membrane along with the particles. Moreover, the mean HELIOS fluorescence per cell did not increase following the iEDDA reaction. On the contrary, a lower mean HELIOS fluorescence intensity was observed for NP-EXP/TCO compared to NP-EXP (see **Figure 8 E**). This result was unexpected, as Meimetis, Carlson, et al. successfully visualized EGFR expression on cells incubated with α -EGFR-TCO

Chapter 3

antibodies. They reported bright, membrane-specific staining upon subsequent addition of a HELIOS probe. [18] It should be feasible to replace the TCO labeled antibody with a dual-functionalized NP – one ligand for receptor targeting and TCO for the iEDDA reaction. However, the demonstration of iEDDA-based NP functionalization directly on target cells failed likely due to a combination of suboptimal iEDDA reaction efficiency and the poor turn-on ratio of the fluorogenic probe. The nonpolar, cell-permeable fluorophore presumably entered the cells rapidly, potentially reducing its availability for the iEDDA reaction on the cell surface. The slightly enhanced colocalization between NP and HELIOS fluorescence observed for iEDDA-capable NPs may suggest that part of the probe reacted with TCO-functionalized NPs on the cell surface during its passage into the cell. However, the turn-on ratio of the fluorogenic probe was significantly lower than reported by Meimetis, Carlson, et al. (see SI section XIII). The quenched HELIOS fluorophore already exhibited notable fluorescence, making small changes in fluorescence intensity challenging to detect.

In conclusion, while EXP3174-functionalized NPs were successfully anchored on cells as expected, the iEDDA reaction likely did not proceed to the desired extent and was difficult to monitor. Using a cell-uptake-promoting ligand instead of the fluorogenic probe could provide a more polar, non-cell-permeable alternative. This would potentially improve NP functionalization directly on the target cell. Further studies could employ flow cytometry to evaluate whether NP uptake is increased by attaching a cell uptake-promoting ligand via iEDDA reaction. This may offer a more robust readout for successful NP functionalization than the observation via the fluorogenic probe in CLSM images simultaneously paving the way towards the application of the NPs in drug delivery.

4. Conclusion

In this study, well-defined iEDDA-reactive NPs were successfully prepared. The modular design based on PLGA and varying ratios of TCO-functionalized and non-functionalized PLA-PEG block copolymers, enabled the production of customized NPs. Furthermore, the fluorescence behavior of the fluorogenic HELIOS probe was analyzed, allowing the derivation of an equation to accurately model the fluorescence intensity kinetics. Unexpectedly, it was observed that the iEDDA reaction of the fluorogenic probe proceeded significantly faster on the NP surface compared to its reaction in free solution. This phenomenon was attributed to hydrophobic effects, which were identified as the driving force behind the exceptionally rapid iEDDA reaction on the NP. Investigation of the iEDDA reaction between the fluorogenic probe and TCO-functionalized NPs in various biologically relevant media demonstrated that the NPs could undergo rapid functionalization even in the presence of numerous other functional groups. These findings suggest that the iEDDA reaction holds great potential for *in vivo* NP

Switchable Fluorescence

modification. Stability studies of the iEDDA reaction partners confirmed that a sufficient time window exists for the intended biological applications. However, an attempt to visualize NP functionalization directly at the target cell membrane using the fluorogenic HELIOS probe was not successful. This was likely due to incomplete iEDDA reaction and a suboptimal turn-on ratio of the fluorogenic probe. Notably, the HELIOS probe, used as a surrogate in this study, does not exhibit properties well-matched to the cell-uptake-promoting ligands for future applications. Unlike the highly hydrophobic fluorogenic probe, the peptidic ligands for subsequent applications are unlikely to be affected by significant hydrophobic effects. Overall, the fluorogenic probe effectively demonstrated a switchable NP fluorescence in solution, providing a valuable tool for monitoring NP functionalization. The findings indicate that the iEDDA reaction is highly suitable for functionalizing NPs in complex biological environments.

Chapter 3

References

1. Sletten EM, Bertozzi CR (2009) Bioorthogonal chemistry: fishing for selectivity in a sea of functionality. *Angewandte Chemie International Edition* 48(38), 6974–6998. 10.1002/anie.200900942.
2. Zhang Q, Kuang G, Wang L, Duan P, Sun W, Ye F (2023) Designing Bioorthogonal Reactions for Biomedical Applications. *Research (Washington, D.C.)* 6, 251. 10.34133/research.0251.
3. Handula M, Chen K-T, Seimbille Y (2021) IEDDA: An Attractive Bioorthogonal Reaction for Biomedical Applications. *Molecules (Basel, Switzerland)* 26(15), 4640. 10.3390/molecules26154640.
4. Knall A-C, Slugovc C (2013) Inverse electron demand Diels-Alder (IEDDA)-initiated conjugation: a (high) potential click chemistry scheme. *Chem. Soc. Rev.* 42(12), 5131–5142. 10.1039/C3CS60049A.
5. Oliveira BL, Guo Z, Bernardes GJL (2017) Inverse electron demand Diels-Alder reactions in chemical biology. *Chem. Soc. Rev.* 46(16), 4895–4950. 10.1039/C7CS00184C.
6. Elliott TS, Townsley FM, Bianco A, Ernst RJ, Sachdeva A, Elsässer SJ, Davis L, Lang K, Pisa R, Greiss S, Lilley KS, Chin JW (2014) Proteome labeling and protein identification in specific tissues and at specific developmental stages in an animal. *Nat Biotechnol* 32(5), 465–472. 10.1038/nbt.2860.
7. Li Z, Wang D, Li L, Pan S, Na Z, Tan CYJ, Yao SQ (2014) “Minimalist” cyclopropene-containing photo-cross-linkers suitable for live-cell imaging and affinity-based protein labeling. *Journal of the American Chemical Society* 136(28), 9990–9998. 10.1021/ja502780z.
8. Seckute J, Yang J, Devaraj NK (2013) Rapid oligonucleotide-templated fluorogenic tetrazine ligations. *Nucleic acids research* 41(15), e148. 10.1093/nar/gkt540.
9. Uttamapinant C, Howe JD, Lang K, Beránek V, Davis L, Mahesh M, Barry NP, Chin JW (2015) Genetic code expansion enables live-cell and super-resolution imaging of site-specifically labeled cellular proteins. *Journal of the American Chemical Society* 137(14), 4602–4605. 10.1021/ja512838z.
10. Idiago-López J, Moreno-Antolín E, La Fuente JM de, Fratila RM (2021) Nanoparticles and bioorthogonal chemistry joining forces for improved biomedical applications. *Nanoscale Adv.* 3(5), 1261–1292. 10.1039/D0NA00873G.
11. Kramer S, Svatunek D, Alberg I, Gräfen B, Schmitt S, Braun L, van Onzen AHAM, Rossin R, Koynov K, Mikula H, Zentel R (2019) HPMa-Based Nanoparticles for Fast, Bioorthogonal IEDDA Ligation. *Biomacromolecules* 20(10), 3786–3797. 10.1021/acs.biomac.9b00868.
12. Lumen D, Näkki S, Imlimthan S, Lambidis E, Sarparanta M, Xu W, Lehto V-P, Airaksinen AJ (2019) Site-Specific ¹¹¹In-Radiolabeling of Dual-PEGylated Porous Silicon Nanoparticles and

- Their In Vivo Evaluation in Murine 4T1 Breast Cancer Model. *Pharmaceutics* 11(12). 10.3390/pharmaceutics11120686.
13. Goos JACM, Davydova M, Dilling TR, Cho A, Cornejo MA, Gupta A, Price WS, Puttick S, Whittaker MR, Quinn JF, Davis TP, Lewis JS (2020) Design and preclinical evaluation of nanostars for the passive pretargeting of tumor tissue. *Nuclear Medicine and Biology* 84-85, 63–72. 10.1016/j.nucmedbio.2020.02.012.
 14. Denk C, Svatunek D, Mairinger S, Stanek J, Filip T, Matscheko D, Kuntner C, Wanek T, Mikula H (2016) Design, Synthesis, and Evaluation of a Low-Molecular-Weight (11)C-Labeled Tetrazine for Pretargeted PET Imaging Applying Bioorthogonal in Vivo Click Chemistry. *Bioconjugate Chemistry* 27(7), 1707–1712. 10.1021/acs.bioconjchem.6b00234.
 15. Feng Y, Wu Y, Zuo J, Tu L, Que I, Chang Y, Cruz LJ, Chan A, Zhang H (2019) Assembly of upconversion nanophotosensitizer in vivo to achieve scatheless real-time imaging and selective photodynamic therapy. *Biomaterials* 201, 33–41. 10.1016/j.biomaterials.2019.02.015.
 16. Mao W, Dong P, Du W, Wu H (2025) Fluorogenic Tetrazine Bioorthogonal Probes for Advanced Application in Bioimaging and Biomedicine. *Chemical & biomedical imaging* 3(1), 1–4. 10.1021/cbmi.4c00095.
 17. Choi S-K, Kim J, Kim E (2021) Overview of Syntheses and Molecular-Design Strategies for Tetrazine-Based Fluorogenic Probes. *Molecules (Basel, Switzerland)* 26(7). 10.3390/molecules26071868.
 18. Meimetis LG, Carlson JCT, Giedt RJ, Kohler RH, Weissleder R (2014) Ultrafluorogenic coumarin-tetrazine probes for real-time biological imaging. *Angewandte Chemie (International ed. in English)* 53(29), 7531–7534. 10.1002/anie.201403890.
 19. Schorr K, Beck S, Zimmer O, Baumann F, Keller M, Witzgall R, Goepferich A (2025) The quantity of ligand-receptor interactions between nanoparticles and target cells. *Nanoscale Horiz.* 10.1039/D4NH00645C.
 20. Walter M, Baumann F, Schorr K, Goepferich A (2023) Ectoenzymes as promising cell identification structures for the high avidity targeting of polymeric nanoparticles. *International Journal of Pharmaceutics* 647, 123453. 10.1016/j.ijpharm.2023.123453.
 21. Abstiens K, Maslanka Figueroa S, Gregoritz M, Goepferich AM (2019) Interaction of functionalized nanoparticles with serum proteins and its impact on colloidal stability and cargo leaching. *Soft Matter* 15(4), 709–720. 10.1039/C8SM02189A.
 22. Qian H, Wohl AR, Crow JT, Macosko CW, Hoye TR (2011) A Strategy for Control of “Random” Copolymerization of Lactide and Glycolide: Application to Synthesis of PEG-b-PLGA Block Polymers Having Narrow Dispersity. *Macromolecules* 44(18), 7132–7140. 10.1021/ma201169z.

Chapter 3

23. Fessi H, Puisieux F, Devissaguet JP, Ammoury N, Benita S (1989) Nanocapsule formation by interfacial polymer deposition following solvent displacement. *International Journal of Pharmaceutics* 55(1), R1-R4. 10.1016/0378-5173(89)90281-0.
24. Abstiens K, Goepferich AM (2019) Microfluidic manufacturing improves polydispersity of multicomponent polymeric nanoparticles. *Journal of Drug Delivery Science and Technology* 49, 433–439. 10.1016/j.jddst.2018.12.009.
25. Garg S, Patel P, Gupta GD, Kurmi BD (2024) Pharmaceutical Applications and Advances with Zetasizer: An Essential Analytical Tool for Size and Zeta Potential Analysis. *MNS* 16(3), 139–154. 10.2174/0118764029301470240603051432.
26. Filipe V, Hawe A, Jiskoot W (2010) Critical evaluation of Nanoparticle Tracking Analysis (NTA) by NanoSight for the measurement of nanoparticles and protein aggregates. *Pharm Res* 27(5), 796–810. 10.1007/s11095-010-0073-2.
27. Knall A-C, Hollauf M, Slugovc C (2014) Kinetic studies of inverse electron demand Diels-Alder reactions (iEDDA) of norbornenes and 3,6-dipyridin-2-yl-1,2,4,5-tetrazine. *Tetrahedron Letters* 55(34), 4763–4766. 10.1016/j.tetlet.2014.07.002.
28. Maslanka Figueroa S, Fleischmann D, Beck S, Tauber P, Witzgall R, Schweda F, Goepferich A (2020) Nanoparticles Mimicking Viral Cell Recognition Strategies Are Superior Transporters into Mesangial Cells. *Advanced Science* 7(11), 1903204. 10.1002/advs.201903204.
29. Grynkiewicz G, Poenie M, Tsien RY (1985) A new generation of Ca²⁺ indicators with greatly improved fluorescence properties. *The Journal of biological chemistry* 260(6), 3440–3450.
30. Schindelin J, Arganda-Carreras I, Frise E, Kaynig V, Longair M, Pietzsch T, Preibisch S, Rueden C, Saalfeld S, Schmid B, Tinevez J-Y, White DJ, Hartenstein V, Eliceiri K, Tomancak P, Cardona A (2012) Fiji: an open-source platform for biological-image analysis. *Nature methods* 9(7), 676–682. 10.1038/nmeth.2019.
31. Bolte S, Cordelières FP (2006) A guided tour into subcellular colocalization analysis in light microscopy. *Journal of microscopy* 224(Pt 3), 213–232. 10.1111/j.1365-2818.2006.01706.x.
32. Abstiens K, Gregoritz M, Goepferich AM (2019) Ligand Density and Linker Length are Critical Factors for Multivalent Nanoparticle-Receptor Interactions. *ACS applied materials & interfaces* 11(1), 1311–1320. 10.1021/acsami.8b18843.
33. Schubert S, Delaney JJT, Schubert US (2011) Nanoprecipitation and nanoformulation of polymers: from history to powerful possibilities beyond poly(lactic acid). *Soft Matter* 7(5), 1581–1588. 10.1039/C0SM00862A.
34. Galeta J, Dzija R, Obořil J, Dračinský M, Vrabel M (2020) A Systematic Study of Coumarin-Tetrazine Light-Up Probes for Bioorthogonal Fluorescence Imaging. *Chemistry (Weinheim an der Bergstrasse, Germany)* 26(44), 9945–9953. 10.1002/chem.202001290.

35. Hild F, Werther P, Yserentant K, Wombacher R, Herten D-P (2022) A dark intermediate in the fluorogenic reaction between tetrazine fluorophores and trans-cyclooctene. *Biophysical reports* 2(4), 100084. 10.1016/j.bpr.2022.100084.
36. Pinto-Pacheco B, Carbery WP, Khan S, Turner DB, Buccella D (2020) Fluorescence Quenching Effects of Tetrazines and Their Diels-Alder Products: Mechanistic Insight Toward Fluorogenic Efficiency. *Angewandte Chemie International Edition* 59(49), 22140–22149. 10.1002/anie.202008757.
37. Karver MR, Weissleder R, Hilderbrand SA (2011) Synthesis and evaluation of a series of 1,2,4,5-tetrazines for bioorthogonal conjugation. *Bioconjugate Chemistry* 22(11), 2263–2270. 10.1021/bc200295y.
38. Hu J, Wen C-Y, Zhang Z-L, Xie M, Xie H-Y, Pang D-W (2014) Recognition kinetics of biomolecules at the surface of different-sized spheres. *Biophysical Journal* 107(1), 165–173. 10.1016/j.bpj.2014.05.005.
39. Stéen E JL, Jørgensen JT, Johann K, Nørregaard K, Sohr B, Svatunek D, Birke A, Shalgunov V, Edem PE, Rossin R, Seidl C, Schmid F, Robillard MS, Kristensen JL, Mikula H, Barz M, Kjær A, Herth MM (2020) Trans-Cyclooctene-Functionalized PeptoBrushes with Improved Reaction Kinetics of the Tetrazine Ligation for Pretargeted Nuclear Imaging. *ACS nano* 14(1), 568–584. 10.1021/acsnano.9b06905.
40. Jones G, Jackson WR, Kanoktanaporn S, Halpern AM (1980) Solvent effects on photophysical parameters for coumarin laser dyes. *Optics Communications* 33(3), 315–320. 10.1016/0030-4018(80)90252-7.
41. Kunjappu JT (1993) Photophysical properties of five laser dyes (C120, C1, C102, C1F and C153) in homogeneous, surfactant and membrane media. *Journal of Photochemistry and Photobiology A: Chemistry* 71(3), 269–273. 10.1016/1010-6030(93)85009-W.
42. Moreira LM, Melo MM de, Martins PA, Lyon JP, Romani AP, Codognoto L, Santos SCd, Oliveira HPM de (2014) Photophysical Properties of Coumarin Compounds in Neat and Binary Solvent Mixtures: Evaluation and Correlation Between Solvatochromism and Solvent Polarity Parameters. *Journal of the Brazilian Chemical Society*. 10.5935/0103-5053.20140051.
43. Bhattacharya B, Nakka S, Guruprasad L, Samanta A (2009) Interaction of bovine serum albumin with dipolar molecules: fluorescence and molecular docking studies. *The journal of physical chemistry. B* 113(7), 2143–2150. 10.1021/jp808611b.
44. Svatunek D, Wilkovitsch M, Hartmann L, Houk KN, Mikula H (2022) Uncovering the Key Role of Distortion in Bioorthogonal Tetrazine Tools That Defy the Reactivity/Stability Trade-Off. *Journal of the American Chemical Society* 144(18), 8171–8177. 10.1021/jacs.2c01056.

Chapter 3

45. Rossin R, van den Bosch SM, Hoeve W ten, Carvelli M, Versteegen RM, Lub J, Robillard MS (2013) Highly reactive trans-cyclooctene tags with improved stability for Diels-Alder chemistry in living systems. *Bioconjugate Chemistry* 24(7), 1210–1217. 10.1021/bc400153y.
46. Choi CHJ, Zuckerman JE, Webster P, Davis ME (2011) Targeting kidney mesangium by nanoparticles of defined size. *Proceedings of the National Academy of Sciences of the United States of America* 108(16), 6656–6661. 10.1073/pnas.1103573108.
47. Hennig R, Pollinger K, Vesper A, Breunig M, Goepferich A (2014) Nanoparticle multivalency counterbalances the ligand affinity loss upon PEGylation. *Journal of controlled release official journal of the Controlled Release Society* 194, 20–27. 10.1016/j.jconrel.2014.07.062.
48. Hild W, Pollinger K, Caporale A, Cabrele C, Keller M, Pluym N, Buschauer A, Rachel R, Tessmar J, Breunig M, Goepferich A (2010) G protein-coupled receptors function as logic gates for nanoparticle binding and cell uptake. *Proceedings of the National Academy of Sciences of the United States of America* 107(23), 10667–10672. 10.1073/pnas.0912782107.

Chapter 3

Chapter 3

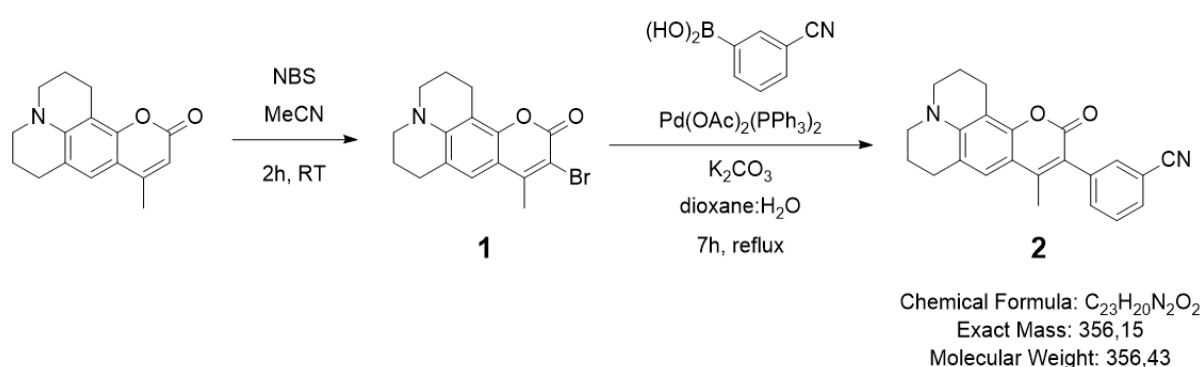
Supplementary Information

Chapter 3 – Supplementary Information

I. Synthesis of the fluorogenic tetrazine coumarin HELIOS400Me

The synthesis follows the procedure reported by Meimetis, Carlson et al. [1]

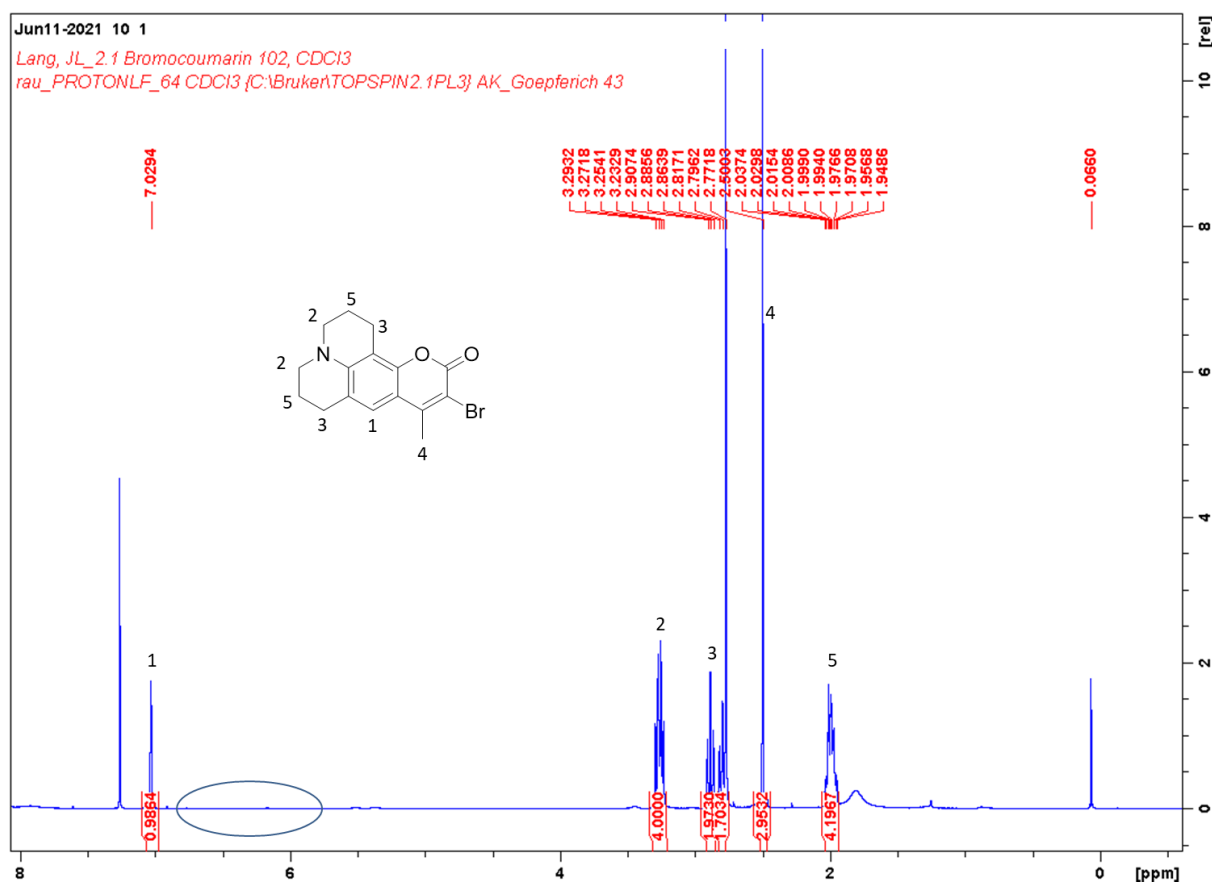
Synthesis of bromocoumarin **1** and nitrile coumarin **2**



For bromination, coumarin 102 (127 mg, 0.5 mmol, 1 equiv.) was dissolved in 10 mL acetonitrile and N-bromosuccinimide (NBS, 100 mg, 0.55 mmol, 1.1 equiv.) was added. The reaction mixture was stirred for 2 h at room temperature protected from light. The solvent was removed using a rotary evaporator and the crude product **1** was used for the Suzuki reaction in the next synthesis step without further purification. To the bromocoumarin crude product **1** dissolved in 8 mL dioxane:water (3:1) was added 3-cyanophenylboronic acid (146.9 mg, 1 mmol, 2 equiv.), the catalyst bis(triphenylphosphine) palladium(II) diacetate (18.9 mg, 0.025 mmol, 0.05 equiv.) and potassium carbonate (140 mg, 1 mmol, 2 equiv.) as base. The reaction mixture was refluxed for 7 hours after which it was concentrated using a rotary evaporator. The product was purified by column chromatography (hexanes : ethyl acetate gradient, 5:1 to 5:2) and 113 mg (0.32 mmol, 63%) of the desired product nitrile coumarin **2** was obtained.

¹H NMR (CDCl₃): δ = 7.61–7.46 (m, 4H), 7.04 (s, 1H), 3.28–3.22 (q, 4H), 2.92–2.87 (t, 2H), 2.80–2.76 (t, 2H), 2.15 (s, 3H), 2.03–1.95 (m, 4H) ppm.

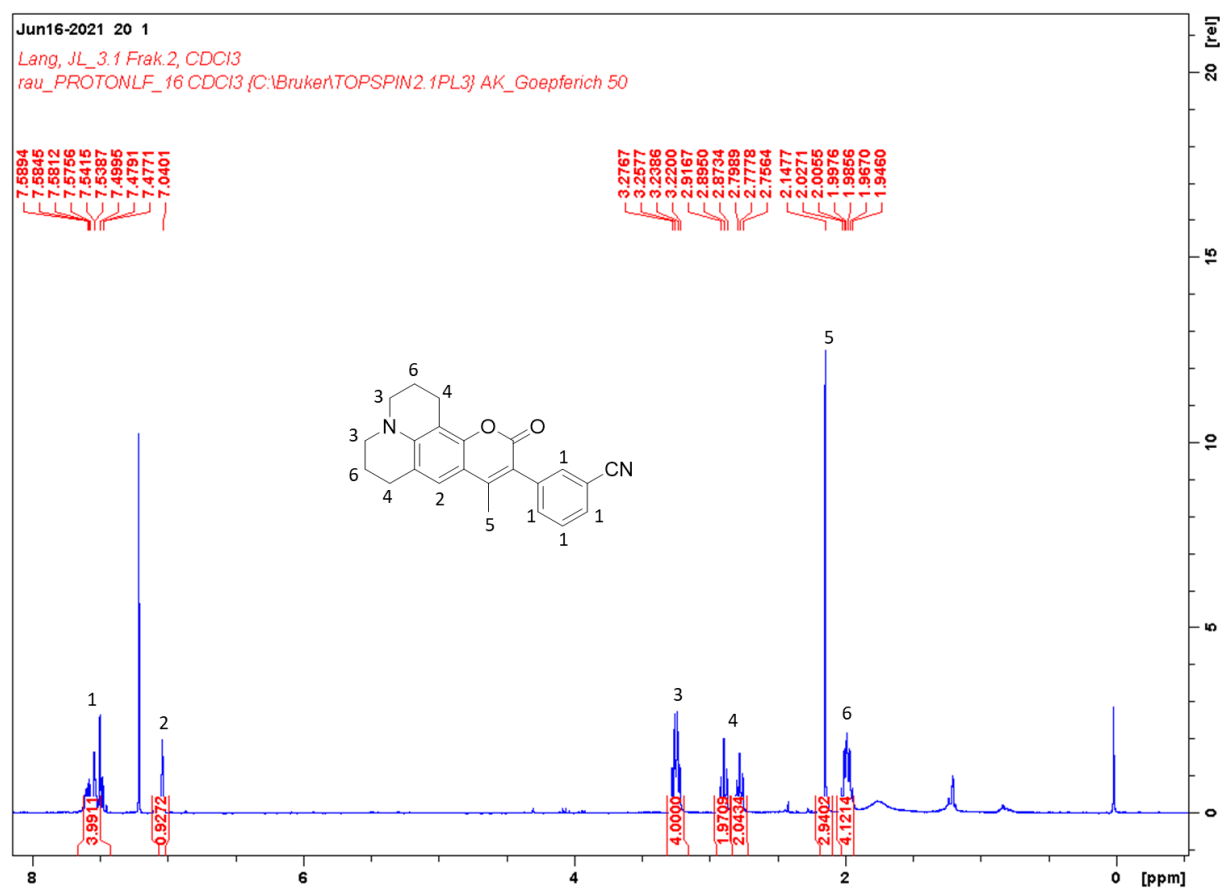
Supplementary Information – Switchable Fluorescence



SI Figure 1. ¹H NMR spectra of bromocoumarin **1** crude product recorded in CDCl₃ at 400 MHz.

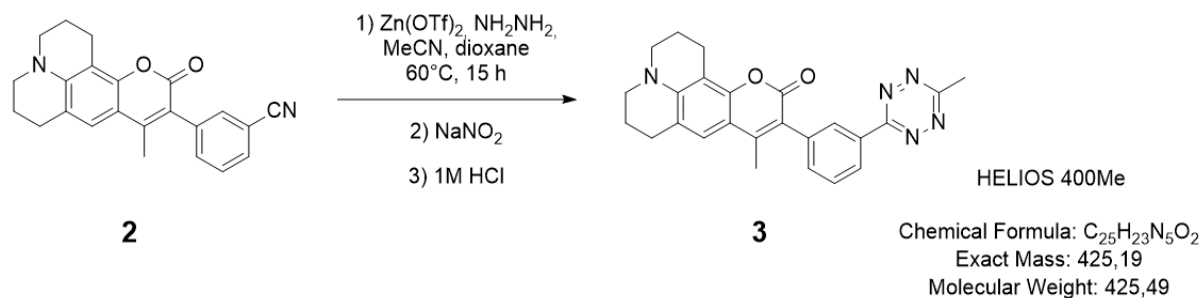
The conversion of coumarin 102 to bromocoumarin **1** with NBS appears to be complete. The signal of the proton, which is replaced by a bromine atom, at approx. 6.3 ppm disappears completely (see marked region in **SI Figure 1**). Since there are hardly any impurities in the NMR spectrum, column chromatography appears to be dispensable. The crude product still contains a residue of NBS, but this should probably not interfere with the next synthesis step.

Chapter 3 – Supplementary Information



SI Figure 2. ^1H NMR spectra of nitrile coumarin **2** recorded in CDCl_3 at 400 MHz.

Synthesis of methyltetrazine coumarin **3**



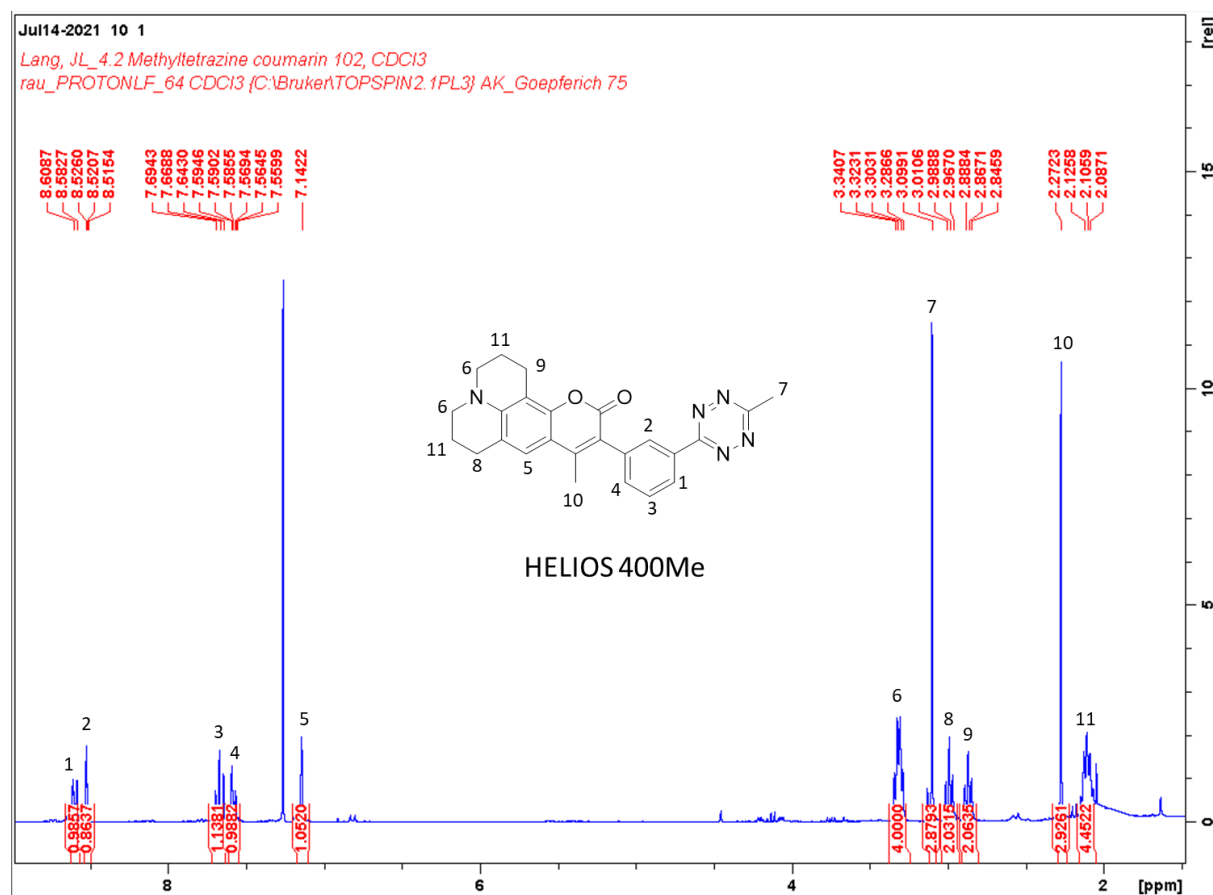
To nitrile coumarin **2** (34.9 mg, 98 μmol , 1 equiv.) zinc triflate (17.9 mg, 49 μmol , 0.5 equiv.) as Lewis acid catalyst, acetonitrile (51.4 μL , 0.98 mmol, 10 equiv.), hydrazine monohydrate (N_2H_4 64-65 %; 237

Supplementary Information – Switchable Fluorescence

μL , 4.89 mmol, 50 equiv.) and 120 μL dioxane were added under a stream of argon. The microwave reaction tube was sealed pressure-tight and stirred for 17 h at 60°C. It was then allowed to cool to room temperature and the septum was removed. To the reaction mixture sodium nitrite (135 mg, 1.95 mmol, 20 equiv.) in 5 mL of water was added followed by 1 M hydrochloric acid until pH = 3 was reached. The aqueous phase was extracted three times with 20 mL DCM. The combined organic extracts were dried with magnesium sulfate and concentrated using a rotary evaporator. The crude product was purified by column chromatography on silica gel (hexanes : ethyl acetate gradient, 5:1 to 3:1) to yield the fluorogenic methyltetrazine coumarin **3** HELIOS400Me (5 mg, 12 μmol , 12%) as an orange-brown solid.

$^1\text{H NMR}$ (CDCl_3): δ = 8.61–8.58 (d, 1H), 8.52 (s, 1H), 7.69–7.64 (t, 1H), 7.59–7.56 (d, 1H), 7.14 (s, 1H), 3.34–3.29 (q, 4H), 3.10 (s, 3H), 3.01–2.97 (t, 2H), 2.89–2.85 (t, 2H), 2.27 (s, 3H), 2.13–2.09 (m, 4H) ppm.

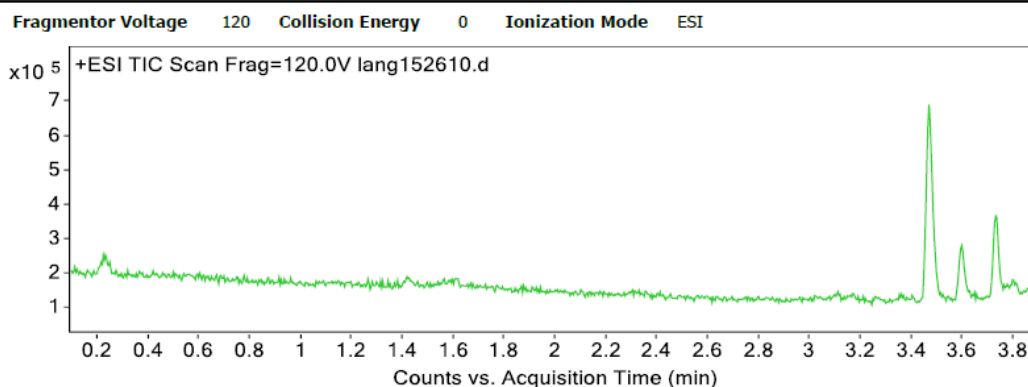
MS (ESI, m/z): Calculated for $([\text{C}_{25}\text{H}_{23}\text{N}_5\text{O}_2] + \text{H})^+$ ($[\text{M} + \text{H}]^+$): 426.1978, Found: 426.1927.



SI Figure 3. $^1\text{H NMR}$ spectra of methyltetrazine coumarin **3** recorded in CDCl_3 at 400 MHz.

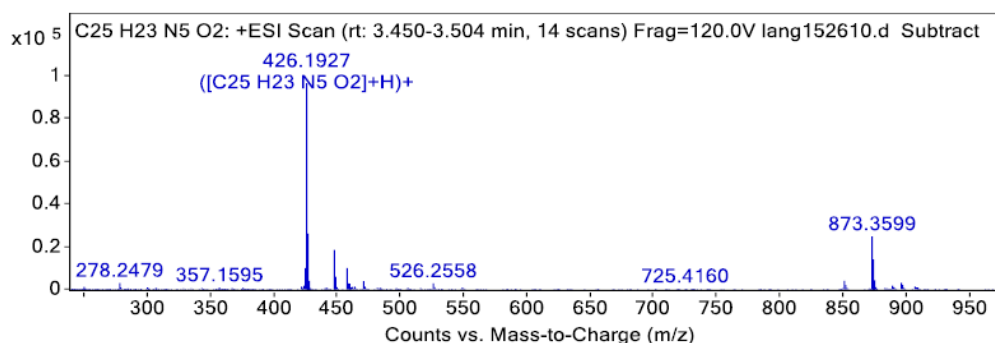
Chapter 3 – Supplementary Information

Chromatograms



Spectra

Spectrum Source Peak (1) in "+ EIC(426.1924) Scan" Fragmentor Voltage 120 Collision Energy 0 Ionization Mode ESI

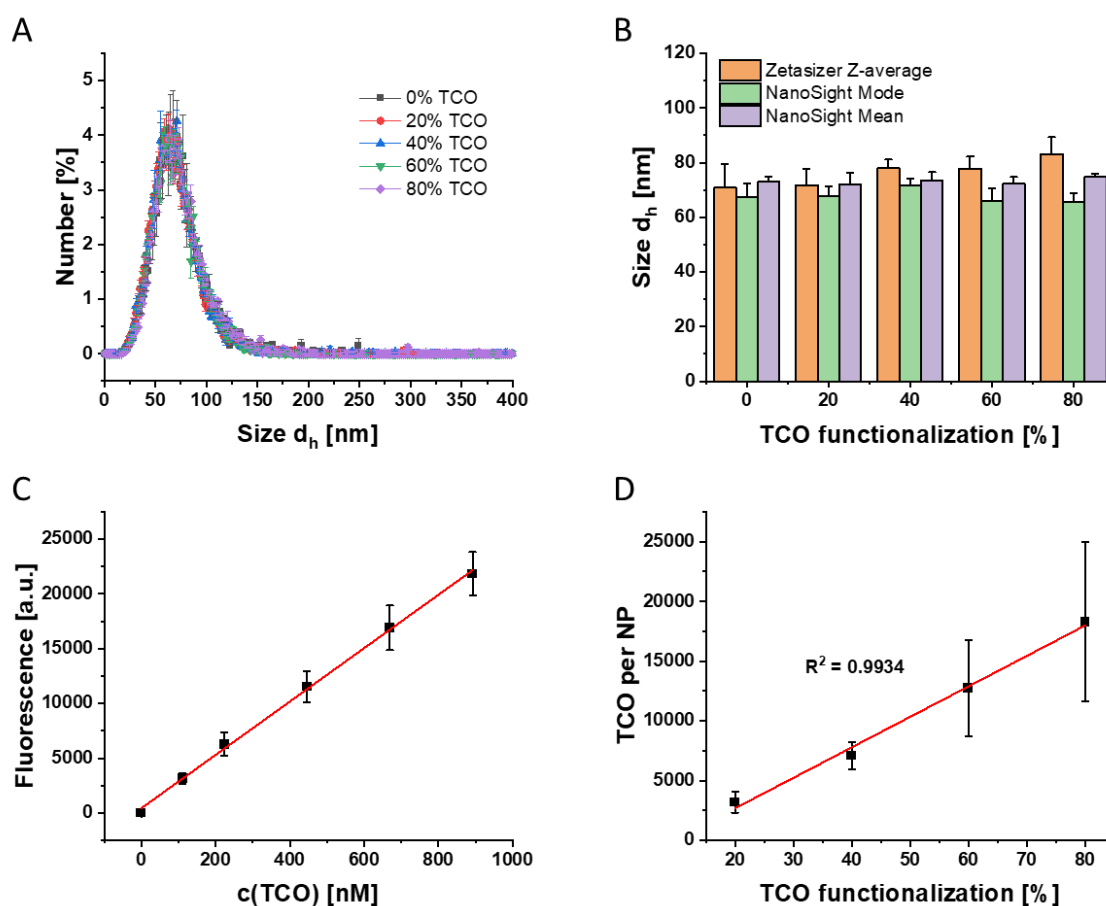


II. Characterization of the TCO functionalized NPs

In addition to determining NP size via dynamic light scattering (DLS) using the Zetasizer, nanoparticle tracking analysis (NTA) was employed as an orthogonal method. The size distribution determined using NTA can be found in **SI Figure 4 A**. The hydrodynamic diameters determined via NTA were generally slightly lower than those obtained by DLS. Notably, NTA did not detect the increase in particle size from approximately 70 nm to 80 nm with increasing TCO functionalization, making the discrepancy between DLS and NTA measurements more apparent at higher TCO functionalization levels (see **SI Figure 4 B**). The observed differences between DLS and NTA measurements may be attributed to the underlying principles of these techniques. DLS measures the intensity fluctuations of scattered light caused by the Brownian motion of particles and derives an intensity-weighted hydrodynamic diameter, which tends to be biased towards larger particles in polydisperse samples. In contrast, NTA tracks individual particles and provides a number-weighted size distribution. [2] It can be speculated that NP

Supplementary Information – Switchable Fluorescence

samples with a high degree of TCO functionalization contain a very small subpopulation of larger particles. In DLS measurements, this subpopulation could contribute to an increase in the observed hydrodynamic diameter due to the intensity-weighted nature of the technique. In contrast, while these larger particles are detected in NTA, their influence on the number-weighted size distribution is negligible, explaining the absence of an apparent size increase in the NTA results.



SI Figure 4. Characterization of the TCO functionalized NPs. (A) Size distribution of the NPs determined by NTA. (B) Comparison of the hydrodynamic diameters of the NPs determined by DLS on the zetasizer with those determined by NTA. (C) Calibration line to determine the TCO ligands per NP. (D) Linear fit between the TCO functionalization used and the TCO per NP found. Results in (A) and (D) are presented as mean \pm SD from one experiment ($n=3$) and results in (B) and (D) are presented as mean \pm SD from $N=4$ independent experiments.

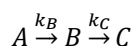
The calibration curve used to determine the number of TCO ligands per NP, based on free TCO, can be found in **SI Figure 4 C**. A good linear correlation was observed between the amount of TCO-functionalized PLA-PEG block copolymer used in the formulation and the number of TCO groups per NP after preparation (see **SI Figure 4 D**). However, it should be noted that dissolving the particles in DMSO allows for the quantification of all TCO units present. This approach does not provide information regarding the actual accessibility of TCO groups for the iEDDA reaction on the NP surface.

Chapter 3 – Supplementary Information

It is possible that the relatively hydrophobic TCO preferentially resides within the PEG brush of the NP, potentially affecting its availability for reaction.

III. Derivation of an equation to describe the fluorescence intensity

The reaction between the tetrazine-coumarin fluorophore and TCO was described by a pseudo-first-order reaction. The subsequent tautomerization of the resulting 4,5-dihydropyridazine intermediate to 1,4-dihydropyridazine could also be described as a first-order reaction. The further reaction to aromatic pyridazine, which forms through oxidation after prolonged times (typically several days), was not considered here, as the goal was to establish an equation for fitting the fluorescence intensity during the first minutes of the reaction. Therefore, the system can be approximated as a sequence of two consecutive first-order reactions:



Here, A represents the quenched tetrazine-coumarin fluorophore before the iEDDA reaction, B is the 4,5-dihydropyridazine intermediate, and C is the 1,4-dihydropyridazine formed after tautomerization. Using the rate constants k_B and k_C , the following rate equations can be established:

$$\frac{d[A]}{dt} = -k_B[A]$$

$$\frac{d[B]}{dt} = k_B[A] - k_C[B]$$

$$\frac{d[C]}{dt} = k_C[B]$$

Given that none of the products are present at the beginning, the initial conditions are $[B]_0 = [C]_0 = 0$. The solution for $[A]$ is straightforward:

$$[A] = [A]_0 \cdot e^{-k_B \cdot t}$$

For $[B]$, the differential equation takes the following form:

$$\frac{d[B]}{dt} + k_C[B] = k_B[A]_0 \cdot e^{-k_B \cdot t}$$

Solving this, we obtain:

Supplementary Information – Switchable Fluorescence

$$[B] = \frac{k_B[A]_0}{k_C - k_B} \cdot (e^{-k_B \cdot t} - e^{-k_C \cdot t})$$

[C] can be determined using the boundary conditions and mass balance $[C] = [A]_0 - [A] - [B]$.

$$[C] = [A]_0 \left(1 - e^{-k_B \cdot t} - \frac{k_B}{k_C - k_B} \cdot (e^{-k_B \cdot t} - e^{-k_C \cdot t}) \right)$$

The measured fluorescence intensity cannot be described solely by the presence of species *B*. Both *A* and *C* also contribute to the total fluorescence, albeit to a much lesser extent. To calculate the fluorescence intensity *F* at any given time, all species and their respective fluorescence *f* must be considered:

$$F = f_A \cdot [A] + f_B \cdot [B] + f_C \cdot [C]$$

Substituting for [A], [B], and [C], we get:

$$F = f_A \cdot [A]_0 \cdot e^{-k_B \cdot t} + f_B \cdot \frac{k_B[A]_0}{k_C - k_B} \cdot (e^{-k_B \cdot t} - e^{-k_C \cdot t}) + f_C \cdot [A]_0 \left(1 - e^{-k_B \cdot t} - \frac{k_B}{k_C - k_B} \cdot (e^{-k_B \cdot t} - e^{-k_C \cdot t}) \right)$$

At the beginning of the measurement, only species *A* is present. Therefore, the initial fluorescence is:

$$F_0 = f_A \cdot [A]_0 \quad \rightarrow \quad f_A = \frac{F_0}{[A]_0}$$

At very long times, all of species *A* should have reacted to form species *C*, giving the final fluorescence as:

$$F_\infty = f_C \cdot [A]_0 \quad \rightarrow \quad f_C = \frac{F_\infty}{[A]_0}$$

Thus, the fluorescence intensity can be expressed as:

$$F = F_0 \cdot e^{-k_B \cdot t} + f_B \cdot \frac{k_B[A]_0}{k_C - k_B} \cdot (e^{-k_B \cdot t} - e^{-k_C \cdot t}) + F_\infty \cdot \left(1 - e^{-k_B \cdot t} - \frac{k_B}{k_C - k_B} \cdot (e^{-k_B \cdot t} - e^{-k_C \cdot t}) \right)$$

By defining $f_B \cdot [A]_0 = F_B$ and rearranging, the equation becomes:

$$F = F_\infty + (F_0 - F_\infty) \cdot e^{-k_B \cdot t} + (F_B - F_\infty) \cdot \frac{k_B}{k_C - k_B} \cdot (e^{-k_B \cdot t} - e^{-k_C \cdot t})$$

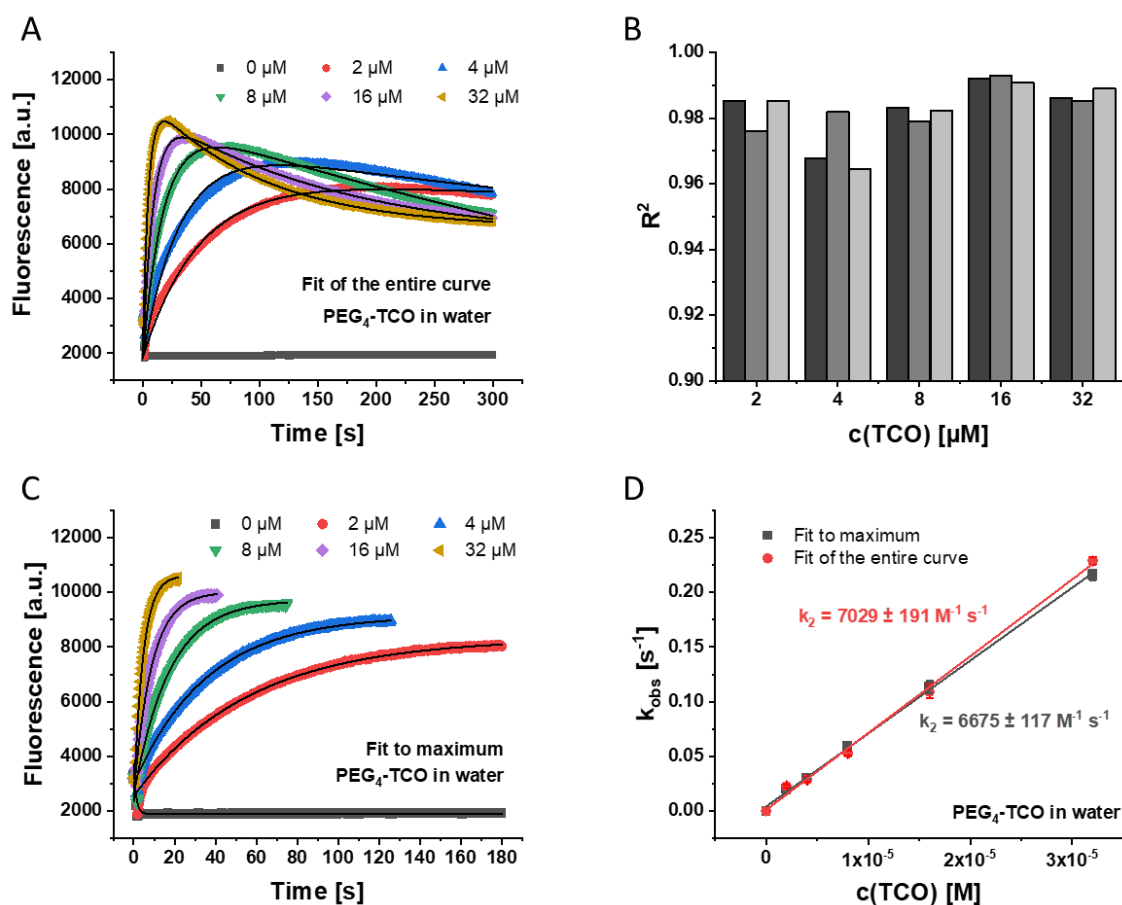
This equation was used to fit the measured fluorescence intensity over time. F_0 was determined from measurements without TCO addition, leaving the parameters F_B , F_∞ , k_B and k_C for fitting. k_B represents the pseudo-first-order rate constant of the iEDDA reaction, which was subsequently plotted against TCO concentration to determine the second-order rate constant.

IV. Fitting of the fluorescence intensity curves

The derived equation described the experimental data well (see **SI Figure 5 A**), with an R^2 value consistently above 0.96 for all fits performed (see **SI Figure 5 B**), indicating a high degree of correlation between the model and the experimental observations. Alternatively, the fluorescence intensity curves could be fitted only up to the maximum (see **SI Figure 5 C**). The subsequent decline in fluorescence intensity is simply truncated. For this approach, an equation for exponential growth to saturation can be used, which essentially corresponds to the first part of the previously derived equation.

$$F = F_{max} + (F_0 - F_{max}) \cdot e^{-k \cdot t}$$

As shown in **SI Figure 5 D**, the fits for the full curve and for the truncated curve up to the maximum yielded nearly identical pseudo first-order rate constants. When plotted against TCO concentration, the linear fit showed virtually no difference between the two approaches. Therefore, it is possible to simplify the fitting procedure by only fitting up to the maximum, provided the goal is not to describe the entire fluorescence intensity curve, but rather to determine the rate constant for the first reaction step.



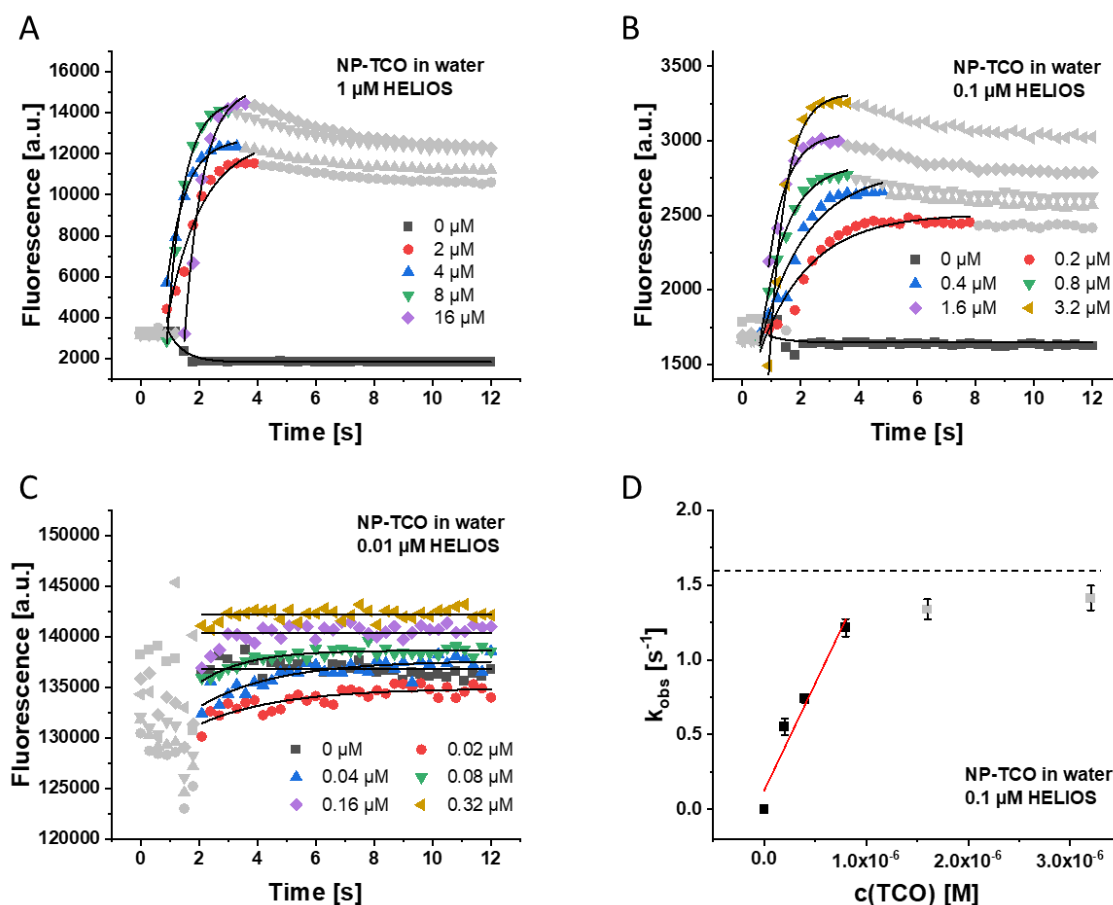
SI Figure 5. Considerations for fitting the fluorescence intensity curves. (A) Fit of the entire curves with the derived equation. (B) Coefficient of determination for the fits with the derived equation. (C) Curves fitted with a function for exponential growth to saturation only up to the maximum in the observed fluorescence intensity. The

Supplementary Information – Switchable Fluorescence

rest of the curve is truncated. (D) Plot of pseudo first order rate constants vs. TCO concentration. Results in (D) are presented as mean \pm SD ($n = 3$).

V. Slowing down the iEDDA reaction on the NP by diluting the reactants

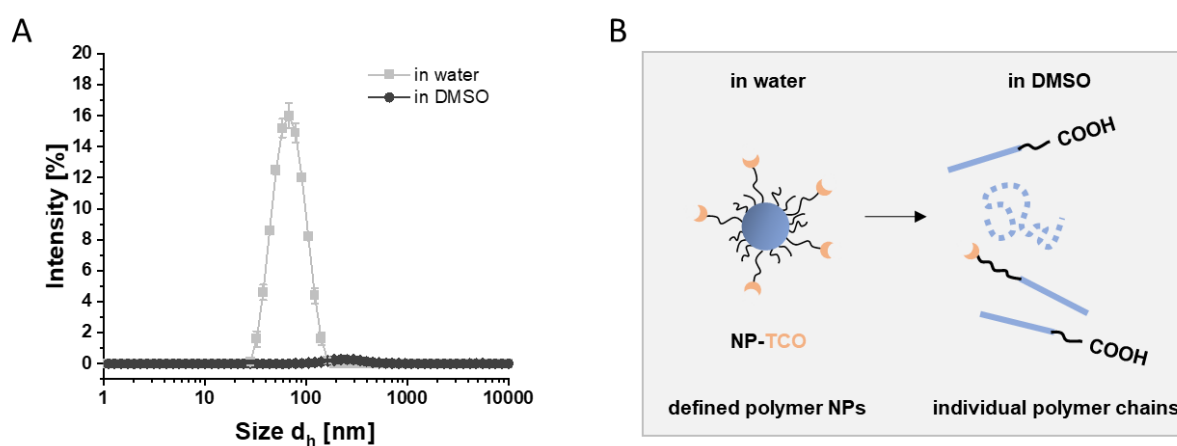
Since the iEDDA reaction on the NP was considerably faster than free in solution with PEG₄-TCO, it was necessary to evaluate a suitable concentration at which the second order rate constant of the reaction could be determined (see SI Figure 6).



SI Figure 6. iEDDA reaction between HELIOS400Me and NP-TCO at different HELIOS concentrations. Reaction of 1 μM HELIOS (A), 0.1 μM HELIOS (B), and 0.01 μM HELIOS (C) with various TCO excesses. (D) Plot of the pseudo-first-order rate constant, determined from the fit of the data with 0.1 μM HELIOS, against the TCO concentration to determine the second-order rate constant. Data not considered in the fits are shaded in gray. Results in (D) are presented as mean \pm SD ($n = 3$).

VI. Disintegration of the polymer NPs in DMSO

To illustrate the dissolution of the polymer NPs in DMSO, 50 μL of NP sample was diluted with 150 μL of DMSO, as in the experiment for the determination of the second order rate constant in DMSO. The size distribution of the NPs was measured using DLS on the Zetasizer. The intensity was weighted with the derived count rate to take into account that only a small number of scattering species were present in DMSO.

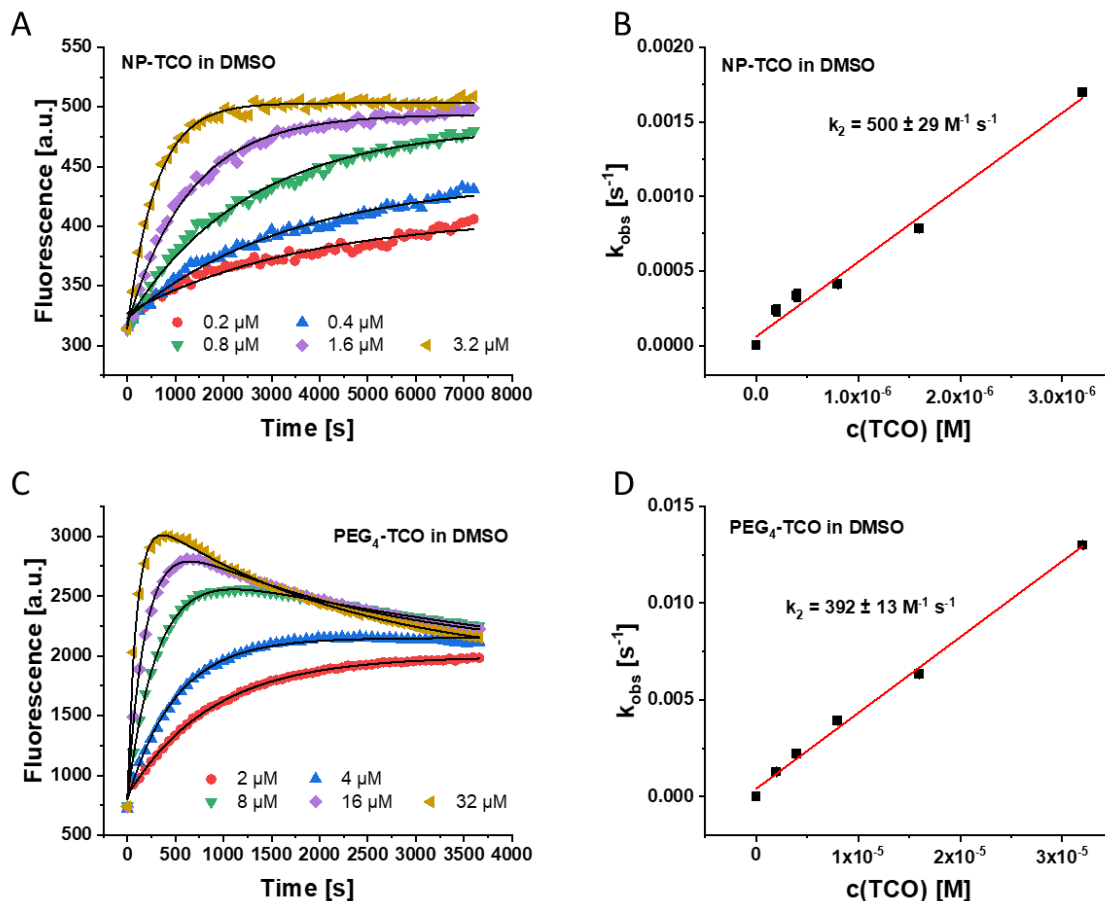


SI Figure 7. Dissolution of the polymer NPs in DMSO. (A) Size distribution of NP-TCO in water and in DMSO measured on the Zetasizer. (B) Schematic illustrating the disintegration of polymer NPs in DMSO to individual dissolved polymer chains. Results in (A) are presented as mean \pm SD ($n = 3$).

As expected, defined particles were observed in water (see **SI Figure 7 A**). These had a hydrodynamic diameter of approx. 64 nm. In DMSO, however, the derived count rate of the Zetasizer was very low (approx. 400 instead of 22000 kpcs in water), which confirmed that hardly any scattering species were present. Only minor aggregates with a hydrodynamic diameter around 230 nm could be detected. The defined polymer NPs disintegrated in DMSO, and individually dissolved polymer chains were present (see **SI Figure 7 B**).

VII. Kinetics of the iEDDA reaction in DMSO

The kinetics of the iEDDA reaction of polymer NPs dissolved in DMSO as well as free PEG₄-TCO in DMSO were observed. Since the reactions proceed significantly slower than in water, the observation time was extended (see SI Figure 8 A+C). Plotting the pseudo first order rate constants against the TCO concentration showed a good linear relationship in both cases (see SI Figure 8 B+D).



SI Figure 8. iEDDA reaction of HELIOS400Me with NP-TCO and PEG₄-TCO in DMSO. (A) Fluorescence intensity vs. time for the iEDDA reaction between HELIOS400Me and NP-TCO dissolved in DMSO. (B) Pseudo first order rate constants plotted against the TCO concentration on the dissolved NPs. (C) Fluorescence intensity vs. time for the iEDDA reaction between HELIOS400Me and PEG₄-TCO in DMSO. (D) Pseudo first order rate constants plotted against PEG₄-TCO concentration. Results in (B) and (D) are presented as mean \pm SD ($n = 3$).

VIII. Hansen solubility parameters for the tetrazine coumarin fluorophore HELIOS400Me

The Hansen Solubility Parameters (HSP) were developed to estimate the compatibility (solubility, miscibility, etc.) of molecules. [3] They can therefore also help in describing the compatibility of the

Chapter 3 – Supplementary Information

tetrazine coumarin fluorophore with the polymer components of the NP or with simple solvents. Hansen took into account in his concept that intermolecular interactions result from different parameters. Thus, three distinct solubility parameters were introduced to represent each type of interaction: the dispersion parameter δ_D reflecting non-polar, van der Waals interactions between molecules; the polar parameter δ_P representing dipole-dipole interactions; and the hydrogen bonding parameter δ_H accounting for hydrogen bonding interactions. [3] The three parameters can serve as coordinates for a point in a 3D space. The nearer two molecules are in this three-dimensional space also known as the Hansen space, the more likely they are to dissolve into each other.

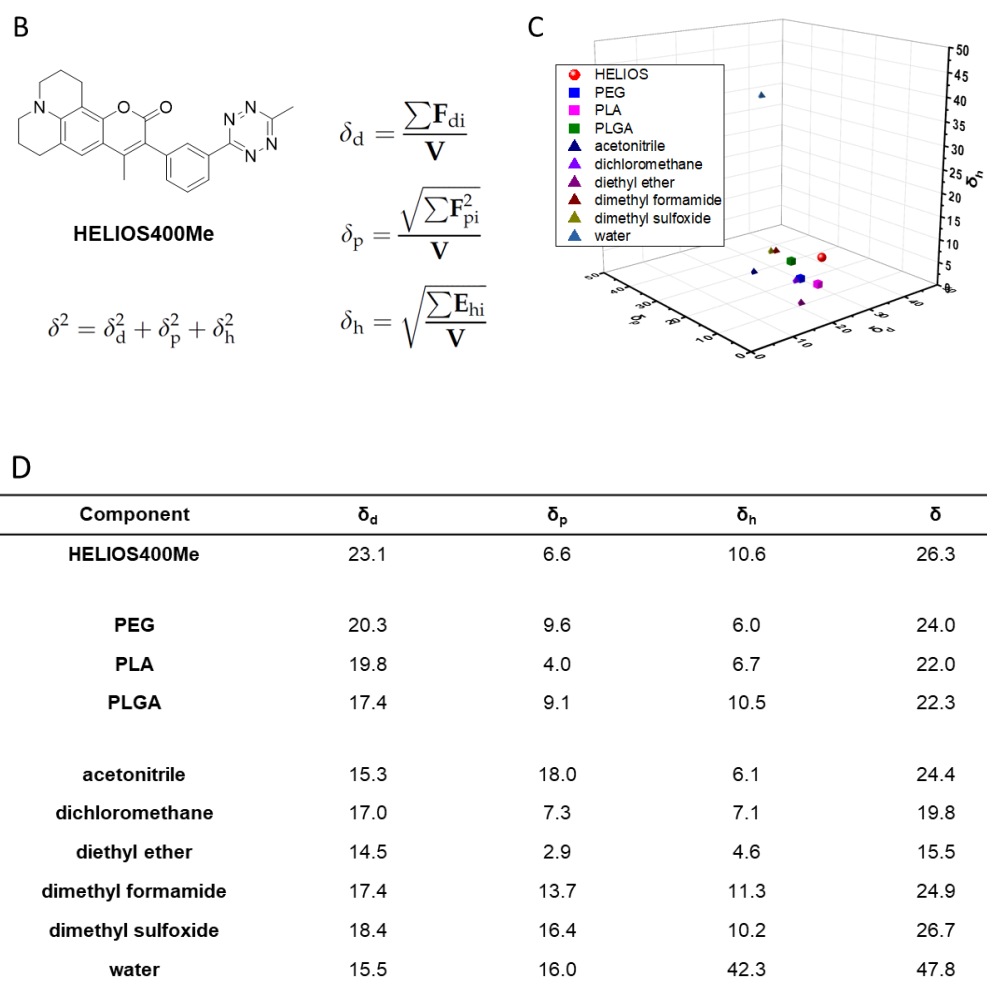
$$D = \sqrt{4(\delta_{D2} - \delta_{D1})^2 + (\delta_{P2} - \delta_{P1})^2 + (\delta_{H2} - \delta_{H1})^2}$$

The distance D between two molecules (e.g., solute and solvent) can be calculated using the presented formula, where the subscripts 1 and 2 refer to the two different molecules. The prediction of Hansen solubility parameters for HELIOS400Me was performed using group contributions according to the Hoftyzer - Van Krevelen method [4] and the molar volume was estimated via group contributions according to the method reported by Fedors. [5] The HSP for standard solvents and the polymer components of the NP can be found in the literature. [3, 6] The segments of the PLA-PEG block copolymer were considered separately.

A

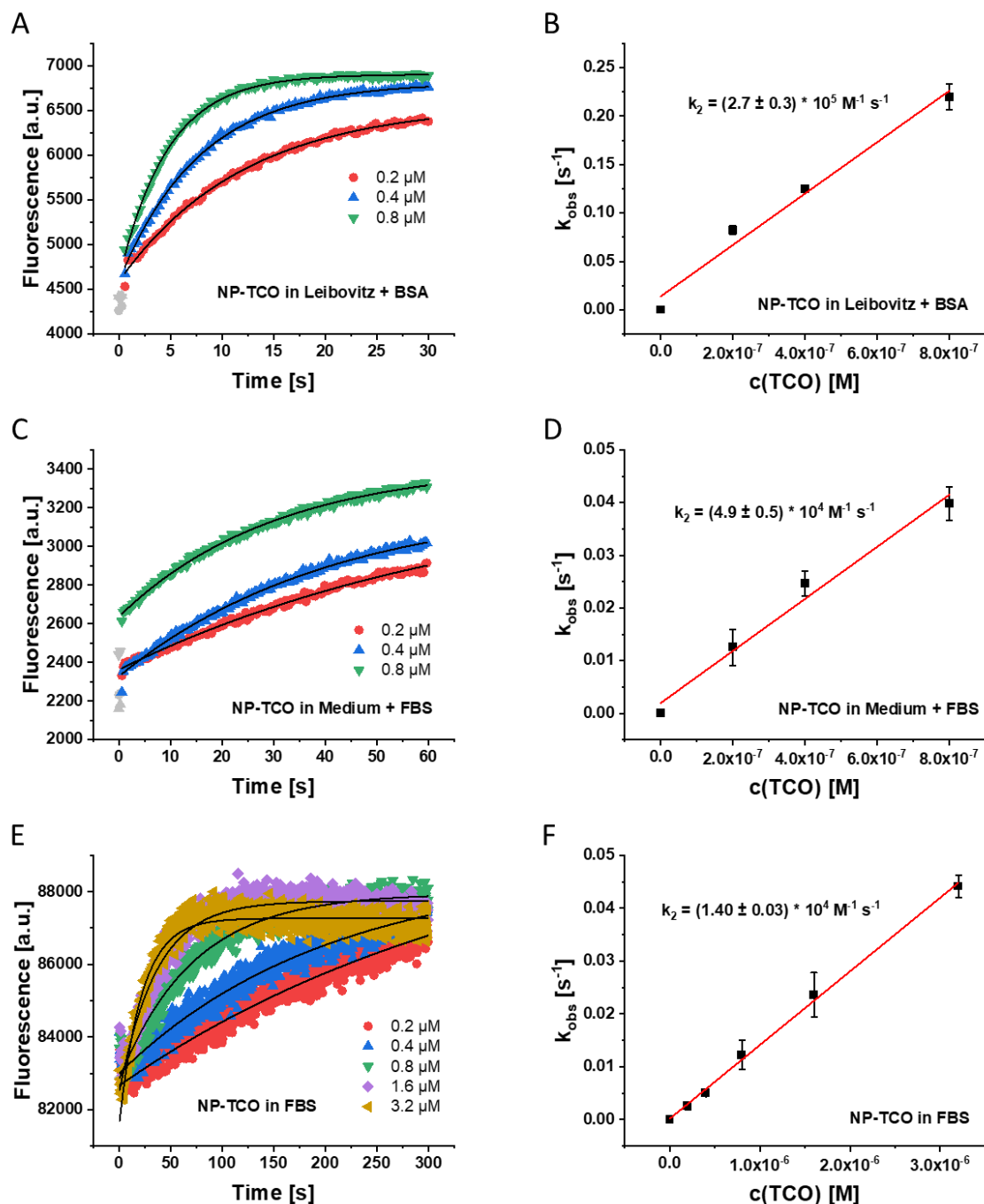
Structural group	Hoftyzer–Van Krevelen method			Fedors method
	F_{di}	F_{pi}^2	E_{ni}	V [cm ³ /mol]
CH ₃	420	0	0	33.5
2 =C<	140	0	0	-11
4 =N-	80	2560000	20000	20
Ring closure	190	0	0	16
Phenylene (o, m, p)	1270	12100	0	52.4
2 =C<	140	0	0	-11
CH ₃	420	0	0	33.5
-COO-	390	240100	7000	18
Ring closure	190	0	0	16
Phenyl (pentasubstituted)	1270	12100	0	-4.6
>N-	20	640000	5000	-9
6 -CH ₂ -	1620	0	0	96.6
2 Ring closure	380	0	0	32
Sum	6530	3464300	32000	282.4

Supplementary Information – Switchable Fluorescence



SI Figure 9. Hansen solubility parameters for the tetrazine coumarin fluorophore HELIOS400Me. (A) Prediction of Hansen solubility parameters for HELIOS400Me using group contributions according to the Hoftyzer - Van Krevelen method. [4] Listing of the individual contributions of the structural groups. Estimation of the molar volume of HELIOS400Me via group contributions according to the method reported by Fedors. [5] (B) Structural formula of HELIOS400Me and key equations for determining the solubility parameters via group contributions. [4] (C) Solubility parameters plotted in 3D Hansen space. (D) Table with the calculated solubility parameters for the tetrazine coumarin fluorophore as well as literature values for the NP-forming polymers (according to Maslanka Figueroa, Fleischmann et al. [6]) and standard solvents (according to Hansen [3]).

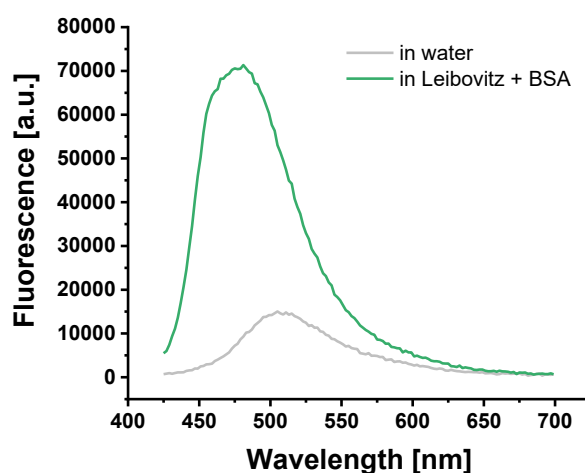
IX. Kinetics of the iEDDA reaction between HELIOS400Me and NP-TCO in different biological media



SI Figure 10. Kinetics of the iEDDA reaction between HELIOS400Me and NP-TCO in different biological media. Fluorescence intensity vs. time for the iEDDA reaction in Leibovitz's L-15 medium with 0.1% BSA (A), in RPMI 1640 cell culture medium with 10% FBS supplement (C) and in pure FBS (E). Pseudo first order rate constants plotted against the TCO concentration for the iEDDA reaction in Leibovitz's L-15 medium with 0.1% BSA (B), in RPMI 1640 cell culture medium with 10% FBS supplement (D) and in pure FBS (F). Results in (B), (D) and (F) are presented as mean \pm SD ($n = 3$).

X. Adsorption of the tetrazine coumarin fluorophore to hydrophobic domains of BSA

To illustrate the adsorption of the hydrophobic fluorogenic probe to BSA, fluorescence emission spectra were recorded in water and Leibovitz's L-15 medium with 0.1% BSA supplement. Initially, 4 μL of a 5 mM tetrazine-coumarin fluorophore solution (HELIOS400Me) in DMSO was added to a white 96-well plate. For the measurement in water, 196 μL of Millipore water was added. For the measurement in Leibovitz medium with 0.1% BSA, 46 μL of Millipore water and 150 μL of Leibovitz's L-15 medium with 0.1% BSA supplement were added. Emission spectra were recorded at an excitation wavelength of 400 nm using a Synergy Neo2 plate reader.

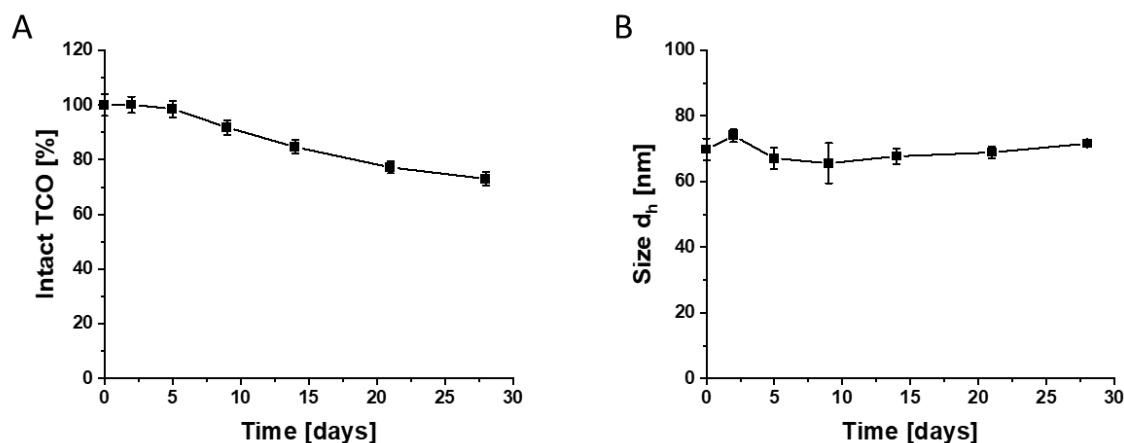


SI Figure 11. Fluorescence emission spectra of HELIOS400Me indicating entry to the hydrophobic domains of BSA. Comparison of the emission spectrum in water and in Leibovitz's L-15 medium with 0.1% BSA supplement.

In water, the emission maximum was observed at 505 nm with relatively weak intensity, whereas in Leibovitz's L-15 medium supplemented with 0.1% BSA, the emission maximum shifted to 481 nm, accompanied by significantly higher fluorescence intensity (see **SI Figure 11**). In the presence of BSA, a pronounced blue shift (approximately 24 nm) and an enhancement of fluorescence intensity were observed (approximately 4.75-fold). A blue shift is generally characteristic of coumarin fluorophores when exposed to less polar environments. Typically, such environments also result in increased fluorescence intensity. [7] These findings suggest that the tetrazine-functionalized coumarin fluorophore, similar to other coumarin dyes, incorporates into the hydrophobic domains of BSA. [8] Consequently, the HELIOS fluorophore resides in a less polar microenvironment, which explains the observed spectral changes. It should be kept in mind that the HELIOS fluorophore, when embedded in the hydrophobic regions of BSA, is not available for an iEDDA reaction.

XI. TCO stability on NP-TCO during storage in the refrigerator

The stability of TCO on the particles during storage in the refrigerator was determined using the same approach as for incubation at 37°C. The 60% TCO-functionalized NPs were prepared according to the general protocol. 240 μL of the 4 mg/mL NP solution were diluted with 4560 μL of water and stored in the refrigerator (4°C). At specific time points, 160 μL of the cooled NP sample were added via the plate reader's pump system to 40 μL of the 50 μM tetrazine coumarin fluorophore solution in a white 96-well plate. The fluorescence intensity (excitation 380 nm, emission 485 nm) was measured on a FLUOstar Omega microplate reader (total TCO concentration approx. 1 μM ; tetrazine coumarin fluorophore concentration 10 μM). The fluorescence intensity immediately after the addition of the diluted NP sample served as an indicator of the intact TCO. The corresponding blank value for the fluorophore in water without NP-TCO was subtracted. The amount of intact trans-cyclooctene after various incubation times was determined by dividing the fluorescence intensity at each respective time point by the maximum fluorescence observed at the beginning. Additionally, at each time point, the NP sample was also measured with the NanoSight NS300.



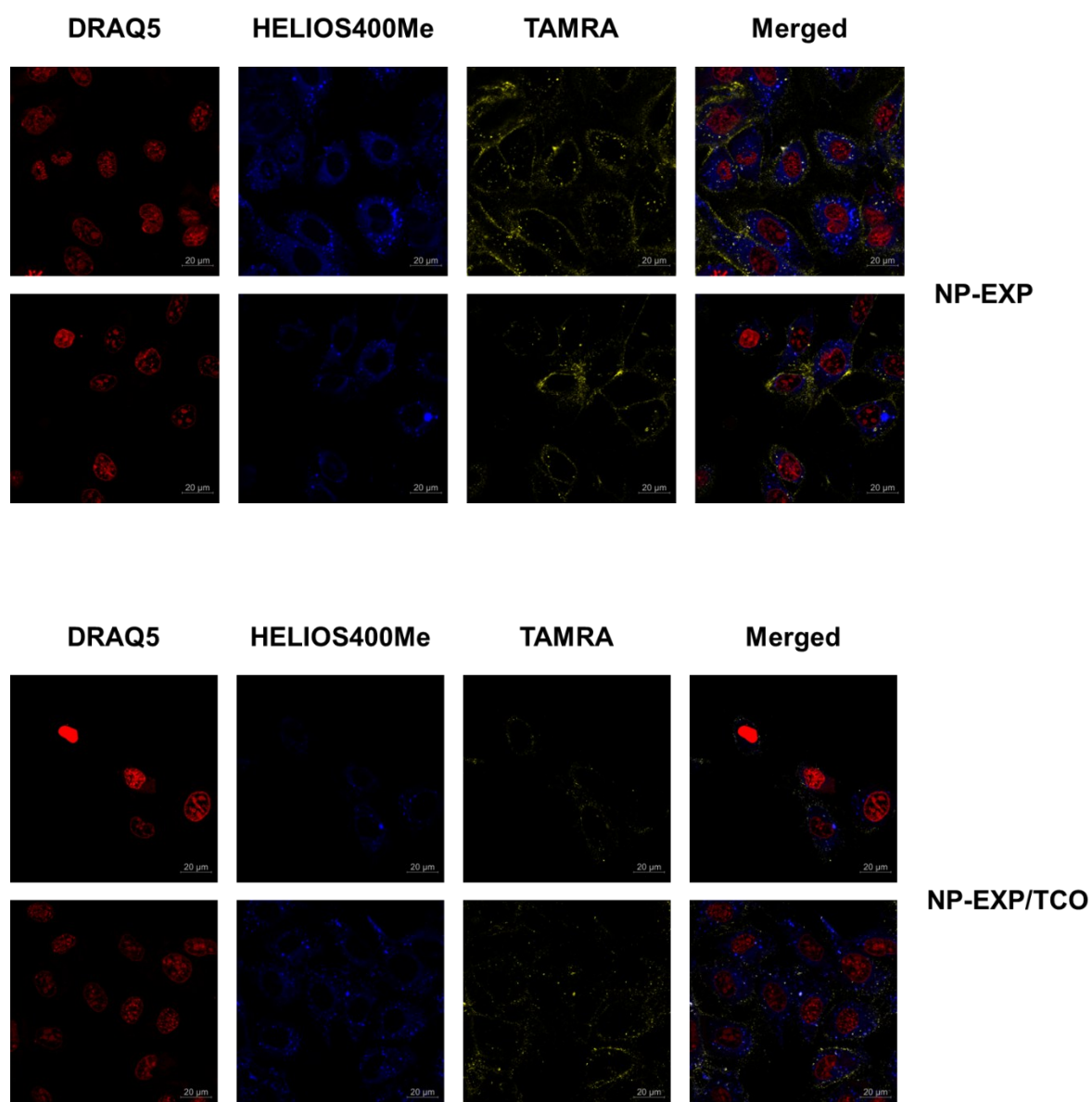
SI Figure 12. Stability of NP-TCO during storage in the refrigerator. (A) Intact TCO on the NP vs. storage time. (B) Hydrodynamic diameter of NPs vs. storage time. Results are presented as mean \pm SD ($n = 3$).

The TCO on the NPs degraded slightly during storage in the refrigerator. After one month, approximately 75% of the TCO remained intact (see **SI Figure 12 A**). During the first week, the decrease in intact TCO was negligible. Thus, NP-TCO can be used in experiments for up to one week without any concern for reduced reactivity due to inactivated TCO. The hydrodynamic diameter of the NPs,

Supplementary Information – Switchable Fluorescence

approximately 70 nm, remained stable throughout the observation period, with no aggregation detected during storage (see SI Figure 12 B). The colloidal stability of the NP-TCO was maintained.

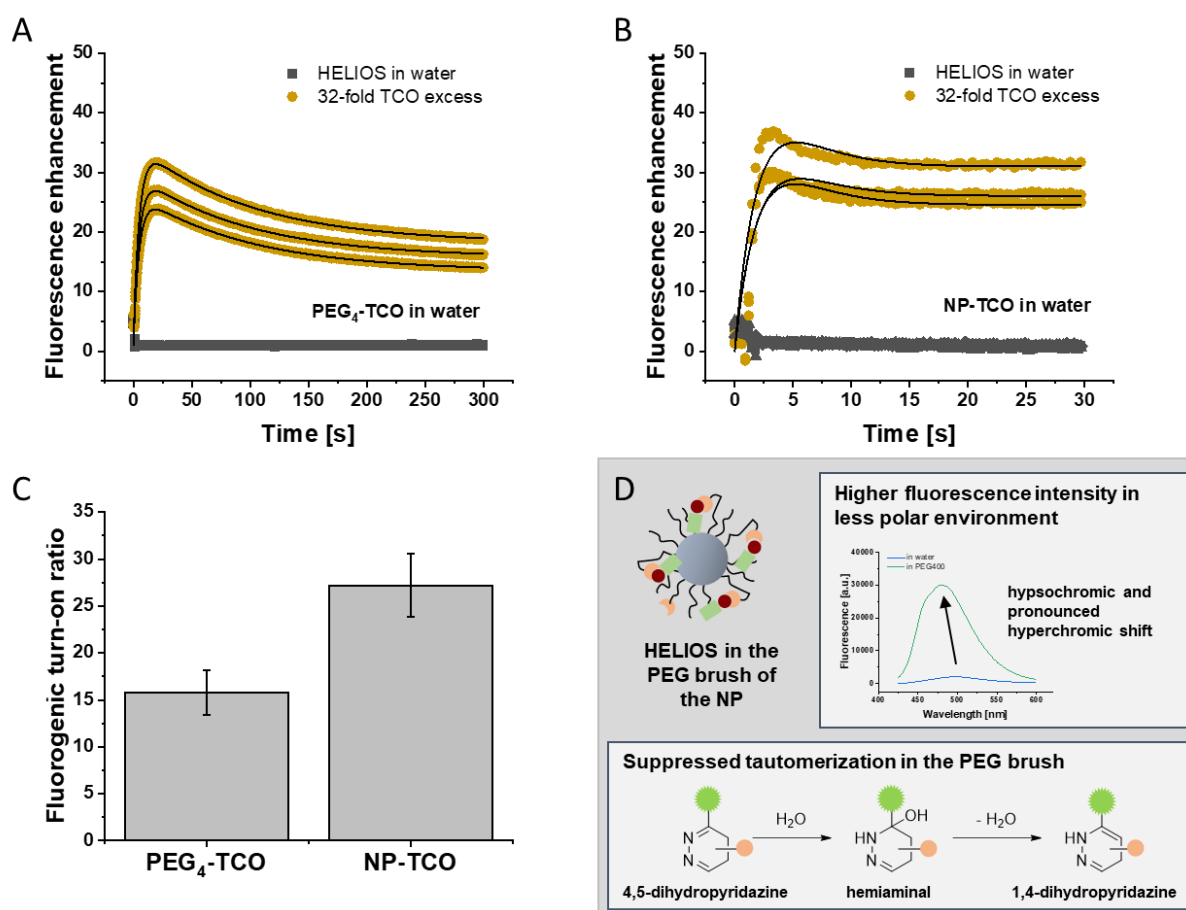
XII. Further CLSM images for NP localization and iEDDA reaction with HELIOS



SI Figure 13. NP localization on target cells and iEDDA reaction with HELIOS analyzed using CLSM. TAMRA labeled NPs are shown in yellow, HELIOS400Me in blue and nuclear staining by DRAQ5 in red. Image sections are shown here in addition to the Z-stacks in the main part of the chapter.

XIII. Fluorogenic turn-on ratio of HELIOS

To determine the fluorogenic turn-on ratio of the HELIOS fluorophore, data from the experiments of the iEDDA reaction kinetics were analyzed. The blank value for pure water was recorded and subtracted from all measurements, resulting in the exclusive HELIOS fluorescence. The fluorescence enhancement was calculated based on the ratio of the fluorescence intensity of the HELIOS probe following the addition of excess TCO to the background fluorescence intensity of the quenched HELIOS fluorophore. The data were normalized to set the mean background fluorescence of the quenched HELIOS probe to one, as shown in SI Figure 14 A+B for three measurements. The fluorogenic turn-on ratio was determined from the fluorescence enhancement observed at the plateau, corresponding to the formation of the 1,4-dihydropyridazine product after the iEDDA reaction and subsequent tautomerization. The fitted values from the three experimental runs were averaged, and the standard deviation was calculated (see SI Figure 14 C).



SI Figure 14. Fluorogenic turn-on ratio of HELIOS. Fluorescence enhancement through the iEDDA reaction of HELIOS with free PEG₄-TCO (A) and on NP-TCO (B) in water. (C) Overview of the fluorogenic turn-on ratios after complete iEDDA reaction. (D) Illustration of possible reasons for the higher turn-on ratio on the NP. Results in (C) are presented as mean ± SD (n = 3).

Supplementary Information – Switchable Fluorescence

For PEG₄-TCO in water, a fluorogenic turn-on ratio of approximately 16 was determined, whereas the turn-on ratio for the iEDDA reaction with NP-TCO was around 27. The higher turn-on ratio observed for the NP may be attributed to the fluorophore being situated in a more hydrophobic environment within the PEG brush of the NP. Less polar environments are generally known to enhance the emission intensity of coumarin fluorophores. [7] This could also be well reproduced here for the unquenched HELIOS400Me fluorophore, with a hypsochromic and pronounced hyperchromic shift when switching from water to PEG400 as solvent (see **SI Figure 14 D**). Furthermore, it is evident that the fluorescence decrease due to tautomerization of the 4,5- to the 1,4-dihydropyridazine is less pronounced in the case of the NP. This reduced tautomerization might also be explained by the embedding of the fluorophore within the PEG brush, which could hinder the tautomerization pathway via the intermediate hemiaminal, proceeding through the addition and elimination of a water molecule (see **SI Figure 14 D**). [9] Overall, it should be noted that the turn-on ratios determined in this study were several orders of magnitude lower than the value of 4000 reported by Meimetis, Carlson et al. for this fluorophore. [1] Meimetis, Carlson et al. utilized a fresh aliquot of the fluorophore collected from an analytical HPLC elution. Unfortunately, collecting eluates from analytical HPLC runs before every experiment is highly labor-intensive and does not allow for higher concentrations of the HELIOS fluorophore. Instead, in our approach, the HELIOS fluorophore was purified using preparative HPLC, followed by the preparation of a 5 mM stock solution in DMSO, aliquoted, and stored in a freezer until use. Given the good stability of the methyl-substituted tetrazine, this approach should still provide sufficiently pure material for the experiments. However, even minor fluorescent impurities, which Meimetis, Carlson et al. could reliably remove through HPLC purification prior to their experiments, can lead to significantly lower observable turn-on ratios. Whether this can fully account for the large discrepancy between the turn-on ratios observed in this study and those reported by Meimetis, Carlson et al. remains unclear. Additionally, Meimetis, Carlson et al. likely observed higher fluorescence enhancement due to the absence of fluorescence quenching through tautomerization of the dihydropyridazine, which, in their case, intriguingly did not occur.

Chapter 3 – Supplementary Information

References

1. Meimetis LG, Carlson JCT, Giedt RJ, Kohler RH, Weissleder R (2014) Ultrafluorogenic coumarin-tetrazine probes for real-time biological imaging. *Angewandte Chemie (International ed. in English)* 53(29), 7531–7534. 10.1002/anie.201403890.
2. Filipe V, Hawe A, Jiskoot W (2010) Critical evaluation of Nanoparticle Tracking Analysis (NTA) by NanoSight for the measurement of nanoparticles and protein aggregates. *Pharm Res* 27(5), 796–810. 10.1007/s11095-010-0073-2.
3. Hansen CM (2007) Hansen solubility parameters: A user's handbook, 2nd edn. Boca Raton: Taylor & Francis.
4. Krevelen DW (2009) Properties of Polymers: Their Correlation with Chemical Structure; their Numerical Estimation and Prediction from Additive Group Contributions, 4th edn. Oxford: Elsevier Science & Technology.
5. Fedors RF (1974) A method for estimating both the solubility parameters and molar volumes of liquids. *Polymer Engineering & Sci* 14(2), 147–154. 10.1002/pen.760140211.
6. Maslanka Figueroa S, Fleischmann D, Beck S, Goepferich A (2020) Thermodynamic, Spatial and Methodological Considerations for the Manufacturing of Therapeutic Polymer Nanoparticles. *Pharm Res* 37(3), 59. 10.1007/s11095-020-2783-4.
7. Moreira LM, Melo MM de, Martins PA, Lyon JP, Romani AP, Codognoto L, Santos SCd, Oliveira HPM de (2014) Photophysical Properties of Coumarin Compounds in Neat and Binary Solvent Mixtures: Evaluation and Correlation Between Solvatochromism and Solvent Polarity Parameters. *Journal of the Brazilian Chemical Society*. 10.5935/0103-5053.20140051.
8. Bhattacharya B, Nakka S, Guruprasad L, Samanta A (2009) Interaction of bovine serum albumin with dipolar molecules: fluorescence and molecular docking studies. *The journal of physical chemistry. B* 113(7), 2143–2150. 10.1021/jp808611b.
9. Siegl SJ, Galeta J, Dzajak R, Vázquez A, Del Río-Villanueva M, Dračinský M, Vrabel M (2019) An Extended Approach for the Development of Fluorogenic trans-Cyclooctene-Tetrazine Cycloadditions. *Chembiochem a European journal of chemical biology* 20(7), 886–890. 10.1002/cbic.201800711.

Supplementary Information – Switchable Fluorescence

Chapter 3 – Supplementary Information

Chapter 4

Towards a Switchable Nanoparticle Behavior Using Inverse Electron-Demand Diels-Alder Chemistry and Ectoenzyme-Based Ligand Activation

Published in *European Journal of Pharmaceutical Sciences*

2025, 204, 106944

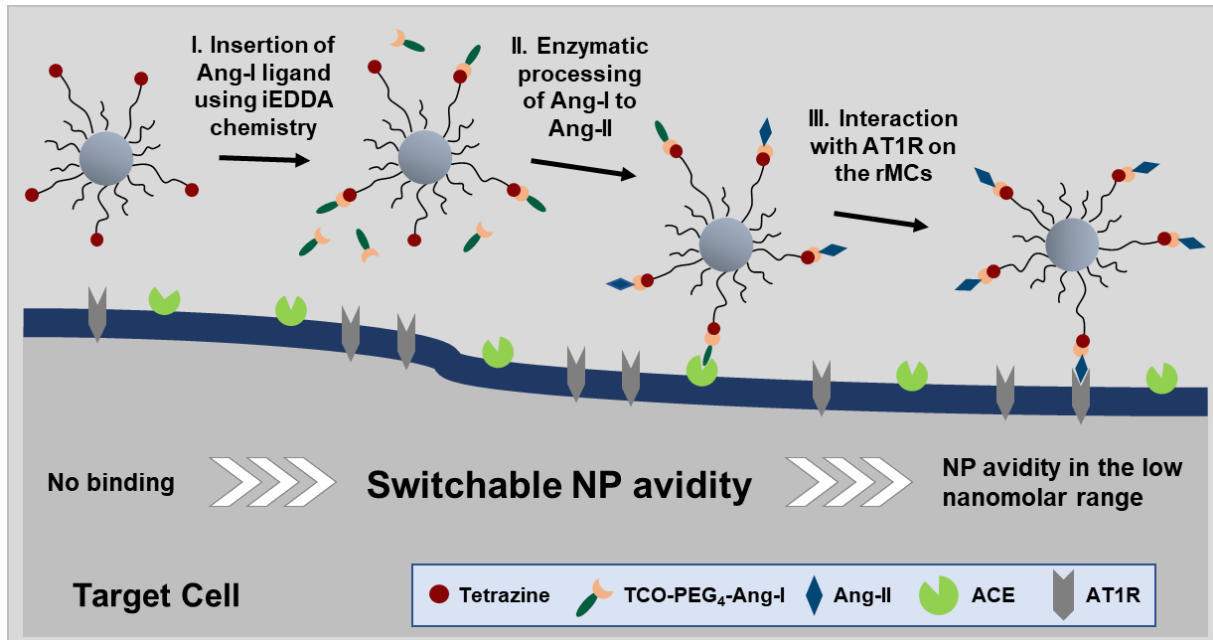
This chapter was published as: Lang, Johannes; Schorr, Kathrin; Goepferich, Achim. Towards a Switchable Nanoparticle Behavior Using Inverse Electron-demand Diels-Alder Chemistry and Ectoenzyme-based Ligand Activation. *European Journal of Pharmaceutical Sciences* 2025, 204, 106944. DOI: 10.1016/j.ejps.2024.106944. Published Online: Oct. 24, 2024.

Chapter 4

Abstract

Nanoparticles (NPs) as drug delivery platforms encounter numerous obstacles on their journey from administration to the target site. Often, diametrically opposing particle properties are desirable to overcome biological and physical barriers. Therefore, stimuli-responsive NPs have been developed to allow for specific particle adaptation. In this work, it was demonstrated that NPs can be rendered switchable with respect to their interaction with a receptor through an external chemical stimulus. A combination of the inverse electron-demand Diels-Alder (iEDDA) reaction for subsequent NP functionalization and ectoenzyme-based ligand activation allowed for specific particle tailoring. Building on this, a two-step process for target cell recognition was developed: First, NPs were functionalized with Angiotensin-I (Ang-I) as inactive ligand using iEDDA chemistry. At the target site, the ligand was enzymatically processed to Angiotensin-II (Ang-II) by cellular ectoenzymes. Ang-II binds as active ligand to the angiotensin II type 1 (AT1) receptor on the target cell surface. This enzymatic activation aims to minimize the biological effect of the ligand prior to particle binding, while the NP target cell specificity is increased by a two-step recognition with enzymatic processing and receptor binding.

Graphical Abstract



Schematic representation of the concept to render NPs switchable regarding their avidity for the AT1 receptor through post-functionalization using the iEDDA reaction and ectoenzyme-based ligand activation.

Chapter 4

1. Introduction

NPs have gained considerable attention as drug delivery platforms due to their advantageous properties, including enhanced stability and solubility of encapsulated payloads, as well as reduced systemic toxicity. [1] As a result, research in the field of NP-based drug delivery has seen a steady increase in recent years. [2] Typically, NPs retain their size, shape, and surface properties during the journey through the organism. However, this rigid design limits the ability of NPs to adapt to the diverse physical and biological barriers. [3] Following intravenous administration, NPs face several challenges that can impede their delivery, such as blood flow dynamics and clearance by the reticuloendothelial system (RES). Upon reaching target tissues, extravasation and cellular internalization present further barriers, and even after successful uptake, intracellular trafficking may affect the final delivery of the payload. [4] Throughout this journey from administration to the target site, NP properties like size, shape, surface charge, and functionalization play pivotal roles. [2] However, different stages of this journey often require distinct and sometimes contradictory NP properties. [5] For instance, NPs require stealth surfaces to evade RES clearance. Yet, these same stealth properties may hinder the effective internalization of NPs once they reach their target cells. [6]

To address this challenge and tailor NPs to specific situations, stimuli-responsive NPs have been developed. [7, 8] In cancer therapy, for instance, one can leverage the acidic and hypoxic environment of the tumor and design pH- or hypoxia-responsive NPs. [9] Other endogenous triggers include high levels of enzymes [10, 11], reactive oxygen species (ROS) [12, 13], or adenosine triphosphate (ATP) [14, 15]. Additionally, exogenous triggers can be used to modify the particles. Essentially, photo- [16], thermal- [17], and ultrasound-responsive [18] NPs are considered in this context. These designs allow for the modification of key NP properties in response to designated stimuli. [5] Furthermore, cell uptake-promoting ligands can be activated by a stimulus. Several approaches to achieve this controlled ligand activation have been discussed in the literature. [3] Commonly, NPs are fully equipped with all functional components at the time of administration. The ligand for active targeting is often concealed and revealed through the cleavage of a component in response to a specific stimulus. [19, 20] However, such methods may lack temporal precision, potentially exposing targeting ligands prematurely or before the NP has reached its target site.

In contrast, the present study aims to lay the groundwork for an approach where NPs can be modified in a controlled, constructive manner near the target site. To achieve this, an *in vivo*-compatible bioorthogonal click reaction was assessed to functionalize the NPs. The [4+2] cycloaddition of tetrazine (Tz) and trans-cyclooctene (TCO), known as the inverse electron-demand Diels-Alder (iEDDA) reaction, is particularly suitable for this application due to the extremely fast reaction even at low concentrations and its selectivity in the multitude of functional groups of the organism. [21] While the iEDDA reaction has primarily been employed for *in vivo* particle functionalization in the context of pre-

targeted imaging, where radiotracers for positron emission tomography (PET) are attached to NPs post-accumulation in tumors [22], its potential for use in stimuli-responsive drug delivery systems has yet to be fully explored. In this study, we sought to demonstrate that the iEDDA reaction can enable the switchable activation of NPs. The delayed addition of a ligand - acting as a chemical stimulus - could serve as a novel mechanism to initiate receptor-mediated target cell recognition. This approach would offer unique control over the timing of ligand activation rendering the NP delivery process in future applications more controllable.

The feasibility of this approach was investigated *in vitro* using angiotensin as an exemplary ligand targeting the angiotensin II type 1 (AT1) receptor on mesangial cells. [23] Angiotensin-I (Ang-I), modified with TCO for the iEDDA reaction, was designed to react with Tz-functionalized NPs. Once bound to the NP surface, Ang-I required further activation by the membrane-bound ectoenzyme angiotensin-converting enzyme (ACE) to convert into the active form, Angiotensin-II (Ang-II). [24] This additional activation step was included to minimize the biological activity of the ligand prior to processing. Moreover, the dual requirement of ACE and the AT1 receptor on target cells may further increase the specificity of NP targeting. The combination of the iEDDA reaction and ectoenzyme-mediated ligand activation provided a new strategy for creating NPs with switchable targeting properties. This stimuli-responsive design holds promise for future *in vivo* applications, where non-functionalized NPs could initially exploit their stealth properties to evade immune recognition, followed by temporally controlled ligand activation to promote specific cellular uptake. The presented concept, utilizing a two-step activation process, could potentially open new avenues for enhancing target specificity and thus therapeutic efficacy in NP-based drug delivery.

2. Materials and Methods

2.1 Materials

PEG derivatives (COOH-PEG2k-OH, mPEG2k-OH, COOH-PEG5k-OH and tBoc-NH-PEG5k-OH) were obtained from JenKem Technology USA Inc. (Allen, TX, USA). Lysine N-modified Ang-I and Ang-II (Lys-Ang-I Sequence KDRVYIHPFHL and Lys-Ang-II Sequence KDRVYIHPF) were synthesized according to order from Genscript (Piscataway, NJ, USA). The nitrile 3-(4-cyanophenyl)-propionic acid as starting compound for the synthesis of tetrazine was purchased from aber GmbH (Karlsruhe, Germany). TCO-PEG₄-NHS ester (axial isomer) was obtained from Lumiprobe (Hannover, Germany). The cellulose dialysis membranes, which were used to purify the polymers after ligand

Chapter 4

coupling, were purchased from Spectrum Laboratories Inc (Rancho Dominguez, CA, USA). NP solutions were concentrated with centrifugal devices (30 or 100 kDa molecular weight cutoff) which were purchased from Pall Life Sciences (Portsmouth, UK). QuantiPro™ BCA assay kit for angiotensin quantification, angiotensin-converting enzyme from rabbit lung (≥ 2.0 units/mg protein (modified Warburg-Christian)) for enzymatic activation and RPMI-1640 medium and hydrocortisone for cell culture were obtained from Sigma Aldrich (Taufkirchen, Germany). Fetal bovine serum (FBS, South America origin, 0.2 μm sterile filtered, Lot No.: P201004) was sourced from PAN Biotech GmbH (Aidenbach, Germany) and insulin-transferrin-selenium was purchased from Life Technologies Corporation (Grand Island, NY, USA). Fura-2 AM as ratiometric Ca^{2+} indicator was ordered from Thermo Fisher Scientific (Waltham, MA, USA). All other materials were reagent grade and obtained from Merck KGaA (Darmstadt, Germany). Millipore water was generated using a Milli-Q water purification system (Millipore, Schwalbach, Germany).

2.2 Polymer synthesis and ligand coupling

The PLA-PEG block copolymers with diverse functional groups were synthesized using the respective carboxylic acid-, amine-, or methoxy-terminated PEG derivatives as macroinitiators, as previously reported by our group. [25] The ring-opening polymerization of cyclic lactide, using 1,8-diazabicyclo[5.4.0]undec-7-ene (DBU) as a catalyst, yielded copolymers with approximately 10 kDa PLA and 2 kDa or 5 kDa PEG chains with the corresponding functional group on the PEG depending on the chosen starting material. More detailed information regarding the synthesis of the copolymers and ^1H NMR spectra for characterization can be found in the SI section I. The ligand coupling was performed using peptide chemistry with either hexafluorophosphate benzotriazole tetramethyl uronium (HBTU) or 1-ethyl-3-(3-dimethylaminopropyl)carbodiimide (EDC)/ N-hydroxysuccinimide (NHS) as coupling reagents and N,N-diisopropylethylamine (DIPEA) as base in dimethylformamide (DMF). Tetrazine with carboxy functionality was coupled to the PLA10k-PEG5k-NH₂ block copolymer using HBTU. For the coupling of the Angiotensin ligands Ang-I and Ang-II, PLA10k-PEG5k-COOH was activated with EDC/NHS, excess EDC was quenched with 2-mercapthoethanol, and the Angiotensin ligands were subsequently added. Reaction times were sufficiently long to allow for complete coupling. The reaction mixtures were then precipitated in a 10-fold volume of ice-cold diethyl ether and centrifuged at 4°C. The supernatant was discarded, and the pellet was dried before being dissolved in acetonitrile. This precipitation-centrifugation-dissolution cycle was repeated once more. The pellets were dissolved in MeCN, the polymer solutions were dropwise added into vigorously stirring Millipore water, and the polymer micelles were stirred for approximately 2 hours. Further purification was achieved through dialysis (RC, 6-8 kDa MWCO) against 4 L Millipore water. Finally, the ligand-

functionalized block copolymers were lyophilized for 3 days. For product characterization, a ^1H NMR in CDCl_3 or DMSO-d_6 was recorded on a Bruker Avance III HD 400 (Bruker BioSpin GmbH, Rheinstetten, Germany). Details regarding ligand coupling, ^1H NMR for characterization, and determination of coupling efficiency can be found in the SI Section III.

2.3 NP preparation and characterization

A 10 mg/mL solution with a PEG-PLA block copolymer to particle-core-forming poly(lactic-co-glycolic acid) (PLGA) mass ratio of 70:30 in acetonitrile was prepared. The copolymer fraction was adjusted to ensure that 20% of the PEG-PLA copolymers carried the ligand (PLA10k-PEG5k-Tz, -Ang-I, or -Ang-II), with PLA10k-PEG2k-COOH serving as the filler polymer. NPs were prepared via bulk nanoprecipitation, wherein the polymer solution in acetonitrile (10 mg/mL) was added dropwise to vigorously stirred (800 rpm) Millipore water. [26] The NPs were left stirring for 3 h until the organic solvent (MeCN) was completely evaporated. The resulting 1 mg/mL NP solution was concentrated through centrifugation using a 100-kDa molecular weight cutoff Microsep advance centrifugal device (Pall Life Sciences) for 30 minutes at 3000 g. Subsequently, NP size and concentration were determined in Millipore water using nanoparticle tracking analysis on a NanoSight NS300 (Malvern Panalytical GmbH, Kassel, Germany). [27] The dilution was adjusted so that between 10 and 50 particles per frame could be measured and the detection threshold in the evaluation was set to 3. Unless otherwise stated, the mode value given by NanoSight NS300 is reported as the hydrodynamic diameter of the particles. The polydispersity index (PDI) was calculated from the nanoparticle tracking analysis data according to Clayton, Salameh et al. using the following formula. [28]

$$PDI = \left(\frac{\sigma}{d}\right)^2 \quad (1)$$

The PDI results from the standard deviation σ of the particle diameter distribution divided by the mean particle diameter d . The molar NP concentration was determined based on the particle concentration (particles/mL) output by the instrument using Avogadro's number. The zeta potential of 1 nM NPs was measured in 10% PBS at 25°C on a Malvern ZetaSizer Nano ZS (Malvern Instruments GmbH, Kassel, Germany).

Chapter 4

2.4 Quantification of ligands per NP

For the quantification of tetrazine ligands per NP, 50 μL of the concentrated NP sample was dispensed into a transparent 384-well plate (Corning, Corning, NY, USA) and diluted with 50 μL dimethyl sulfoxide (DMSO) to initiate NP dissolution. For the calibration curve, 50 μL of free tetrazine diluted to different concentrations in DMSO was added to 50 μL of Millipore water (tetrazine total concentration in the well 100–500 μM). The absorbance at the absorption maximum of tetrazine at λ 532 nm was measured on a FLUOstar Omega microplate reader (BMG Labtech, Ortenberg, Germany). The tetrazine concentration in the NP sample, determined using the calibration curve, was referenced to the NP concentration determined through nanoparticle tracking analysis, thus quantifying the number of tetrazine ligands per particle.

Ang-I or -II ligands per NP were quantified using a BCA assay following the manufacturer's protocol for the QuantiPro™ BCA Assay Kit. For calibration, free Lys-Ang-I or -II was diluted from a 10 mM solution in DMSO to suitable concentrations in Millipore water (15–75 μM Angiotensin). 40 μL of the calibration solution or the sample with a 10 nM NP solution was dispensed into a transparent 384-well plate. Subsequently, 40 μL of QuantiPro working reagent per well were added, and the solution was mixed by pipetting up and down. The plate was sealed with a plate sealer and incubated at 60°C for 1 hour. The absorption at λ 562 nm was immediately determined using a FLUOstar Omega microplate reader. Similar to the tetrazine ligands, the angiotensin concentration calculated via the calibration curve was referenced to the NP concentration.

In both cases, the surface area of the particles was additionally calculated from the hydrodynamic diameter of the NPs, assuming a spherical shape. This, along with the number of ligands per NP, was used to determine the ligand density.

2.5 Investigation of iEDDA reaction kinetics

TCO-PEG₄-COOH was diluted from a stock solution in DMSO into the wells of a 96-well quartz plate (Hellma GmbH, Müllheim, Germany) with water, resulting in 2, 4, 8, 16, and 32-fold excess relative to tetrazine. The DMSO content in all wells was adjusted to 4% (v/v). Tetrazine (either free in solution, on polymer micelles, or on NPs) was added via the plate reader's pump system to achieve a final tetrazine concentration of 10 μM per well. The micelles, like the NPs, were functionalized with 20% tetrazine but did not contain core-forming PLGA. Immediately after automated addition, the decrease in tetrazine absorbance at λ 276 nm was monitored (0.3 s kinetic interval time; 25°C). Data were fitted with an exponential decay, yielding pseudo-first-order rate constants (k_{obs}). The k_{obs} values were plotted against

the TCO concentration, and a linear fit was performed. The slope of the line yields the second-order rate constant.

2.6 Cell Culture

Rat mesangial cells (rMCs) were generously provided by Professor Dr. Armin Kurtz (Institute of Physiology at the University of Regensburg, Regensburg, Germany). The cell line was selected as the target cells due to their stable AT1R expression, as previously demonstrated in studies conducted by our research group. [23, 24, 29] The cells were cultured in RPMI 1640 medium supplemented with 10% fetal bovine serum, insulin-transferrin-selenium, and 100 nM hydrocortisone and in T-75 cell culture flasks (Corning, Corning, NY, USA) at 37 °C with a 5% CO₂ atmosphere.

2.7 Fura-2 AM-based Ca²⁺ mobilization assay

To investigate the affinity of the ligands, both in their free form and NP-bound, towards the AT1R, a ratiometric Fura-2 AM Ca²⁺ assay as previously reported by our group was used. [29] 50 µg of Fura-2 AM were dissolved in 50 µL of DMSO. From this stock solution, the Fura-2 AM loading medium was prepared by combining the 50 µL stock solution with 20 µL of a 20% Pluronic F127 solution and diluting it to a final volume of 6 mL in Leibovitz's medium containing 2.5 mM Probenecid. The rMCs at passages 78 or 79 were allowed to grow in a T75 cell culture flask at 37°C in the CO₂ incubator until they reached at least 90 % confluence. On the day of the experiment, the cells were washed with 10 mL of DPBS and harvested by incubation with 0.25% trypsin. Subsequently, 9 mL of serum-containing medium was added, and the cells were centrifuged at 200 rcf for 5 minutes using a 5702 R centrifuge (Eppendorf, Germany). The supernatant was discarded, and the cell pellet was gently resuspended in the Fura-2 AM loading medium. The rMCs were incubated for 1 hour at room temperature on a laboratory shaker at 50 rpm, protected from light. The Fura-2 AM-loaded cells were centrifuged using the settings mentioned earlier, and the loading medium was removed. The cells were carefully (so as not to expose the cells to shear stress) resuspended in a measurement buffer based on Leibovitz's medium containing 2.5 mM OAT inhibitor Probenecid. The cell number was determined using a Neubauer-improved counting chamber (Marienfeld, Germany) and adjusted to 1 million rMCs per mL.

In the direct procedure to determine EC₅₀ values, the cell suspension was immediately used for measurements on the FLUOstar Omega plate reader. 90 µL of Fura-2 AM-loaded cells were added to 10 µL of the sample (in 10% PBS) via the plate reader's pump system with a low pump speed of 100 µL/s to minimize mechanical impact/shearing. In the approach described in this paper as the inverse

Chapter 4

procedure, the ligand for the AT1 receptor was first incubated with the Fura-2 AM-loaded cells. After a specified time interval, free Lys-Ang-II was added through the plate reader's pump system to stimulate the cells. In this case, the focus is not on examining the calcium influx caused by the binding of the ligand to the AT1R but, conversely, assessing the extent to which the Lys-Ang-II signal could be reduced. This serves as a measure of AT1R binding by the previously added ligand. In the inverse procedure applied to determine IC_{50} values, 90 μ L of the cell suspension were incubated for 1 hour with 10 μ L of the ligands in 10% PBS, either in their free or NP-bound form. Cell stimulation was then carried out using 100 μ L of a 300 nM Lys-Ang-II solution in 10% PBS. The inverse procedure was also used to examine the kinetics of the enzymatic processing and subsequent AT1R interaction of the angiotensin ligands on the rMCs. For this purpose, 90 μ L of Fura-2-loaded rMCs in suspension were incubated with 50 μ L of the free ligand TCO-PEG₄-Ang-I (10 μ M total concentration of free ligand) or 60 μ L of the respective NPs in 10% PBS (2 nM total concentration of NPs) for varying durations at 37°C under gentle agitation. For measurements, cells were stimulated in this case with 50 μ L of the free agonist Lys-Ang-II (1 μ M solution in 10% PBS). A compilation illustrating the experimental procedure for the direct and inverse approach can be found in **SI Table 1**.

Both in the direct and in the inverse procedure the fluorescence intensity was measured for 30 seconds whereby the sample was alternately excited at λ 340 and λ 380 nm, and emission at λ 510 nm was detected. The highest measured ratio R between the resulting fluorescence under excitation at λ 340 and λ 380 nm was utilized to calculate the intracellular calcium concentration applying the Grynkiewicz equation (eq. 2). [30]

$$[Ca^{2+}] = K_d \left(\frac{R - R_{min}}{R_{max} - R} \right) \left(\frac{S_{f2}}{S_{b2}} \right) \quad (2)$$

To determine the maximum ratio R_{max} , 90 μ L of Fura-2 AM-loaded cells introduced via the pump system were lysed with 10 μ L of 1% Triton X-100 in PBS. The minimum ratio R_{min} was determined using 10 μ L of 1% Triton X-100 in PBS supplemented with 45 mM EGTA in 0.5 M NaOH to chelate the total Ca^{2+} with EGTA as the chelating agent. S_{f2} represents the maximum emission of free Fura-2 AM (determined after cell lysis and Ca^{2+} chelation with EGTA) and S_{b2} stands for the maximum emission of Fura-2 AM with bound Ca^{2+} (determined after cell lysis, but without chelation of Ca^{2+}), in each case at an excitation wavelength of λ 380 nm. The value for 10% PBS as blank was subtracted from all intracellular calcium concentrations calculated via the Grynkiewicz equation (eq. 2) and the values were normalized against the highest concentration. Experimental data were fitted using a four-parameter nonlinear regression model (eq. 3) to obtain binding curves and EC_{50} or IC_{50} values. For the fit of binding curves where the corresponding plateau could not be reached, the bottom asymptote $A1$ was set to 0 (**Figure 5 A** curve for NP-Ang-I and NP-Tz-TCO-Ang-I) or the top asymptote $A2$ to 100 (**Figure 4 C**

curve for NP-Tz-TCO-Ang-I and NP-Tz-TCO-Ang-I + ACE). Further, x_0 stands for the EC_{50} or IC_{50} value and p represents the hill slope describing the steepness of the curves.

$$y = A1 + \frac{A2 - A1}{1 + 10^{(\text{LOG}x_0 - x) p}} \quad (3)$$

In the kinetics experiments, the extent to which the Lys-Ang-II signal could be reduced provides insights into the degree of AT1R saturation by the free ligand or NPs, thus allowing assessments of ligand/NP-cell interactions. The kinetics of AT1R saturation were fitted with equation 4 for an exponential plateau, where y_0 stands for the initial value and y_S for the saturation value and k is a rate constant.

$$y = y_S - (y_S - y_0) \cdot e^{-kx} \quad (4)$$

2.8 Post-Functionalization, enzymatic activation and NP avidity for the AT1R

To functionalize NP-Tz with Ang-I through iEDDA reaction, a 20 nM NP-Tz solution was incubated with 400 μM TCO-PEG₄-Ang-I for 1 hour at 37°C, followed by the removal of free TCO-modified Ang-I through size-exclusion chromatography (SEC). The SEC was carried out with 4% Agarose Beads (Agarose Beads Technologies, Madrid, Spain) using a gravity protocol. NP fraction was detected on the Zetasizer (Malvern Panalytical GmbH, Kassel, Germany) and collected accordingly. The NPs were concentrated using a 30-kDa molecular weight cutoff Microsep advance centrifugal device for 30 minutes at 3000 g. To assess the extent of Ang-I removal, a control experiment was conducted using 20 nM NP-COOH incubated with 400 μM TCO-PEG₄-Ang-I, where the absence of tetrazine on the NP prevents covalent binding. Free TCO-modified Ang-I was similarly separated via SEC, and the NPs were concentrated by centrifugation. The concentrated NPs were measured on the Nanosight NS300 in both cases to determine size and NP concentration. The BCA assay for quantifying the Ang-I ligands on the NP was performed as described above, using free Lys-Ang-I as a standard for calibration. The value for the non-functionalized NPs was subtracted from the functionalized NPs as a blank value.

The particles functionalized via iEDDA reaction with Ang-I were tested either directly in a Fura-2 AM Ca^{2+} assay or additionally activated with soluble ACE. A 1 nM NP solution was incubated for 4 hours at 37°C in DPBS (pH 7.4) with 100 nM soluble ACE. The NPs were concentrated by centrifugation using a 30-kDa molecular weight cutoff centrifugal filter. Subsequently, NP size and concentration were determined using nanoparticle tracking analysis. For the Fura-2 AM Ca^{2+} mobilization assay, the concentrated NP sample was diluted 1:3 and 1:10. These two solutions were further diluted 1:10 and the corresponding dilution series were prepared. 10 μL of the sample were added in triplicate to a white 96-

Chapter 4

well plate, and the Fura-2 AM Ca^{2+} assay was performed according to the direct procedure as previously described.

To investigate the NP avidity for the AT1R after enzymatic activation not by soluble ACE but by cell membrane-bound enzyme, the Fura-2 AM Ca^{2+} assay was conducted using the inverse procedure. Dilution series were prepared again from the tetrazine-functionalized NPs, the post-functionalized NPs, as well as from directly Ang-I and Ang-II functionalized NPs for comparison. 10 μL of the sample was added in triplicate to a white 96-well plate. The NP solutions were incubated with 90 μL of cell suspension for 1 hour at 37°C , followed by the addition of 100 μL of 300 nM Ang-II solution for stimulation, as described in Section 2.7.

2.9 Data analysis

Fit of experimental data and statistical analysis was performed using Origin software (Version 2020, OriginLab Corporation, Northampton, MA, USA). One-way ANOVA with a Tukey's multiple comparison test was used for statistical evaluation of significance. The number of performed experiments is stated in the figure caption and levels of statistical significance are indicated as $*p \leq 0.05$, $**p \leq 0.01$, $***p \leq 0.001$, and $****p \leq 0.0001$ in the respective figures.

3. Results and Discussion

3.1 Preparation and characterization of PEG-PLA copolymer NPs

Tetrazine-functionalized NPs were synthesized, capable of undergoing an iEDDA reaction with TCO-modified Ang-I. Additionally, blank NP-COOH and directly Ang-I as well as Ang-II functionalized NPs were prepared for comparison. The PEG-PLA copolymer particles well established in our research group with a PLGA-stabilized core served as excellent model for this study. Pre-functionalization of the polymer with the desired ligand prior to NP formation allows tailoring of NP properties such as size, zeta potential, and particularly ligand density per NP. [31] Functionalization was consistently chosen so that 20% of the PEG-PLA copolymers carry the ligand (tetrazine, Ang-I, or Ang-II). To enhance flexibility and accessibility of the ligands, they were attached to longer PEG5k chains, whereas the spacer chains were designed with PEG2k polymer (see **Figure 1 A**). The use of COOH-terminated spacer chains resulted in a negative zeta potential due to the deprotonation of the acid in aqueous solution. The carboxy blank particles exhibited a strongly negative zeta potential of -28 ± 3 mV, whereas

Switchable Target Cell Recognition

tetrazine-functionalized NPs showed a less negative zeta potential of -14.5 ± 0.4 mV due to tetrazine's neutral charge contribution (see **Figure 1 B** and **SI Figure 7 A**). Particles prepared by nanoprecipitation showed a size in the range of about 60 to 80 nm (see **Figure 1 C**, for the size distribution of the NPs see also **SI Figure 7 B**). The NPs functionalized with Angiotensin were slightly larger than the tetrazine-functionalized or the carboxy blank particles. The PDI was between 0.1 and 0.2 for all NP types, indicating a narrow size distribution.

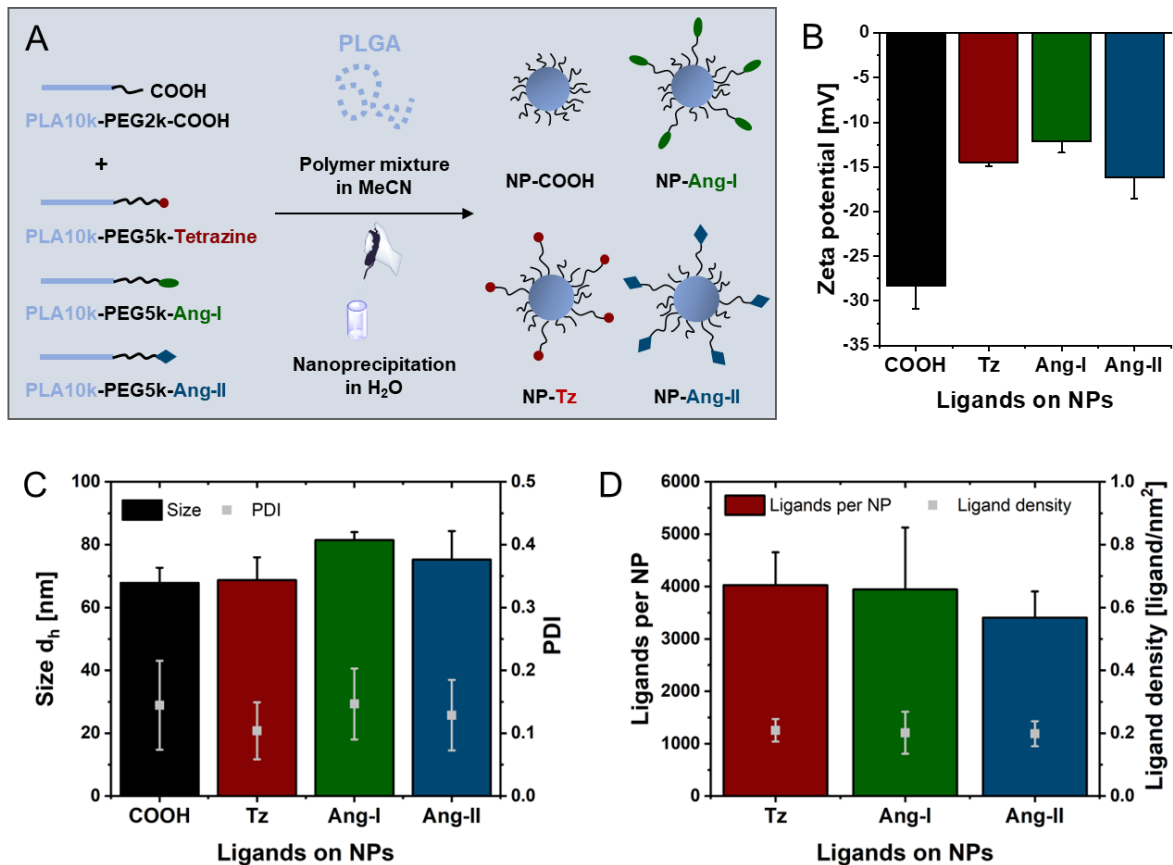


Figure 1. NP preparation and characterization. (A) Scheme for the preparation of the different NPs. (B) Zeta potential of the NPs in 10% PBS. Results are presented as mean \pm SD of $n = 3$ measurements. (C) Size and PDI of the NPs measured by nanoparticle tracking analysis. (D) Quantification of ligands per NP and calculated ligand density on the NP. Results in C and D are presented as mean \pm SD of at least $N = 3$ experiments.

Both the tetrazine-functionalized and angiotensin-functionalized NPs showed around 4000 ligands per particle, corresponding to a ligand density of approximately 0.2 ligands per nm^2 (see **Figure 1 D** and **SI Figure 8** for details on the quantification of ligands per NP). Since the PEG density on the NP is very high and the PEG conformation can be assigned to the “dense brush” regime, a backfolding of the long ligand-bearing PEG5k chains towards the particle core is rather unlikely. There should be no room for a loop of the PEG chains, so that ligands could hide in the PEG brush of the particle. Thus, virtually all ligands should be available for interaction with the target cell (see **SI Figure 9** for calculations to

Chapter 4

estimate the PEG conformation on the particle). In addition, thinking towards the *in vivo* application envisaged in the future, the PEG conformation, being distinctly in the dense brush regime, should be ideally suited to avoid uptake by immune cells and prevent clearance of the NPs. [32] To summarize, it can be stated that similar zeta potentials, sizes, and ligand densities of the NPs allowed for good comparability among the particles and enabled the observation of effects induced solely by the different ligands.

3.2 iEDDA reaction kinetics on the NP

While numerous studies in the literature confirm the fast kinetics for iEDDA reaction in solution [33], this study investigated whether the reaction also proceeds robustly on the copolymer NPs (see **Figure 2 A**). To follow the reaction kinetics, the decrease in tetrazine absorbance in the UV range was examined (considerations regarding this can be found in **SI Figure 10**). The change in absorbance with increasing reaction time was fitted with an exponential decay, obtaining pseudo first-order rate constants k_{obs} . These k_{obs} values were plotted against the TCO concentration, with the second-order rate constant derived from the slope of the linear fit. After initially investigating the reaction between free tetrazine in solution and different TCO excesses, micelles and NPs were prepared with 20% tetrazine functionalization. The micelles did not contain core-forming PLGA and were approximately half the size of the NP-Tz (see **Figure 2 B**). The iEDDA reaction was also followed with different TCO excesses. Interestingly, the iEDDA reaction proceeded at an accelerated rate on the NP compared to the reaction in solution although anchoring the tetrazine on the NP or micelle might typically suggest a reduced collision density between tetrazine and TCO (see **Figure 2 C**). A possible explanation for the faster reaction on the NP could lie in the hydrophobic nature of the TCO. It is well known that under aqueous conditions, iEDDA reactions are significantly accelerated due to the hydrophobic effect. [33] On the NP, this effect could be amplified, as the hydrophobic TCO may preferentially accumulate within the PEG brush of the NP to avoid interaction with water. This would result in a locally higher concentration, which could have contributed to the observed faster reaction on the NP. In solution, a second-order rate constant of $492 \pm 31 \text{ M}^{-1} \text{ s}^{-1}$ at 25°C was determined. This value aligns well with rate constants reported in the literature for comparable TCO/tetrazine pairs. [34] For example, Karver et al. found a second-order rate constant of $820 \pm 70 \text{ M}^{-1} \text{ s}^{-1}$ for the reaction of a methyl-substituted tetrazine, which should be comparable to the one used in this study, with TCO at 37°C . Given the fact that reaction rates can be assumed to double every 10°C [35], this would result in a constant of approximately $400 \text{ M}^{-1} \text{ s}^{-1}$ at 25°C . A second order rate constant of $550 \pm 83 \text{ M}^{-1} \text{ s}^{-1}$ was found for the tetrazine on the polymer micelles. This in turn also matches well with the rate constant k_2 of around $600 \text{ M}^{-1} \text{ s}^{-1}$ reported by Kramer et al. for endgroup tetrazine-functionalized polymer micelles at 25°C . [36] On the NP surface, a second-order rate constant

Switchable Target Cell Recognition

of $726 \pm 85 \text{ M}^{-1} \text{ s}^{-1}$ was determined (see **Figure 2 D**). For instance, for $10 \mu\text{M}$ tetrazine coupled to the NP surface (corresponding to a NP concentration of approximately 2.5 nM) and an 8-fold TCO excess, the reaction was almost completed in less than 30 s. In summary, although the trade-off between reactivity and stability for the methyl-substituted tetrazine used in this study was more on the side of stability, the iEDDA reaction on the NP surface still proceeded rapidly.

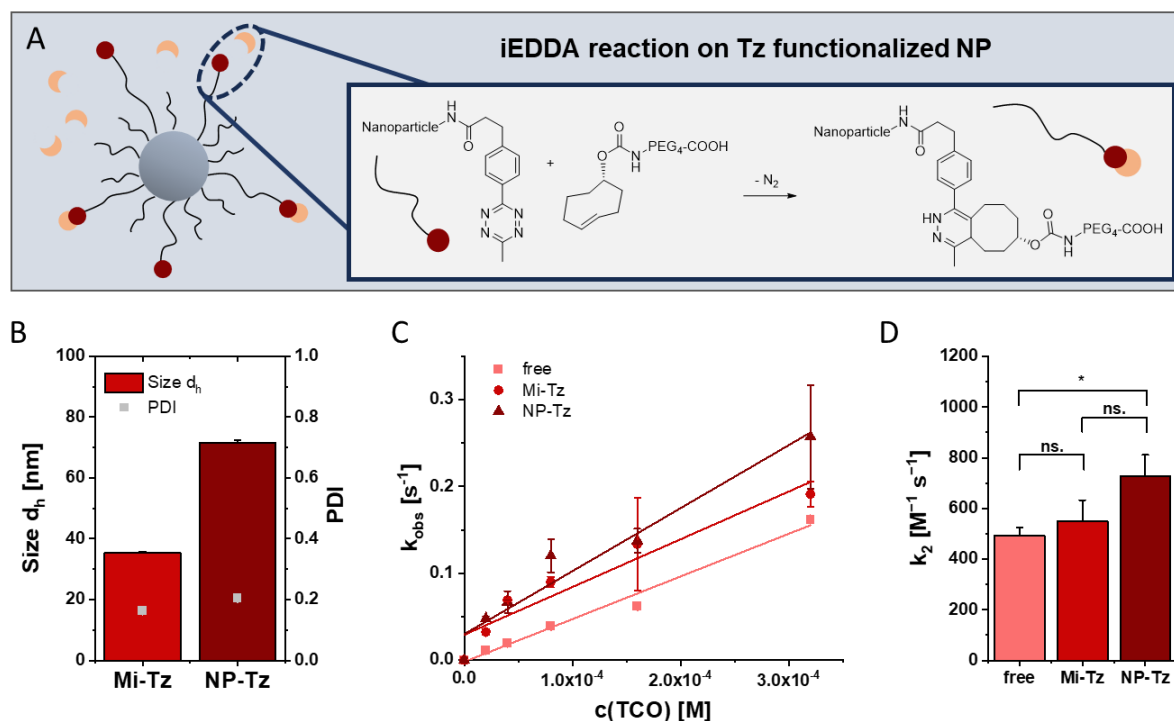


Figure 2. Investigation of the iEDDA reaction kinetics on the NP. (A) Scheme of the iEDDA reaction between tetrazine functionalized NPs and TCO-PEG₄-COOH. (B) Hydrodynamic diameter and PDI of the tetrazine functionalized micelles (Mi-Tz) and tetrazine functionalized NPs (NP-Tz) determined at the Zetasizer. (C) Plot of the pseudo first-order rate constant (k_{obs}) vs. TCO concentration to determine the second-order rate constants. (D) Second-order rate constants for the iEDDA reaction between free tetrazine (free), tetrazine on polymer micelles (Mi-Tz) and tetrazine on NP (NP-Tz), each with TCO-PEG₄-COOH at 25°C. Results are presented as mean \pm SD of $n = 3$ measurements.

3.3 Affinity of free angiotensin ligands for the AT1R

After confirming a rapid iEDDA reaction for subsequent NP functionalization, the interaction of free TCO-PEG₄-Ang-I ligand with the target cell was investigated. TCO-PEG₄-Ang-I was incubated with rMC cell suspension for varying durations, leading to enzymatic processing of Ang-I to Ang-II by cell membrane-bound ACE. The extent of binding to the AT1 receptor following enzymatic activation was

Chapter 4

determined using an inverse Fura-2 AM Ca^{2+} mobilization assay. [37] Cells were stimulated with additional free Ang-II, and the degree to which calcium influx could be suppressed by receptor saturation was measured (for further explanation see **SI Figure 11**). Initially, as expected, no AT1R binding was observed. However, over time, enzymatic processing gradually led to receptor saturation, with a plateau reached after approximately 90 minutes (see **Figure 3 A**). In contrast, the iEDDA reaction of an equivalent amount of TCO with tetrazine-functionalized NPs was completed within approximately 5 minutes. Consequently, it was conceivable that the ligand undergoes the iEDDA reaction with tetrazine on the NP prior to experiencing enzymatic activation of Ang-I to Ang-II and subsequent interaction with the AT1R. The rapid kinetics of the iEDDA reaction, in conjunction with the slower enzymatic processing, could facilitate initial particle functionalization *in vitro*.

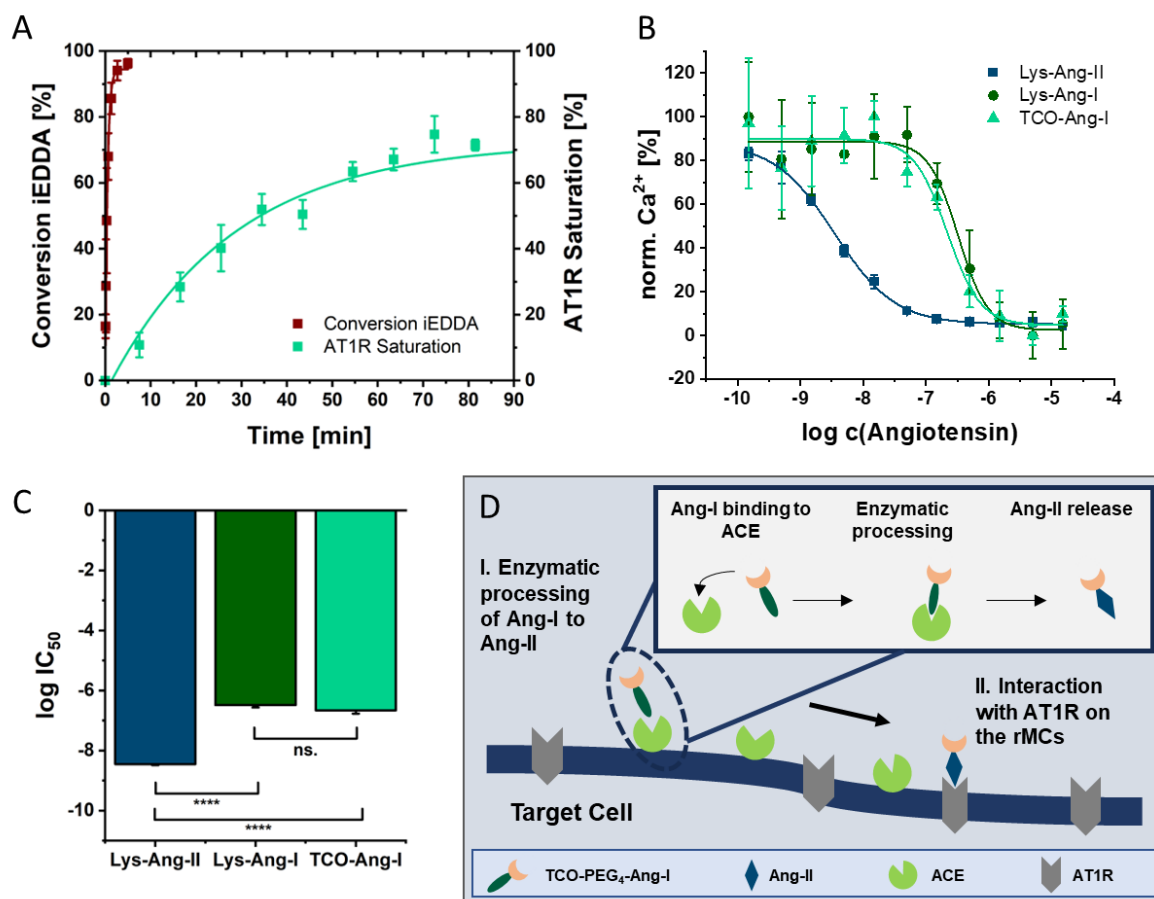


Figure 3. Interaction of free angiotensin ligands with the AT1 receptor. (A) Comparison of the conversion of the iEDDA reaction with AT1R inhibition. The kinetics of the iEDDA reaction of 10 μM TCO-PEG₄-COOH with an equimolar amount of tetrazine on the NP was investigated by monitoring the decrease in tetrazine absorbance in the UV range (data presented as mean \pm SD $n=2$); AT1R saturation of 10 μM TCO-PEG₄-Ang-I by enzymatic processing of Ang-I to -II and subsequent binding to the receptor was examined by inverse Fura-2 AM Ca^{2+} mobilization assay (data presented as mean \pm SD $n=3$). (B) Affinity of free angiotensin ligands for the AT1R after 1 h incubation with the cells. Binding curves determined via Fura-2 AM Ca^{2+} mobilization assay by inverse stimulation with free Ang-II. Results are presented as mean \pm SD of at least $n = 3$ measurements. (C) $\log\text{IC}_{50}$ values for the free ligands obtained from the fit of the Fura-2 AM Ca^{2+} assay data. (D) Schematic of the enzymatic activation of TCO-PEG₄-Ang-I and subsequent binding to the AT1R.

Switchable Target Cell Recognition

Furthermore, the affinity of free angiotensin ligands for the AT1 receptor was examined. Various dilutions of ligands were incubated with Fura-2 AM loaded cell suspension for 1 hour. With Lys-Ang-II, the expected binding curve was observed, yielding an IC_{50} value of 3.5 ± 0.3 nM, consistent with the value reported by Maslanka et al. [37] The binding curves of Lys-Ang-I and TCO-PEG₄-Ang-I were nearly identical (see **Figure 3 B**). IC_{50} values of 0.33 ± 0.06 μ M for Lys-Ang-I and 0.22 ± 0.06 μ M for TCO-PEG₄-Ang-I were determined. The affinity for the AT1R was lower than that for Lys-Ang-II (compare **Figure 3 C**), as the ligands first had to be activated by cell membrane-bound ACE (see **Figure 3 D**). Comparable IC_{50} values for Lys-Ang-I and TCO-PEG₄-Ang-I suggested that modification of Lys-Ang-I with TCO as a partner of the iEDDA reaction did not interfere with enzymatic processing or receptor binding. **SI Figure 12** additionally provides a comparison with N-terminal acetylated angiotensin. In summary, due to the rapid iEDDA reaction and slower enzymatic processing, it is probable that *in vitro* NP functionalization occurs initially before free ligand activation. Further, it was demonstrated that TCO modification does not adversely affect affinity, with similar affinities found for Lys-Ang-I and TCO-PEG₄-Ang-I for AT1R.

3.4 Post-functionalization of NP-Tz with angiotensin-I via iEDDA reaction and avidity for the AT1R after enzymatic activation

To render the NPs switchable concerning their interaction with the AT1R, two fundamental steps had to be implemented. First, the particle had to undergo post-functionalization through the iEDDA reaction. Subsequently, the Ang-I-functionalized NPs had to be enzymatically processed to Ang-II by ACE. The NPs functionalized only with tetrazine were incubated with TCO-PEG₄-Ang-I for 1 hour to allow sufficient time for the iEDDA reaction on the particle. Excess TCO-PEG₄-Ang-I was separated by SEC, and the Ang-I was then quantified using a BCA assay. Based on the NP concentration, the number of Ang-I ligands per NP was determined (see **Figure 4 A**). With 3442 ± 303 Ang-I ligands per NP, slightly fewer than tetrazine ligands before functionalization were present, indicating efficient iEDDA reaction on the NP (approx. 86%). Functionalization with Ang-I resulted in minimal size increase of the NPs from 60 ± 4 nm for NP-Tz to 67 ± 4 nm for NP-Tz-TCO-Ang-I. Subsequently, the post-functionalized NPs were incubated with soluble ACE for 4 hours at 37°C. The particles were then expected to be fully activated to Ang-II. [24] Incubation with soluble ACE resulted in further size increase to 84 ± 6 nm, with the size distribution also becoming significantly broader (compare **Figure 4 B**). The NPs were examined for their avidity to the AT1R using a Fura-2 AM Ca²⁺ mobilization assay. The NPs only functionalized with tetrazine showed no Ca²⁺ influx, thus indicating no interaction with the AT1R. In contrast, the post-functionalized and subsequently enzymatically activated particles interact with the receptor (see **Figure 4 C**). An EC_{50} value of 2.0 ± 0.5 nM was determined, illustrating sufficient avidity

Chapter 4

of the NPs (see **Figure 4 D**). Surprisingly, the post-functionalized NPs without enzymatic activation showed Ca^{2+} influx at the highest concentrations. This indicates that Ang-I may be converted to Ang-II by membrane-bound ACE within the short measurement period, suggesting that ACE on the cell membrane alone might be sufficient to activate the particles.

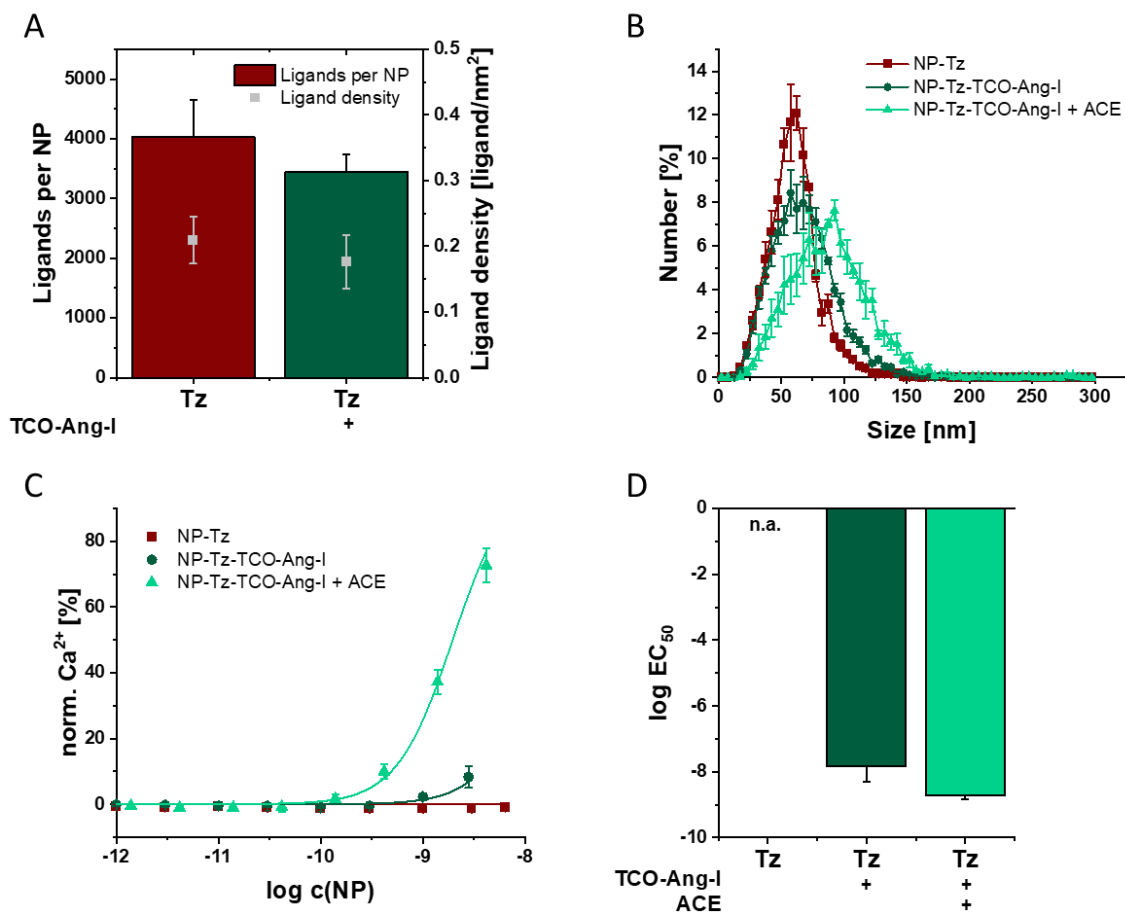


Figure 4. Post-functionalization of NP-Tz with Ang-I via iEDDA reaction and avidity for the AT1R on rMCs. (A) Number of ligands per NP and derived ligand density before and after functionalization with Ang-I via iEDDA reaction. Tetrazine was quantified using its absorption in the visible range; Ang-I content after functionalization was determined using a BCA assay; the ligand concentrations were referred to the NP concentrations determined by NTA. (B) Size alteration of the particles by post functionalization and enzymatic processing with soluble ACE. Size distribution measured by nanoparticle tracking analysis. (C) Avidity for the AT1 receptor of the tetrazine-only functionalized NPs (NP-Tz), the subsequently Ang-I functionalized NPs (NP-Tz-TCO-Ang-I) and the NPs additionally activated with soluble ACE (NP-Tz-TCO-Ang-I + ACE). Binding curves derived from Fura-2 AM Ca^{2+} mobilization assays using the direct procedure with immediate measurement of Ca^{2+} influx after addition of the cell suspension. (D) Corresponding $\log\text{EC}_{50}$ values for the NPs obtained from the fit of the Fura-2 AM Ca^{2+} assay data. Results in Figure A are presented as mean \pm SD of $N = 3$ independent experiments. The results in Figures B-D are presented as mean \pm SD from a single experiment with $n = 3$ measurements.

3.5 Activation of NPs by cell membrane-bound ACE and kinetics of particle-AT1R interaction

Next, it was investigated whether the particles post-functionalized with Ang-I via iEDDA reaction can be activated, as required for later application, by membrane-bound ACE. The rMCs used as a model cell line exhibit a high ACE activity of approx. 0.35 pmol of hydrolyzed substrate per minute and per μg of protein. [24] The NPs were initially incubated with the cell suspension for 1 hour, and subsequently the extent to which the influx of Ca^{2+} triggered by the addition of free Ang-II could be reduced was measured (for further explanation see **SI Figure 11**). While the NPs functionalized only with tetrazine did not bind to the AT1 receptor, the particles post-functionalized with Ang-I showed interaction at higher concentrations (see **Figure 5 A**). Here, a sufficient number of Ang-I ligands appeared to have been processed to Ang-II by ACE on the cell membrane during incubation. The directly Ang-I functionalized NPs behaved similarly and also saturated the receptor at higher concentrations. NP-Ang-II, tested for comparison, where all ligands were directly available for receptor binding, showed an IC_{50} value in the picomolar range (see **SI Figure 13** for a comparison with NP-Ang-II with acetylation at the N-terminus of angiotensin). In contrast, the IC_{50} value for Ang-I functionalized NPs was in the nanomolar range. Comparable values of 2.9 ± 0.5 nM for NPs directly Ang-I functionalized and 1.5 ± 0.2 nM for NPs post-functionalized via iEDDA reaction were found. It could be concluded that the attachment of the Ang-I ligand through the iEDDA reaction did not hinder enzymatic activation and binding to the AT1R.

Intracellular calcium measurements were conducted over a 3-hour period to explore the interactions between NPs and cells. The degree to which different NPs could reduce calcium signaling triggered by the addition of free agonist Ang-II served as an indicator of the extent to which these NPs had bound to the AT1 receptors. This approach allowed to observe the kinetics of these interactions. NPs lacking ligands for the AT1R, such as NP-Tz, exhibited minimal receptor binding. Conversely, particles functionalized with Ang-I through the iEDDA reaction exhibited a slow binding to the AT1 receptor. This could be attributed to the requirement for enzymatic processing of Ang-I to Ang-II on the particle before the successful interaction between NPs and the AT1 receptors on the target cell surface. [37] After approximately 1 hour, saturation was achieved with slightly over 60% AT1R inhibition (see **Figure 5 B**). The NP-Tz incubated with cells and exposed to TCO-PEG₄-Ang-I displayed a trend similar to the particles functionalized with Ang-I via the iEDDA reaction prior to the experiment, albeit with slightly lower AT1R inhibition. In summary, it could be concluded that pre-functionalized NPs, such as NP-Tz-TCO-Ang-I, were activated to Ang-II through cell membrane-bound ACE and subsequently interact with AT1 receptors (see **Figure 5 D**). This likely holds true for particles that were functionalized *in vitro* as well. Since NP-Tz did not interact with the AT1R, NPs could be activated by the addition of TCO-PEG₄-Ang-I and subsequent enzymatic processing, allowing them to bind to the AT1 receptor,

Chapter 4

potentially leading to internalization. The fundamental requirement for a switchable particle was established.

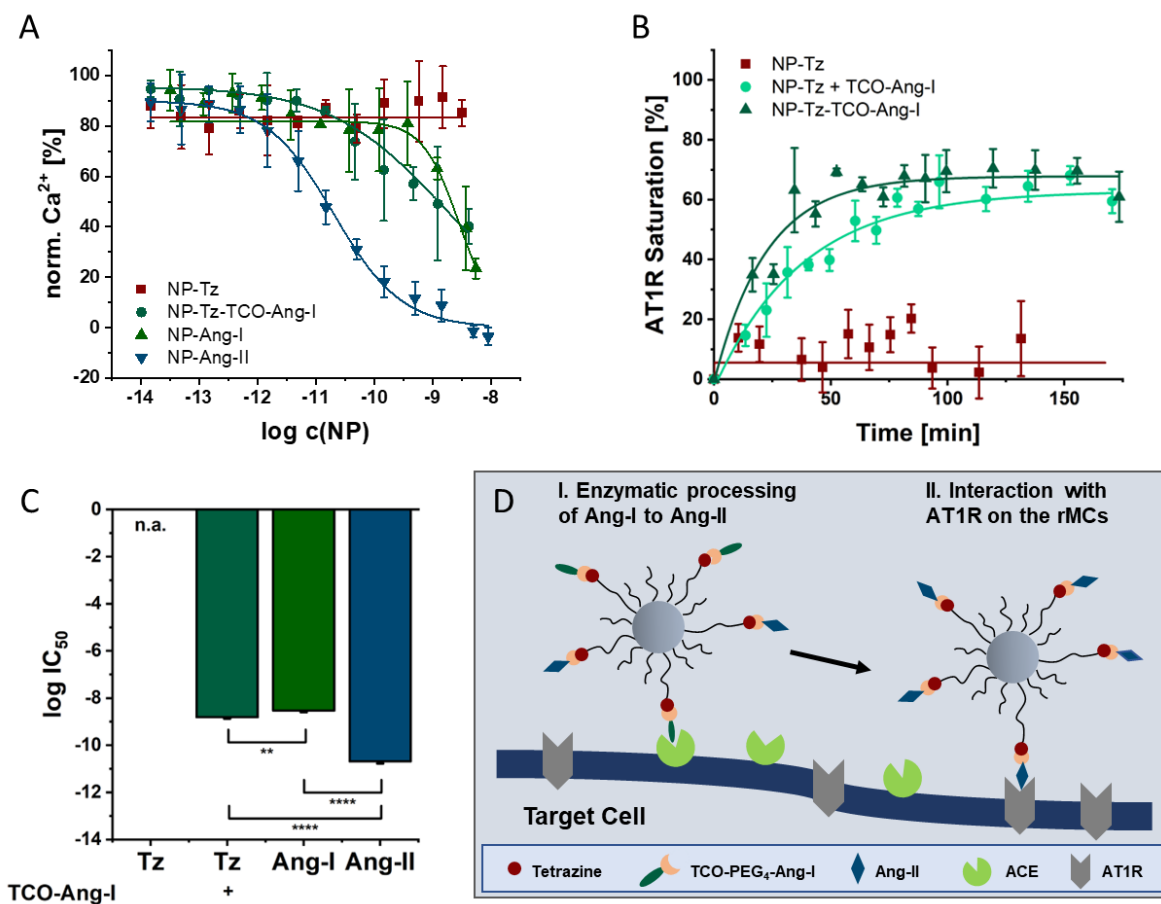


Figure 5. Characterizing NP-cell interactions through intracellular calcium measurements. (A) Particle avidity for the AT1R after 1 h incubation with the cells. Binding curves determined via Fura-2 AM Ca^{2+} mobilization assay by inverse stimulation with free Ang-II. (B) Investigation of the kinetics of NP-cell interaction by determination of AT1R binding over time. The particles investigated included those functionalized only with tetrazine (NP-Tz), tetrazine-functionalized NPs that were already incubated with the cells and exposed to TCO-Ang-I *in vitro* (NP-Tz + TCO-Ang-I), and particles functionalized with Ang-I post-experimentally (NP-Tz-TCO-Ang-I). (C) $\log \text{IC}_{50}$ values for the NPs obtained from the fit of the Fura-2 AM Ca^{2+} assay data. (D) Scheme of NP cell interaction with enzymatic processing and subsequent binding to the AT1R. Results in Figures A and C are presented as mean \pm SD of $N = 3$ independent experiments. Results in Figure B are presented as mean \pm SD of $n = 3$ measurements from one experiment.

4. Conclusion

We demonstrated that NPs can be rendered switchable with respect to their interaction with a receptor through an external chemical stimulus. The combination of iEDDA reaction for subsequent NP functionalization and ectoenzyme-based ligand activation allows for specific particle tailoring. Scenarios wherein the stealth effect of non-functionalized NPs is initially leveraged for prolonged circulation, followed by temporally controlled identification of target cells, are conceivable. This approach may potentially reduce off-target accumulations and enhance the efficacy of NPs for drug delivery. The iEDDA reaction, as a rapid and robust bioorthogonal reaction, proved to be well-suited for ligand conjugation, facilitating the creation of ligand-switchable particles. The additional processing of ligands by an ectoenzyme offers the advantage of minimizing biological effects prior to activation. Furthermore, two-step recognition involving ectoenzyme and the receptor to which subsequent binding is desired enhances specificity for the target cell. In general, this proof-of-concept study can be regarded as an initial step in exploring the potential of the iEDDA reaction for the switchable design of NPs.

Chapter 4

References

1. Mitchell MJ, Billingsley MM, Haley RM, Wechsler ME, Peppas NA, Langer R (2021) Engineering precision nanoparticles for drug delivery. *Nat Rev Drug Discov* 20(2), 101–124. 10.1038/s41573-020-0090-8.
2. Zhao Z, Ukidve A, Krishnan V, Mitragotri S (2019) Effect of physicochemical and surface properties on in vivo fate of drug nanocarriers. *Advanced Drug Delivery Reviews* 143, 3–21. 10.1016/j.addr.2019.01.002.
3. Li X, Montague EC, Pollinzi A, Lofts A, Hoare T (2022) Design of Smart Size-, Surface-, and Shape-Switching Nanoparticles to Improve Therapeutic Efficacy. *Small* 18(6), e2104632. 10.1002/smll.202104632.
4. Blanco E, Shen H, Ferrari M (2015) Principles of nanoparticle design for overcoming biological barriers to drug delivery. *Nat Biotechnol* 33(9), 941–951. 10.1038/nbt.3330.
5. Lu Q, Yu H, Zhao T, Zhu G, Li X (2023) Nanoparticles with transformable physicochemical properties for overcoming biological barriers. *Nanoscale* 15(32), 13202–13223. 10.1039/D3NR01332D.
6. Jin Q, Deng Y, Chen X, Ji J (2019) Rational Design of Cancer Nanomedicine for Simultaneous Stealth Surface and Enhanced Cellular Uptake. *ACS nano* 13(2), 954–977. 10.1021/acsnano.8b07746.
7. Mura S, Nicolas J, Couvreur P (2013) Stimuli-responsive nanocarriers for drug delivery. *Nature Mater* 12(11), 991–1003. 10.1038/nmat3776.
8. Crucho CIC (2015) Stimuli-responsive polymeric nanoparticles for nanomedicine. *ChemMedChem* 10(1), 24–38. 10.1002/cmde.201402290.
9. Su Y, Jin G, Zhou H, Yang Z, Wang L, Mei Z, Jin Q, Lv S, Chen X (2023) Development of stimuli responsive polymeric nanomedicines modulating tumor microenvironment for improved cancer therapy. *Medical Review* 3(1), 4–30. 10.1515/mr-2022-0048.
10. Yao Q, Kou L, Tu Y, Zhu L (2018) MMP-Responsive ‘Smart’ Drug Delivery and Tumor Targeting. *Trends in Pharmacological Sciences* 39(8), 766–781. 10.1016/j.tips.2018.06.003.
11. He Y, Lei L, Cao J, Yang X, Cai S, Tong F, Huang D, Mei H, Luo K, Gao H, He B, Peppas NA (2021) A combinational chemo-immune therapy using an enzyme-sensitive nanoplatform for dual-drug delivery to specific sites by cascade targeting. *Science advances* 7(6). 10.1126/sciadv.aba0776.
12. Cao Z, Li D, Wang J, Yang X (2021) Reactive oxygen species-sensitive polymeric nanocarriers for synergistic cancer therapy. *Acta Biomaterialia* 130, 17–31. 10.1016/j.actbio.2021.05.023.
13. Wang S, Yu G, Wang Z, Jacobson O, Lin L-S, Yang W, Deng H, He Z, Liu Y, Chen Z-Y, Chen X (2019) Enhanced Antitumor Efficacy by a Cascade of Reactive Oxygen Species Generation and

- Drug Release. *Angewandte Chemie International Edition* 58(41), 14758–14763. 10.1002/anie.201908997.
14. Deng J, Walther A (2020) ATP-Responsive and ATP-Fueled Self-Assembling Systems and Materials. *Advanced Materials* 32(42), e2002629. 10.1002/adma.202002629.
 15. Yu M, Zeng W, Ouyang Y, Liang S, Yi Y, Hao H, Yu J, Liu Y, Nie Y, Wang T, Deng Y, Wu M (2022) ATP-exhausted nanocomplexes for intratumoral metabolic intervention and photoimmunotherapy. *Biomaterials* 284, 121503. 10.1016/j.biomaterials.2022.121503.
 16. Tao Y, Chan HF, Shi B, Li M, Leong KW (2020) Light: A Magical Tool for Controlled Drug Delivery. *Adv. Funct. Mater.* 30(49), 2005029. 10.1002/adfm.202005029.
 17. Sponchioni M, Capasso Palmiero U, Moscatelli D (2019) Thermo-responsive polymers: Applications of smart materials in drug delivery and tissue engineering. *Materials science & engineering. C, Materials for biological applications* 102, 589–605. 10.1016/j.msec.2019.04.069.
 18. Tu L, Liao Z, Luo Z, Wu Y-L, Herrmann A, Huo S (2021) Ultrasound-controlled drug release and drug activation for cancer therapy. *Exploration* 1(3), 20210023. 10.1002/EXP.20210023.
 19. Li H, Miteva M, Kirkbride KC, Cheng MJ, Nelson CE, Simpson EM, Gupta MK, Duvall CL, Giorgio TD (2015) Dual MMP7-proximity-activated and folate receptor-targeted nanoparticles for siRNA delivery. *Biomacromolecules* 16(1), 192–201. 10.1021/bm501394m.
 20. Jin E, Zhang B, Sun X, Zhou Z, Ma X, Sun Q, Tang J, Shen Y, van Kirk E, Murdoch WJ, Radosz M (2013) Acid-active cell-penetrating peptides for in vivo tumor-targeted drug delivery. *Journal of the American Chemical Society* 135(2), 933–940. 10.1021/ja311180x.
 21. Oliveira BL, Guo Z, Bernardes GJL (2017) Inverse electron demand Diels-Alder reactions in chemical biology. *Chem. Soc. Rev.* 46(16), 4895–4950. 10.1039/C7CS00184C.
 22. Idiago-López J, Moreno-Antolín E, La Fuente JM de, Fratila RM (2021) Nanoparticles and bioorthogonal chemistry joining forces for improved biomedical applications. *Nanoscale Adv.* 3(5), 1261–1292. 10.1039/D0NA00873G.
 23. Hennig R, Pollinger K, Tessmar J, Goepferich A (2015) Multivalent targeting of AT1 receptors with angiotensin II-functionalized nanoparticles. *Journal of Drug Targeting* 23(7-8), 681–689. 10.3109/1061186X.2015.1035276.
 24. Maslanka Figueroa S, Vesper A, Abstiens K, Fleischmann D, Beck S, Goepferich A (2019) Influenza A virus mimetic nanoparticles trigger selective cell uptake. *Proceedings of the National Academy of Sciences of the United States of America* 116(20), 9831–9836. 10.1073/pnas.1902563116.
 25. Abstiens K, Maslanka Figueroa S, Gregoritz M, Goepferich AM (2019) Interaction of functionalized nanoparticles with serum proteins and its impact on colloidal stability and cargo leaching. *Soft Matter* 15(4), 709–720. 10.1039/C8SM02189A.
 26. Abstiens, K, Goepferich, AM (2019) Microfluidic manufacturing improves polydispersity

Chapter 4

- of multicomponent polymeric nanoparticles. *J. Drug Deliv. Technol.* 49, 433–439. 10.1016/j.jddst.2018.12.009.
27. Filipe, V, Hawe, A, Jiskoot, W (2010) Critical evaluation of Nanoparticle Tracking Analysis (NTA) by NanoSight for the measurement of nanoparticles and protein aggregates. *Pharm. Res.* 27 (5), 796–810. 10.1007/s11095-010-0073-2.
28. Clayton KN, Salameh JW, Wereley ST, Kinzer-Ursem TL (2016) Physical characterization of nanoparticle size and surface modification using particle scattering diffusometry. *Biomicrofluidics* 10(5). 10.1063/1.4962992.
29. Zimmer O, Goepferich A (2023) How clathrin-coated pits control nanoparticle avidity for cells. *Nanoscale Horiz.* 8(2), 256–269. 10.1039/D2NH00543C.
30. Grynkiewicz G, Poenie M, Tsien RY (1985) A new generation of Ca²⁺ indicators with greatly improved fluorescence properties. *The Journal of biological chemistry* 260(6), 3440–3450.
31. Maslanka Figueroa S, Fleischmann D, Beck S, Goepferich A (2020) The Effect of Ligand Mobility on the Cellular Interaction of Multivalent Nanoparticles. *Macromolecular Bioscience* 20(4), e1900427. 10.1002/mabi.201900427.
32. Yang Q, Jones SW, Parker CL, Zamboni WC, Bear JE, Lai SK (2014) Evading immune cell uptake and clearance requires PEG grafting at densities substantially exceeding the minimum for brush conformation. *Molecular pharmaceutics* 11(4), 1250–1258. 10.1021/mp400703d.
33. Darko A, Wallace S, Dmitrenko O, Machovina MM, Mehl RA, Chin JW, Fox JM (2014) Conformationally Strained trans-Cyclooctene with Improved Stability and Excellent Reactivity in Tetrazine Ligation. *Chemical science* 5(10), 3770–3776. 10.1039/C4SC01348D.
34. Karver MR, Weissleder R, Hilderbrand SA (2011) Synthesis and evaluation of a series of 1,2,4,5-tetrazines for bioorthogonal conjugation. *Bioconjugate Chemistry* 22(11), 2263–2270. 10.1021/bc200295y.
35. Leenson IA (1999) Old Rule of Thumb and the Arrhenius Equation. *J. Chem. Educ.* 76(10), 1459. 10.1021/ed076p1459.
36. Kramer S, Svatunek D, Alberg I, Gräfen B, Schmitt S, Braun L, van Onzen AHAM, Rossin R, Koynov K, Mikula H, Zentel R (2019) HEMA-Based Nanoparticles for Fast, Bioorthogonal iEDDA Ligation. *Biomacromolecules* 20(10), 3786–3797. 10.1021/acs.biomac.9b00868.
37. Maslanka Figueroa S, Fleischmann D, Beck S, Tauber P, Witzgall R, Schweda F, Goepferich A (2020) Nanoparticles Mimicking Viral Cell Recognition Strategies Are Superior Transporters into Mesangial Cells. *Advanced Science* 7(11), 1903204. 10.1002/adv.201903204.

Switchable Target Cell Recognition

Chapter 4

Chapter 4

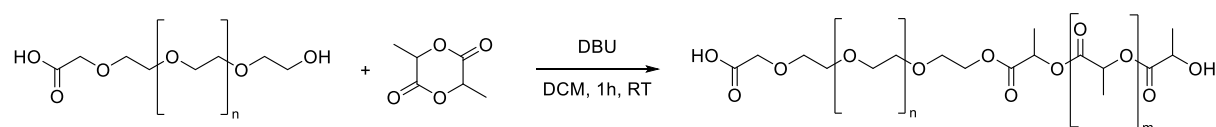
Supplementary Information

I. Synthesis of PLA-PEG block copolymers

General method for the synthesis of block copolymers

The synthesis of PLA-PEG block copolymers reported by our group [1, 2] is based on the method of Qian, Wohl et al. [3] with minor adaptations. Initially, cyclic lactide (3,6-dimethyl-1,4-dioxane-2,5-dione) was purified by recrystallization from anhydrous ethyl acetate (boiling point 77°C; set oil bath to 90°C; reflux, gentle stirring, initial solute:solvent ratio 1:2; added to saturation, and cooled with an ice slurry, followed by solvent removal with a pipette) and dried under vacuum overnight at 40°C. The PEG derivatives, serving as macroinitiators for ring-opening polymerization, were also dried overnight at 40°C using an oil vacuum pump. The respective PEG was then dissolved in anhydrous DCM, and the purified 3,6-dimethyl-1,4-dioxane-2,5-dione was added. Subsequently, 1,8-diazabicyclo[5.4.0]undec-7-ene (DBU) was added as a catalyst for polymerization. After stirring at room temperature for 1 hour, the polymerization was quenched with benzoic acid. The reaction mixture was precipitated in at least ten times its volume of ice-cold diethyl ether and centrifuged (4°C, 3000 g for 10 minutes). The supernatant was discarded, and the pellet was briefly dried before being dissolved in acetonitrile and precipitated again. The precipitation-centrifugation-dissolution cycle was repeated twice for further purification. The pellets of PLA-PEG block copolymers were finally dried under vacuum and ¹H NMR spectra (approximately 10 mg block copolymer in 0.7 mL CDCl₃) were recorded on a Bruker Avance III HD 400 (Bruker BioSpin GmbH, Rheinstetten, Germany).

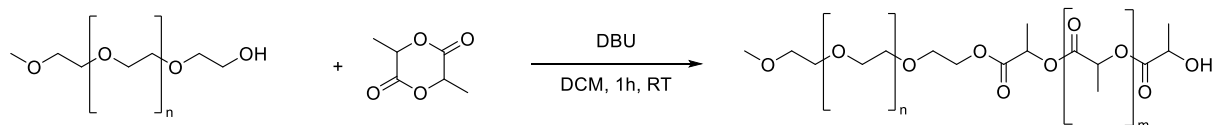
Synthesis of PLA10k-PEG2k-COOH



PLA10k-PEG2k-COOH was synthesized according to the general method using 808 mg (0.40 mmol, 1 equiv.) COOH-PEG2k-OH, 4608 mg (31.97 mmol, 79.1 equiv.) 3,6-dimethyl-1,4-dioxane-2,5-dione, 241 μ L (1.62 mmol, 4 equiv.) DBU and 494 mg (4.04 mmol, 10 equiv.) benzoic acid to quench the reaction. After purification, 4.99 g (0.38 mmol, 94%) of the desired product were obtained ($M_n = 13145$ g/mol).

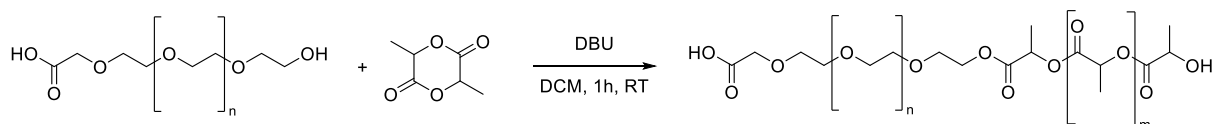
Supplementary Information - Switchable Target Cell Recognition

Synthesis of PLA10k-PEG2k-OMe



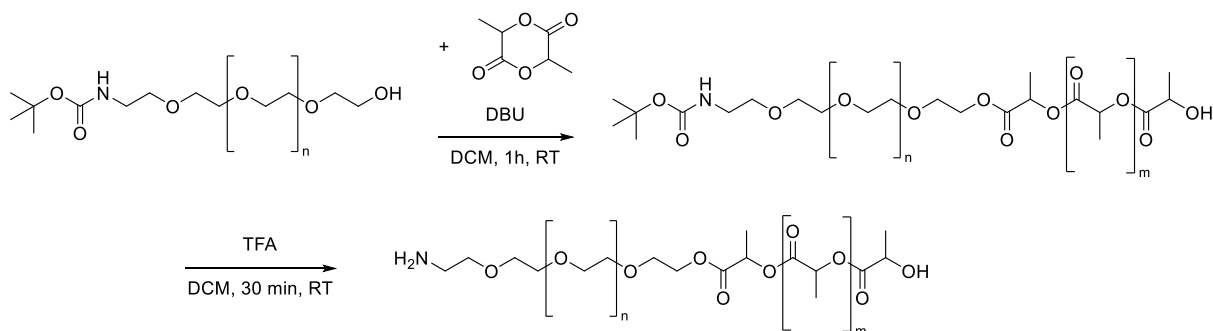
PLA10k-PEG2k-OMe was prepared starting from 250 mg (0.125 mmol, 1 equiv.) of mPEG2k-OH with 1425 mg (9.89 mmol, 79.1 equiv.) of freshly recrystallized 3,6-dimethyl-1,4-dioxane-2,5-dione according to the general method. The catalyst used was 38.8 μ L (0.25 mmol, 2 equiv.) DBU. The reaction was quenched with 153 mg (1.25 mmol, 10 equiv.) benzoic acid. Finally, 1.42 g (0.11 mmol, 92%) of PLA10k-PEG2k-MeO ($M_n = 12893$ g/mol) were obtained.

Synthesis of PLA10k-PEG5k-COOH



To synthesize PLA10k-PEG5k-COOH, 0.80 g (0.16 mmol, 1 equiv.) of COOH-PEG5k-OH was reacted with 1.60 g (11.1 mmol, 69.4 equiv.) of 3,6-dimethyl-1,4-dioxane-2,5-dione. The synthesis was carried out according to the general method using 96 μ L (0.64 mmol, 4 equiv.) DBU as catalyst. The reaction was terminated by the addition of 195 mg (1.6 mmol, 10 equiv.) benzoic acid to yield 1.94 g (0.13 mmol, 81%) of the desired product after purification ($M_n = 14932$ g/mol).

Synthesis of PLA10k-PEG5k-NH₂



PLA10k-PEG5k-NH₂ was synthesized according to the general method using 900 mg (0.18 mmol, 1 equiv.) tBoc-NH-PEG5k-OH, 2052 mg (14.24 mmol, 79.1 equiv.) 3,6-dimethyl-1,4-dioxane-2,5-dione

Chapter 4 – Supplementary Information

and 56 μL (0.36 mmol, 2 equiv.) DBU. The reaction was quenched with 220 mg (1.8 mmol, 10 equiv.) benzoic acid. The still Boc-protected polymer must be further deprotected. For this purpose, tBoc-NH-PEG5k-PLA10k was dissolved in a minimal amount of DCM (10 mL) and half of this volume of trifluoroacetic acid (5 mL) was added. The solution was incubated at room temperature for a maximum of 30 minutes and then precipitated in ice-cold diethyl ether (4x 40 mL). To remove trifluoroacetic acid, the precipitation-centrifugation-dissolution cycle was repeated three more times. The product was then dried under vacuum as in the general method. Finally, 2.05 g (0.13 mmol, 74%) of PLA10k-PEG5k-NH₂ ($M_n = 15384$ g/mol) were obtained.

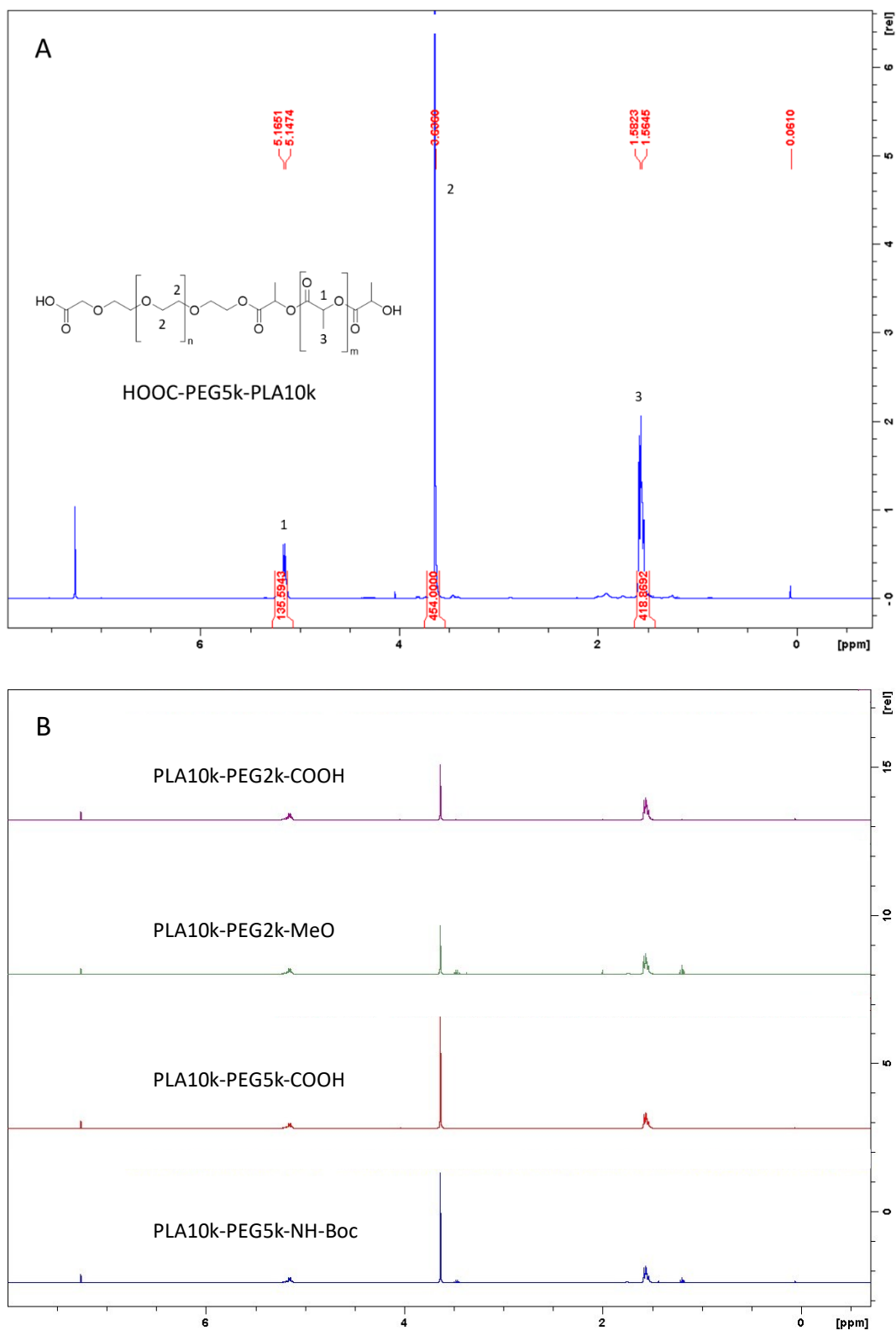
Characterization of PLA-PEG block copolymers via ¹H NMR

The number-average molecular weight of PLA-PEG block copolymers was determined by integrating the signals in the ¹H NMR spectrum using TopSpin Software 4.0.8 (Bruker Corporation, Billerica, MA, USA). For commercially acquired PEG derivatives, the molecular weight is known, and using the molecular weight of a repeat unit in the PEG chain (44.03 g/mol), the units per PEG chain can be calculated. Multiplying by 4 for the four protons per PEG unit (-OCH₂CH₂-) yields an integral of approximately 182 for PEG2kDa and approximately 454 for PEG5kDa. The integrals were set accordingly, and the integrals of the PLA signals were evaluated in relation to them.

$$M(\text{PLA} - \text{PEG}) = \frac{\frac{A_{\text{PLA CH}_3}}{3} + \frac{A_{\text{PLA CH}}}{1}}{2} \cdot 72.06 \frac{\text{g}}{\text{mol}} + M(\text{PEG}) \quad (\text{SI 1})$$

Poly(lactic acid) is responsible for a peak at approximately 1.6 ppm (-CH₃) and another at approximately 5.2 ppm (-CH-). The values for the integrals were divided by the number of protons per unit to determine the number of PLA units. The mean was multiplied by the molecular weight of the PLA unit (72.06 g/mol) to obtain the number-average molecular weight of the PLA polymer block. Adding the known molecular weight of the PEG segment provides the total molecular weight of the block copolymer (compare eq. SI 1).

Supplementary Information - Switchable Target Cell Recognition

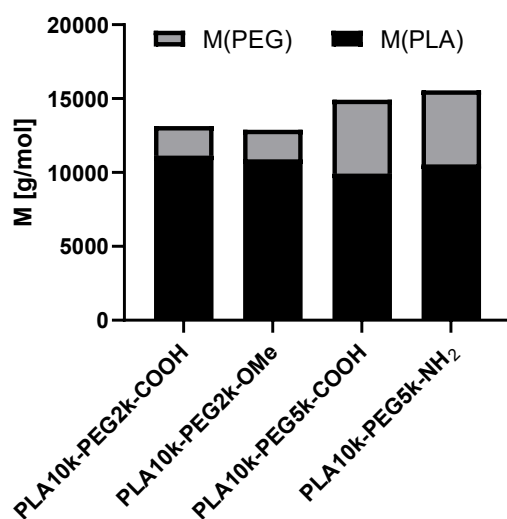


SI Figure 1. ^1H NMR spectra for the characterization of the synthesized PLA-PEG block copolymers. (A) ^1H NMR of PLA10k-PEG5k-COOH as an example for the assignment of the signals and the determination of the molecular weight. ^1H NMR (CDCl₃): $\delta = 7.26$ (solvent peak), 5.17 (m, 136H, -C(CH₃)H-), 3.64 (s, 454H, -OCH₂CH₂-), 1.56 (m, 419H, -C(CH₃)H-). $M(\text{PLA-PEG}) = 14\,932$ g/mol. (B) Overview of all ^1H NMR spectra of the synthesized copolymers.

Chapter 4 – Supplementary Information

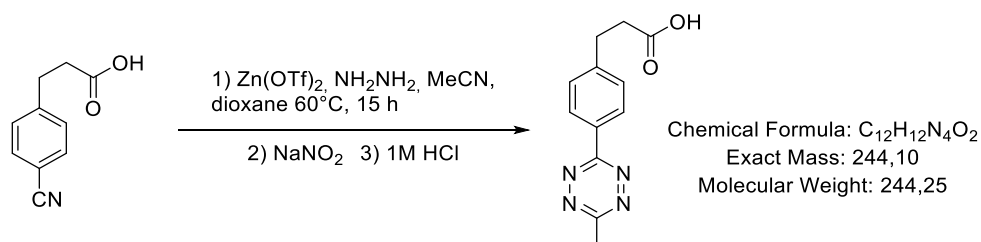
PLA-PEG block copolymers as a basis for polymer NPs

The ring-opening polymerization of cyclic lactide with the corresponding PEG derivatives as macroinitiators is ideally suited to synthesize the desired PLA-PEG block copolymers. The PLA segment was approximately 10kDa as determined by ^1H NMR (see SI Figure 2). The PLA-PEG block copolymers with different functional groups at the PEG end served as the basis for the polymer NPs. While PLA10k-PEG2k-COOH and -MeO with their shorter PEG chains were used as filler polymers, the copolymers with the longer PEG chains, PLA10k-PEG5k-COOH and -NH₂, were further modified with ligands.



SI Figure 2. Molecular weight of all synthesized PLA-PEG block copolymers determined by ^1H NMR.

II. Synthesis of the tetrazine ligand



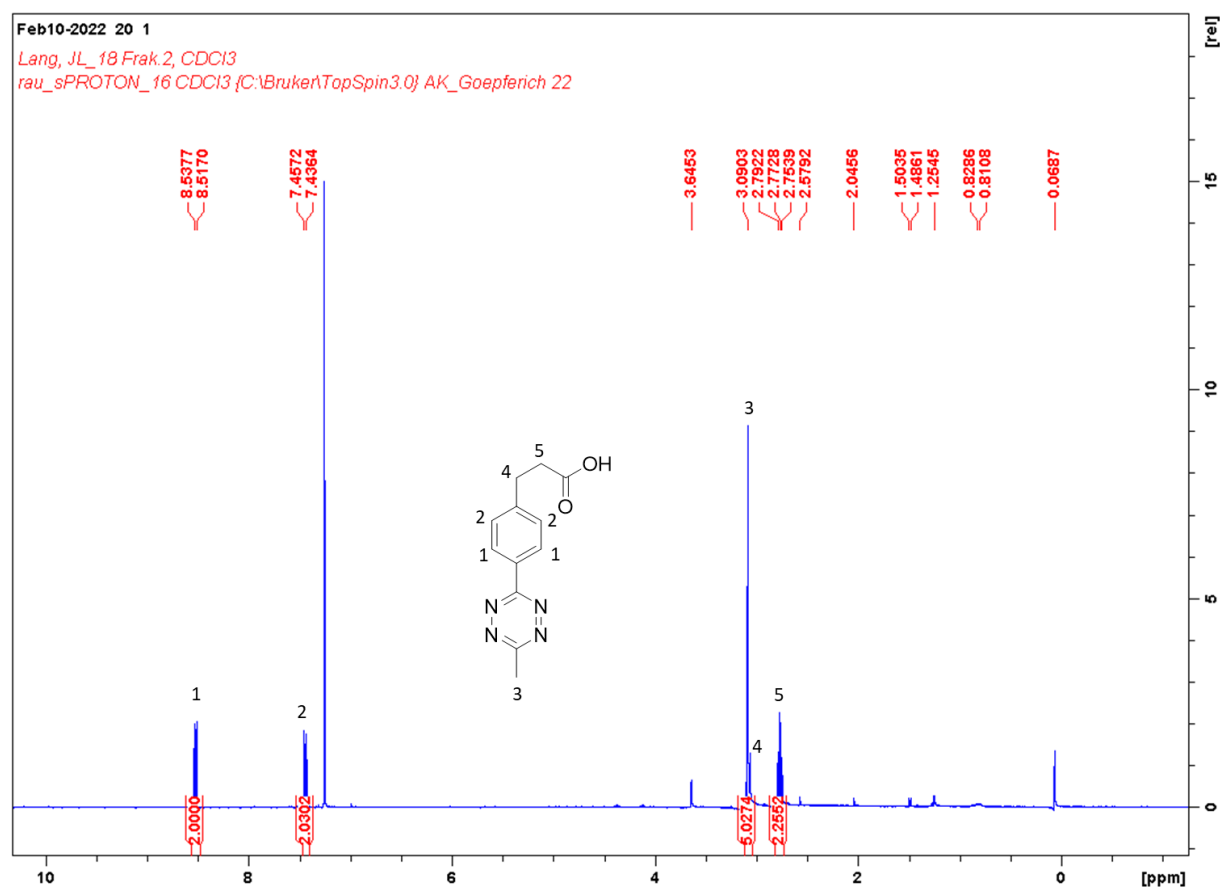
The synthesis of methyltetrazine phenylpropionic acid was based on the procedure of Meimetis, Weissleder et al. [4] with minor modifications. To the nitrile (3-(4-cyanophenyl)-propionic acid; 0.876

Supplementary Information - Switchable Target Cell Recognition

g, 5 mmol, 1 equiv) under a stream of argon was added zinc triflate (0.911 g, 2.5 mmol, 0.5 equiv) as Lewis acid catalyst, acetonitrile (2.6 mL, 50 mmol, 10 equiv), hydrazine monohydrate (N₂H₄ 64-65 %; 12 mL, 250 mmol, 50 equiv) and 6 mL dioxane. The microwave reaction tube was sealed and stirred at 60°C for 15 h. It was then allowed to cool, the septum was removed and sodium nitrite (6.906 g, 100 mmol, 20 equiv) in 10 mL of water was added to the reaction mixture followed by hydrochloric acid until pH = 3 was reached. The nitrous gas produced oxidizes the dihydrotetrazine intermediate into the corresponding tetrazine, whereby the formation of tetrazine results in a colour change to intense pink. The aqueous phase was extracted three times with DCM (250 mL) and subsequently the combined organic extracts were dried with magnesium sulfate. The raw mixture was concentrated on the rotary evaporator and adsorbed onto silica gel. The product was isolated using column chromatography (hexanes : ethyl acetate gradient, 3:1 to 1:3) to yield methyltetrazine phenylpropionic acid (3-(4-(6-methyl-1,2,4,5-tetrazin-3-yl)phenyl)propanoic acid; 507.1 mg, 2.08 mmol, 42%) as a deep purple solid.

¹H NMR (CDCl₃): δ = 8.54–8.52 (d, J = 8.4 Hz, 2H), 7.46–7.44 (d, J = 8.4 Hz, 2H), 3.11–3.07 (m, 5H), 2.79-2.75 (t, J = 7.7 Hz, 2H).

MS (ESI, m/z): Calculated for ([C₁₂H₁₂N₄O₂]+H)⁺ ([M+H]⁺): 254.1078, Found: 245.1034.

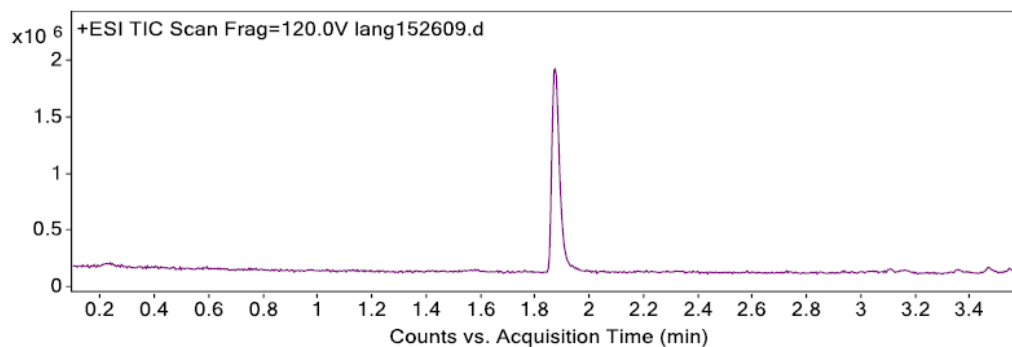


SI Figure 3. ¹H NMR spectra of methyltetrazine phenylpropionic acid recorded in CDCl₃ at 400 MHz.

Chapter 4 – Supplementary Information

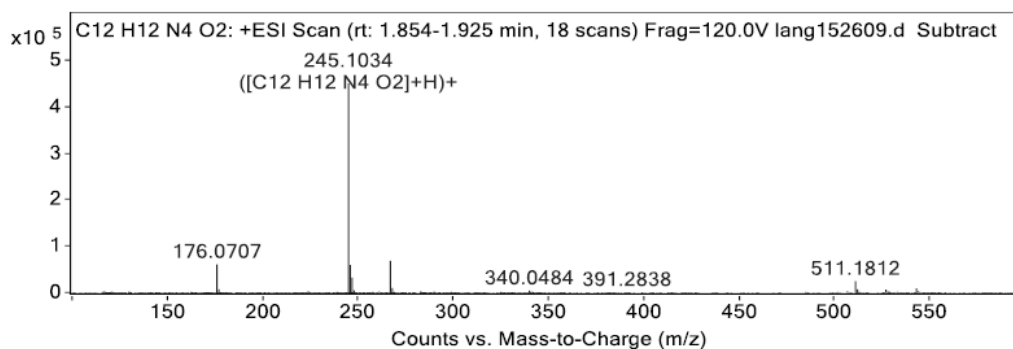
Chromatograms

Fragmentor Voltage 120 Collision Energy 0 Ionization Mode ESI



Spectra

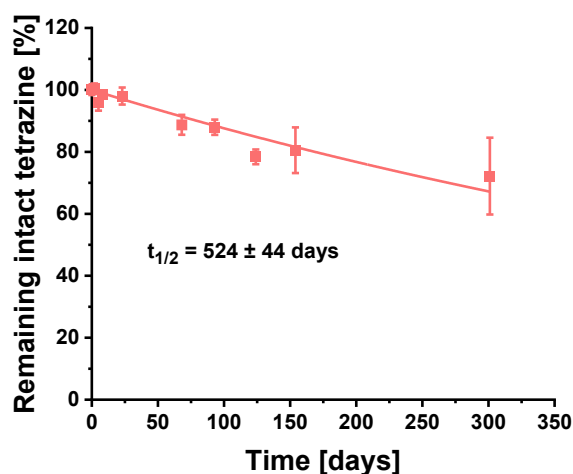
Spectrum Source Peak (1) in "+ EIC(245.1032) Scan" Fragmentor Voltage 120 Collision Energy 0 Ionization Mode ESI



Tetrazine stability at 37°C in PBS

The tetrazine solution in PBS was incubated at 37°C in a water bath, and samples were taken at specified time intervals. The absorbance of the samples at 520 nm was measured in triplicate in a transparent 96-well plate. The decrease in absorbance was plotted relative to the initial absorbance, and the data were fitted with an exponential decay.

Supplementary Information - Switchable Target Cell Recognition



SI Figure 4. Tetrazine stability at 37°C in PBS. Data fitted with an exponential decay. Results are presented as mean \pm SD (n = 3).

The decrease in tetrazine absorption at 520 nm served as a measure of tetrazine decomposition. As shown in **SI Figure 4**, the synthesized methyl-substituted tetrazine is highly stable when incubated at 37°C in PBS, with a half-life significantly exceeding one year. In general, methyl-substituted tetrazines are very stable, which was confirmed for the derivative here.

III. Coupling of the ligands to the PLA-PEG block copolymers

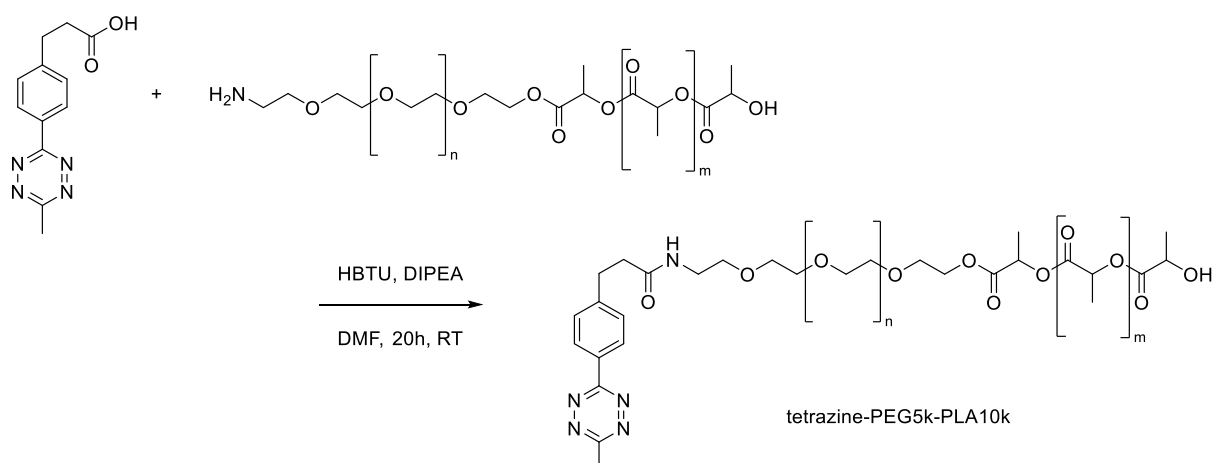
General Method for Purification of the Polymer after Ligand Coupling

Following an adequate reaction time for the coupling, the reaction mixture was precipitated in ice-cold diethyl ether (in 50 mL centrifuge tubes from the -80°C freezer, at least 10 times the volume of the reaction mixture) and subsequently centrifuged at 4°C (3000 g, until the supernatant was no longer turbid, and a well-defined pellet had formed, typically 10 minutes). The supernatant was discarded, and the pellet was dried before being dissolved in acetonitrile. This precipitation-centrifugation-dissolution cycle was repeated once more. Finally, the precipitate was dissolved in MeCN, and the solution was added dropwise into vigorously stirring Millipore water. The resulting polymeric micelles were stirred for 2 hours. The product was further purified through dialysis (RC, 6-8 kDa MWCO) against 4 L Millipore water for at least 6 hours with a minimum of 3 water changes. The block copolymer was lyophilized for 3 days (typically 48 h primary drying at -20°C and 0.0010 mbar, and 20 h secondary

Chapter 4 – Supplementary Information

drying at 25°C and 0.0050 mbar) using a Christ freeze dryer Alpha 2-4 LSCplus (Martin Christ Gefriertrocknungsanlagen GmbH, Osterode am Harz, Germany). For product characterization, a ^1H NMR in CDCl_3 or DMSO-d_6 was recorded on a Bruker Avance III HD 400 (Bruker BioSpin GmbH, Rheinstetten, Germany). The molar mass of the block copolymers post-coupling was determined, as described in Section I, based on the known PEG integral. The coupling efficiency was also estimated via ^1H NMR relative to the PEG integral. The signals were assigned to the protons of the ligands, integrated and the integral was divided by the number of expected protons. The mean value was formed from all the coupling efficiencies determined in this manner and the standard deviation was calculated.

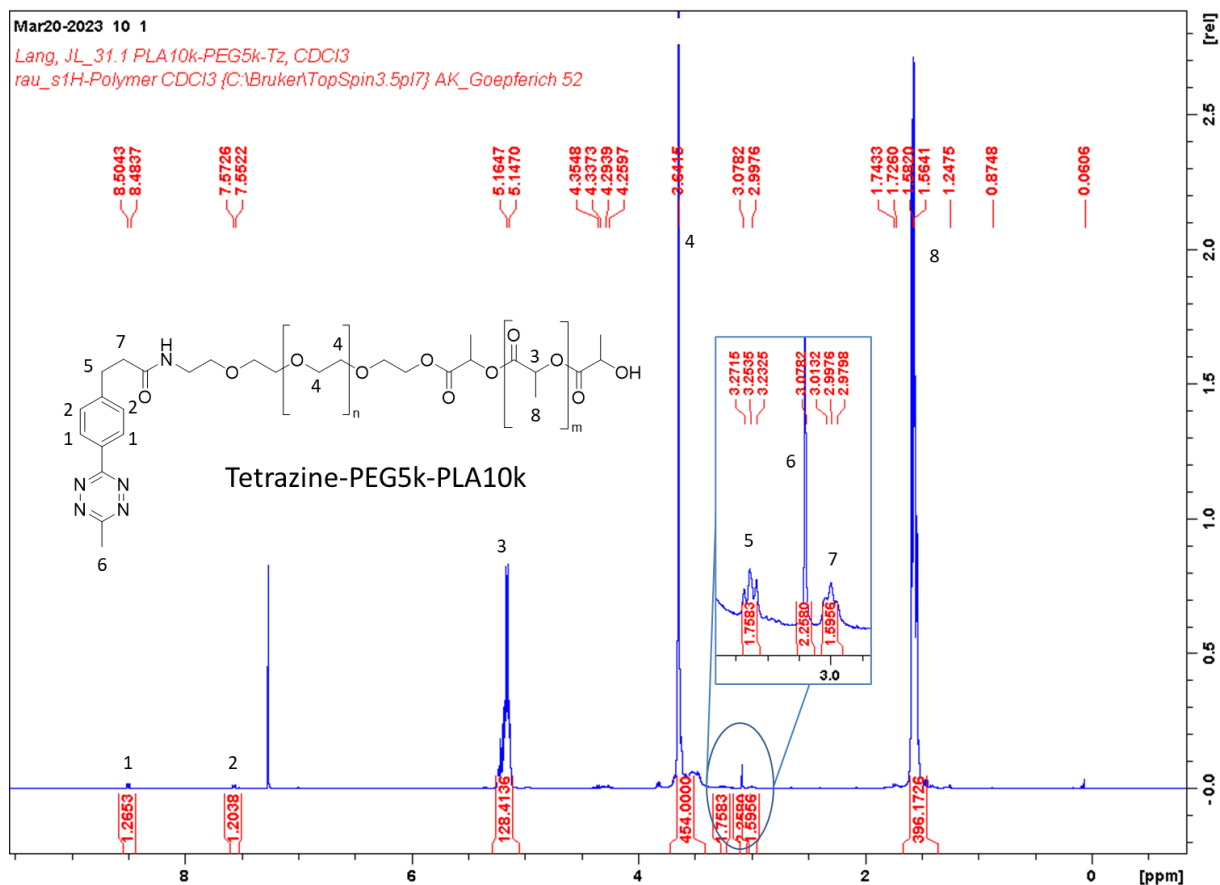
Synthesis of PLA10k-PEG5k-tetrazine



Methyltetrazine phenylpropanoic acid (15.9 mg, 65 μmol , 2.5 equiv.) was dissolved in 6 mL anhydrous DMF and DIPEA (44.2 μL , 260 μmol , 10 equiv.) was added. HBTU (49.3 mg, 130 μmol , 5 equiv.) was also dissolved in 6 mL DMF and slowly added to the reaction mixture. Finally, the block copolymer PLA10k-PEG5k- NH_2 (400 mg, 26 μmol , 1 equiv.) was added and the reaction mixture was stirred at RT overnight. The product was purified according to the general method for polymer purification after ligand coupling (described in Section III), and 364 mg of PLA10k-PEG5k-tetrazine (25 μmol , 96%) were obtained as a pink lyophilizate.

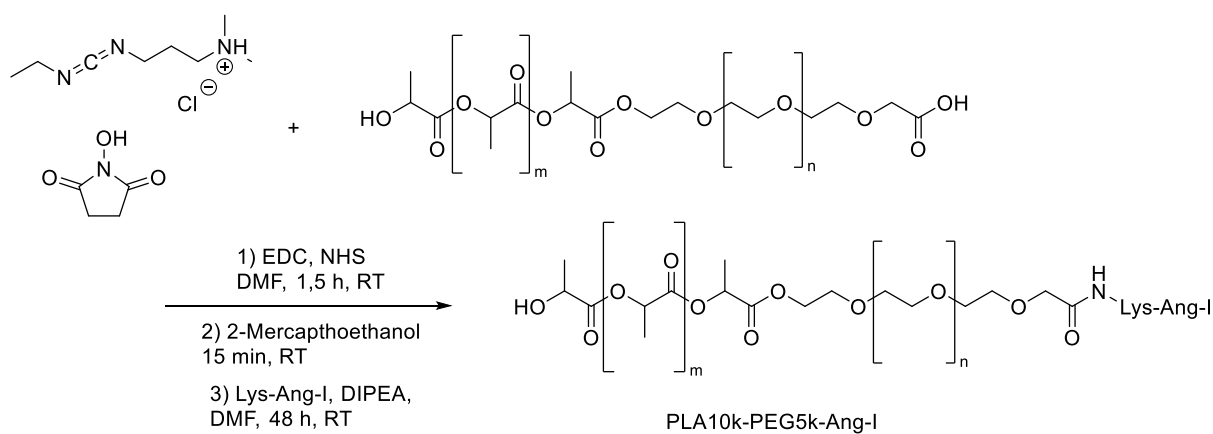
^1H NMR (CDCl_3): δ = 8.49 (d, J = 8.3 Hz, 1.27H), 7.56 (d, J = 8.2 Hz, 1.20H), 5.16 (m, 128H), 3.64 (s, 454H), 3.25 (t, 1.76H), 3.08 (s, 2.26H), 3.00 (t, 1.60H), 1.56 (m, 396H). $M(\text{PLA10k-PEG5k-tetrazine})$ = 14 594 g/mol. Coupling efficiency determined via ^1H NMR 73 ± 12 %.

Supplementary Information - Switchable Target Cell Recognition



SI Figure 5. ¹H NMR spectra of PLA10k-PEG5k-tetrazine recorded in CDCl₃ at 400 MHz.

Synthesis of PLA10k-PEG5k-Ang-I

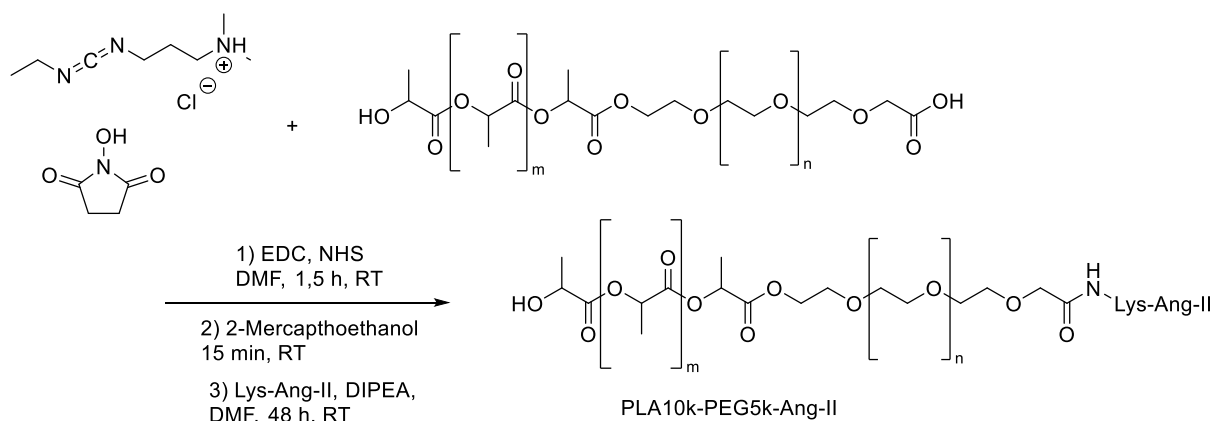


Chapter 4 – Supplementary Information

The block copolymer PLA10k-PEG5k-COOH (287 mg, 19 μmol , 1 equiv.) was activated for 90 min with EDC (36.4 mg, 190 μmol , 10 equiv.) and NHS (21.9 mg, 190 μmol , 10 equiv.) in 4 mL anhydrous DMF. Then 2-mercaptoethanol (19.9 μL , 285 μmol , 15 equiv.) was added and the reaction mixture was stirred at RT for another 15 min. Finally, DIPEA (16.2 μL , 95 μmol , 5 equiv.) was added and Lys-Ang-I (40.6 mg, 29 μmol , 1.5 equiv.), dissolved in 3 mL anhydrous DMF, was added dropwise to the reaction mixture. The reaction was stirred at RT for 48 h and the work-up was carried out according to the general method. 220 mg (16.3 μmol , 86%) of the desired product were obtained as a white lyophilizate.

$^1\text{H NMR}$ (DMSO- d_6): δ = 7.24 (m, 4.82H, aromatic protons of phenylalanine), 6.97 (m, 1.23H, aromatic protons of tyrosine), 6.64 (m, 0.88H, aromatic protons of tyrosine), 5.18 (m, 117H), 3.49 (s, 454H), 1.45 (m, 362H). $M(\text{PLA10k-PEG5k-Ang-I}) = 14\,970\text{ g/mol}$. Coupling efficiency determined via $^1\text{H NMR}$ $67 \pm 27\%$.

Synthesis of PLA10k-PEG5k-Ang-II

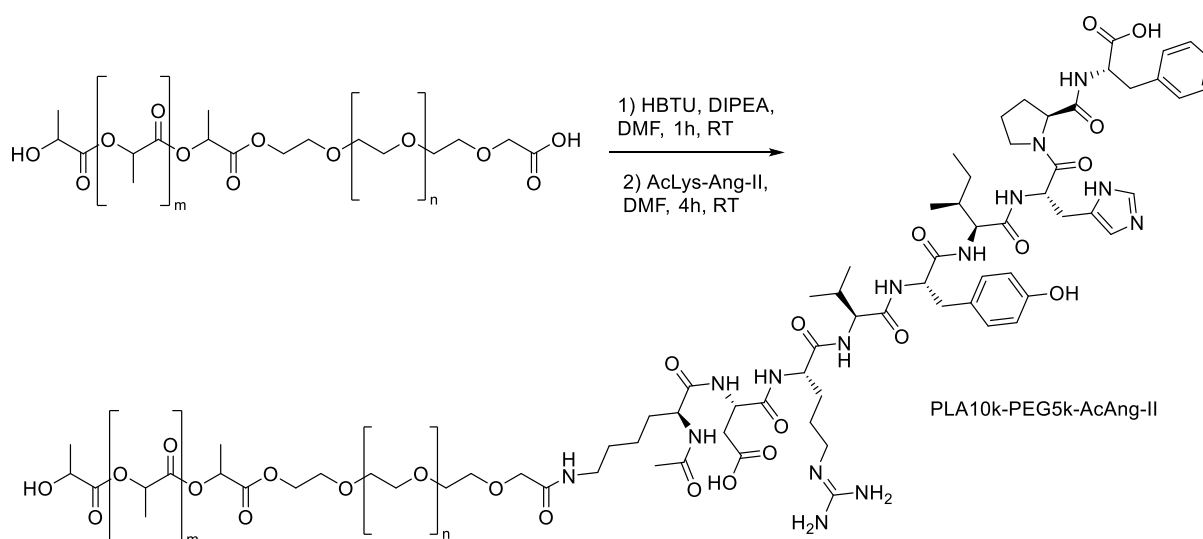


The block copolymer PLA10k-PEG5k-COOH (200 mg, 13.8 μmol , 1 equiv.), EDC (66 mg, 172.5 μmol , 12.5 equiv.) and NHS (40 mg, 172.5 μmol , 12.5 equiv.) were dissolved in 1 mL anhydrous DMF and stirred for 3 h at RT. 120 μL of 2-mercaptoethanol (862.5 μmol , 62.5 equiv.) were added to quench excess EDC. To the reaction mixture 23 μL DIPEA (66.0 μmol , 4.8 equiv.) were added. The lysine-N-modified angiotensin II (19.6 mg, 16.7 μmol , 1.2 equiv.) was dissolved in 0.5 mL anhydrous DMF and added dropwise. The reaction mixture was stirred for 48 h at RT. After purification, 178 mg PLA10k-PEG5k-Ang-II (11.6 μmol , 84%) were yielded as a white lyophilizate.

Supplementary Information - Switchable Target Cell Recognition

^1H NMR (DMSO- d_6): δ = 7.17 (m, 2.19H, aromatic protons of phenylalanine), 7.00 (m, 0.60H, aromatic protons of tyrosine), 6.59 (m, 1.17H, aromatic protons of tyrosine), 5.19 (m, 128H), 3.50 (s, 454H), 1.46 (m, 385H). $M(\text{PLA10k-PEG5k-Ang-I}) = 15\,392$ g/mol. Coupling efficiency determined via ^1H NMR 44 ± 14 %.

Synthesis of PLA10k-PEG5k-AcAng-II



The block copolymer PLA10k-PEG5k-COOH (211.38 mg, 14 μmol , 1 equiv.) and HBTU (5.3 mg, 14 μmol , 1 equiv.) were dissolved in 4.5 mL anhydrous DMF and then DIPEA (11.9 μL , 70 μmol , 5 equiv.) was added. The reaction mixture was stirred at RT for 1 h, thereby activating the carboxylic acid on the polymer. Finally, AcLys-Ang-II (20.4 mg, 17 μmol , 1.2 equiv.) was added and the reaction was stirred at RT for at least 4 more hours. Purification was performed according to the general method (described in section III) to yield 169 mg PLA10k-PEG5k-AcAng-II (12.0 μmol , 86%) as a white lyophilizate.

^1H NMR (DMSO- d_6): δ = 7.14 (m, 3.65H, aromatic protons of phenylalanine), 7.01 (d, $J = 8.3$ Hz, 1.28H, aromatic protons of tyrosine), 6.60 (d, $J = 8.4$ Hz, 1.21H, aromatic protons of tyrosine), 5.18 (m, 110H), 3.50 (s, 454H), 1.45 (m, 333H). $M(\text{PLA10k-PEG5k-AcAng-II}) = 14\,161$ g/mol. Coupling efficiency determined via ^1H NMR 66 ± 6 %.

Chapter 4 – Supplementary Information

Determination of Coupling Efficiencies

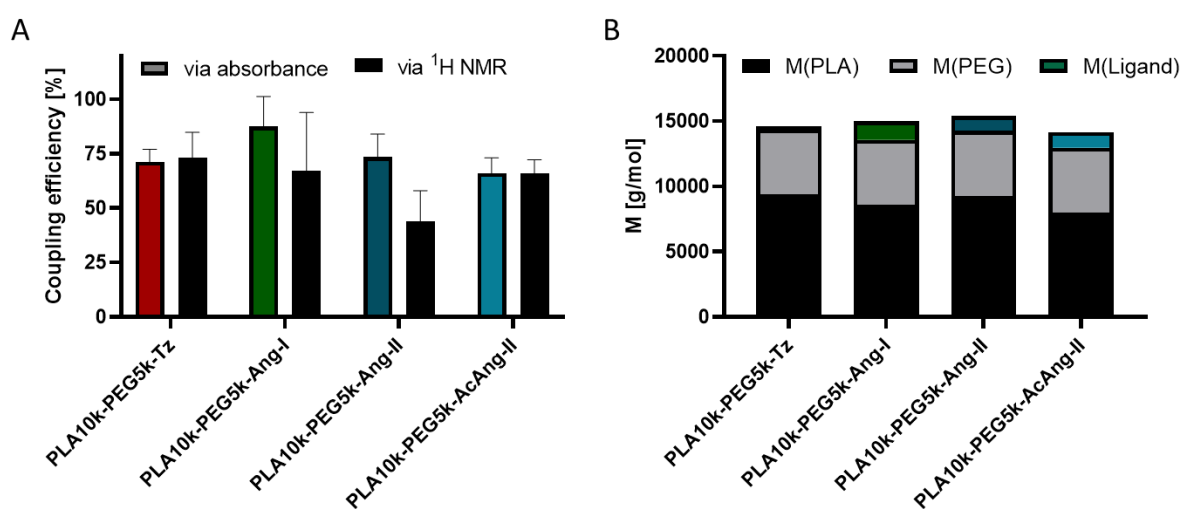
The coupling efficiency of tetrazine to PLA10k-PEG5k-NH₂ was assessed photometrically by measuring the absorption of tetrazine at 540 nm. The purified product, PLA10k-PEG5k-Tz, was dissolved in DMSO, and the absorbance of a 2.5 mM solution was measured in a transparent 384-well plate using an FLUOstar Omega microplate reader (BMG Labtech, Ortenberg, Germany). Calibration was performed using free tetrazine, also dissolved in DMSO (0.5 to 3 mM). The tetrazine concentration was determined based on the calibration curve, allowing for the calculation of coupling efficiency relative to the polymer concentration. To determine the coupling efficiency of Angiotensin ligands to the block copolymer PLA10k-PEG5k-COOH, polymer micelles were prepared. 200 μ L of a 20 mg/mL solution of the respective polymer in acetonitrile was dropwise added to 2 mL vigorously stirred (800 rpm) Millipore water. After 90 minutes of stirring, allowing for the evaporation of acetonitrile, a 2 mg/mL polymer micelle solution was obtained. The polymer micelle solution was used undiluted and diluted 1:2 and 1:4 with Millipore water. The Angiotensin content was quantified using a BCA assay following the manufacturer's protocol for the QuantiPro™ BCA Assay Kit (Sigma-Aldrich, St. Louis, MO, USA). For calibration, free Lys-Ang-I, -II, or AcLys-Ang-II (Genscript, Piscataway, NJ, USA) was diluted from a 10 mM solution in DMSO to suitable concentrations in Millipore water (15–75 μ M Angiotensin). After dispensing 40 μ L of polymer micelle solution or free Angiotensin in triplicate into a transparent 384-well plate, 40 μ L of QuantiPro working reagent was added per well. The solution was mixed by pipetting up and down. The plate was sealed with a plate sealer and incubated at 60°C for 1 hour. Subsequently, absorption at 562 nm was measured using a FLUOstar Omega microplate reader (BMG Labtech, Ortenberg, Germany). The molar polymer concentration was determined from the mass concentration of the polymer micelle solution using the molecular weight obtained via ¹H NMR. The molar concentration of Angiotensin determined by the calibration curve of the BCA assay was referenced to this concentration, allowing for the determination of the coupling efficiency of the Angiotensin ligand to the copolymer.

Ligand-modified PLA-PEG block copolymers

The ligand coupling using classical peptide chemistry with either HBTU or EDC/NHS as coupling reagents and DIPEA as a base in DMF was deemed acceptable; however, surprisingly, in most cases, coupling efficiency exceeding 90% was not achieved, as anticipated for this chemistry. For the coupling of tetrazine with carboxy functionality to PLA10k-PEG5k-NH₂ using HBTU, a coupling efficiency of slightly above 70% was determined. Evaluation through integration of signals in the ¹H NMR spectrum and measurement of tetrazine absorbance at 540 nm yielded nearly identical values. The signals of

Supplementary Information - Switchable Target Cell Recognition

tetrazine in the ^1H NMR spectrum of the ligand-modified polymer could be unequivocally assigned, while the assignment of signals for Angiotensin ligands proved challenging. Essentially, only the aromatic protons could be identified, specifically those of phenylalanine and tyrosine. Since these signals are marginally above the background noise, the coupling efficiency determined via ^1H NMR is to be interpreted more as an estimation. Through the BCA assay, coupling efficiencies of approximately 70% were determined for PLA10k-PEG5k-Ang-II and its acetylated variant PLA10k-PEG5k-AcAng-II, aligning well with the coupling efficiency of tetrazine (see SI Figure 6 A).



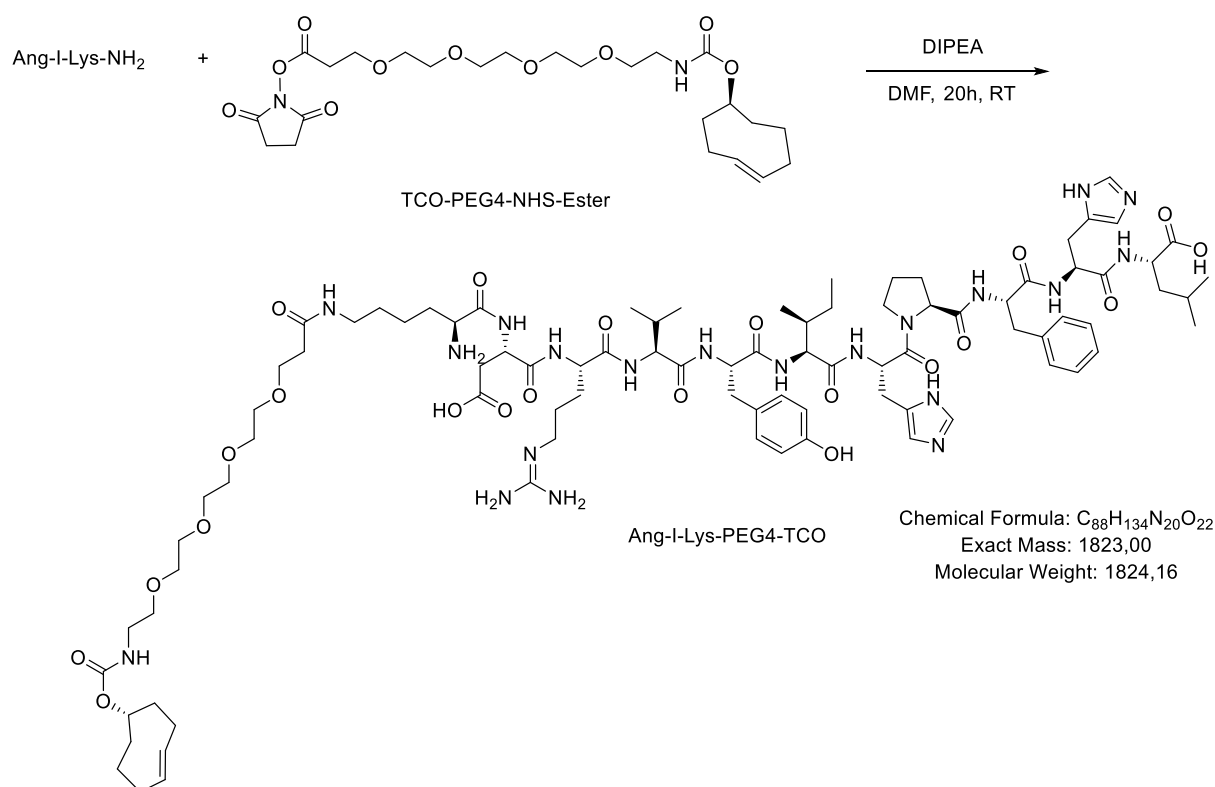
SI Figure 6. Characterization of ligand functionalized PLA-PEG block copolymers. (A) Coupling efficiency of the various ligands to the copolymer determined by absorbance (absorbance of the tetrazine at 540 nm or absorbance in the BCA assay for the angiotensin ligands at 562 nm) and by integration of the signals in the ^1H NMR spectrum. (B) Number-average molecular weight of the ligand functionalized PLA-PEG block copolymers determined by ^1H NMR spectroscopy.

As depicted in SI Figure 6 B, the molar mass of the PLA segment decreased, presumably due to the purification of ligand-modified polymers via dialysis. During dialysis, hydrolysis of the PLA segment of the PLA-PEG block copolymer occurs, allowing the degradation products of PLA to escape through the dialysis membrane. The PLA block no longer has a molar mass of 10 kDa but, depending on the dialysis time, ranges between approximately 8 and 9 kDa. Nevertheless, the polymers are referred to as PLA10k-PEG5k block copolymers throughout, irrespective of their actual reduced molar mass, to account for the starting material and maintain clarity in nomenclature. Together with the attached ligands, the ligand-modified polymers still exhibited a molar mass of approximately 15 kDa. When referring to independent experiments, it is understood as the preparation, concentration, and characterization of NPs on different experimental days. However, the same batch of ligand-modified polymer is used for the preparation.

Chapter 4 – Supplementary Information

A significant advantage of assembling NPs modularly from the specified polymers is the flexibility in composition variation. In cases of incomplete functionalization of the polymers, this can be compensated by increasing the respective polymer content in the formulation. Consequently, the number of ligands per NP can be customized, allowing consistent ligand density on the NPs even with varying coupling efficiencies.

IV. Synthesis of TCO-PEG₄-Ang-I

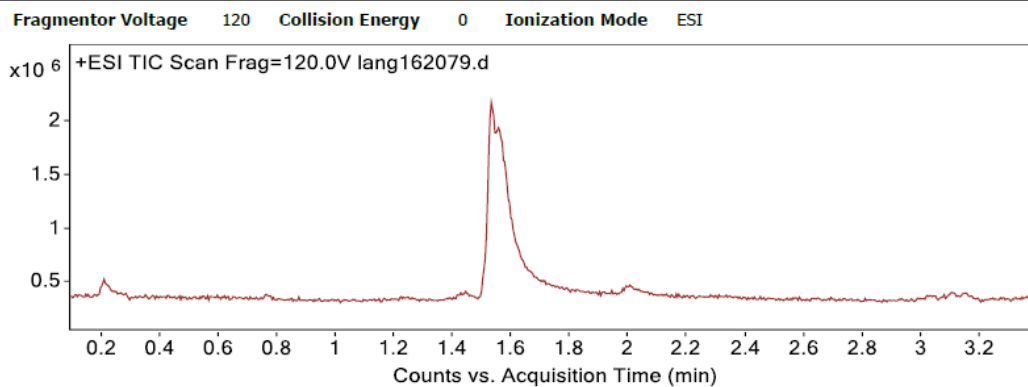


TCO-PEG₄-NHS ester (6.76 mg, 12.4 μmol, 1 equiv) and Lys-Ang-I (21.16 mg, 14.9 μmol, 1.2 equiv) were dissolved in 2 mL anhydrous DMF and 12.7 μL DIPEA (74.4 μmol, 5 equiv) were added. The yellowish reaction mixture was stirred overnight at room temperature and subsequently diluted with 3 mL Millipore water. Purification was achieved by preparative HPLC (0 min 10% ACN; 20 min 50% ACN; gradient 2%/min, product after approx. 14 min). After freeze-drying the product fraction, 7.58 mg of desired product TCO-PEG₄-Ang-I were obtained as a white solid (4.2 μmol, 34%).

MS (ESI, m/z): Calculated for ([C₈₈H₁₃₄N₂₀O₂₂]+3H)³⁺ ([M+3H]³⁺): 609.0078, Found: 609.0087;
Calculated for ([C₈₈H₁₃₄N₂₀O₂₂]+2H)²⁺ ([M+2H]²⁺): 913.0078, Found: 913.0084.

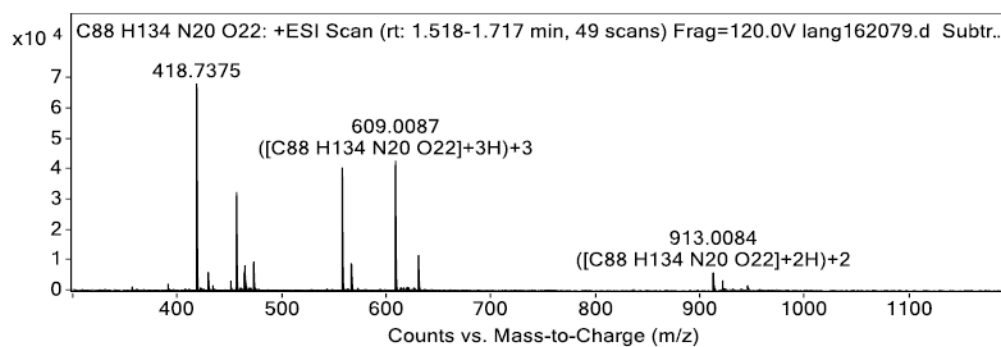
Supplementary Information - Switchable Target Cell Recognition

Chromatograms

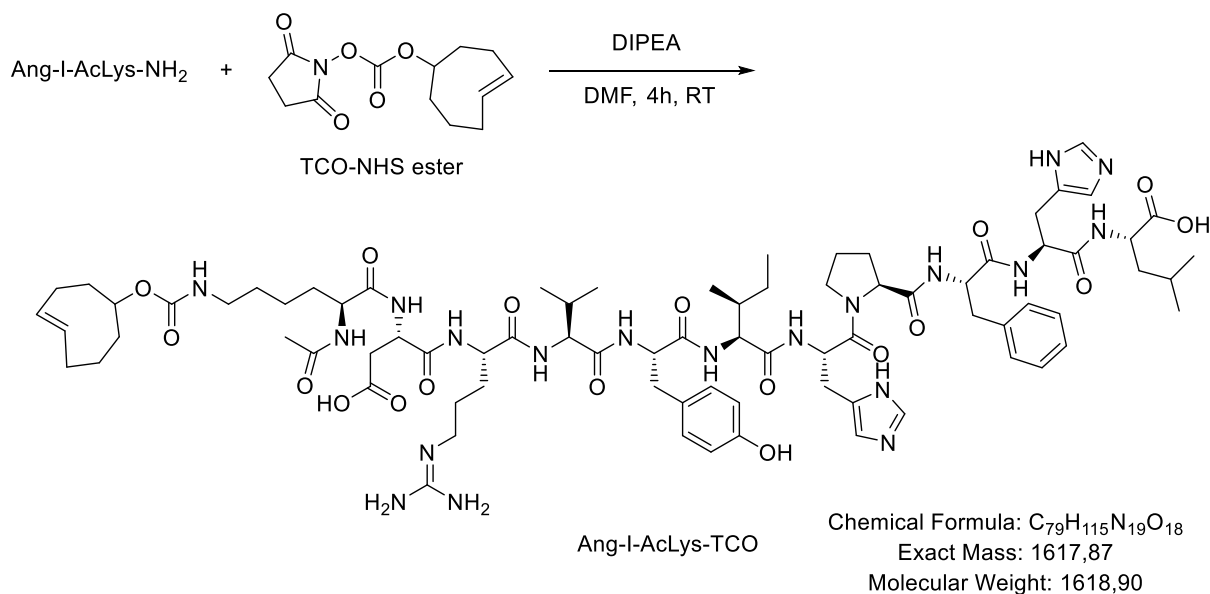


Spectra

Spectrum Source Peak (1) in "+ EIC(608.6754) Scan" Fragmentor Voltage 120 Collision Energy 0 Ionization Mode ESI



V. Synthesis of TCO-AcAng-I

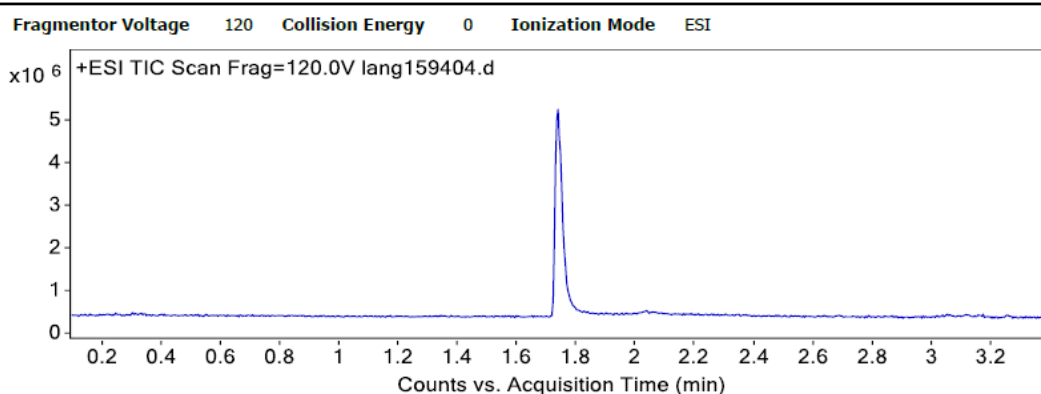


Chapter 4 – Supplementary Information

AcLys-Ang-I (34.86 mg, 23.9 μmol , 1 equiv) and trans-Cyclooctene-NHS ester (8.25 mg, 29.8 μmol , 1.25 equiv) were dissolved in 1 mL anhydrous DMF and 20 μL DIPEA (119.3 μmol , 5 equiv) were added. The reaction mixture was incubated at room temperature for 4 h and then purified by preparative HPLC (0 min 10% ACN; 20 min 50% ACN; gradient 2%/min, product after approx. 15 min). After freeze-drying, 22.43 mg of the desired product TCO-AcLys-Ang-I were obtained as a white lyophilizate (13.9 μmol , 58%).

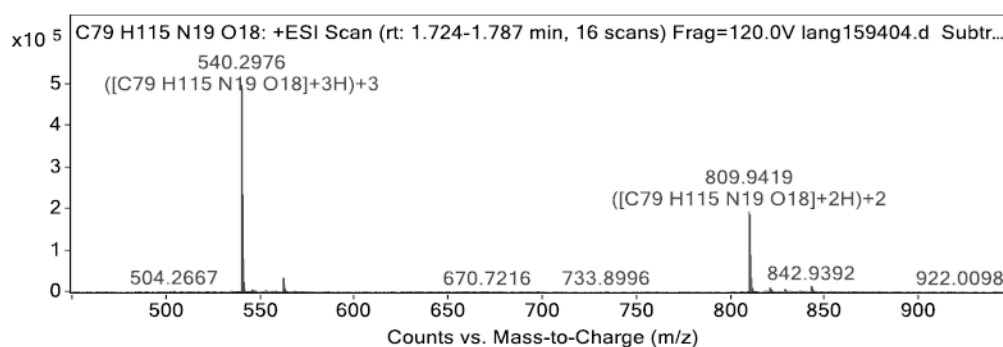
MS (ESI, m/z): Calculated for $([\text{C}_{79}\text{H}_{115}\text{N}_{19}\text{O}_{18}]+3\text{H})^{3+}$ ($[\text{M}+3\text{H}]^{3+}$): 540.2978, Found: 540.2976;
Calculated for $([\text{C}_{79}\text{H}_{115}\text{N}_{19}\text{O}_{18}]+2\text{H})^{2+}$ ($[\text{M}+2\text{H}]^{2+}$): 809.9428, Found: 809.9419.

Chromatograms

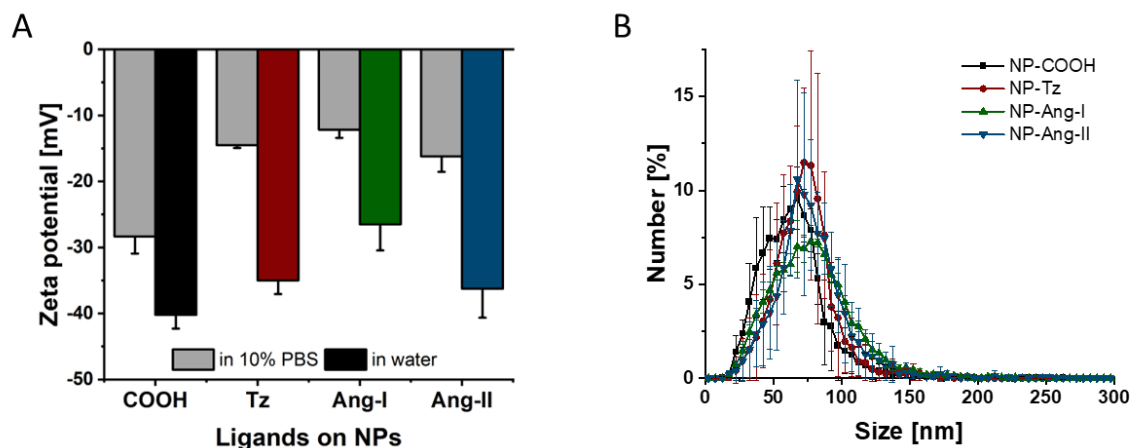


Spectra

Spectrum Source Fragmentor Voltage Collision Energy Ionization Mode
Peak (1) in "+ EIC(540.2980) Scan" 120 0 ESI



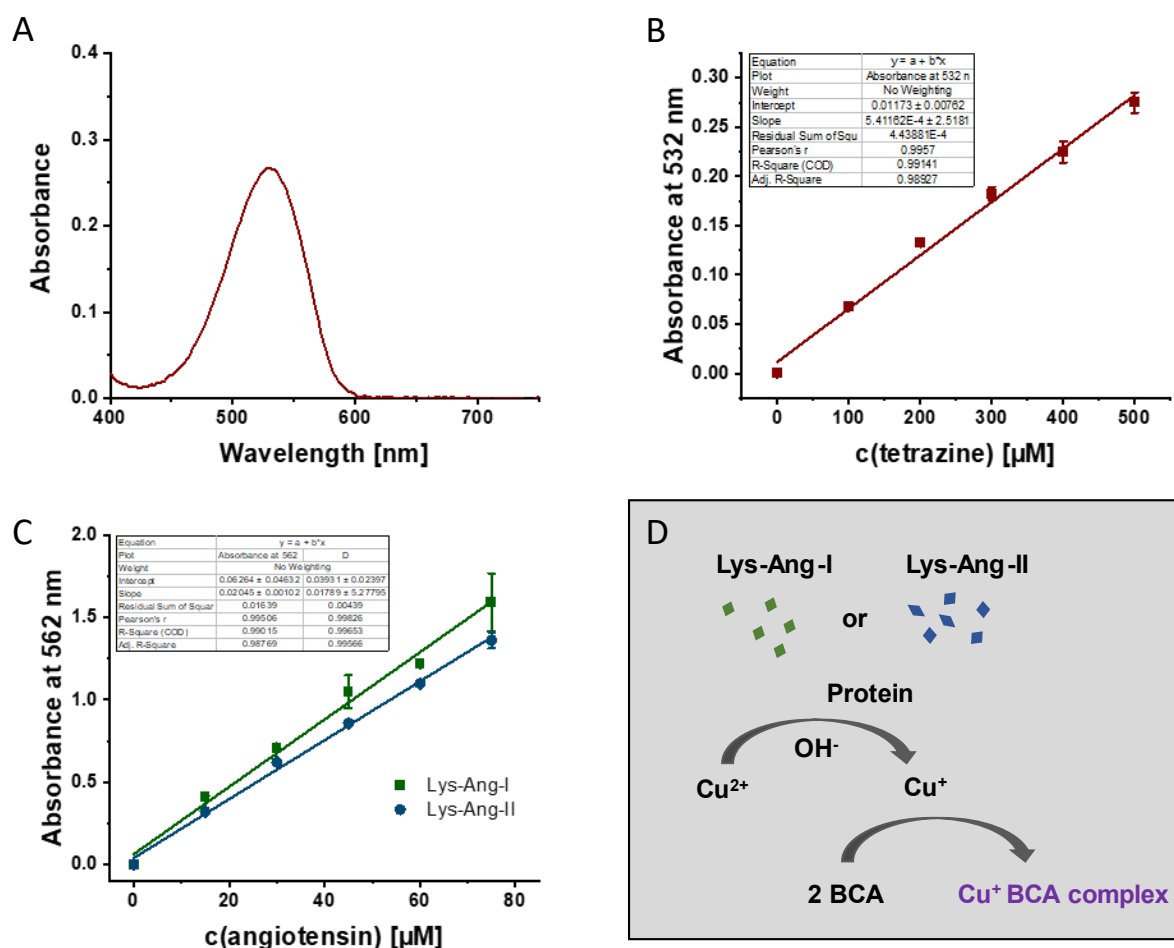
VI. Preparation and characterization of PEG-PLA copolymer NPs



SI Figure 7. Characterization of polymer NPs. (A) Zeta potential of the NPs measured after preparation in water, and for comparison, zeta potential of the NPs after concentration and subsequent dilution in 10% PBS to a 1 nM particle concentration. The zeta potential in water was determined from at least $N = 3$ experiments. The dilution of the concentrated NPs in 10% PBS was performed only once, and the results are presented here as mean \pm SD from $n = 3$ measurements. (B) Size distribution of the NPs determined by nanoparticle tracking analysis. Results are presented as mean \pm SD from at least $N = 3$ experiments.

For the zeta potential of the NPs measured after preparation in water, the same trend was observed as for the particles that were first concentrated and then diluted in 10% PBS, as expected (see **SI Figure 7 A**). The size distribution was similar for all particles, with NPs ranging from approximately 25 to 125 nm in hydrodynamic diameter (see **SI Figure 7 B**). In the paper, the mode value reported by the NanoSight is presented as the size d_h .

Chapter 4 – Supplementary Information



SI Figure 8. Quantification of ligands per NP. (A) Vis spectrum of 500 μM tetrazine in 50% DMSO and 50% water (v/v). (B) Calibration line for determination of tetrazine concentration in the NP sample. (C) Calibration line of the BCA assay with Ang-I and Ang-II for determination of angiotensin concentration in the NP samples. (D) Schematic representation of the principle of the bicinchoninic acid (BCA) assay. Results in (B) and (C) are presented as mean ± SD of an experiment with measurement in triplicate.

The angiotensin concentration in the NP samples was determined using a BCA assay. Cu^{2+} is reduced to monovalent copper ions by proteins, in this case either Ang-I or Ang-II, in an alkaline environment. In the presence of bicinchoninic acid (BCA) sodium salt, the copper ions Cu^+ form a purple complex with BCA (see **SI Figure 8 D**). This complex can be quantified by photometry at a wavelength of 562 nm. [5] Particularly, the amino acids cysteine, cystine, tryptophan, and tyrosine contribute to the reduction of divalent copper ions. Angiotensin containing tyrosine in the amino acid sequence can therefore be well analyzed by a BCA assay. At 60°C, Cu^{2+} is also reduced by the peptide bonds. [6] Presumably, this is why the calibration curve for Ang-I was slightly steeper than for Ang-II, as Ang-I consists of two more amino acids and thus also introduces two more peptide bonds.

VII. PEG conformation on the particle surface

Assuming that the PEG segment of the PLA-PEG block copolymer is always oriented outward, forming a PEG brush on the NP surface, while the PLA segment is oriented inward, the conformation of PEG on the NP can be described through theoretical considerations. [7] Based on the hydrodynamic diameter of the particle d_h , the mass of a single NP $m(NP)$ can be calculated using the density ρ (1.25 g/cm³) [8] with the following formula:

$$m(NP) = \frac{4}{3}\pi\rho\left(\frac{d_h}{2}\right)^3$$

The number of PEG chains in this NP can then be determined by considering only the mass contribution from the PEG and dividing by the molar mass of a PEG chain M_{PEG} . [9] Here, f represents the mass fraction of PEG in the blend of PLA-PEG block copolymer and PLGA. Multiplying by Avogadro's number N_A gives the number of PEG chains n :

$$n = \frac{m(NP) f N_A}{M_{PEG}}$$

Next, the surface area A that each PEG chain occupies on the hydrophobic particle core formed by PLGA and the PLA segments was calculated. To estimate the diameter of the solid particle core, the ratio k of the TEM-measured diameter of blank particles to their hydrodynamic diameter was used (for characterization of blank NPs using TEM images and DLS see Schorr, Chen et al. [10]). The surface area of the particle core divided by the number of PEG chains gives the area that each PEG chain occupies:

$$A = \frac{\pi (d_h \cdot k)^2}{n}$$

The conformation of the PEG, which extends from the hydrophobic particle core towards the water, was determined following de Gennes' model. [11] The distance between PEG grafting sites D , the Flory radius R_F , and the thickness of the PEG layer (L) were calculated. The distance between PEG grafting sites D was determined from the area A occupied by each PEG chain assuming that the PEG chain occupies a circular footprint on the particle surface. [7]

$$D = 2 \sqrt{\frac{A}{\pi}}$$

The Flory radius R_F is determined by the number of monomers per polymer chain N and the length of a single monomer ($\alpha = 0.35$ nm) [12]. The number of monomers in the PEG chain can easily be

Chapter 4 – Supplementary Information

calculated by dividing the molar mass of the PEG chain by the molar mass of a PEG repeating unit (44.03 g/mol).

$$R_F = \alpha N^{3/5}$$

The thickness of the PEG layer was calculated using the following formula:

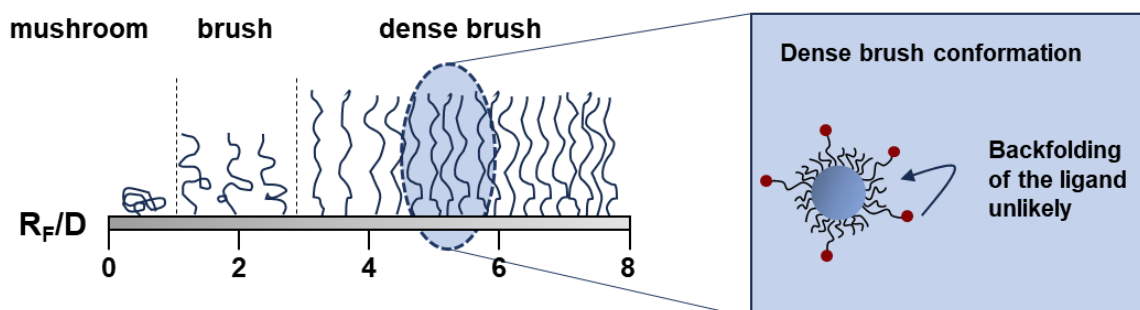
$$L = \frac{N\alpha^{5/3}}{D^{2/3}}$$

The PEG on the surface of the particle can adopt two main conformations described by these parameters. At low PEG densities ($R_F/D \leq 1$), a "mushroom" conformation is observed. At higher PEG densities ($R_F/D > 1$), a "brush" conformation is present. [7] Furthermore, a "dense brush" conformation can be defined if the PEG layer thickness exceeds the Flory radius by at least two-fold ($L/R_F > 2$ equal to $R_F/D > 2.8$). [7, 13, 14] Since the ligands were attached to longer PEG5k arms, while the spacer polymers had only PEG2k arms, the average molar mass of PEG was calculated based on the ratio used (20% PEG5k for the block copolymers with ligand, 80% PEG2k for the spacer block copolymer). This resulted in an average molar mass of 2600 g/mol for PEG on this particle type.

A

Particle	Size d_h [nm]	D [nm]	R_F [nm]	L [nm]	R_F/D	L/R_F	PEG conformation
NP-COOH	68	0,73	3,45	9,7	4,7	2,8	dense brush
NP-Tz	69	0,76	4,04	12,4	5,4	3,1	dense brush
NP-Ang-I	81	0,69	4,04	13,1	5,8	3,2	dense brush
NP-Ang-II	75	0,72	4,04	12,8	5,6	3,2	dense brush

B

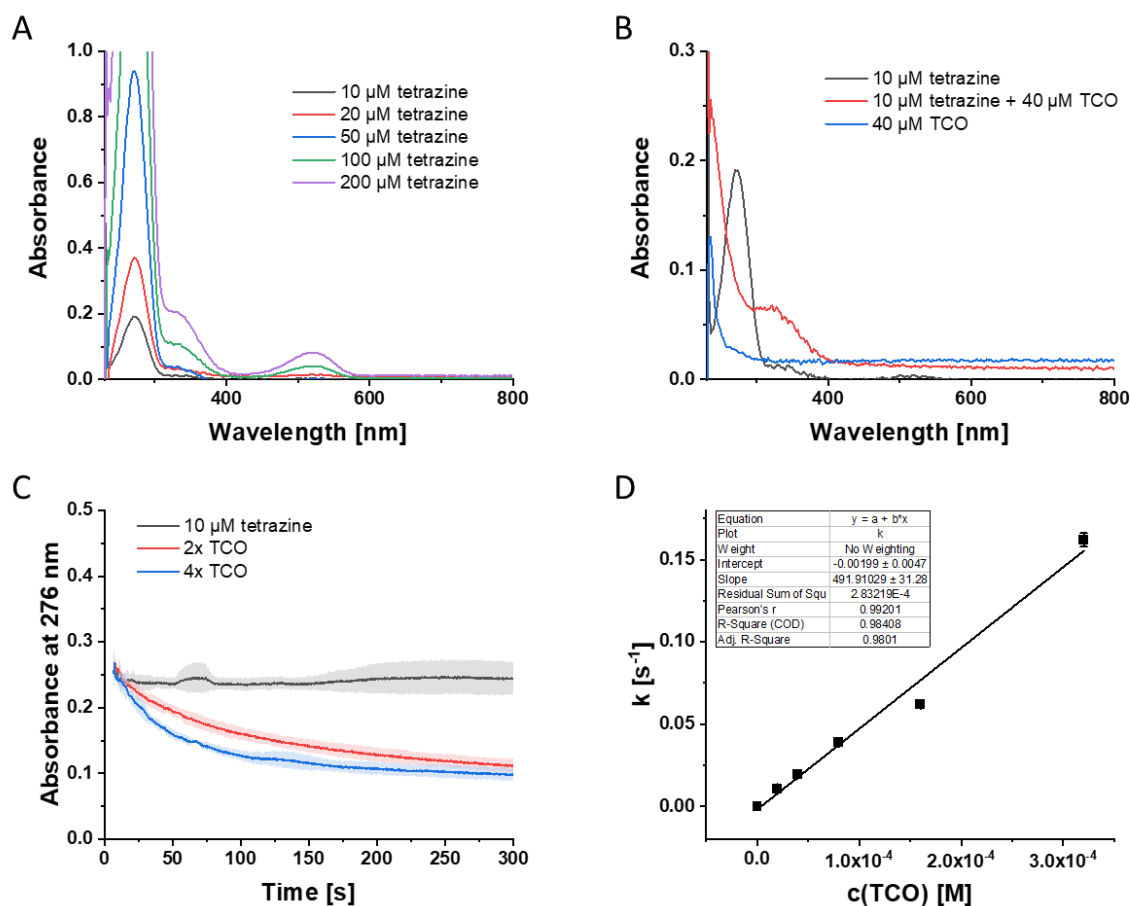


SI Figure 9. PEG conformation on the NP surface. (A) Table with a comparison of distance between PEG grafts (D), the Flory Radius (R_F), and Length/Thickness of the PEG Layer (L) as well as a conclusion on the PEG conformation of the respective NPs. (B) Illustration of the possible conformations and the rather unlikely backfolding of the ligands due to the dense brush conformation of the NPs produced. The illustration of the possible PEG conformations was based on Yang, Jones et al. [14]

Supplementary Information - Switchable Target Cell Recognition

The estimation revealed that PEG on all produced NPs exists in the "dense brush" conformation (see **SI Figure 9 A**). This makes the backfolding of ligands attached to the longer PEG5k arms highly unlikely, as there should be no space for a loop to form towards the NP core (see **SI Figure 9 B**). Ligands hidden within the PEG brush should therefore, if present at all, be minimal. Thus, the ligands should be accessible for interaction with the target cell. Furthermore, it is worth noting that the PEG conformation, being distinctly in the dense brush regime, should be ideally suited to avoid uptake by immune cells and prevent clearance. As reported by Yang, Jones et al., the transition from the mushroom to the brush conformation, often cited as the threshold for achieving effective stealth behavior [15], is insufficient for the effective suppression of macrophage uptake. [14] Instead, PEG densities with R_F/D values exceeding 2.8, indicative of PEG grafting in the dense brush regime, should be employed. This can be readily achieved with the polymer NPs used in this study. Based on these estimations, a pronounced stealth effect of the NPs can be expected.

VIII. iEDDA Reaction Kinetics



SI Figure 10. Considerations and evaluation of iEDDA reaction kinetics. (A) UV/Vis spectra of tetrazine at different concentrations. (B) Comparison of the UV/Vis spectra of tetrazine and TCO-PEG₄-COOH as reactants

Chapter 4 – Supplementary Information

of the iEDDA reaction and the resulting product after the reaction. (C) Decrease in tetrazine absorbance at 276 nm as reaction time progresses (2x TCO stands for a twofold excess of TCO-PEG₄-COOH relative to tetrazine (10 μM); 4x TCO analogously for a fourfold excess). (D) Pseudo first order rate constants (k_{obs}) determined from the decrease in tetrazine absorbance plotted against the TCO concentration. The second order rate constant results from the slope of the linear fit. Results in (C) and (D) are presented as mean \pm SD of $n = 3$ measurements.

An obvious approach to investigate the kinetics of the iEDDA reaction would be to monitor the decrease in tetrazine absorbance in the visible range spectrophotometrically. [16] When tetrazine reacts in the iEDDA reaction and is thus consumed, there is a rapid fading in the characteristic pink color of tetrazine. For the slower reaction between tetrazine and norbornene, the absorbance decrease in the visible range can be monitored after addition via the pump system on the plate reader. However, with the significantly faster-reacting TCO, the measurement setup clearly reaches its limits. The iEDDA reaction, as the fastest bioorthogonal reaction known to date [17], is so rapid that it is not possible to determine the absorbance decrease in the visible range on a plate reader. In addition to the absorption maximum in the visible range at 532 nm, tetrazine also has another absorption maximum in the UV region at 276 nm. This is significantly more intense, so that even for a highly diluted tetrazine solution with a concentration of 10 μM, an absorbance of approximately 0.2 is measured (see **SI Figure 10 A**). Unlike the visible range, switching to the absorption maximum in the UV range allows for the investigation of significantly more diluted solutions. At these low concentrations, the iEDDA reaction proceeds slowly, allowing it to be monitored on the plate reader. As seen in **SI Figure 10 B**, TCO-PEG₄-COOH only absorbs minimally in the UV range and the iEDDA reaction causes the absorption maximum of tetrazine to vanish, resulting in a new shoulder at approximately 330 nm. The absorbance decrease of tetrazine at 276 nm was investigated with different excesses of TCO. **SI Figure 10 C** illustrates the change in absorbance over time exemplarily for a two-fold and four-fold TCO excess relative to tetrazine (10 μM free in solution). The data were fitted with an exponential decay, yielding pseudo first-order rate constants k_{obs} . These were then plotted against the TCO concentration (see **SI Figure 10 D** exemplarily for tetrazine free in solution). Based on $k_{\text{obs}} = c(\text{TCO}) k_2$, the second-order rate constant was obtained from the slope of the linear fit. [18] Similarly, the approach was applied to tetrazine on polymer micelles and NPs.

IX. Remarks on the direct and inverse procedure of the Ca^{2+} mobilization assay

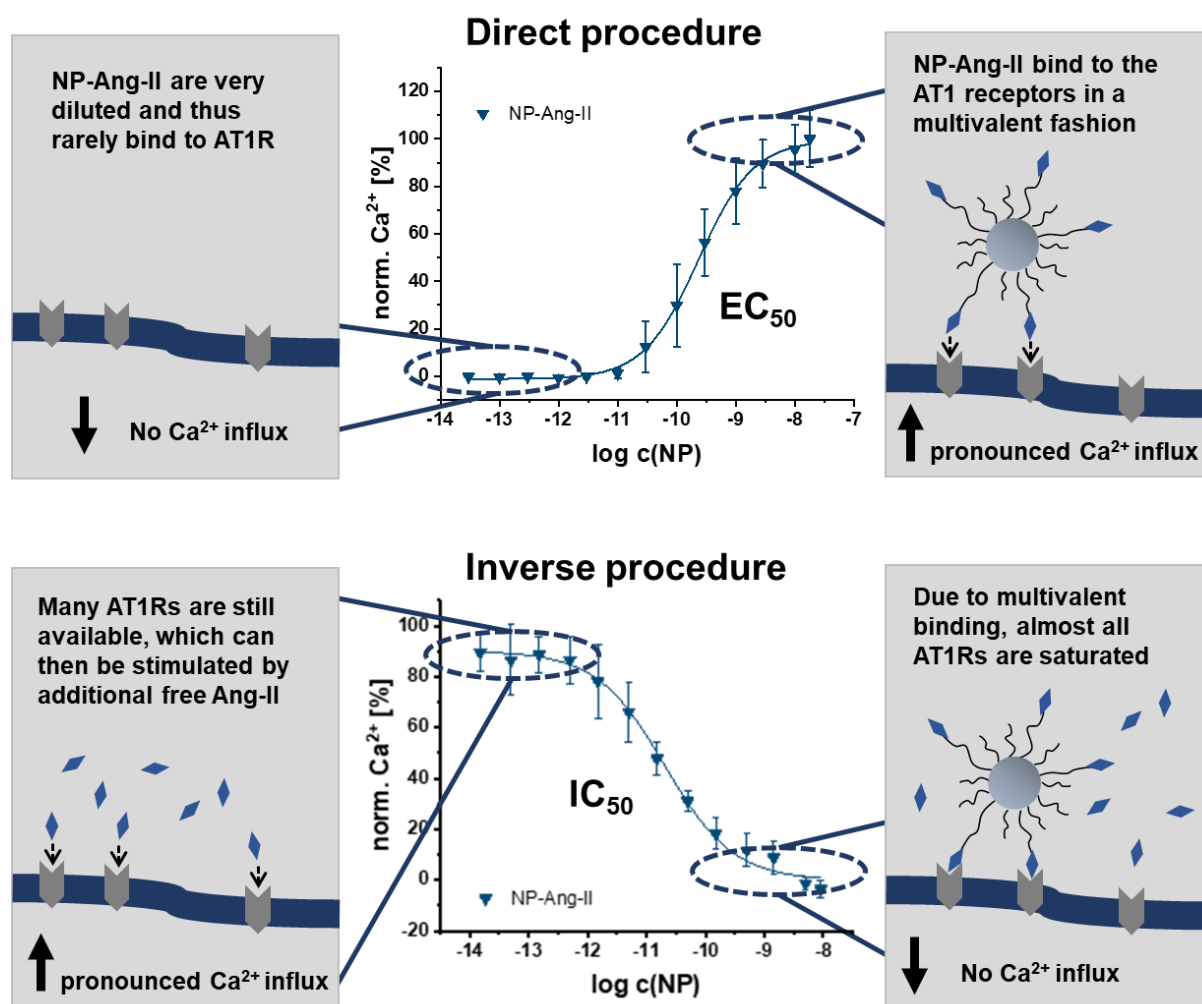
SI Table 1. Comparison of the experimental procedure for the direct and inverse approach of the Ca^{2+} mobilization assay. The volumes given refer to one well in each case, whereby the experiments were carried out in white 96-well plates. The addition directly before the measurement was always carried out via the pump system of the plate reader.

Direct procedure	Inverse procedure	
Used to record binding curves and EC_{50} values	Used to record binding curves and IC_{50} values	To investigate the kinetics of AT1R saturation
10 μL of the ligand for the AT1 receptor, either free or NP bound, in 10% PBS at various dilutions	10 μL of the ligand for the AT1 receptor, either free or NP bound, in 10% PBS at various dilutions	50 μL of the free ligand TCO-PEG ₄ -Ang-I (10 μM total concentration of free ligand) or 60 μL of the respective NPs in 10% PBS (2 nM total concentration of NPs)
90 μL of Fura-2 AM-loaded cells	90 μL of Fura-2 AM-loaded cells	90 μL of Fura-2 AM-loaded cells
Measurement of fluorescence intensity for 30 s	Incubation for 1 h at 37°C	Incubation for varying durations at 37°C under gentle agitation
	Cell stimulation with 100 μL of a 300 nM Lys-Ang-II solution in 10% PBS	Cell stimulation with 50 μL of a 1 μM Lys-Ang-II solution in 10% PBS
	Measurement of fluorescence intensity for 30 s	Measurement of fluorescence intensity for 30 s

In the approach described in this paper as the direct procedure, the Fura-2 AM-loaded cell suspension was added to the ligand for the AT1 receptor, either free or NP bound, and the measurement was started immediately. Binding of Ang-II to the AT1 receptor initiates the activation of phospholipase C, catalyzing the formation of diacylglycerol (DAG) and inositol trisphosphate (IP_3). Inositol trisphosphate in turn induces the intracellular release of Ca^{2+} from the endoplasmic reticulum (ER), allowing for the monitoring of ligand interaction with the AT1R through cytosolic calcium measurements. [19] At very low ligand concentrations, few receptors were activated, resulting in a correspondingly low Ca^{2+} influx. Conversely, at high concentrations, a pronounced Ca^{2+} influx was observed, reaching a corresponding plateau. Here, many ligands bound to the AT1 receptors, with multivalent binding playing a role for NP-

Chapter 4 – Supplementary Information

bound ligands. The EC_{50} value could be determined by fitting the binding curve. In the inverse procedure, the ligand for the AT1 receptor, either in free form or NP-bound, was first incubated with the Fura-2 AM-loaded cell suspension. During the incubation time, the ligands bound to the AT1R. After a certain period, free Lys-Ang-II was added via the plate reader's pump system, and fluorescence intensity at alternating excitation wavelengths was measured for 30 seconds. At low concentrations of the previously added ligand, many AT1 receptors were still available and could be stimulated by the additional free Lys-Ang-II, resulting in a pronounced Ca^{2+} influx and the corresponding plateau. At high concentrations of the previously added ligand, many receptors were no longer available, having been saturated by the binding of the previously added ligands, with the multivalent binding effect again playing a role for NP-bound ligands. Consequently, no Ca^{2+} influx was observed. From the fit of the binding curve, the IC_{50} value could be determined in this case, despite Ang-II being the receptor's agonist. The IC_{50} value should not be interpreted as half-maximal inhibition but rather as half-maximal receptor saturation due to prior agonistic binding. This value provides insights into the affinity of the free ligands or NP avidity for the AT1 receptor. The inverse procedure was primarily applied and is of particular interest because it allows for the investigation of the interaction of Ang-I with the receptor. During the incubation period, Ang-I can be converted to Ang-II by cell membrane-bound ACE. This two-step interaction with the target cell, first via the ectoenzyme and second the receptor, can be studied under relevant conditions.

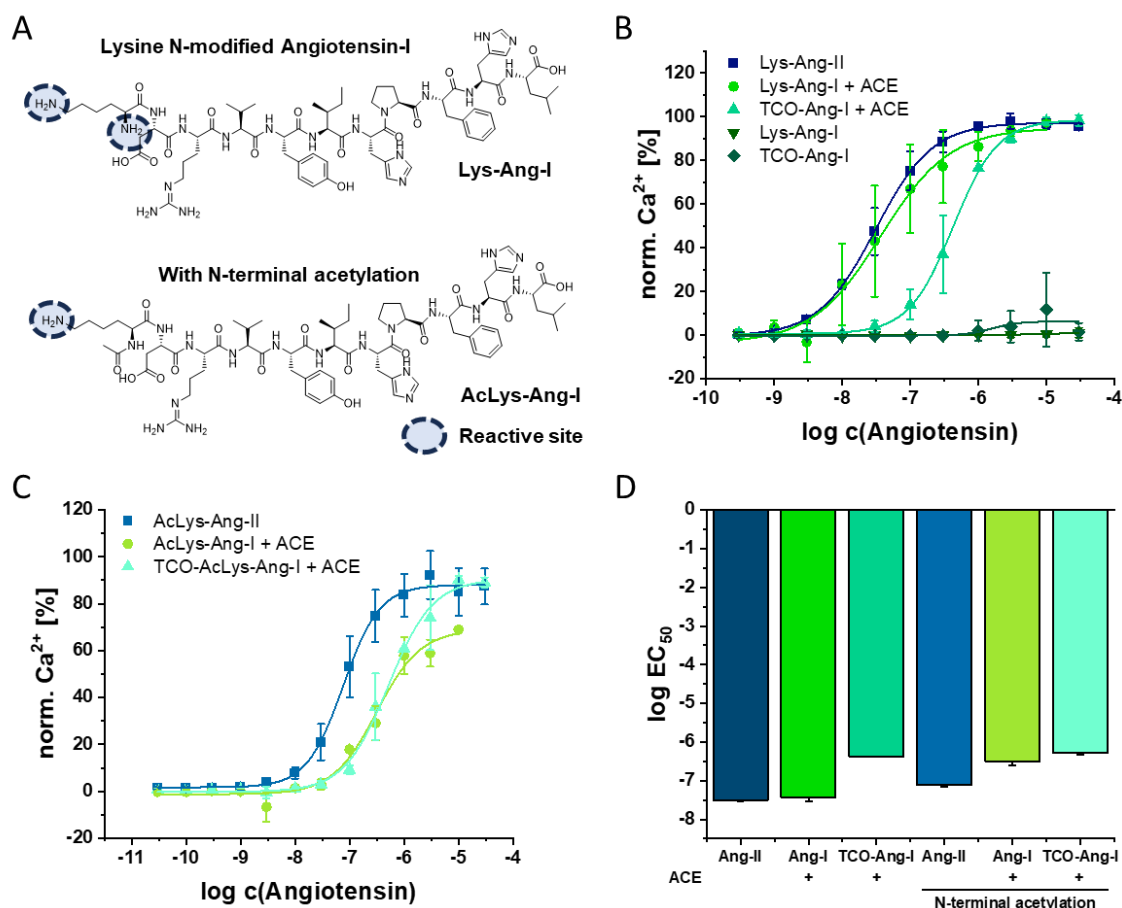


SI Figure 11. Comparison of direct and inverse procedure of Ca^{2+} mobilization assay. The binding curves of NP-Ang-II for both the direct and the inverse approach are shown here as examples, supplemented by explanatory diagrams of the respective situation. Results are presented as mean \pm SD of $N = 3$ experiments.

X. Comparison of non-acetylated and acetylated angiotensin

Initially, angiotensin with N-terminal acetylation was used in this project. Acetylated angiotensin can selectively be modified or attached to the polymer through the amino group on lysine, whereas non-acetylated angiotensin also has the capability to react with the amino group at the N-terminus (compare SI Figure 12 A). Consequently, it was assumed that a mixture would be formed with non-acetylated angiotensin, which is why acetylated angiotensin was initially favored. However, since the amino group on lysine ($\text{pK}_a \approx 10$) is more basic than the N-terminal amino group ($\text{pK}_a \approx 6-8$) [20] and hence more nucleophilic in the utilized solvent (DMF), it is presumed that the reaction with non-acetylated angiotensin still predominantly occurs as desired, primarily at the lysine ϵ -amino group.

Chapter 4 – Supplementary Information



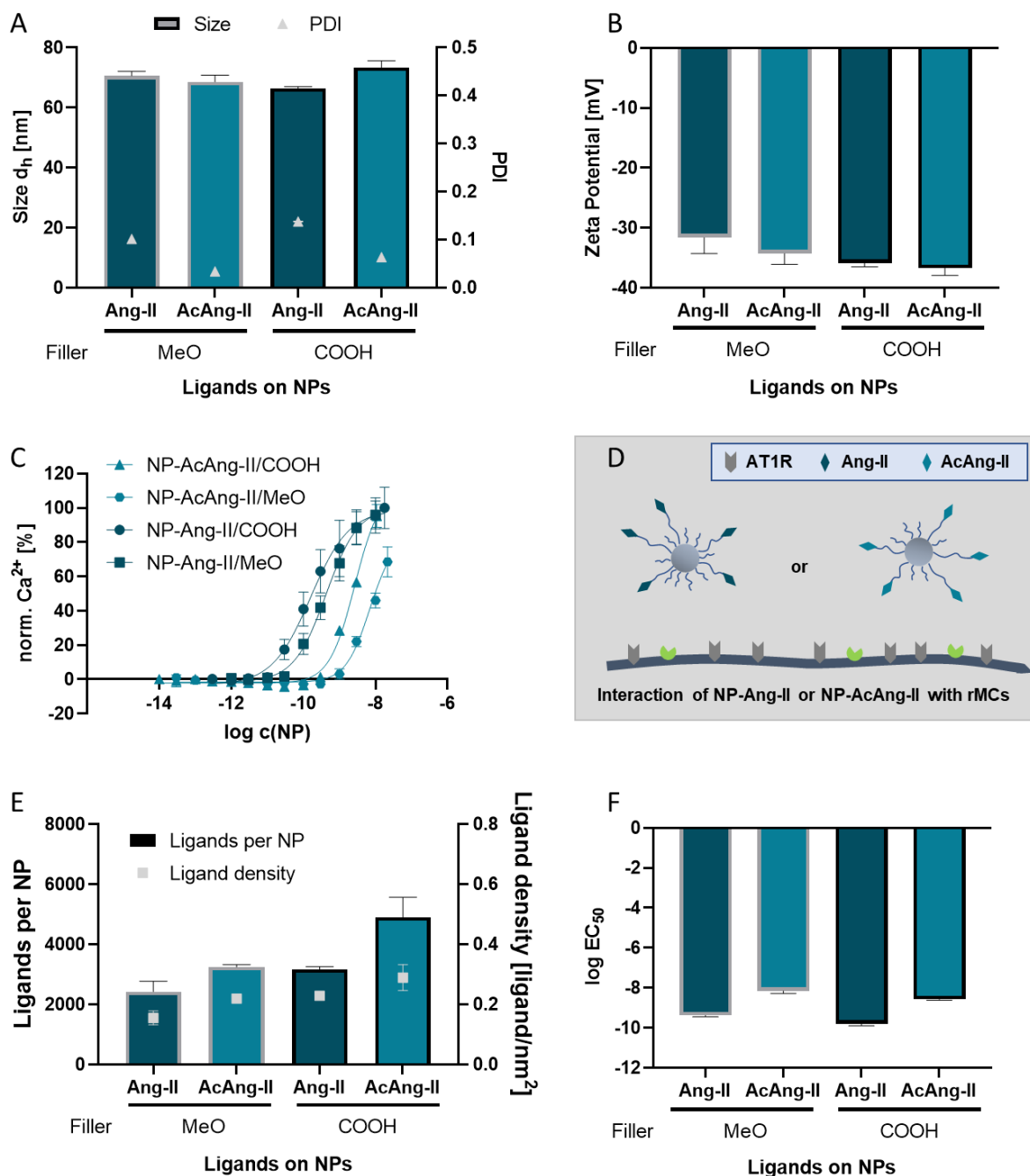
SI Figure 12. Interaction of acetylated angiotensin with the AT1 receptor. (A) Structural formulas of lysine N-modified Ang-I and additionally n-terminal acetylated Lys-Ang-I to illustrate the differences in the reactive sites. Binding curves of non-acetylated angiotensin (B) and acetylated angiotensin (C) determined by Fura-2 AM Ca²⁺ mobilization assay with rMCs using the direct procedure. (D) LogEC₅₀ values determined for acetylated angiotensin and comparison to non-acetylated angiotensin. Results are presented as mean ± SD of at least N = 2 experiments.

Looking at the affinity of angiotensin with and without acetylation for the AT1R, it is noteworthy that the affinity was consistently higher without acetylation (see **SI Figure 12 D**). However, the differences were not too pronounced. Acetylated Ang-II showed an EC₅₀ value of 76 ± 5 nM, whereas the non-acetylated counterpart showed a value of 31 ± 1 nM. It was continued to modify the acetylated Ang-I for binding via iEDDA reaction with TCO (synthesis detailed in Section V). Also, with the TCO modification the EC₅₀ values were in a similar range. After enzymatic activation by soluble ACE, values of 0.52 ± 0.06 μ M were found for the acetylated TCO-AcLys-Ang-I and 0.43 ± 0.02 μ M for the non-acetylated TCO-Lys-Ang-I.

XI. Comparison of angiotensin-II functionalized NPs with and without acetylation at the N-terminus of angiotensin

Subsequently, the effect of acetylation at the N-terminus of angiotensin was investigated not only for the free ligands, but also for the interaction of the NPs with the AT1R (see **SI Figure 13 D**). NPs functionalized with acetylated Ang-II as well as NPs with Ang-II without acetylation were prepared. In addition, methoxy and carboxy terminated PEG was tested as filler. The NPs were all around 70 nm in size (see **SI Figure 13 A**). As expected, the particles with MeO filler showed a slightly less negative zeta potential than the particles with carboxy terminated PEG as filler (see **SI Figure 13 B**). Going from non-acetylated Ang-II NPs to NP-AcAng-II, the avidity for the AT1 receptor decreased significantly. The EC_{50} value increased from 0.16 ± 0.04 nM to 2.7 ± 0.4 nM for the NPs with COOH filler (see **SI Figure 13 F**). NPs with MeO filler exhibited a slightly lower affinity for the AT1R in both cases. The plateau could no longer be reached with NP-AcAng-II/MeO (see **SI Figure 13 C**). The lower avidity of the particles with MeO filler for the AT1R could be due to the fact that the NPs carry less Ang-II. This difference was particularly noticeable for the NPs with acetylated Ang-II. Here, the particles with MeO filler were functionalized with approx. 3000 AcAng-II, whereas the NPs with COOH filler carried almost 5000 AcAng-II (see **SI Figure 13 E**). Regardless of the filler used, however, it could be stated that the NPs with acetylated Ang-II clearly lose avidity for the AT1 receptor. The N-terminal acetylation of angiotensin, contrary to initial expectations, proved to be highly obstructive for AT1 receptor binding. Experiments with acetylated angiotensin were terminated at this point and only non-acetylated angiotensin was used in the following (see main section). For this purpose, Ang-I without acetylation was modified with TCO. To allow more flexibility, a short PEG linker was introduced between TCO and Ang-I. Details regarding the synthesis can be found in Section IV.

Chapter 4 – Supplementary Information



SI Figure 13. Comparison of Ang-II functionalized NPs with and without acetylation at the N-terminus of angiotensin and different filler polymers. (A) Size and PDI of the NPs determined by NTA. (B) Zeta potential of the NPs in water. (C) Binding curves of the functionalized NPs determined by a Fura-2 AM Ca^{2+} mobilization assay with rMCs. (D) Schematic of the interaction of the different NPs with the AT1R on the rMCs. (E) Number of Ang-II ligands per NP determined by BCA assay and calculated ligand density. (F) LogEC₅₀ values for the investigated NPs determined by the fit of the Ca^{2+} mobilization assay binding curves. Results are presented as mean \pm SD of at least $n = 3$ measurements.

References

1. Abstiens K, Maslanka Figueroa S, Gregoritz M, Goepferich AM (2019) Interaction of functionalized nanoparticles with serum proteins and its impact on colloidal stability and cargo leaching. *Soft Matter* 15(4), 709–720. 10.1039/C8SM02189A.
2. Maslanka Figueroa S, Vesper A, Abstiens K, Fleischmann D, Beck S, Goepferich A (2019) Influenza A virus mimetic nanoparticles trigger selective cell uptake. *Proceedings of the National Academy of Sciences of the United States of America* 116(20), 9831–9836. 10.1073/pnas.1902563116.
3. Qian H, Wohl AR, Crow JT, Macosko CW, Hoye TR (2011) A Strategy for Control of “Random” Copolymerization of Lactide and Glycolide: Application to Synthesis of PEG-b-PLGA Block Polymers Having Narrow Dispersity. *Macromolecules* 44(18), 7132–7140. 10.1021/ma201169z.
4. Meimetis LG, Carlson JCT, Giedt RJ, Kohler RH, Weissleder R (2014) Ultrafluorogenic coumarin-tetrazine probes for real-time biological imaging. *Angewandte Chemie (International ed. in English)* 53(29), 7531–7534. 10.1002/anie.201403890.
5. Smith PK, Krohn RI, Hermanson GT, Mallia AK, Gartner FH, Provenzano MD, Fujimoto EK, Goeke NM, Olson BJ, Klenk DC (1985) Measurement of protein using bicinchoninic acid. *Analytical Biochemistry* 150(1), 76–85. 10.1016/0003-2697(85)90442-7.
6. Olson BJSC (2016) Assays for Determination of Protein Concentration. *Current Protocols in Pharmacology* 73(1), A.3A.1-A.3A.32. 10.1002/cpph.3.
7. Perry JL, Reuter KG, Kai MP, Herlihy KP, Jones SW, Luft JC, Napier M, Bear JE, DeSimone JM (2012) PEGylated PRINT nanoparticles: the impact of PEG density on protein binding, macrophage association, biodistribution, and pharmacokinetics. *Nano letters* 12(10), 5304–5310. 10.1021/nl302638g.
8. Rabanel J-M, Faivre J, Tehrani SF, Lalloz A, Hildgen P, Banquy X (2015) Effect of the Polymer Architecture on the Structural and Biophysical Properties of PEG–PLA Nanoparticles. *ACS Appl. Mater. Interfaces* 7(19), 10374–10385. 10.1021/acsami.5b01423.
9. Gref R, Lück M, Quellec P, Marchand M, Dellacherie E, Harnisch S, Blunk T, Müller RH (2000) ‘Stealth’ corona-core nanoparticles surface modified by polyethylene glycol (PEG): influences of the corona (PEG chain length and surface density) and of the core composition on phagocytic uptake and plasma protein adsorption. *Colloids and Surfaces B: Biointerfaces* 18(3-4), 301–313. 10.1016/S0927-7765(99)00156-3.
10. Schorr K, Chen X, Sasaki T, Arias-Loza AP, Lang J, Higuchi T, Goepferich A (2024) Rethinking Thin-Layer Chromatography for Screening Technetium-99m Radiolabeled Polymer Nanoparticles. *ACS pharmacology & translational science* 7(9), 2604–2611. 10.1021/acspsci.4c00383.
11. Gennes PG de (1987) Polymers at an interface; a simplified view. *Advances in Colloid and Interface Science* 27(3-4), 189–209. 10.1016/0001-8686(87)85003-0.

Chapter 4 – Supplementary Information

12. Hristova K, Needham D (1995) Phase Behavior of a Lipid/Polymer-Lipid Mixture in Aqueous Medium. *Macromolecules* 28(4), 991–1002. 10.1021/ma00108a029.
13. Damodaran VB, Fee CJ, Ruckh T, Popat KC (2010) Conformational studies of covalently grafted poly(ethylene glycol) on modified solid matrices using X-ray photoelectron spectroscopy. *Langmuir the ACS journal of surfaces and colloids* 26(10), 7299–7306. 10.1021/la9041502.
14. Yang Q, Jones SW, Parker CL, Zamboni WC, Bear JE, Lai SK (2014) Evading immune cell uptake and clearance requires PEG grafting at densities substantially exceeding the minimum for brush conformation. *Molecular pharmaceutics* 11(4), 1250–1258. 10.1021/mp400703d.
15. Jokerst JV, Lobovkina T, Zare RN, Gambhir SS (2011) Nanoparticle PEGylation for imaging and therapy. *Nanomedicine (London, England)* 6(4), 715–728. 10.2217/nnm.11.19.
16. Knall A-C, Hollauf M, Slugovc C (2014) Kinetic studies of inverse electron demand Diels-Alder reactions (iEDDA) of norbornenes and 3,6-dipyridin-2-yl-1,2,4,5-tetrazine. *Tetrahedron Letters* 55(34), 4763–4766. 10.1016/j.tetlet.2014.07.002.
17. Oliveira BL, Guo Z, Bernardes GJL (2017) Inverse electron demand Diels-Alder reactions in chemical biology. *Chem. Soc. Rev.* 46(16), 4895–4950. 10.1039/C7CS00184C.
18. Rossin R, van den Bosch SM, Hoeve W ten, Carvelli M, Versteegen RM, Lub J, Robillard MS (2013) Highly reactive trans-cyclooctene tags with improved stability for Diels-Alder chemistry in living systems. *Bioconjugate Chemistry* 24(7), 1210–1217. 10.1021/bc400153y.
19. Greco S, Elia MG, Muscella A, Storelli C, Marsigliante S (2002) AT1 angiotensin II receptor mediates intracellular calcium mobilization in normal and cancerous breast cells in primary culture. *Cell Calcium* 32(1), 1–10. 10.1016/S0143-4160(02)00077-5.
20. Deng J-R, Lai NC-H, Kung KK-Y, Yang B, Chung S-F, Leung AS-L, Choi M-C, Leung Y-C, Wong M-K (2020) N-Terminal selective modification of peptides and proteins using 2-ethynylbenzaldehydes. *Commun Chem* 3(1), 67. 10.1038/s42004-020-0309-y.

Supplementary Information - Switchable Target Cell Recognition

Chapter 4 – Supplementary Information

Chapter 5

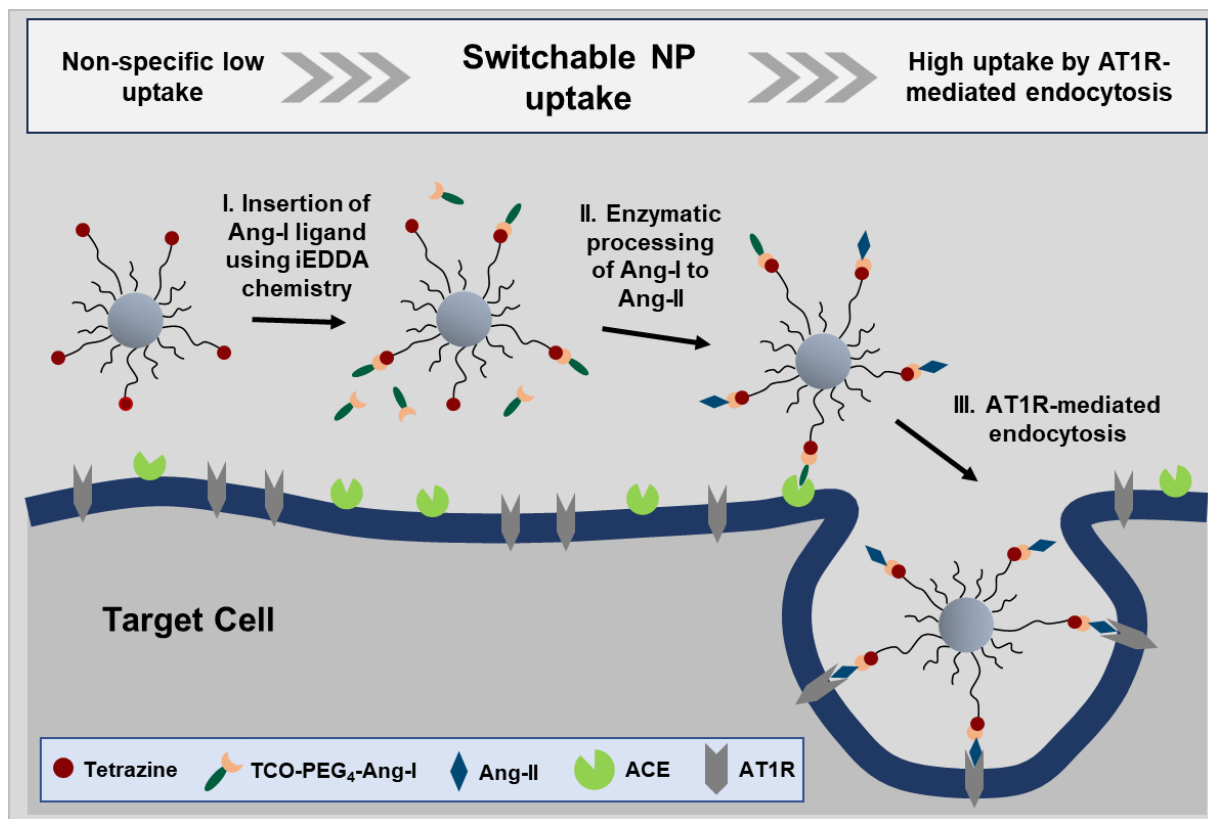
Ligand-Switchable Nanoparticles for Increased Target Cell Specificity and Steerable Nanoparticle Uptake

Chapter 5

Abstract

Nanoparticles (NPs) are often functionalized with ligands for active targeting, aiming to bind specifically to receptors on target cells. However, these receptors are typically present in multiple cell types within the organism. Ligand-switchable NPs have been developed to present the ligand only near the target site. Similarly, the ligand can be attached in the vicinity of the target, for which the rapid bioorthogonal inverse electron-demand Diels-Alder (iEDDA) reaction is well-suited. Following the iEDDA reaction, the pro-ligand can be enzymatically activated, further increasing target cell specificity. The active ligand binds to a target cell receptor, whereby NPs with switchable avidity result. This study aimed to investigate whether the switchable NP avidity, designed via iEDDA reaction and ectoenzyme-based ligand activation, also leads to switchable internalization of the NPs into the target cell. NP uptake was examined using flow cytometry, and to determine the cellular localization of the NPs, confocal laser scanning microscopy (CLSM) was employed. After the expected switchable NP internalization could not be observed, the concept was dissected and investigated step by step. It appears that the prerequisite of increased uptake by the active ligand may not have been met, which posed challenges for the successful implementation of the advanced NP concept.

Graphical Abstract



Schematic illustrating the concept of a switchable NP uptake into the target cell. NP-Tz are functionalized with Ang-I in a time-controlled manner via iEDDA reaction. At the target cell, Ang-I is processed to Ang-II by the ectoenzyme ACE, resulting in uptake of the NPs by AT1R-mediated endocytosis.

Chapter 5

1. Introduction

Nanoparticles (NPs) for drug delivery applications are frequently functionalized with ligands to target specific receptors on diseased cells. [1] However, these receptors are usually present in multiple cell types throughout the entire body. Therefore, it may be advantageous to expose a cell uptake-promoting ligand only at the target site. These so-called ligand-switchable NPs could achieve increased specificity for the target cell and thus enhance the therapeutic efficacy of NP delivery. [2] In this context, several concepts have already been developed. For example, ligands can be blocked by reversible covalent bonds [3] or electrostatic interactions [4]. A stimulus near the target site can then remove the reversible blockade, making the ligand available for interaction with the target cell. Another approach involves attaching longer polymers (e.g., PEG) to the NP, which shield the ligands on shorter linkers. The sterically shielding polymers can be cleaved by a stimulus, uncovering the cell uptake-promoting ligand. [5] Steric shielding was also used for an approach where the ligands on long linker polymers were initially folded towards the particle core and hidden under the PEG corona. The stimulus then caused the polymers to extend, making the ligand on the NP visible. [6]

We recently demonstrated that not only fully equipped NPs hiding the ligands until the NP reaches the target site can be used. It is also possible to functionalize NPs with the desired ligand in a constructive manner near the target site. Through the combination of iEDDA reaction and ectoenzyme-based ligand activation, NPs with switchable avidity for the target cell receptor were created (see **Chapter 4**). This study aimed to investigate whether the switchable avidity also translates into switchable internalization of the NPs. The angiotensin-II type 1 receptor (AT1R) as the target cell receptor is subject to clathrin-mediated endocytosis and is located either on flat membrane sections or clathrin-coated pits (CCPs). [7] The CCPs are highly dynamic structures that undergo constant morphological changes. After ligand binding, the pit rapidly invaginates to form a clathrin-coated vesicle. [8] Membrane pinching is achieved through the activity of dynamin. The internalized NPs then travel from early to late endosomes. [9] Since clathrin-coated vesicles typically have a diameter of approximately 100 nm, NPs up to this size can generally be internalized via this pathway. [8]

In this work, PLGA/PLA-PEG polymer NPs taking into account the upper size limit were prepared. They served as a model platform for investigating the switchable behavior of NPs, using the already established concept. The tetrazine functionalized NPs were equipped with the ligand by the iEDDA reaction with TCO modified Ang-I. The Ang-I proligand was activated to Ang-II by the angiotensin converting enzyme (ACE) on the cell membrane. Finally, the Ang-II decorated NPs could bind to the AT1R, leading to clathrin-mediated endocytosis. [10] The processing by the ectoenzyme offers the potential to minimize the biological effects of the ligand before coupling and to increase the specificity for the target cell through the dual recognition strategy with enzyme processing and receptor binding. [11] The desired switchable NP uptake was investigated using flow cytometry. To reveal the cellular

localization of the NPs and to support the flow cytometry results, confocal laser scanning microscopy (CLSM) was employed.

2. Materials and Methods

2.1 Materials

TCO-PEG₄-NHS ester (axial isomer) and Cyanine-5 amine were purchased from Lumiprobe (Hannover, Germany). PLGA (resomer RG 502 H, poly(D,L-lactide-co-glycolide), acid terminated, Mw 7,000-17,000), HBTU (O-(benzotriazol-1-yl)-N,N,N',N'-tetramethyluronium hexafluorophosphate), anhydrous DMF (dimethylformamide) and DIPEA (N,N-diisopropylethylamine, ReagentPlus®) for the synthesis of PLGA-Cy5 as well as QuantiPro™ BCA assay kit for angiotensin quantification, angiotensin-converting enzyme from rabbit lung (≥ 2.0 units/mg protein (modified Warburg-Christian)) for enzymatic activation, ACE inhibitor captopril, bovine serum albumin (lyophilized powder, BioReagent), RPMI-1640 medium and hydrocortisone for cell culture were obtained from Sigma Aldrich (Taufkirchen, Germany). Lysine N-modified Ang-I and Ang-II (Lys-Ang-I Sequence KDRVYIHPFHL and Lys-Ang-II Sequence KDRVYIHPF) were synthesized according to order from Genscript (Piscataway, NJ, USA). Centrifugal devices (30 or 100 kDa molecular weight cutoff) from Pall Life Sciences (Portsmouth, UK) were used to concentrate the NPs. Folded capillary zeta cells for the measurement of the zeta potential were obtained from Malvern Panalytical (Kassel, Germany). Fetal bovine serum (FBS, South America origin, 0.2 μ m sterile filtered, Lot No.: P201004) was sourced from PAN Biotech GmbH (Aidenbach, Germany). Insulin-transferrin-selenium and Leibovitz's L-15 medium were purchased from Life Technologies Corporation (Grand Island, NY, USA). EXP3174 was synthesized by oxidation of losartan according to a protocol established in our research group and was kindly provided by Kathrin Schorr. [12] 24-well polystyrene cell culture plates for flow cytometry experiments were purchased from Corning (Kennebunk, ME, USA). CellTracker™ green (CTG), DAPI (4',6-diamidino-2-phenylindole), and Dulbecco's phosphate buffered saline (DPBS) were ordered from Thermo Fisher Scientific (Waltham, MA, USA). Eight-well ibidi μ -slides for microscopic experiments were purchased from ibidi (Gräfelfing, Germany). All other materials were reagent grade and obtained from Merck KGaA (Darmstadt, Germany). Millipore water was generated using a Milli-Q water purification system (Millipore, Schwalbach, Germany).

Chapter 5

2.2 Polymer synthesis and ligand coupling

The synthesis of the PLA-PEG block copolymers and the conjugation of ligands to these were performed as described in Chapter 2, following protocols established in our research group. [13] The particle core-forming PLGA was additionally labeled with the fluorophore Cyanine-5. [14] Cyanine-5 amine, acid-terminated PLGA, and HBTU as the coupling reagent were dissolved in anhydrous DMF, and N,N-diisopropylethylamine (DIPEA) was added. The blue reaction mixture was stirred overnight at room temperature. The crude product was then precipitated in ice-cold diethyl ether, centrifuged, the supernatant discarded, and the polymer pellet dried before being redissolved in acetonitrile. For purification, the precipitation-centrifugation-decantation cycle was repeated several times. Detailed information on the synthesis and characterization of the PLGA-Cy5 product can be found in the SI Section I.

2.3 NP preparation and characterization

The polymer NPs were produced according to the method established in our research group. [15] Stock solutions of PEG-PLA block copolymers and poly(lactic-co-glycolic acid) (PLGA) in acetonitrile were combined to result in a 10 mg/mL solution with a 70:30 mass ratio of copolymers to particle-core-forming PLGA. Cyanine-5 labeled PLGA was used to enable the observation of NPs by means of flow cytometry and CLSM. For the preparation of ligand decorated NPs, the copolymer fraction was adjusted so that 20% of the PEG-PLA copolymers carried the ligand. Filler polymer (PLA10k-PEG2k-OMe or PLA10k-PEG2k-COOH) and functionalized polymer (PLA10k-PEG5k-Tz or PLA10k-PEG5k-Ang-II) were mixed accordingly. NPs were prepared via bulk nanoprecipitation. [16] The 10 mg/mL polymer solution in acetonitrile was added dropwise into rapidly stirring (800 rpm) Millipore water (final concentration 1 mg/mL NP). Particles were stirred for 3 h allowing the organic solvent (MeCN) to evaporate and concentrated by centrifugation using a 30-kDa molecular weight cutoff centrifugal device for 15 min at 2000 g and 15°C.

NP size and concentration were determined in Millipore water using nanoparticle tracking analysis (NTA) on a NanoSight NS300 (Malvern Panalytical GmbH, Kassel, Germany). [17] The dilution was chosen so that between 20 and 30 particles per frame could be measured and the detection threshold in the evaluation was set to 3. Based on the concentration in particles/mL output by the instrument, the molar NP concentration was determined using the Avogadro number. The widely used polydispersity index (PDI) was calculated from the NTA data according to the formula reported by Clayton, Salameh et al. [18] Subsequently, the zeta potential was determined on a Malvern ZetaSizer Nano ZS (Malvern Panalytical GmbH, Kassel, Germany). NPs were diluted to 1 nM in 10% PBS and measured in a folded capillary cell at 25°C. To determine the fluorescence of the NPs, 10 μ L NP solution was diluted with 90

μL DMSO in a black 96-well plate. The fluorescence intensity was measured using a FLUOstar Omega microplate reader (BMG Labtech, Ortenberg, Germany) with an excitation wavelength of 640 nm and an emission wavelength of 680 nm. The fluorescence of NP-Tz/MeO was normalized to 100%. The fluorescence intensities of the other NP types, initially set to the same NP concentration, were reported relative to this value.

2.4 Quantification of ligands per NP

The tetrazine ligands per NP were determined based on the absorbance of tetrazine at 532 nm. 50 μL of the concentrated NP solutions were added to a transparent 384 well plate (Corning, Corning, NY, USA) and diluted with 50 μL of DMSO. For the calibration line, free tetrazine diluted in DMSO was added to the well plate and to keep the ratio between DMSO and aqueous fraction equal, 50 μL of water was added here. The UV/Vis spectra from 300 to 800 nm were recorded on a FLUOstar Omega microplate reader. To determine the absorbance resulting from tetrazine alone for NPs labeled also with cyanine-5, the equally weighted absorbance spectrum of a cyanine-5 labeled NP without tetrazine was subtracted. The concentration of tetrazine in the NP solution was then determined from the difference spectrum at 532 nm using the calibration line. To calculate the tetrazine ligands per NP, the tetrazine concentration was referenced to the NP concentration determined via NTA.

Ang-II ligands per NP were determined using a BCA assay following the manufacturer's protocol for the QuantiPro™ BCA Assay Kit (Sigma-aldrich, St Louis, MO, USA). The calibration was prepared using free Lys-Ang-II (Genscript, Piscataway, NJ, USA) at appropriate dilutions. To 40 μL of Lys-Ang-II solution or sample with NP solution (3, 5, and 10 nM) in a transparent 384 well plate, 40 μL of QuantiPro working reagent was added, mixed by pipetting up and down, and the plate was covered with a plate sealer. The plate was incubated at 60°C for 1 h, after which absorbance was measured at 562 nm on a FLUOstar Omega microplate reader. The Ang-II concentration in the NP solution calculated via the calibration was referenced to the respective NP concentration.

The ligand density on the NPs was determined by first calculating the surface area of the particles. The hydrodynamic diameter determined via NTA was employed and the surface area was calculated assuming a spherical shape. The number of ligands per NP was then related to this.

2.5 Post-functionalization of NP-Tz with Ang-I and activation with soluble ACE

NP-Tz with both methoxy and carboxy fillers were post-functionalized through iEDDA reaction with TCO modified Ang-I. A 30 nM NP solution was incubated with 300 μM TCO-PEG₄-Ang-I for 1 hour at 37°C. Subsequently, excess TCO-PEG₄-Ang-I was removed using a 30-kDa molecular weight cutoff

Chapter 5

centrifugal device, followed by three washing steps with Millipore water (4 mL each). The concentrated NPs were analyzed using nanoparticle tracking analysis to determine NP concentration and size. As a control to assess the efficiency of Ang-I removal, 30 nM NP-Tz were incubated with non-TCO functionalized Ang-I. Successful functionalization was confirmed through a BCA assay, and the number of Ang-I ligands per NP was determined. The BCA assay was performed following the procedure described above with a 3 nM NP solution. Free Lys-Ang-I served as standard. The Ang-I concentration obtained for NPs incubated with non-TCO functionalized Angiotensin-I was subtracted from the sample with functionalized NPs.

For subsequent investigation of uptake into rMCs, a portion of the NPs was further activated with soluble ACE to convert Ang-I to Ang-II functionalized NPs. The 1 nM NP solution was incubated with 100 nM ACE at 37°C for 12 hours in DPBS (pH 7.4). Subsequently, the NP solution was reconcentrated using the 30-kDa molecular weight cutoff centrifugal filter, and NP concentration and size were determined using NanoSight NS300 analysis.

2.6 NP size in complex biological media

To investigate the NP size in biological media, fluorophore-labeled particles were prepared. The preparation was conducted analogously to the standard method, with a 70:30 mass ratio of block copolymers to particle-core-forming PLGA-Bodipy TMR. The NPs were sterilized by filtration (0.2 µm pore size) under the LAF box. The NPs were diluted 1:2000 in PBS, Leibovitz's L-15 medium with 0.1% BSA, or cell culture medium RPMI 1640 with 10% FBS and subsequently incubated at 37°C for 1 h. The samples were measured in fluorescence mode (excitation by the green laser at 532 nm, filter wheel set at 565 nm) using the NanoSight NS300 (Malvern Panalytical GmbH, Kassel, Germany).

2.7 Cell Culture

Rat mesangial cells (rMCs) were provided by Professor Armin Kurtz from the Institute of Physiology (University of Regensburg, Germany). The cells were cultured in T-75 cell culture flasks (Corning, Corning, NY, USA) at 37 °C with a 5% CO₂ atmosphere. RPMI1640 medium supplemented with 10% fetal bovine serum, along with insulin-transferrin-selenium and 100 nM hydrocortisone was used for cultivation. The characterization of the rMCs regarding their AT1R and ACE expression was previously reported by our research group. [11]

2.8 Investigation of NP uptake using flow cytometry

rMCs (passage 77 or 78) were seeded at a density of 20 000 cells per well in a 24-well plate and incubated for approximately 48 h at 37°C. To demonstrate uptake specificity, cells were preincubated with 1 mM captopril or 1 mM EXP3174 for 15 min prior to particle addition. The medium was discarded, the cells washed with DPBS (0.8 mL), and the cyanine-5 labeled NPs were added. In the experiments with direct *in vitro* functionalization of NPs, the TCO-PEG₄-Ang-I solution was added immediately after NP addition. rMCs were incubated for 1 h with the NP solutions in Leibovitz's medium supplemented with 0.1% BSA (different concentrations from 1 nM down to 30 or 3 pM). To process the cells for the flow cytometry analysis, the NP solutions were first removed, and the cells were washed twice with DPBS (first 0.4 mL, then 0.8 mL). The cells were detached by treatment with trypsin (0.25 %, 0.3 mL; approximately 2 min). FBS-containing medium (0.5 mL) was added and the cell suspension was transferred to centrifuge tubes. The cells were centrifuged (200 g, 7 min, 4°C), the supernatant was decanted off and the cell pellet was resuspended in 0.4 mL DPBS. Fluorescence of the cells induced by NP uptake was examined by flow cytometry on a BD FACSCanto II (BD, Heidelberg, Germany). Excitation was at 633 nm and emission was recorded using a 660/20 nm bandpass filter (corresponding to APC channel). Data analysis was performed using Flowing software 2.5.1. (Turku Centre for Biotechnology), excluding duplicates and gating the population of viable cells. The median was finally used as a measure of fluorescent NP uptake. An example evaluation scheme with gates set can be found in **SI Figure 5**. The median fluorescence intensity of 1 nM NP-Tz/MeO was normalized to 1 in each experiment and further fluorescence intensities for other particle types and concentrations were reported relative to this standard. The binding curves to describe the saturation of the cells with NPs were fitted using a simple one-site specific binding model (eq. 1).

$$y = B_{max} \cdot \frac{x}{K_d + x} \quad (1)$$

Thereby B_{max} represents maximum binding and K_d is the equilibrium dissociation constant.

2.9 Confocal laser scanning microscopy analysis

To analyze the interaction of different NPs with rMCs as target cells, confocal laser scanning microscopy (CLSM) was performed using a Zeiss LSM 710 (Carl Zeiss, Microscopy GmbH, Jena, Germany). For the first experiment (see **Figure 8**), the cells were stained with Cell Tracker Green (CTG) before seeding into ibidi slides. CTG (50 µg) was dissolved in 11 µL DMSO (resulting in a 10 mM solution) and diluted with 11 mL serum-free medium to achieve a final concentration of approximately 10 µM. rMCs at passage 77, grown to at least 90% confluency, were washed with 10 mL DPBS and harvested by incubation with 0.25% trypsin. After adding 9 mL of serum-containing medium, the cells were

Chapter 5

centrifuged at 200 rcf for 5 minutes using a 5702 R centrifuge (Eppendorf, Germany). The supernatant was discarded, and the cell pellet was resuspended in the CTG staining solution. The cells were incubated for 45 min at 37°C on a shaker (50 rpm). The cells were then centrifuged with the aforementioned settings, the supernatant was discarded, and the cell pellet was resuspended in 5 mL DPBS for washing. After another centrifugation, the cell pellet was resuspended in 5 mL FBS-containing medium, and the cell number was determined using a Neubauer-improved counting chamber (Marienfeld, Germany). The rMCs were diluted and 15,000 cells per well were seeded into an 8-well ibidi slide (Ibidi, Planegg, Germany). For the second experiment (see **Figure 9**), the cells were not stained with CTG but were harvested similarly with passage 77 by incubation with trypsin. After counting and appropriate dilution, 20,000 rMCs per well were seeded. For both experiments, the cells were incubated for about 24 hours.

On the day of the experiment, the cells were washed with 200 μ L DPBS, with each washing step consisting of carefully aspirating the old solution, adding DPBS, and aspirating again before the next addition. In the wells pre-incubated with EXP3174, 100 μ L of a 1 mM EXP3174 solution in Leibovitz's L-15 medium (LM) supplemented with 0.1% BSA was added. In all other wells, the same volume of LM supplemented with 0.1% BSA without EXP3174 was added. After 30 minutes of pre-incubation, the different Cy-5 labeled NPs in LM with 0.1% BSA were added (final concentration in the well 300 pM). For the NP-Tz, which were to react with TCO-PEG₄-Ang-I directly in the well, the TCO-modified Ang-I (at least 20-fold excess relative to tetrazine units on the NP) was added after the NP addition. After one hour of incubation at 37°C, the NP solutions were removed. The cells were washed twice with DPBS and fixed with 200 μ L of 4% paraformaldehyde in DPBS for 10 minutes at room temperature. The cells were washed again twice with DPBS and finally stained with DAPI for nuclear labeling. A 1 mg/mL DAPI solution was diluted 1:100 with 10% DPBS, and 200 μ L of this DAPI staining solution were added per well. After a 10-minute incubation, the DAPI solution was removed, and the cells were washed twice with DPBS. In the first experiment, the cells were mounted using Dako Faramount Mounting Medium, whereas in the second experiment, the cells were simply stored under DPBS. The ibidi slides were stored in the fridge (4°C) until microscopy. The images were then visualized using ZEN 3.10 (ZEN lite) software. To compare the CLSM results with the flow cytometry findings, the NP-derived cell-associated fluorescence was estimated from the image sections. Red pixels above a threshold (set at 40) were counted in ImageJ [19] and related to the number of cells.

2.10 Data analysis

All fittings of experimental data were conducted using Origin software (Version 2020, OriginLab Corporation, Northampton, MA, USA). Statistical significance in flow cytometry experiments was assessed via two-way ANOVA with subsequent Tukey's multiple comparison test. The number of

Switchable NP Uptake

performed experiments is stated in the figure caption and levels of statistical significance are indicated as * $p \leq 0.05$, ** $p \leq 0.01$, and *** $p \leq 0.001$ in the respective figures.

3. Results and Discussion

3.1 PLGA/PLA-PEG polymer NPs as a model platform for investigating the switchable behavior of NPs

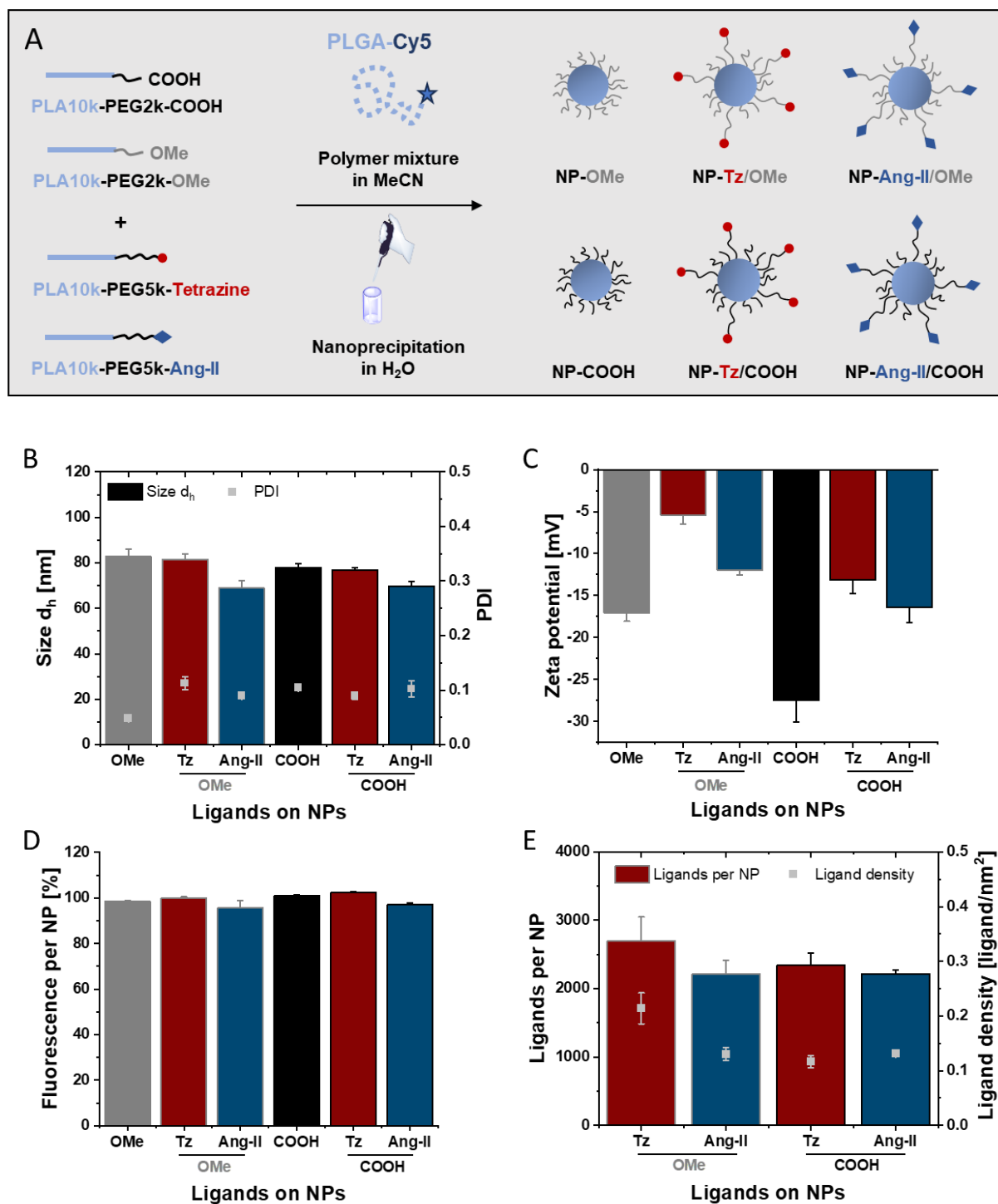


Figure 1. NP preparation and characterization. (A) Scheme for the preparation of the different NPs. (B) Size and PDI of the NPs measured by nanoparticle tracking analysis. (C) Zeta potential of the NPs in 10% PBS analyzed

using the Zetasizer. (D) Relative fluorescence of the NPs. (E) Quantification of ligands per NP and calculated ligand density on the NP. Results are presented as mean \pm SD (n = 3).

In this study, PEG-PLA copolymer nanoparticles with PLGA stabilized core were used as a model platform to explore the switchable properties of NPs. To enable post-functionalization via iEDDA reaction, thus altering the NP characteristics to enhance their cellular uptake, one component of the iEDDA reaction, tetrazine, was attached to the particles. For later comparison, blank NPs and NPs with Ang-II functionalization were also prepared. Functionalization was kept at 20% ligand-functionalized PEG-PLA block copolymer. The ligands, tetrazine or Ang-II, were positioned on longer PEG5k arms to ensure accessibility and flexibility of the ligands. [10] PLA10k-PEG2k-OMe and -COOH were employed as fillers. The filler polymers do not carry any ligands and were blended in to counteract ligand overloading of the NPs. To observe the NPs in subsequent flow cytometry and CLSM experiments, particle core-forming PLGA labeled with a fluorophore was used. [14] NPs were prepared by bulk nanoprecipitation of the polymers dissolved in acetonitrile (see **Figure 1 A**). The resulting particles had a size ranging from approximately 70 to 80 nm, a size range suitable for Clathrin-mediated endocytosis, considering an upper size limit of around 100 nm for this uptake pathway. [9] A relatively narrow size distribution of the NPs was indicated by the polydispersity index of approximately 0.1 (see **Figure 1 B**). Different zeta potentials were observed for the NPs due to the use of different fillers. PLA10k-PEG2k-OMe imparts no charge, resulting in a zeta potential of approximately -5 mV for NP-Tz/MeO, while carboxy-terminated PEG-PLA copolymer as a filler contributes to a more negative zeta potential of approximately -13 mV for NP-Tz/COOH (see **Figure 1 C**). Since the NPs exhibited approximately the same size, they also contained nearly the same amount of fluorophore-labeled PLGA in the particle core. Therefore, the fluorescence per NP was approximately the same for all particle types (see **Figure 1 D**). The cell-associated fluorescence determined in flow cytometry experiments thus directly indicates the number of cell-associated NPs. A further advantage of the particle design used here is that the prior synthesis of the ligand-functionalized PEG-PLA copolymers allows later on fine tuning of the number of ligands per NP during particle preparation. The NPs produced consistently carried between 2000 and 3000 ligands per nanoparticle, corresponding to a ligand density of just over 0.1 ligand/nm² and enabling a robust comparability of the NPs with each other (see **Figure 1 E**).

3.2 Switchable NPs via iEDDA functionalization with Ang-I

It was demonstrated that the NPs can be rendered switchable by subsequently functionalizing the NPs using the iEDDA reaction (see **Figure 2 A**). Tetrazine-functionalized NPs with methoxy or carboxy fillers were incubated with an excess of TCO-PEG₄-Ang-I. After the removal of excess reagents, a BCA assay was employed to quantify approximately 2400 Ang-I ligands per NP for NP-Tz-TCO-PEG₄-Ang-

Chapter 5

I/COOH. This corresponds to a complete iEDDA reaction on the particle. For the NPs with methoxy filler, only about 900 Ang-I ligands per NP were found. The iEDDA reaction proceeded with a yield of approximately 33% (see **Figure 2 B**). It is possible that some tetrazine functionalities may not be readily accessible, possibly due to folding of tetrazine towards the hydrophobic NP core along the extended PEG5k arms. Subsequent functionalization of NPs with carboxy fillers induced only minor alterations in particle size. Notably, following incubation with TCO-PEG₄-Ang-I, NPs with well-defined characteristics, adequately functionalized with Ang-I, were obtained as anticipated. A subset of NP-Tz-TCO-PEG₄-Ang-I was further incubated overnight at 37°C with soluble ACE. The enzyme was expected to process Ang-I on the NPs to Ang-II. This incubation with ACE led to a substantial increase in particle size whereby the size distribution also became significantly broader (see **Figure 2 C**). The change in size was probably due to bound or adsorbed ACE on the particle.

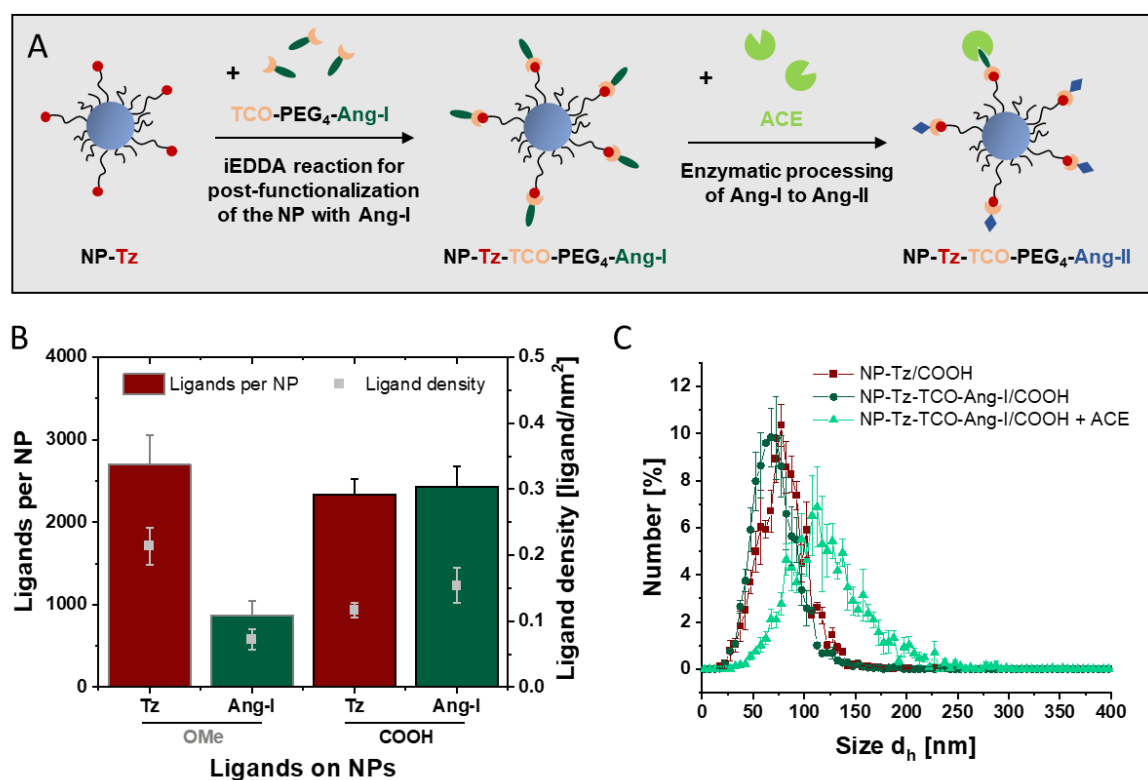


Figure 2. iEDDA reaction between NP-Tz and TCO-PEG₄-Ang-I followed by enzymatic processing to Ang-II. (A) Scheme for Ang-I functionalization of NPs by iEDDA reaction followed by enzymatic activation to Ang-II. (B) Comparison of the number of tetrazine ligands before the iEDDA reaction with attached Ang-I ligands after the iEDDA reaction. (C) Change in size of NPs after iEDDA reaction and subsequent enzymatic processing studied by nanoparticle tracking analysis. Results are presented as mean \pm SD ($n = 3$).

3.3 Assessing NP size in complex biological media using fluorescence-mode NTA

In NP studies, particle size is often measured exclusively in water or PBS, which provides limited insight into the actual size under biological conditions. [20] The observed size increase during incubation with ACE raised the question of whether the polymer NPs used in this study would maintain defined sizes in more complex environments. To investigate the NPs in biologically relevant media containing numerous species in the size range of the particles, the NPs were labeled with a fluorophore and analyzed using nanoparticle tracking analysis in fluorescence mode. [21] In this mode, only the fluorescence signal of the particles is detected, while scattered light is excluded by an appropriate filter. The difference between scatter and fluorescence modes is particularly pronounced in cell culture media containing 10% FBS. In scatter mode, NPs cannot be detected due to overwhelming interference from scattering species, while fluorescence mode enables meaningful measurements (see **SI Figure 3**). The NPs were measured immediately after preparation in water and after a one-hour incubation at 37°C in various media. For both blank particles, either methoxy- or carboxy-functionalized, and their corresponding iEDDA-reactive tetrazine-functionalized counterparts, no significant changes in size distribution were observed (see **Figure 3**). Notably, no aggregation of NPs occurred during incubation in biological media. In Leibovitz's L-15 medium with 0.1% BSA and RPMI 1640 cell culture medium supplemented with 10% FBS, the formation of a protein corona around the NPs is to be expected. However, the minimal increase in size that would result from this was not detectable. It can be concluded that during the incubation of NPs diluted in Leibovitz's L-15 medium with 0.1% BSA with the cells for flow cytometry or confocal microscopy experiments, no changes in NP size are to be expected. The NP size should correspond to the size initially determined in water.

Chapter 5

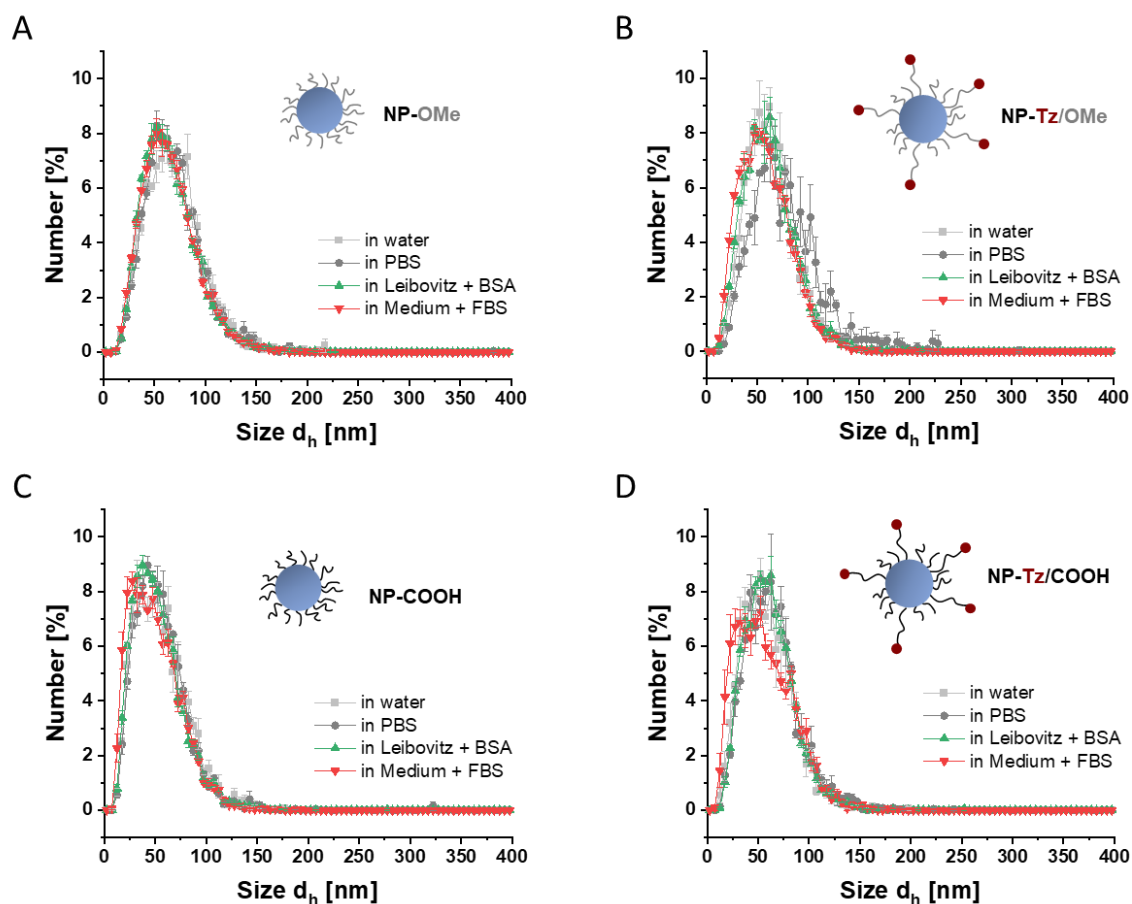


Figure 3. NP size distribution in biological media. Size distribution in various biological media determined via NTA for NP-OMe (A), NP-Tz/OMe (B), NP-COOH (C) and NP-Tz/COOH (D). The measurement in water was carried out directly after production. In PBS, Leibovitz's L-15 medium with 0.1% BSA and RPMI 1640 cell culture medium with 10% FBS supplement, the NPs were first incubated for 1 h at 37°C. Results are presented as mean \pm SD ($n = 3$).

3.4 Flow cytometry to investigate switchable NP uptake

To demonstrate the concept of a switchable NP, TCO-PEG₄-Ang-I was added to NP-Tz incubating with the cells. TCO as the one partner of the iEDDA reaction should react with tetrazine on the NP within a short time, thus functionalizing the NP with Ang-I *in vitro*. Ang-I can be enzymatically activated to Ang-II by the ectoenzyme ACE, which should finally lead to AT1 receptor-mediated uptake of the NP into the cell. Since blank NPs with pure methoxy functionalization generally show lower uptake than with carboxy, the experiments were performed with MeO filler polymer. Unfortunately, NP uptake was not significantly increased by the addition of TCO-PEG₄-Ang-I compared to the tetrazine-only functionalized NPs (see **Figure 4 A** and **C**). Even a significant excess of TCO-PEG₄-Ang-I relative to the tetrazine units present on the NP did not produce the desired result (see **Figure 4 B** and **D**).

Switchable NP Uptake

Preincubation of the cells with captopril as an ACE inhibitor or EXP3174 as an AT1R inhibitor did not significantly alter NP uptake. It would have been expected that the NPs that reacted with TCO-PEG₄-Ang-I would be better taken up than NP-Tz. If the increased uptake was indeed due to AT1R-mediated endocytosis, the uptake should return to the level of NP-Tz upon addition of the inhibitors. It was speculated that expectations were not met because NP functionalization was not successful. In LM supplemented with 0.1% BSA, in which the NPs were diluted for incubation with the cells, a protein corona presumably forms relatively quickly around the particle. It might be that this causes the tetrazine units on the NP to become less accessible and the functionalization fails. It may therefore be worthwhile to take a step back and perform the subsequent functionalization not in biological environment, but beforehand in water without the possibly interfering factor of the protein corona.

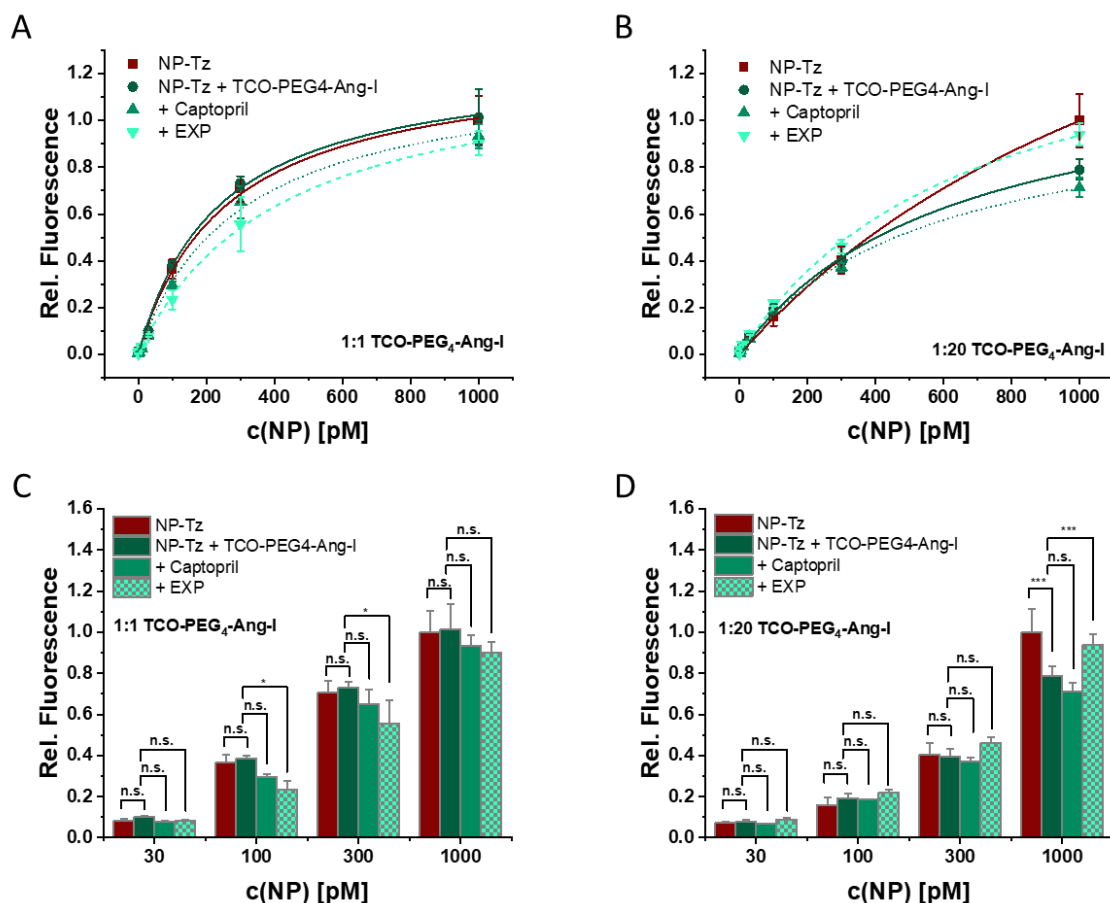


Figure 4. Cellular internalization of NP-Tz with and without TCO-PEG₄-Ang-I to functionalize them *in vitro* with Ang-I analyzed by flow cytometry. Uptake of NPs at different concentrations (3 to 1000 pM) in rMCs as target cell at 1:1 ratio between expected tetrazine units on the NP-Tz and TCO-PEG₄-Ang-I (A) and 20-fold excess of TCO-PEG₄-Ang-I (B). Bar charts with evaluation of statistical significance for 1:1 ratio (C) and 1:20 ratio (D) and in each case uptake inhibition by captopril or EXP3174 to confirm uptake specificity. The NPs employed in this experiment were 20% functionalized with tetrazine on longer PEG5k arms and the remaining 80% were methoxy terminated PLA10k-PEG2k block copolymer as filler. The incubation time of the NP solutions in LM supplemented with 0.1% BSA with the cells was 1 h before processing for flow cytometry analysis. Results are presented as mean ± SD (n = 3).

Chapter 5

3.5 Uptake of NPs previously functionalized with Ang-I via iEDDA reaction

While in the previous paragraph the NPs were modified with Ang-I in the presence of the cells, in this experiment the particles were already fully functionalized before they were added to the cells. The NPs functionalized with Ang-I using the iEDDA reaction were compared with respect to their uptake in rMCs with NP-Tz. No increase in cell uptake was observed despite clear Ang-I functionalization of the NPs (see **Figure 2 B**). Instead, the opposite effect of reduced association with target cells due to Ang-I functionalization was observed (see **Figure 5 A**). Pre-incubation of the cells with EXP3174, an AT1R inhibitor, did not change the cellular association of the NPs, indicating no specific AT1R-mediated uptake. After incubation of the Ang-I functionalized NPs with soluble ACE, an increase in cell-associated fluorescence was observed. For particles with MeO filler, the difference from the solely tetrazine-functionalized NPs was statistically significant at higher concentrations (see **Figure 5 C**). More NPs were either taken up by the cells or adsorbed onto the cell surface. It could be concluded that incubation with ACE activated the Ang-I functionalized NPs to Ang-II, resulting in pronounced receptor-mediated endocytosis through AT1R binding. However, cells pre-incubated with EXP3174 did not show reduced uptake. This suggests that the increased internalization was not due to the enzymatic conversion of angiotensin. Incubation with ACE resulted in an increase in size of the NPs, so it is more likely that this increase, possibly combined with ACE coating of the NPs and potentially different uptake pathways, was responsible for the increased number of cell-associated NPs. Since the expected effects were not observed with the NPs containing methoxy filler polymer, and previous experiments generally used carboxy filler, the series of experiments was repeated with COOH filler polymer.

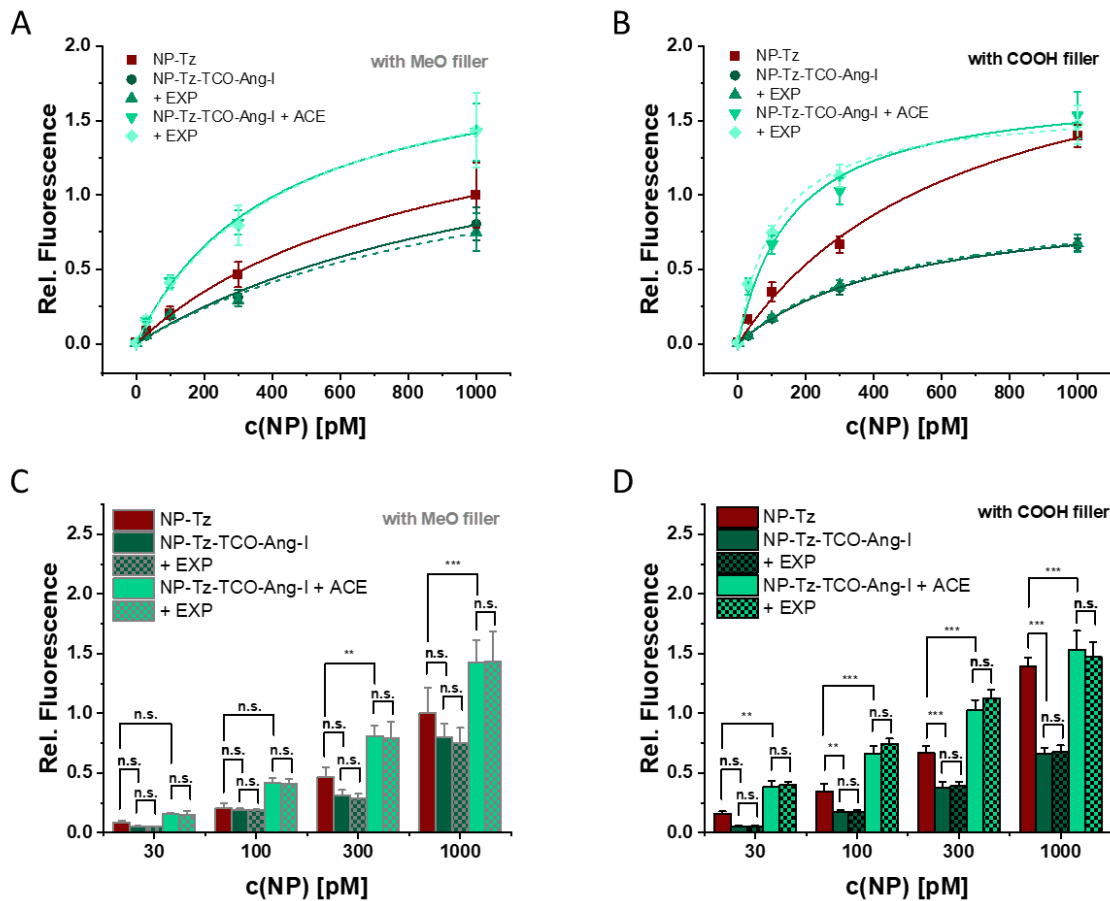


Figure 5. Association with the target cells of NPs pre-functionalized with Ang-I via iEDDA reaction analyzed by flow cytometry. NP-derived cell-associated fluorescence for tetrazine functionalized NPs (NP-Tz), via iEDDA reaction Ang-I functionalized NPs (NP-Tz-TCO-PEG₄-Ang-I) and NPs additionally incubated with soluble ACE (NP-Tz-TCO-PEG₄-Ang-I + ACE) with MeO filler polymer shown as (A) binding curve to illustrate the saturation of the cells with NPs and (C) bar chart to evaluate statistical significance. (B) and (D) show the same for the particles with COOH filler polymer. +EXP3174 indicates pre-incubation of the cells with the AT1R inhibitor EXP3174. The NPs were incubated in Leibovitz's medium supplemented with 0.1% BSA for 1h with rMCs as target cells. Results are presented as mean \pm SD of at least n=2 measurements.

With carboxy filler, the results were almost identical (compare **Figure 5 A** and **B**). The NPs subsequently functionalized with Ang-I using the iEDDA reaction were once again not better taken up than the NPs functionalized only with tetrazine. A statistically significant decrease in cell-associated fluorescence was observed at most concentrations (see **Figure 5 D**). After incubation with ACE, a significant increase in uptake was observed, which, however, was not AT1R specific and presumably resulted from altered particle properties. Since no increased uptake of the Ang-I functionalized NPs through receptor-mediated endocytosis could be observed, the concept was subsequently simplified. The iEDDA reaction for post-functionalization of the particles and the enzymatic processing by the ectoenzyme were omitted. The cell association of directly Ang-II functionalized NPs was investigated and the extent to which AT1R-mediated uptake plays a role was evaluated. Notably, AT1R-mediated

Chapter 5

uptake is an indispensable prerequisite for the successful establishment of NPs with switchable internalization into target cells within this concept.

3.6 Uptake of directly Ang-II functionalized NPs

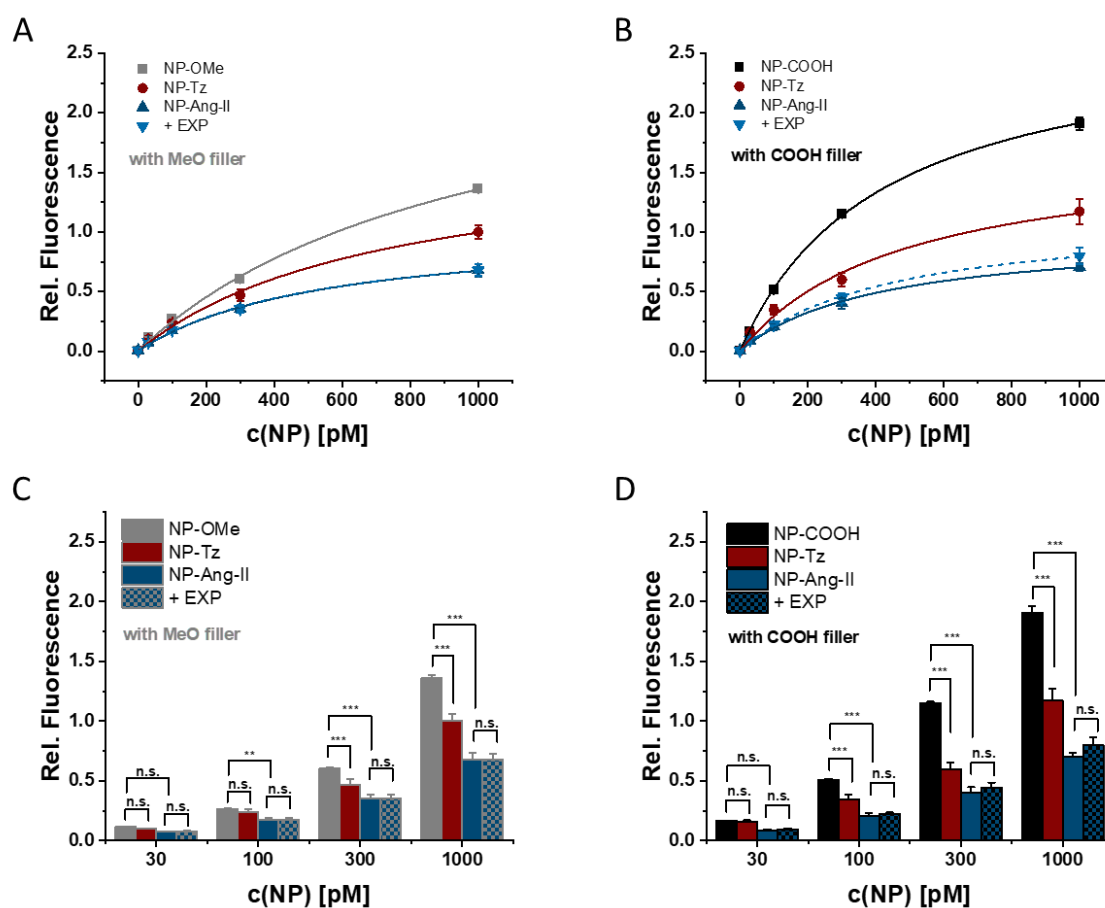


Figure 6. Association with the target cells of blank NPs, only tetrazine functionalized NPs and directly Ang-II functionalized NPs analyzed by flow cytometry. NP-derived cell-associated fluorescence for the particles with MeO filler polymer shown as (A) binding curve to illustrate the saturation of cells with NPs and (C) bar graph to evaluate statistical significance. (B) and (D) show the same for the particles with COOH filler polymer. The NPs were incubated for 1h with the rMCs as target cells. Results are presented as mean \pm SD of n=3 measurements.

Based on previous results, it was assumed that NP-Ang-II would bind to the AT1R and that receptor-mediated endocytosis would occur. This should increase NP uptake in AT1R-bearing rMCs and create a difference to blank NPs, which are taken up only nonspecifically. [10] However, the blank NPs, both methoxy-terminated (see **Figure 6 A**) and carboxy-terminated (see **Figure 6 B**), were always taken up the most. With tetrazine functionalization, fewer cell-associated NPs were observed. Functionalization of the NPs with Ang-II led to a further decrease in cell-associated NPs (see **Figure 6 C** and **D**). When the cells were pre-incubated with EXP3174 and NP-Ang-II were added, no significant difference in cell-

associated fluorescence was observed. Despite the high avidity of NP-Ang-II for the AT1 receptors on the rMCs shown in **Chapter 4** via Ca^{2+} mobilization assays, the NPs did not appear to be internalized via receptor-mediated uptake under the conditions investigated. The advanced concept of activating the NPs for targeted uptake via iEDDA reaction and ectoenzyme-based ligand processing cannot be successfully implemented in this context.

3.7 Comparison of blank NPs and reduced uptake due to functionalization

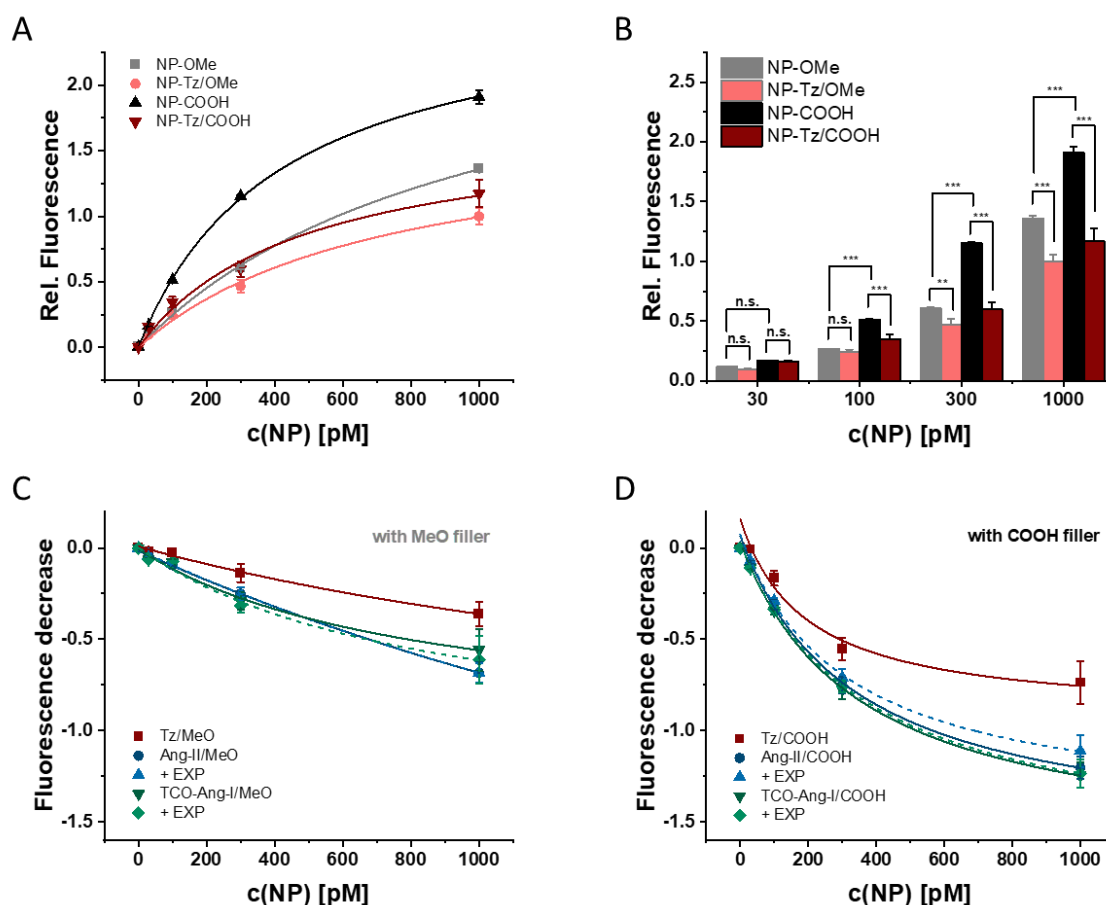


Figure 7. Comparison of the blank NPs and the decrease in uptake due to the NP functionalizations. NP-derived cell-associated fluorescence for the blank NPs shown as (A) binding curve to illustrate the saturation of cells with NPs and (B) bar graph to evaluate statistical significance. Results in (A) and (B) are presented as mean \pm SD of $n=3$ measurements. Decrease in NP-derived cell-associated fluorescence due to functionalization compared to the respective blank NPs for (C) particles with MeO filler polymer and (D) particles with COOH filler polymer. Results in (C) and (D) are presented as mean \pm SD of at least $n=2$ measurements.

Comparing the methoxy and carboxy blank NPs, it is noticeable that the COOH blank NPs were taken up to a significantly higher amount (see **Figure 7 A**). With tetrazine functionalization, the cell-associated fluorescence decreased markedly in both cases. It was found to be in a similar range for particles with

Chapter 5

MeO filler and COOH filler polymer, although tetrazine-functionalized NPs with carboxy filler were still taken up slightly better (see **Figure 7 B**). The NP-derived cell-associated fluorescence decreased even further compared to the blank NPs for particles with angiotensin functionalization. Interestingly, the decrease was almost the same for directly Ang-II functionalized NPs and Ang-I functionalized NPs via iEDDA reaction. This was observed for both particles with MeO filler polymer and particles with COOH filler polymer (see **Figure 7 C** and **D**). The NPs functionalized via iEDDA reaction, which then would also need to be enzymatically activated from Ang-I to Ang-II, appeared to behave similarly in terms of interaction with the target cell as directly Ang-II functionalized NPs. However, as previously discussed, the expected increase was not observed, but rather a selective and consistent decrease in cell-associated NPs caused by the functionalization with angiotensin.

3.8 CLSM images to reveal the cellular localization of the NPs

The uptake of NPs was further investigated using confocal laser scanning microscopy (CLSM). Carboxy blank NPs exhibited a relatively strong interaction with the target cells, showing both adsorption to the cell surface and significant internalization (see **Figure 8**). As these carboxy blank particles did not carry ligands for specific receptor-mediated interactions with the target cell, the pronounced uptake was likely due to nonspecific mechanisms. Tetrazine-functionalized NPs displayed a similar distribution between adsorption on the cell surface and strong internalization but with slightly weaker NP-derived cell-associated fluorescence compared to pure carboxy blank particles. The 20% tetrazine functionalization, with the remainder also being carboxy-terminated filler polymer, appeared to reduce uptake slightly. This effect could actually benefit the concept, as NP-Tz should initially not interact with the target cells. Only the subsequent attachment of Ang-I via iEDDA reaction should lead to an interaction with the target cell by enzymatically activating the Ang-I functionalized NPs to AT1R-binding Ang-II.

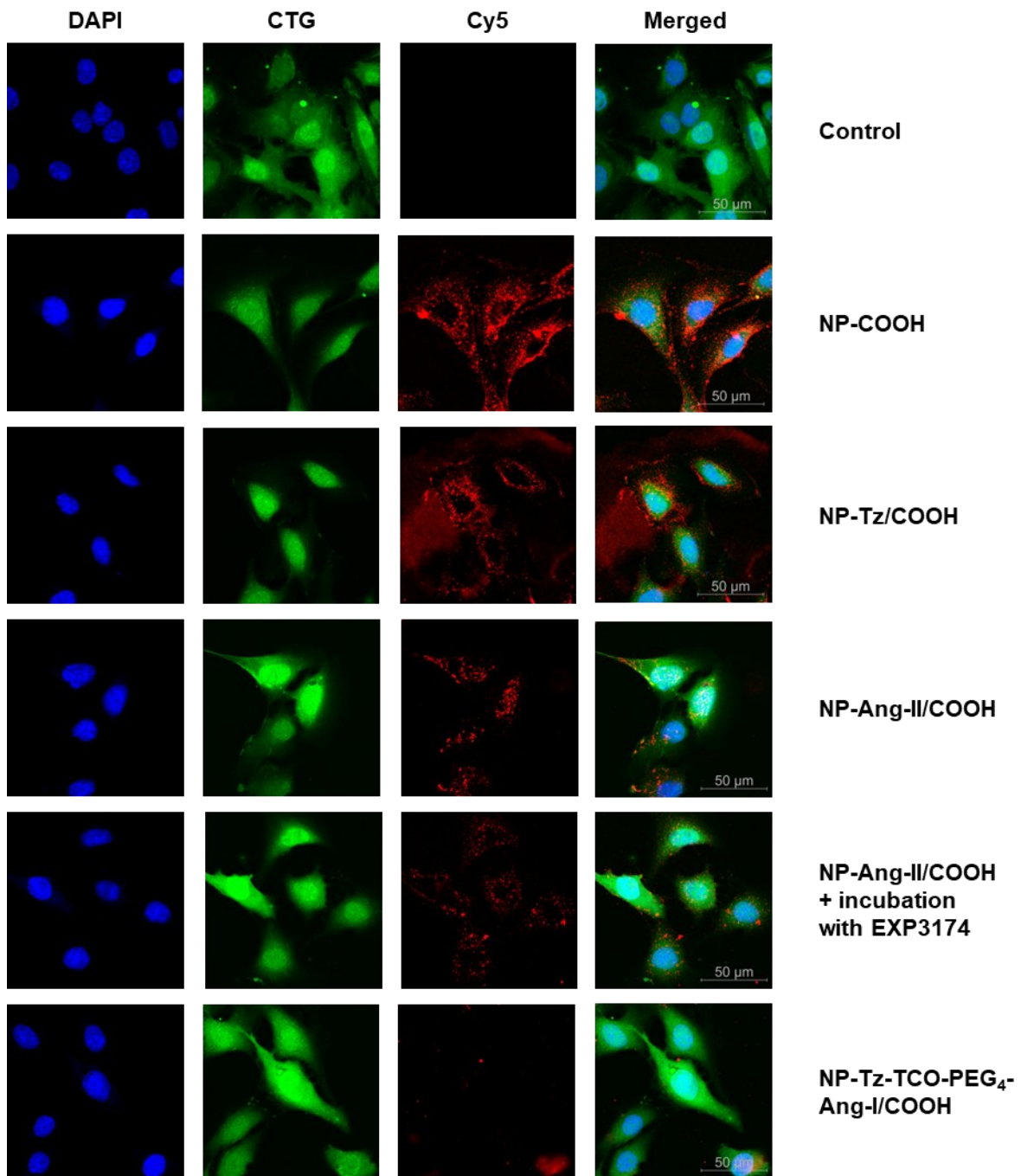


Figure 8. Cellular localization of various NPs in rMCs analyzed by CLSM. Cell nuclei were stained with DAPI (blue), the whole cell itself was localized by cell tracker green (green) and NPs were core-labeled with Cy-5 dye (red). All NPs were incubated with rMCs as target cells at a final concentration of 300 pM in Leibovitz's medium with 0.1% BSA for 1 hour.

However, examining the internalization of directly Ang-II functionalized NPs revealed that these are taken up even less efficiently than NP-Tz (compare **Figure 8**). The cell-associated fluorescence was significantly lower than that of NP-COOH and somewhat lower than that of NP-Tz. Additionally, there was no substantial difference when cells were pre-incubated with EXP3174, an AT1R inhibitor (for

Chapter 5

additional images, see **SI Figure 10**). In this case, all AT1 receptors would be expected to be blocked, making receptor-mediated endocytosis unlikely. However, the distribution of NPs was nearly identical with and without the inhibitor, with a comparable number of cell-associated NPs present. Either the pre-incubation with the AT1R inhibitor losartan carboxylic acid (EXP3174) did not lead to the anticipated receptor blockade, or, more likely under the given conditions, the NP-Ang-II were not endocytosed via receptor mediation. This undermines a fundamental aspect of the intended concept of switchable NP uptake through the attachment of an angiotensin ligand. Nonetheless, NPs functionalized with Ang-I via the iEDDA reaction prior to incubation were also investigated. Surprisingly, almost no cell-associated NPs were found in this case, not even at a lower level like with NP-Ang-II (see NP-Tz-TCO-PEG₄-Ang-I **Figure 8**).

3.9 Z-stacks to substantiate the findings

To substantiate the surprising result of an exceedingly low uptake of NPs functionalized via iEDDA reaction with Ang-I, an additional experiment with a series of CLSM images was conducted. The uptake study of NP-COOH performed as a control showed a NP-derived cell-associated fluorescence consistent with the previous experiment (see NP-COOH **Figure 9**). NP-Tz also demonstrated the expected pattern of particle uptake. For the NPs already functionalized via iEDDA reaction with Ang-I before incubation with the cells (see NP-Tz-TCO-PEG₄-Ang-I **Figure 9**), again virtually neither uptake nor adsorption to the target cell was observed. Consequently, experimental errors such as missed addition of the NP solution, incorrect processing or inadequate microscopy settings can be ruled out. If TCO-PEG₄-Ang-I is added to the tetrazine-functionalized NPs directly in the well of the ibidi slide for *in vitro* functionalization of the particles, it can be observed that the NPs were then no longer taken up (see NP-Tz/COOH + TCO-PEG₄-Ang-I **Figure 9**). This is in sharp contrast to the initially solely tetrazine-functionalized NPs, for which a relatively high degree of internalization was observed. Pre-incubation of the cells with EXP3174 did not result in any difference in NP uptake and cell adsorption, as no particles appeared to interact with the cell after the iEDDA reaction with TCO-PEG₄-Ang-I anyway. Rather than the desired switchable NP uptake, these results suggest a switchable suppression of interaction with the target cell. Consistent with the flow cytometry results, it was observed in these CLSM images that NPs functionalized via the iEDDA reaction with Ang-I and incubated with ACE were taken up to a higher extent (see NP-Tz-TCO-PEG₄-Ang-I + ACE **Figure 9**).

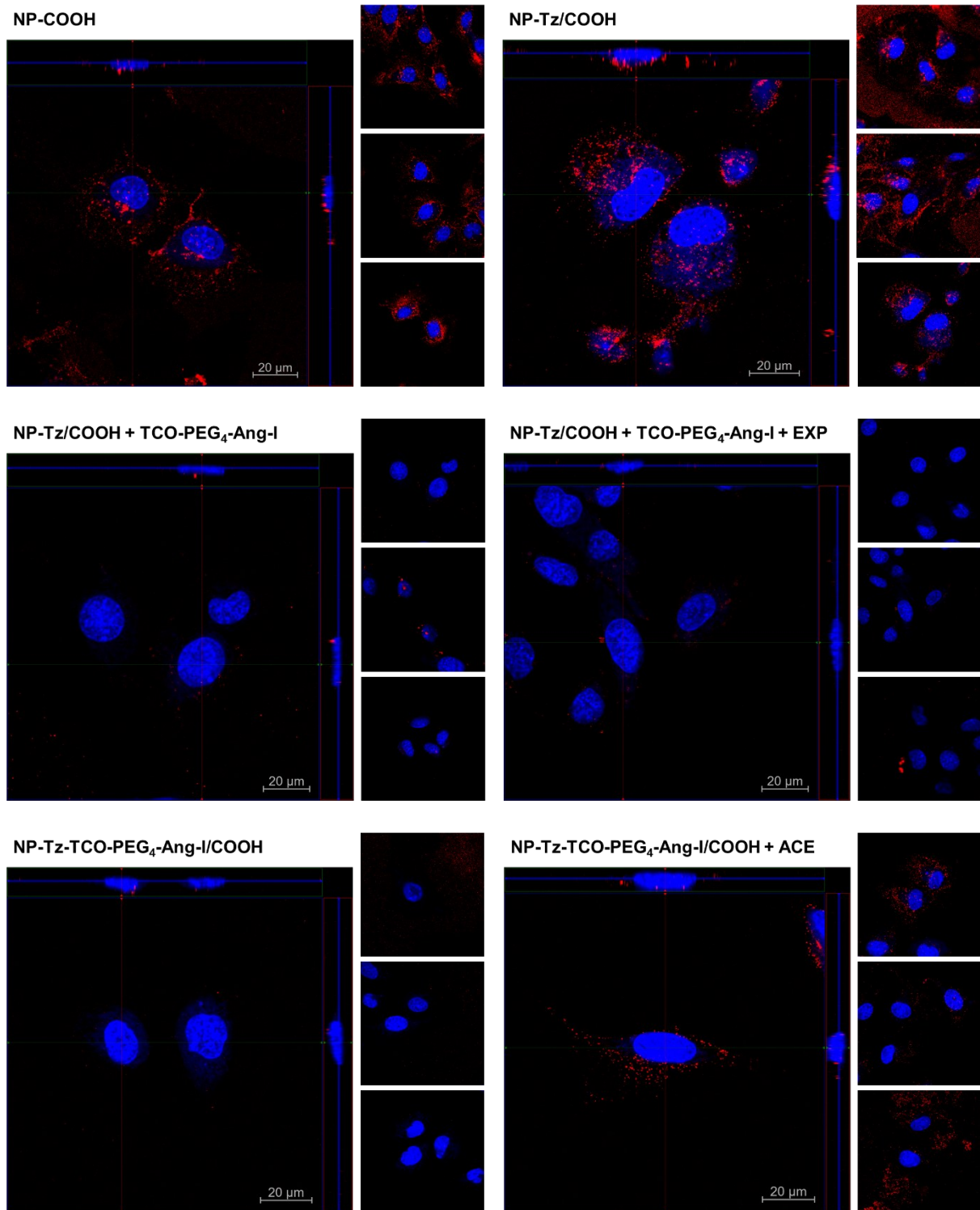


Figure 9. Uptake of different particles analyzed by CLSM. Cy-5 labeled NPs in red and DAPI cell nuclear staining in blue. The large image represents a typical Z-stack, and the three smaller images show additional sections. NP-Tz/COOH represents 20% tetrazine-functionalized particles, with carboxy-terminated polymer as filler; NP-Tz/COOH + TCO-PEG₄-Ang-I refers to the aforementioned NPs to which TCO-modified Ang-I was directly added on the cells in the ibidi slide (approximately 20-fold excess of TCO-PEG₄-Ang-I relative to tetrazine units on the NPs); NP-Tz/COOH + TCO-PEG₄-Ang-I + EXP3174 additionally involved a 30-minute pre-incubation of the cells with 1 mM EXP3174 in Leibovitz's medium with 0.1% BSA; NP-Tz-TCO-PEG₄-Ang-I/COOH denotes 20% tetrazine-functionalized particles with carboxy filler polymer, which were functionalized with Ang-I via iEDDA reaction before being applied to the cells; NP-Tz-TCO-PEG₄-Ang-I/COOH + ACE refers

Chapter 5

to particles that were incubated with soluble ACE for 4 hours at 37°C after the iEDDA reaction (approximately one hundredth the amount of ACE relative to the expected Ang-I concentration on the NPs). All NPs were incubated with rMCs as target cells at a final concentration of 300 pM in Leibovitz's medium with 0.1% BSA for 1 hour.

3.10 Comparison of CLSM and flow cytometry results

As shown in **Figure 10**, similar trends were observed for CLSM and flow cytometry. Pure carboxy blank NPs adhered to or were internalized by the cells more than the 20% tetrazine-functionalized particles, which also contain carboxy-terminated polymer as a filler. Apparently, the tetrazine functionalization resulted in reduced interaction with the cells. According to flow cytometry results, the uptake of directly Ang-II functionalized NPs was slightly lower than the one of the tetrazine-functionalized NPs. This trend was also supported by CLSM, with even fewer NP-Ang-II adhering to or being internalized by the cells compared to flow cytometry. Both methods consistently showed no significant difference with and without pre-incubation of cells with EXP3174. This suggests that the particles were not endocytosed via AT1 receptor mediation. While the uptake of NPs functionalized with Ang-I via iEDDA reaction was comparable to that of directly Ang-II functionalized NPs according to flow cytometry, the CLSM images showed that NP-Tz-TCO-PEG₄-Ang-I were practically neither taken up nor adsorbed onto the cells. Incubation of the particles with ACE consistently led to a strong increase in interaction with the target cells for both methods. Generally, pure carboxy blank NPs seem to be taken up most efficiently, while additional functionalization tends to hinder uptake. It can be concluded that the CLSM images and the estimated number of cell-associated NPs support the results of the flow cytometry experiments.

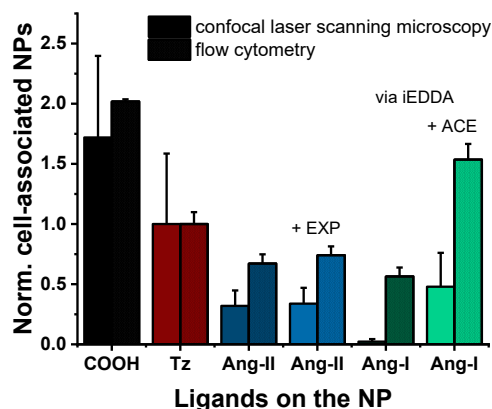


Figure 10. Comparison of CLSM and flow cytometry results. For CLSM, the red pixels per cell served as an estimate of the cell-associated NPs; for flow cytometry, the median fluorescence of the population of viable cells was used as a measure. In both cases, the respective NPs were incubated with rMCs as target cells for 1 hour. The CLSM experiments were conducted at a concentration of 300 pM. Accordingly, the flow cytometry results of 300 pM particles were compared. The cell-associated NPs for both cases were normalized to 1 for NP-Tz. For CLSM

analysis, at least three image sections containing a minimum of 8 cells in total were used. The data are presented as mean \pm SD of at least $n=3$ image sections. The flow cytometry results are given as mean \pm SD of $n=3$ measurements.

4. Conclusion

A stepwise analysis of the proposed concept revealed that the underlying assumption could not be properly confirmed. Under the conditions investigated, there was no increased uptake of Ang-II functionalized NPs via AT1R-mediated endocytosis. Instead, flow cytometry studies showed contrary to expectation that blank NPs appeared to be taken up the most efficiently, while additional functionalization led to reduce cell association of the NPs. Notably, the uptake of NPs functionalized with Ang-I via the iEDDA reaction or NPs functionalized directly with Ang-II decreased to a similar extent. CLSM images seemed to support the flow cytometry results, showing essentially the same trends in cell association of the NPs. No notable differences in cellular localization of the NPs due to different functionalizations were observed, with a similar ratio of adsorption on the cell surfaces and internalization for all particle types. Given that an increase in uptake through clathrin-mediated endocytosis was not apparent, the advanced NP concept with switchable uptake through the iEDDA reaction and ectoenzyme-based ligand activation could not be realized. To get a more comprehensive picture of the situation, further control experiments should be performed. An alternative method for determining the NP concentration could be used. Furthermore, the influence of factors such as incubation time, medium composition and cell density could be evaluated.

Chapter 5

References

1. Yoo J, Park C, Yi G, Lee D, Koo H (2019) Active Targeting Strategies Using Biological Ligands for Nanoparticle Drug Delivery Systems. *Cancers* 11(5), 640. 10.3390/cancers11050640.
2. Li X, Montague EC, Pollinzi A, Lofts A, Hoare T (2022) Design of Smart Size-, Surface-, and Shape-Switching Nanoparticles to Improve Therapeutic Efficacy. *Small* 18(6), e2104632. 10.1002/smll.202104632.
3. Jin E, Zhang B, Sun X, Zhou Z, Ma X, Sun Q, Tang J, Shen Y, van Kirk E, Murdoch WJ, Radosz M (2013) Acid-active cell-penetrating peptides for in vivo tumor-targeted drug delivery. *Journal of the American Chemical Society* 135(2), 933–940. 10.1021/ja311180x.
4. Sethuraman VA, Bae YH (2007) TAT peptide-based micelle system for potential active targeting of anti-cancer agents to acidic solid tumors. *Journal of Controlled Release* 118(2), 216–224. 10.1016/j.jconrel.2006.12.008.
5. Li H, Miteva M, Kirkbride KC, Cheng MJ, Nelson CE, Simpson EM, Gupta MK, Duvall CL, Giorgio TD (2015) Dual MMP7-proximity-activated and folate receptor-targeted nanoparticles for siRNA delivery. *Biomacromolecules* 16(1), 192–201. 10.1021/bm501394m.
6. Ding Y, Liu J, Zhang Y, Li X, Ou H, Cheng T, Ma L, An Y, Liu J, Huang F, Liu Y, Shi L (2019) A novel strategy based on a ligand-switchable nanoparticle delivery system for deep tumor penetration. *Nanoscale Horiz.* 4(3), 658–666. 10.1039/C8NH00415C.
7. Zimmer O, Goepferich A (2023) How clathrin-coated pits control nanoparticle avidity for cells. *Nanoscale Horiz.* 8(2), 256–269. 10.1039/D2NH00543C.
8. Ehrlich M, Boll W, van Oijen A, Hariharan R, Chandran K, Nibert ML, Kirchhausen T (2004) Endocytosis by random initiation and stabilization of clathrin-coated pits. *Cell* 118(5), 591–605. 10.1016/j.cell.2004.08.017.
9. Rennick JJ, Johnston APR, Parton RG (2021) Key principles and methods for studying the endocytosis of biological and nanoparticle therapeutics. *Nat. Nanotechnol.* 16(3), 266–276. 10.1038/s41565-021-00858-8.
10. Maslanka Figueroa S, Fleischmann D, Beck S, Goepferich A (2020) The Effect of Ligand Mobility on the Cellular Interaction of Multivalent Nanoparticles. *Macromolecular Bioscience* 20(4), e1900427. 10.1002/mabi.201900427.
11. Maslanka Figueroa S, Veser A, Abstiens K, Fleischmann D, Beck S, Goepferich A (2019) Influenza A virus mimetic nanoparticles trigger selective cell uptake. *Proceedings of the National Academy of Sciences of the United States of America* 116(20), 9831–9836. 10.1073/pnas.1902563116.
12. Schorr K, Beck S, Zimmer O, Baumann F, Keller M, Witzgall R, Goepferich A (2025) The quantity of ligand-receptor interactions between nanoparticles and target cells. *Nanoscale Horiz.* 10.1039/D4NH00645C.

13. Abstiens K, Gregoritz M, Goepferich AM (2019) Ligand Density and Linker Length are Critical Factors for Multivalent Nanoparticle-Receptor Interactions. *ACS applied materials & interfaces* 11(1), 1311–1320. 10.1021/acsami.8b18843.
14. Walter M, Baumann F, Schorr K, Goepferich A (2023) Ectoenzymes as promising cell identification structures for the high avidity targeting of polymeric nanoparticles. *International Journal of Pharmaceutics* 647, 123453. 10.1016/j.ijpharm.2023.123453.
15. Abstiens K, Goepferich AM (2019) Microfluidic manufacturing improves polydispersity of multicomponent polymeric nanoparticles. *Journal of Drug Delivery Science and Technology* 49, 433–439. 10.1016/j.jddst.2018.12.009.
16. Fessi H, Puisieux F, Devissaguet JP, Ammoury N, Benita S (1989) Nanocapsule formation by interfacial polymer deposition following solvent displacement. *International Journal of Pharmaceutics* 55(1), R1-R4. 10.1016/0378-5173(89)90281-0.
17. Filipe V, Hawe A, Jiskoot W (2010) Critical evaluation of Nanoparticle Tracking Analysis (NTA) by NanoSight for the measurement of nanoparticles and protein aggregates. *Pharm Res* 27(5), 796–810. 10.1007/s11095-010-0073-2.
18. Clayton KN, Salameh JW, Wereley ST, Kinzer-Ursem TL (2016) Physical characterization of nanoparticle size and surface modification using particle scattering diffusometry. *Biomicrofluidics* 10(5). 10.1063/1.4962992.
19. Schindelin J, Arganda-Carreras I, Frise E, Kaynig V, Longair M, Pietzsch T, Preibisch S, Rueden C, Saalfeld S, Schmid B, Tinevez J-Y, White DJ, Hartenstein V, Eliceiri K, Tomancak P, Cardona A (2012) Fiji: an open-source platform for biological-image analysis. *Nature methods* 9(7), 676–682. 10.1038/nmeth.2019.
20. Balog S, Rodriguez-Lorenzo L, Monnier CA, Obiols-Rabasa M, Rothen-Rutishauser B, Schurtenberger P, Petri-Fink A (2015) Characterizing nanoparticles in complex biological media and physiological fluids with depolarized dynamic light scattering. *Nanoscale* 7(14), 5991–5997. 10.1039/C4NR06538G.
21. Bannon MS, López Ruiz A, Corrotea Reyes K, Marquez M, Wallizadeh Z, Savarmand M, LaPres CA, Lahann J, McEnnis K (2021) Nanoparticle Tracking Analysis of Polymer Nanoparticles in Blood Plasma. *Part & Part Syst Charact* 38(6), 2100016. 10.1002/ppsc.202100016.

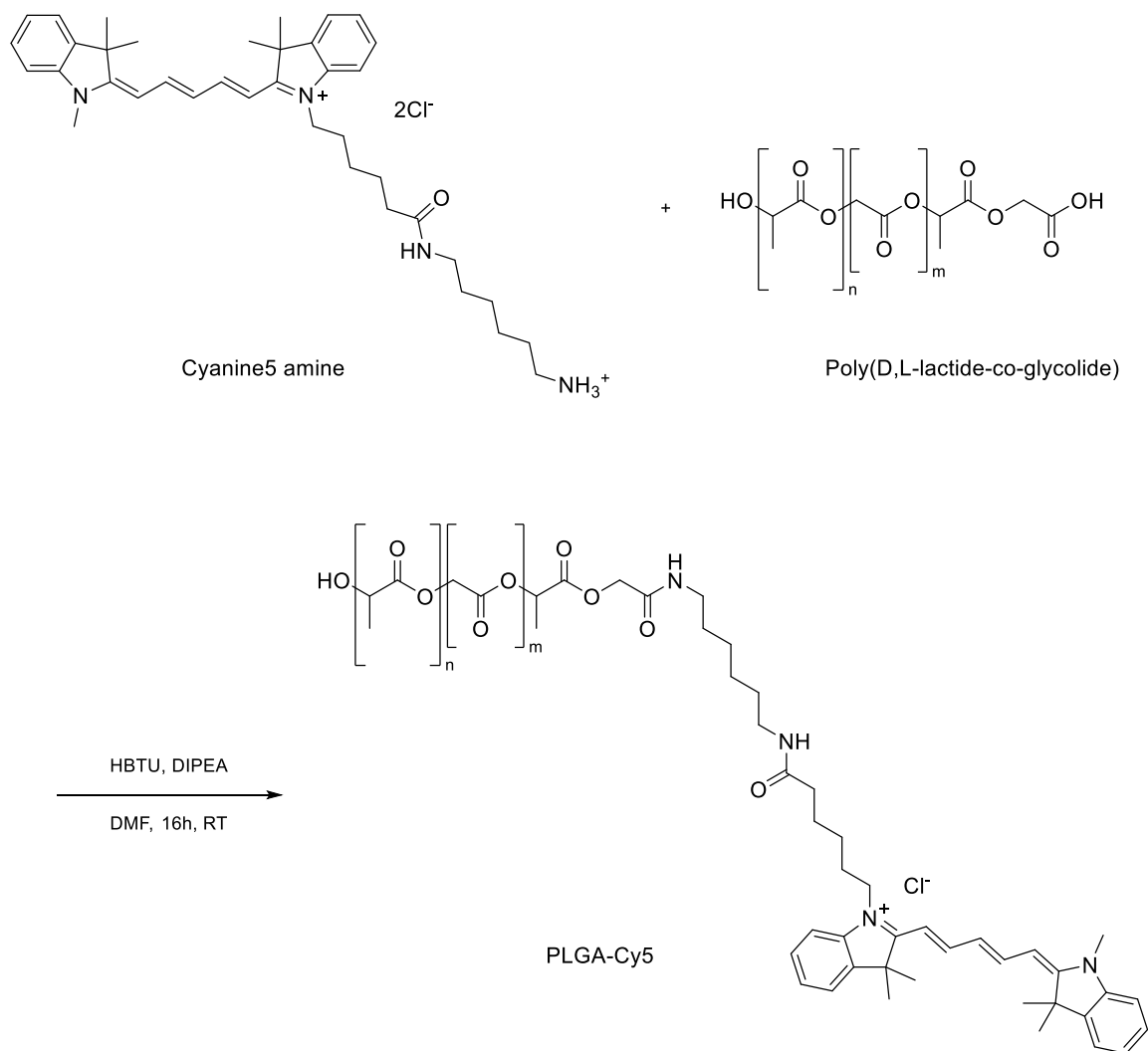
Chapter 5

Chapter 5

Supplementary Information

I. Synthesis of fluorophore labeled PLGA

Synthesis of cyanine-5 labeled PLGA

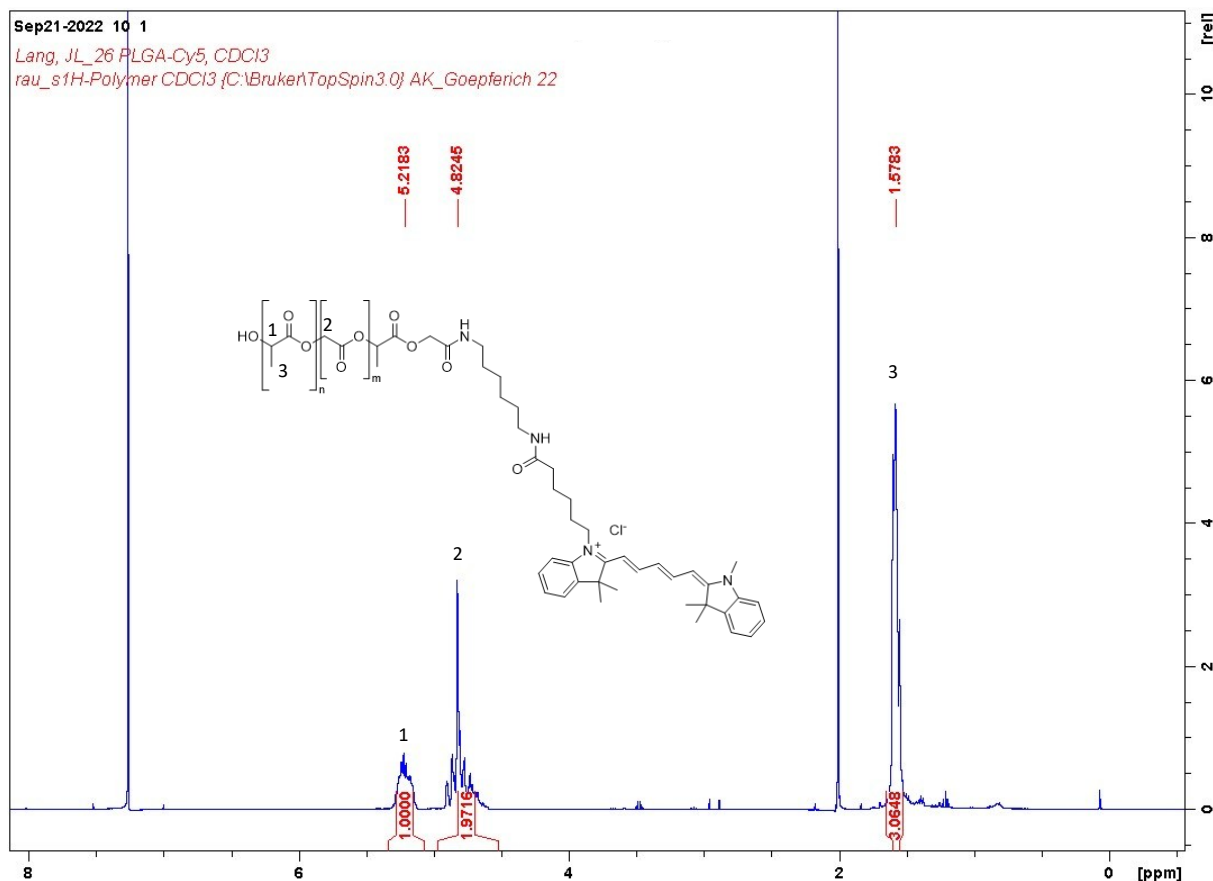


Cyanine-5 amine (14.63 mg, 22 μmol , 1 equiv), PLGA (resomer RG 502 H, poly(D,L-lactide-co-glycolide), acid terminated, Mw 7,000-17,000; 2625 mg, 219 μmol , 10 equiv) and HBTU (O-(benzotriazol-1-yl)-N,N,N',N'-tetramethyluronium hexafluorophosphate; 165.8 mg, 437 μmol , 20 equiv) were dissolved in 12 mL anhydrous DMF and 152 μL DIPEA (N,N-diisopropylethylamine; 875 μmol , 40 equiv) were added. The blue reaction mixture was stirred overnight at room temperature. The crude product was then precipitated in four Falcon tubes with 45 mL of ice-cold diethyl ether each, centrifuged for 15 min at 3000 g and 4°C, the supernatant decanted off and the polymer pellet dried before being redissolved in acetonitrile. This precipitation-centrifugation-decantation cycle was

Supplementary Information - Switchable NP Uptake

repeated four times as described. Finally, the pellets were dried overnight on the oil vacuum pump and 2569 mg PLGA-Cy5 (203 μmol , 93%) were obtained.

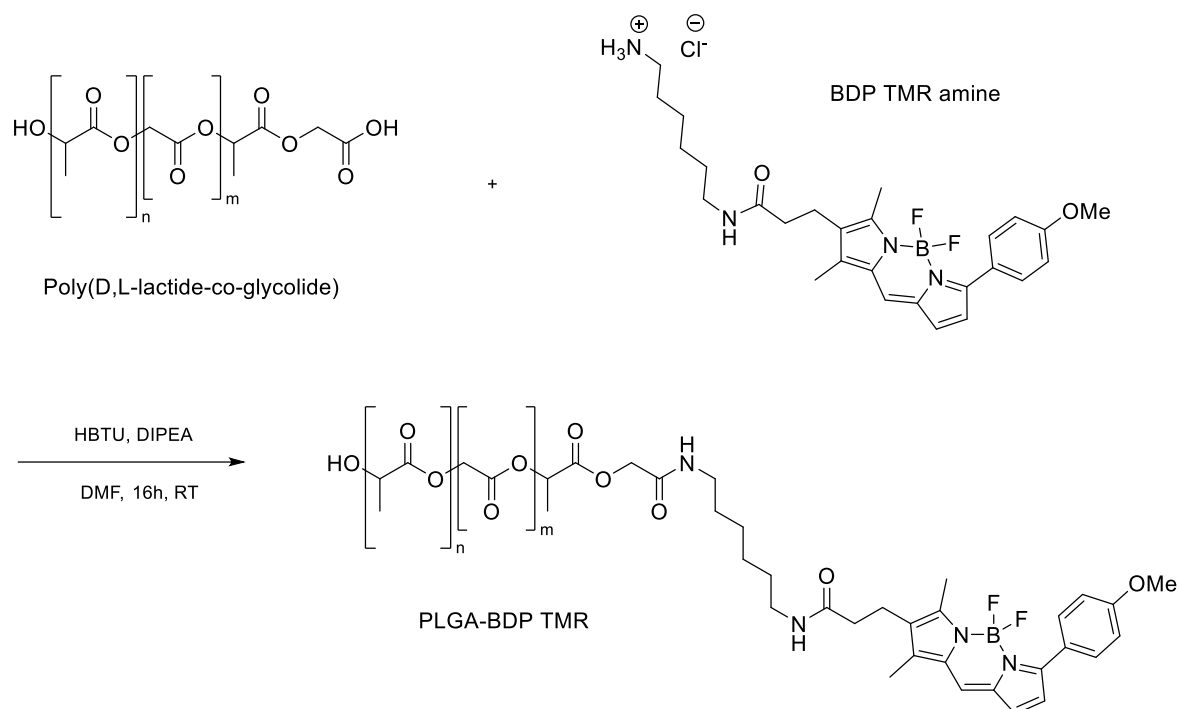
^1H NMR (CDCl_3): $\delta = 5.30\text{--}5.13$ (m, 1H), 4.91–4.59 (m, 2H), 1.61–1.53 (m, 3H).



In the ^1H NMR spectrum, no signals in the aromatic region corresponding to the fluorophore Cyanine-5 were observed. Presumably, there are too few protons on the fluorophore in relation to PLGA, making them challenging to detect in ^1H NMR. Despite this, the functionalization appeared successful, as evident from the intense blue coloration of the product. The ^1H NMR confirmed the appropriate ratio of PLGA integrals to each other.

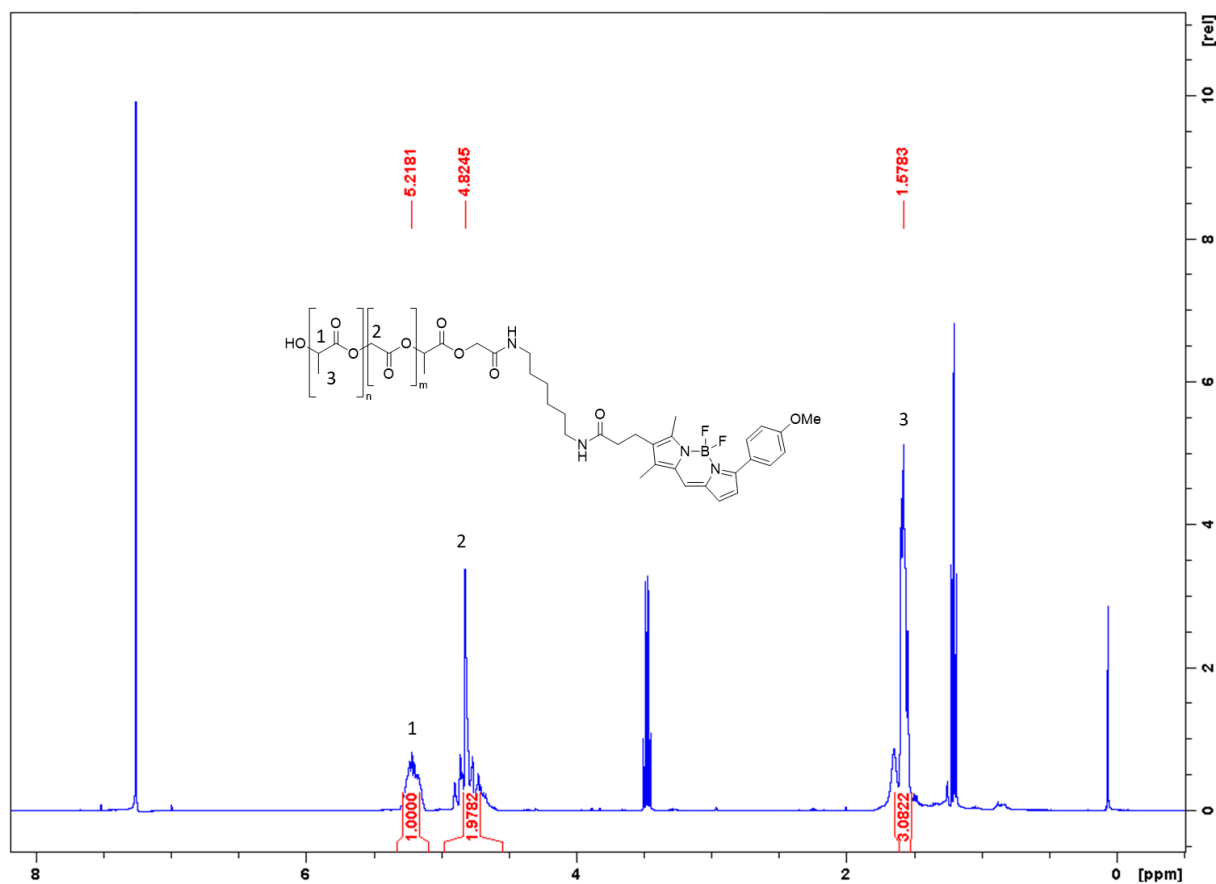
Chapter 5 – Supplementary Information

Synthesis of bodipy tmr labeled PLGA



Bodipy TMR-amine (1,3-dimethyl-2(6-aminohexylaminocarbonyl)-4,4-difluoro-5-(4-methoxyphenyl) borondipyrromethene, 1.0 mg, 1.88 μmol , 1 equiv), PLGA (Poly(D,L-lactide-co-glycolide, resomer RG 502 H, acid terminated; 127 mg, 9.38 μmol , 5 equiv) and HBTU (O-(benzotriazol-1-yl)-N,N,N',N'-tetramethyluronium hexafluorophosphate, 14.2 mg, 37.5 μmol , 20 equiv.) were dissolved in 3.0 mL anhydrous DMF. 13.1 μL of DIPEA (N,N-diisopropyl ethylamine, 75.1 μmol , 40 equiv.) were added. The reaction mixture was stirred overnight at RT. Subsequently, the mixture was precipitated in 10-fold excess of ice-cold diethyl ether. Centrifugation was performed for 15 min at 6000 rcf and 4°C, the supernatant was discarded, the pellet was allowed to dry briefly and then dissolved in acetonitrile. The precipitation-centrifugation-dissolution cycle was repeated two more times as described. Finally, the pellets were dried on the oil vacuum pump and 108.6 mg PLGA-Bodipy TMR (7.75 μmol , 83%) were obtained.

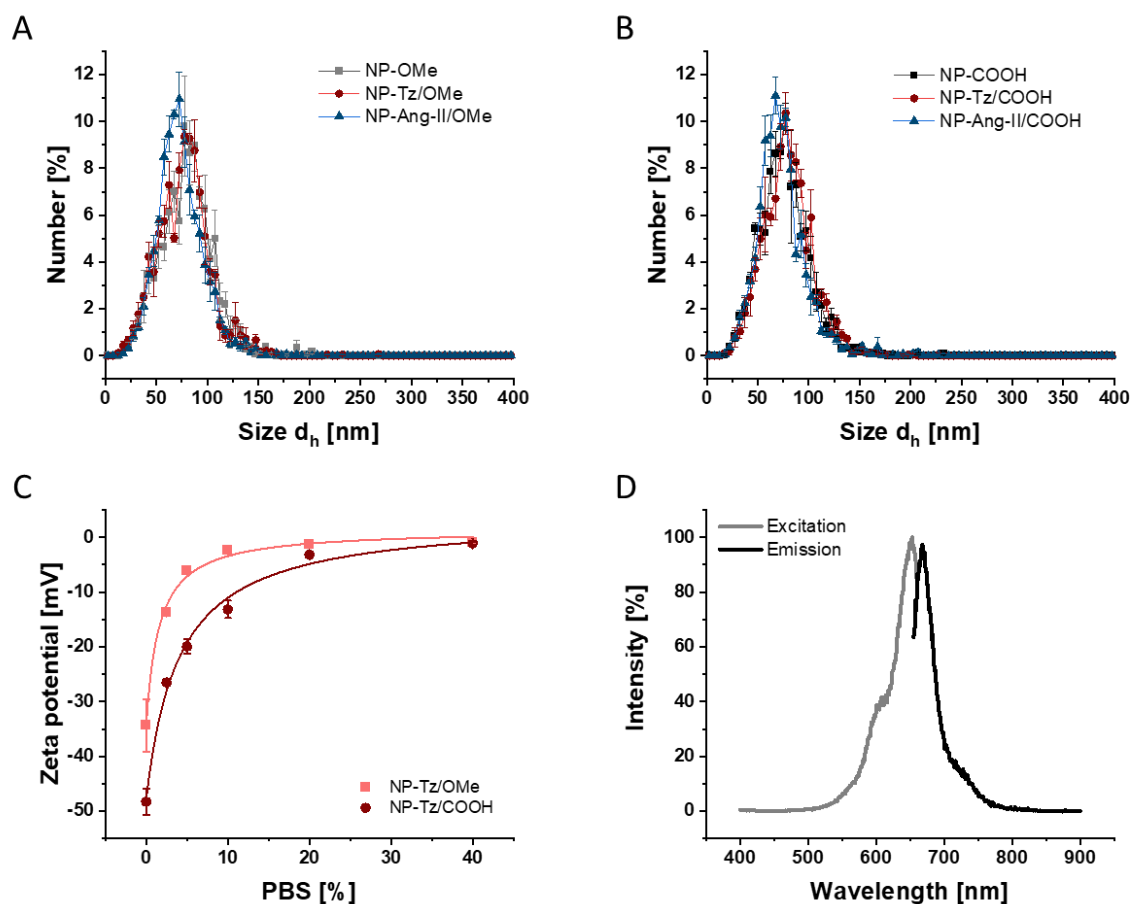
$^1\text{H NMR}$ (CDCl_3): δ = 5.30–5.13 (m, 1H), 4.91–4.59 (m, 2H), 1.61–1.53 (m, 3H).



II. Characterization of PLGA/PLA-PEG polymer NPs

To measure the zeta potential at varying PBS concentrations (see **SI Figure 1 C**), the NPs were diluted with water and the desired amount of PBS to a concentration of 1 nM. For PBS concentrations of 20% and higher, measurements were conducted using the diffusion barrier technique to protect the electrodes. [1] The measurement cell was filled with 2.5% PBS, and then 100 μ L of the respective sample was carefully injected at the bottom bend of the cuvette using a long needle. The fluorescence spectra (see **SI Figure 1 D**) were measured using a Cary Eclipse fluorescence spectrophotometer (Agilent Technologies, Waldbronn, Germany). NP-Tz/MeO were diluted with Millipore water to 10 nM in a black 96-well plate. For recording the excitation spectrum, the emission wavelength was set to 668 nm, and the range from 400 to 660 nm was scanned. For the emission spectrum, an excitation wavelength of 646 nm was chosen, and 655 to 900 nm were recorded.

Chapter 5 – Supplementary Information

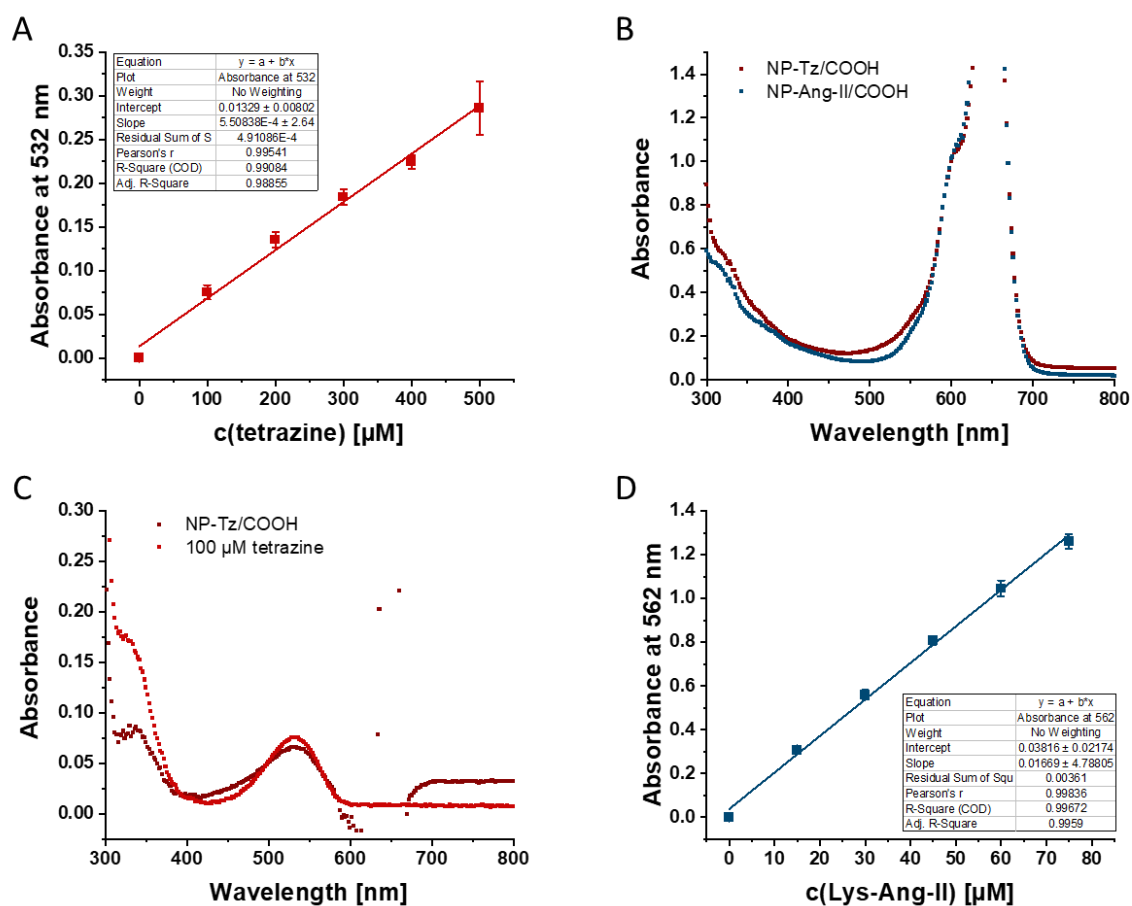


SI Figure 1. Characterization of the polymer NPs. Size distribution of NPs with MeO filler polymer (A) and with COOH filler polymer (B) determined by nanoparticle tracking analysis. (C) Zeta potential of the tetrazine functionalized NPs with MeO and COOH filler polymer at varying PBS content. (D) Fluorescence spectra of the Cy-5 labeled NPs. Results in (A), (B) and (C) are presented as mean \pm SD ($n=3$).

As **SI Figure 1 A + B** shows, the size distribution was similar for all particles, with NPs ranging from approximately 25 to 125 nm in hydrodynamic diameter. The use of methoxy or carboxy filler polymer had no effect on the particle size. In the paper, the mode value reported by the NanoSight is presented as the size d_h . The zeta potential of the NPs decreases with increasing electrolyte concentration in the solution (see **SI Figure 1 C**), as the ions in the solution shield the charge on the surface of the NPs. This reduction in zeta potential corresponds to a decrease in electrostatic repulsion between the particles. [2] Since NP-Tz with a methoxy-terminated filler inherently carry minimal charges, the zeta potential approaches zero with increasing PBS content. This poses challenges regarding colloidal stability. Elevated temperatures, such as incubation at 37°C over extended periods, and centrifugation, as employed during NP concentration at 3000 g, can overcome the energy barrier generated by electrostatic repulsion, leading to NP aggregation. In general, carboxy-terminated PEG-PLA copolymers as fillers appear more suitable, as their charge reliably ensures colloidal stability. **SI Figure 1 D** further shows the fluorescence spectra for Cy-5 labeled NPs. As expected, the excitation and emission spectra closely

correspond to those of the free Cyanine-5 fluorophore. The excitation maximum was at 653 nm, and the emission maximum could be determined at 668 nm.

III. Quantification of ligands per NP



SI Figure 2. Quantification of ligands per NP. (A) Calibration line for determination of tetrazine concentration in NP sample. (B) UV/Vis spectrum of cyanine-5 labeled NP-Tz/COOH and particles without tetrazine, namely NP-Ang-II/COOH. (C) Difference spectrum between equally weighted spectra of NP-Tz/COOH and NP-Ang-II/COOH and UV/Vis spectrum of tetrazine. (D) Calibration line for BCA assay to determine angiotensin-II concentration in NP sample.

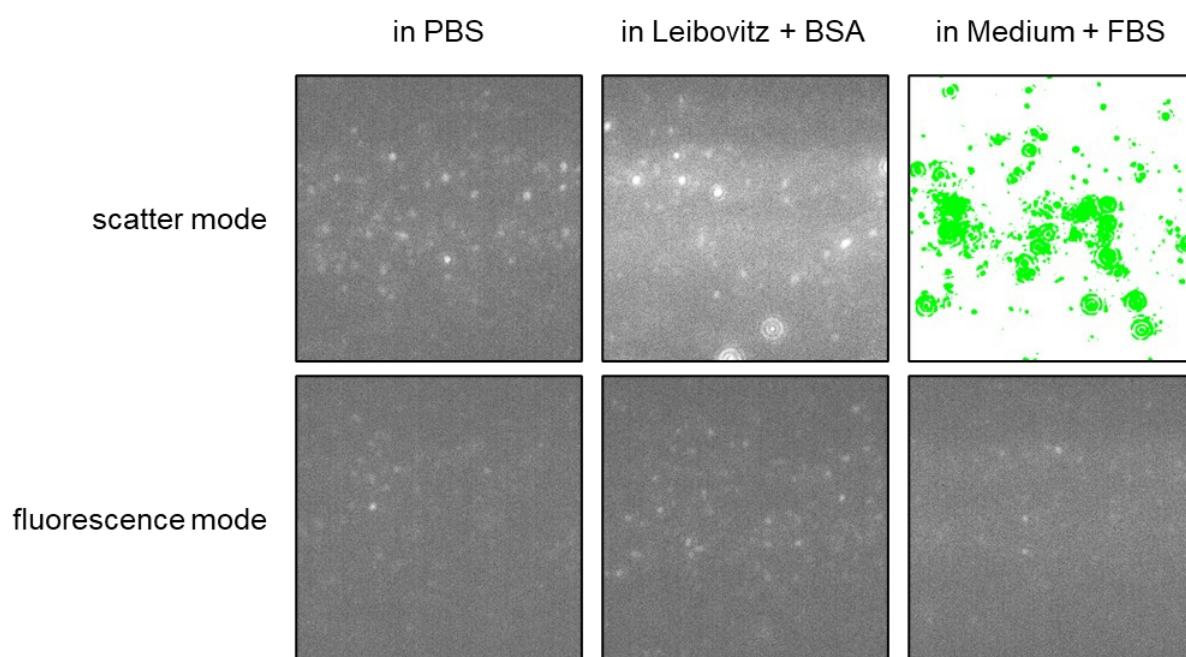
The quantification of tetrazine units per NP was accomplished through the measurement of tetrazine's absorption. UV/Vis spectra were acquired to subtract the absorbance of Cyanine-5 (Cy-5) in order to obtain the pure absorbance of tetrazine. As tetrazine no longer absorbs at 670 nm, whereas Cy-5, used to label the PLGA core of the NPs, does, a weighting factor was determined at this wavelength. The spectra of NPs without tetrazine (NP-Ang-II/MeO or NP-Ang-II/COOH) were multiplied by this factor and subsequently subtracted from the spectra of NPs with tetrazine. **SI Figure 2 B** displays the spectra

Chapter 5 – Supplementary Information

of NPs with and without tetrazine, equally weighted. Aside from the strong absorption of Cy-5, it is evident that the absorption with tetrazine is slightly higher in the range of 500 to approximately 550 nm. The difference spectrum corresponds to a typical tetrazine spectrum; however, the absorbance is very low (see **SI Figure 2 C**). Tetrazine concentration was then determined using the calibration curve at the absorption maximum of tetrazine at 532 nm (see **SI Figure 2 A**). **SI Figure 2 D** shows the calibration curve for the BCA assay, which was employed for Angiotensin-II quantification.

IV. Comparison of NTA scatter and fluorescence mode

In the commonly used scatter mode, the NPs are detectable in PBS, whereas this becomes more challenging in Leibovitz medium with BSA. In cell culture medium with 10% FBS, the particles cannot be localized (see **SI Figure 3**). FBS as a complex mixture of biomolecules including plasma proteins, growth factors, fats, and hormones [3], contains numerous components with hydrodynamic diameters within the size range captured by nanoparticle tracking analysis. Hence, with 10% FBS addition, the image captured by the camera in scatter mode is overloaded by scattering species and appears very bright. No meaningful measurement is possible here. BSA was added to the Leibovitz medium at only 0.1%. With a hydrodynamic diameter of approximately 7.8 nm [4], it minimally interferes with the measurement of the ~60 nm NP-COOH, but may contribute to a slightly brighter background, making it more difficult to capture individual NPs. BSA aggregates could also be included in a measurement and lead to biased results.



SI Figure 3. Comparison of scatter and fluorescence mode for bodipy TMR-labeled carboxy blank particles NP-COOH in different media. Image excerpts from the NanoSight video (Screen Gain 4, Camera Level 16).

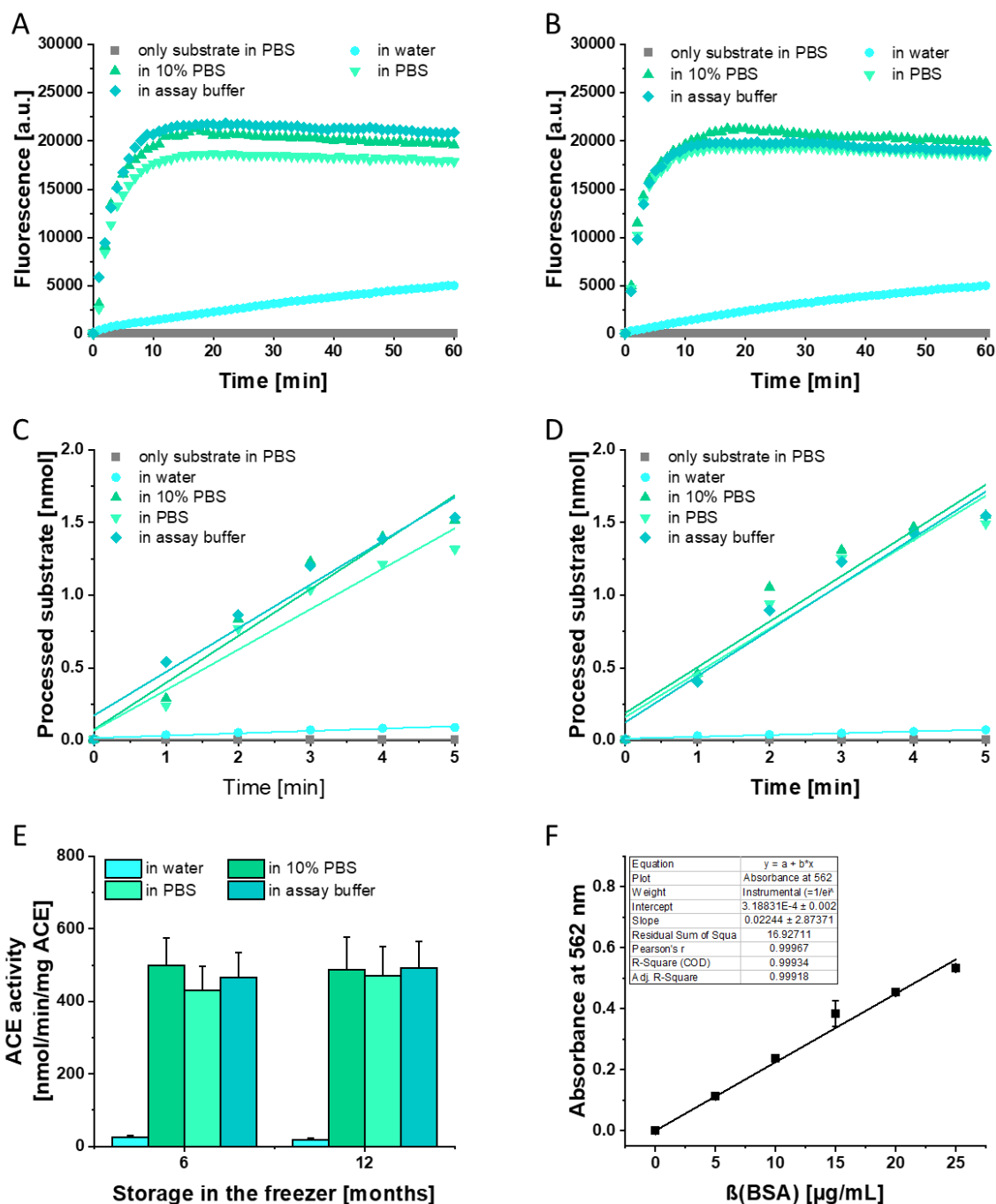
Supplementary Information - Switchable NP Uptake

To measure the particles in complex biological environments such as those with FBS addition, the fluorophore bodipy TMR with suitable excitation and emission maxima for the fluorescence mode of the NanoSight300 was covalently attached to particle core-forming PLGA (see section I). Since the scattered light is blocked in fluorescence mode by the corresponding filter, only the fluorescence signal of the particles is displayed. This is often quite dim [5], as is the case for the NPs produced here from bodipy TMR labeled PLGA. However, the signal is still sufficient for the particles to be observed regardless of the medium used. In summary, labeling the NPs with a suitable fluorophore and observing them in NTA fluorescence mode enables the measurement of NPs in complex biological media with numerous interfering species. [6]

V. ACE Activity Assay

Since the increased uptake after incubation with soluble ACE was not mediated by AT1R, it was investigated whether the enzyme was intact and capable of processing Ang-I to AT1R-binding Ang-II. A fluorogenic ACE substrate (o-aminobenzoic acid-phenylalanyl-arginine-lysine (2,4-dinitrophenyl)-proline) was added into a black 96-well plate and diluted with water or buffers. The assay buffer according to Carmona, Schwager et al. was prepared by dissolving 12.1 g Tris-base, 2.92 g NaCl and 1.4 mg ZnCl₂ in 1 L Millipore water. The pH was adjusted to 7 with 6 M HCl. [7] Immediately before measurement, ACE was added from a stock solution. The variation of fluorescence intensity over time was recorded using a BioTek Synergy Neo2 Hybrid Multimode Reader (Agilent Technologies, Waldbronn, Germany) with an excitation wavelength of 320 nm and an emission wavelength of 420 nm at an incubation temperature of 37°C (measurement every minute with 20 s slow orbital shaking before each measurement). The final substrate concentration in the well was 10 μM (corresponding to 2 nmol of fluorogenic ACE substrate in a volume of 200 μL per well). The ACE concentration was determined using a BCA assay following the manufacturer's protocol for the QuantiPro™ BCA Assay Kit with bovine serum albumin (BSA) as the standard. [8] The concentration was found to be 3.2 μg/mL (equivalent to 0.65 μg ACE). The ACE activity determined from the conversion of 10 μM fluorogenic substrate was related to the ACE amount measured by the BCA assay.

Chapter 5 – Supplementary Information



SI Figure 4. ACE activity test. Plot of fluorescence intensity with increasing incubation time for ACE stored for 6 months (A) and ACE stored for 12 months (B) in the freezer. Enzymatic processing was tested in water, 10% PBS, PBS and assay buffer consisting of 0.1 M Tris buffer with 50 mM NaCl and 10 μ M ZnCl₂ at pH 7. As a control, the change in fluorescence intensity of the fluorogenic substrate without enzyme was examined. Linear fit of the data from the first 5 minutes to determine the rate of enzymatic conversion for ACE after six months of storage (C) and ACE after twelve months of storage (D). The slope indicates the conversion rate in nmol of substrate per minute. (E) ACE activity after different storage durations in the freezer, expressed as nmol of converted substrate per minute per mg of ACE. (F) Calibration curve of a BCA assay with BSA as standard used to determine the ACE concentration.

Supplementary Information - Switchable NP Uptake

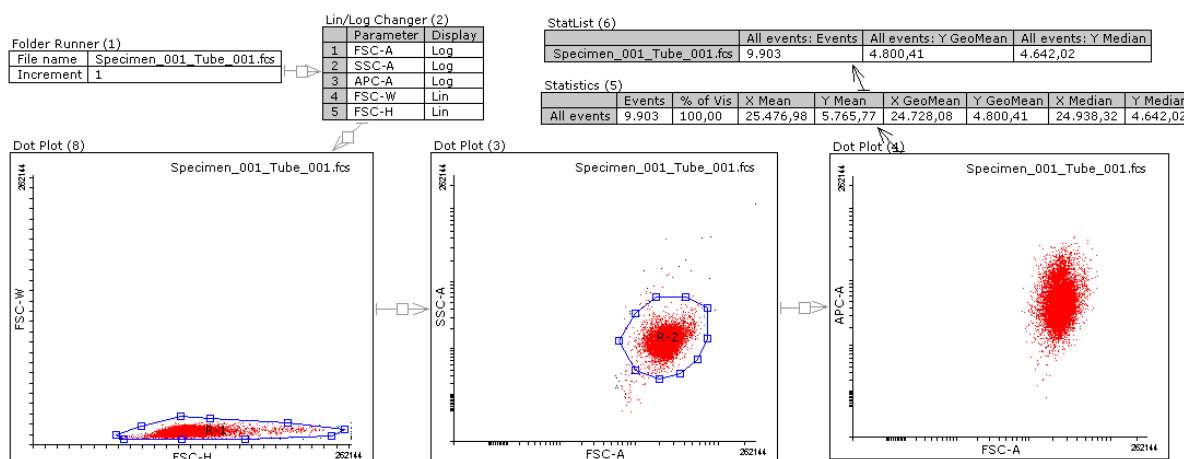
Intact ACE cleaves the internally quenched peptide substrate, o-aminobenzoic acid-phenylalanyl-arginine-lysine (2,4-dinitrophenyl)-proline (Abz-FRK(Dnp)-P), resulting in an increase in fluorescence intensity. [9] For the enzyme in 10% PBS, undiluted PBS, and assay buffer, there was a rapid increase in fluorescence intensity. In water, a significantly slower increase was observed (see **SI Figure 4 A+B**). Therefore, buffered solutions should always be used. The type of buffer does not appear to have a significant impact. It seems that the special assay buffer is not necessarily required, as a standard PBS buffer also appeared to be effective. As a control, the substrate was tested in the absence of the enzyme. The substrate remained quenched, the resulting background fluorescence was minimal, and no nonspecific cleavage of the peptide occurred over time (see **SI Figure 4 A+B**). In buffered media, the fluorescence intensity reached a plateau after approximately 15 minutes. It can be concluded that all available substrate had been converted by this time, preventing any further increase in fluorescence intensity. This clearly indicates intact enzyme activity. The fluorescence at the plateau is proportional to the amount of cleaved substrate Abz-FR-OH, allowing the conversion of arbitrary fluorescence units into nanomoles of processed peptide. [7] To determine ACE activity after six months and twelve months of storage in the freezer, the values from the first 5 minutes were plotted (see **SI Figure 4 C+D**). No significant difference was observed for the different storage durations. The slope of the linear fit indicates the conversion rate in nmol of substrate per minute. This rate was related to the amount of ACE present, resulting in an ACE activity of approximately 500 nmol of substrate per minute per mg of ACE, regardless of the buffer used or storage duration (see **SI Figure 4 E**). A direct comparison with the manufacturer's activity specification was not possible, as they used a protocol with a different substrate, buffer, and quantification method. [10] Overall, it can be concluded that the enzyme remains active for over a year when stored as a 0.1 mg/mL solution in water in the freezer. Therefore, the NPs functionalized with Ang-I via the iEDDA reaction should be converted to Ang-II through incubation with this soluble ACE.

VI. Flow cytometry data evaluation

In order to exclude cell aggregates, in particular doublets, from the analysis, the width (FSC-W) was first plotted against the height (FSC-H) of the forward scattered light signals. Cell doublets can be discriminated particularly well via the width signal, as the signal is significantly larger than that of a single cell. However, it can be noted that cell aggregates were hardly present in the collected data. Next, the side scattered light (SSC-A) was plotted against the forward scattered light (FSC-A). The FSC results mainly from the light diffraction around the cell and the intensity is usually proportional to the diameter of the cell. The FSC signal can thus be used to separate cells by size. SSC, on the other hand, is from

Chapter 5 – Supplementary Information

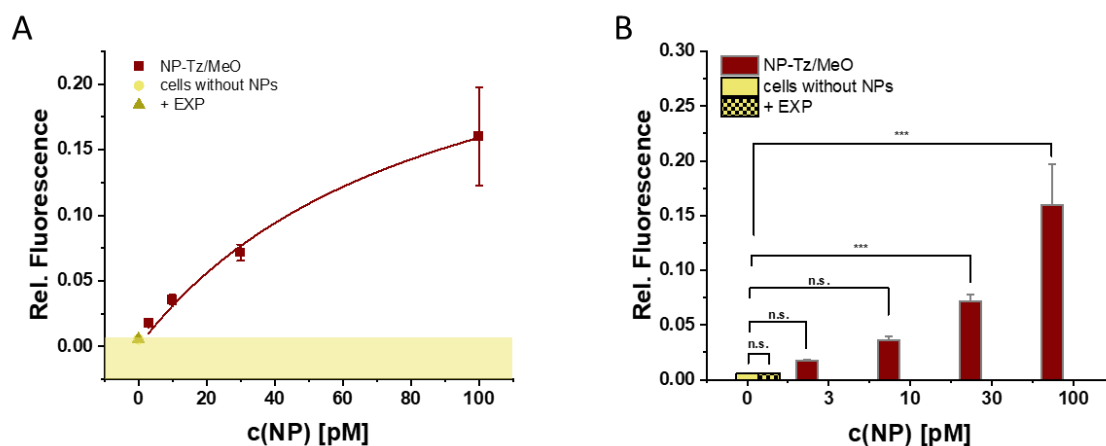
the light refracted or reflected at the interface between the laser and intracellular structures, such as granules and nucleus. Hence, SSC provides information about the internal complexity (i.e. granularity) of a cell. Since only one cell type was analyzed, a cloud resulted in the dot plot due to comparable size and granularity of rMCs as target cells. Events outside this cloud, mostly at low FSC and SSC, were excluded by gating, as these events are mostly debris and cell fragments. They only occurred to a very small extent in the recorded data. Based on the population of viable cells, the fluorescence (APC-A) was plotted against the forward scattered light (FCS-A). The median of the fluorescence served as the measure of cell association of fluorescently labeled NPs. It is important to note that flow cytometry cannot distinguish between NP uptake or adsorption of NPs on the cell surface. It was therefore generally referred to as cell association of NPs, which includes both uptake and adsorption. [11]



SI Figure 5. Evaluation scheme of the flow cytometry data. Exemplary excerpt from the flowing software.

VII. Background fluorescence of cells without NP addition

With the chosen settings, the background fluorescence of the cells without NP addition was very low. This allowed for the investigation of low NP concentrations, starting from 3 pM. However, the difference between background fluorescence and NP-derived cell-associated fluorescence was statistically significant only at concentrations of 30 pM and above. Therefore, 30 pM was used as the lowest concentration for further experiments, and unless otherwise stated, the concentration range from 30 pM to 1000 pM was examined.

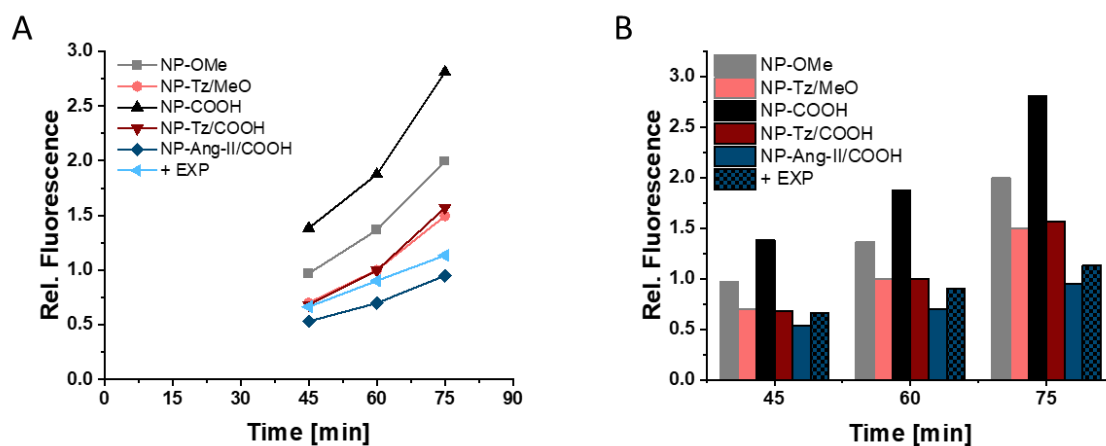


SI Figure 6. Background fluorescence of cells without NP addition. (A) Saturation curve of tetrazine functionalized NPs with MeO filler (NP-Tz/MeO) at low concentrations. The background fluorescence emanating from the cells without NP addition is colored yellow. (B) Comparison of cells without NPs with and without EXP3174 pre-incubation with the cells exposed to low NP concentrations (3 to 100 pM) shown as a bar chart for evaluation of statistical significance. Results are presented as mean \pm SD of at least $n=3$ measurements.

VIII. Variation of the incubation time

Incubation time is a crucial factor influencing the extent of NP uptake. In the presented experiments, the incubation time of NPs with the cells was consistently set at 1 hour. This incubation period was chosen because kinetic measurements of NP-Ang-I interaction with the AT1R showed receptor saturation after approximately one hour. Subsequently, the incubation time was varied over a small range. When incubating for only 45 minutes instead of one hour, fewer NPs were taken up. However, the trend of better uptake of blank particles compared to the corresponding functionalized ones remained the same. The same observation was made when the incubation time was extended to 75 minutes. The trends in NP cell association remained unchanged. Overall, more NPs were taken up due to the longer incubation time (see **SI Figure 7 B**). As discussed by Aberg [12], the increase in cell-associated NPs over time seems to lie between a linear and a quadratic trend (see **SI Figure 7 A**). However, a broader data basis with values at additional incubation times would be required for a fit and more substantial conclusions. It can be noted that slightly shorter and longer incubation times than 1 hour did not change the surprising finding of low cell association of Ang-II functionalized NPs.

Chapter 5 – Supplementary Information

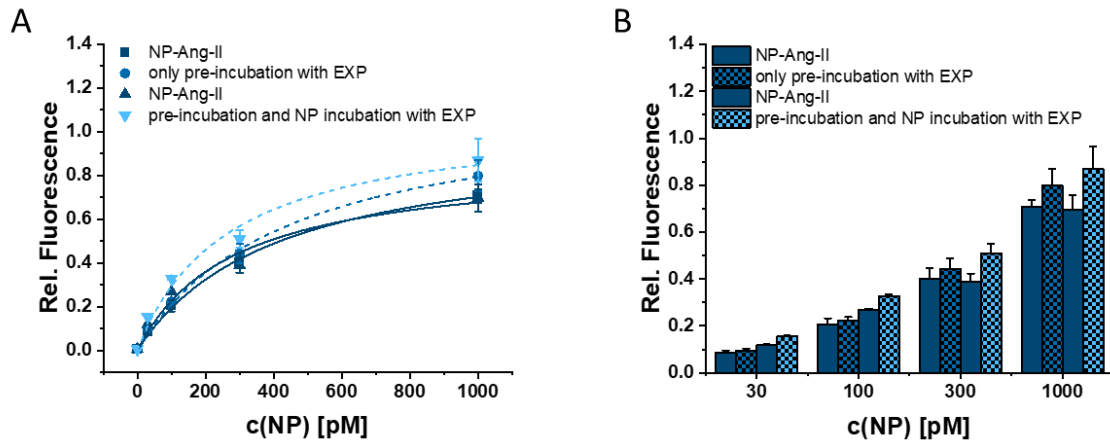


SI Figure 7. Variation of the incubation time. (A) Time course of NP-derived cell-associated fluorescence for various particle types. (B) Column diagrams of the cell association of the NPs at different incubation times. The values at an NP concentration of 1000 pM were shown here as an example; the other concentrations were also examined showing essentially the same trends.

IX. Comparison of different EXP3174 treatments of the cells

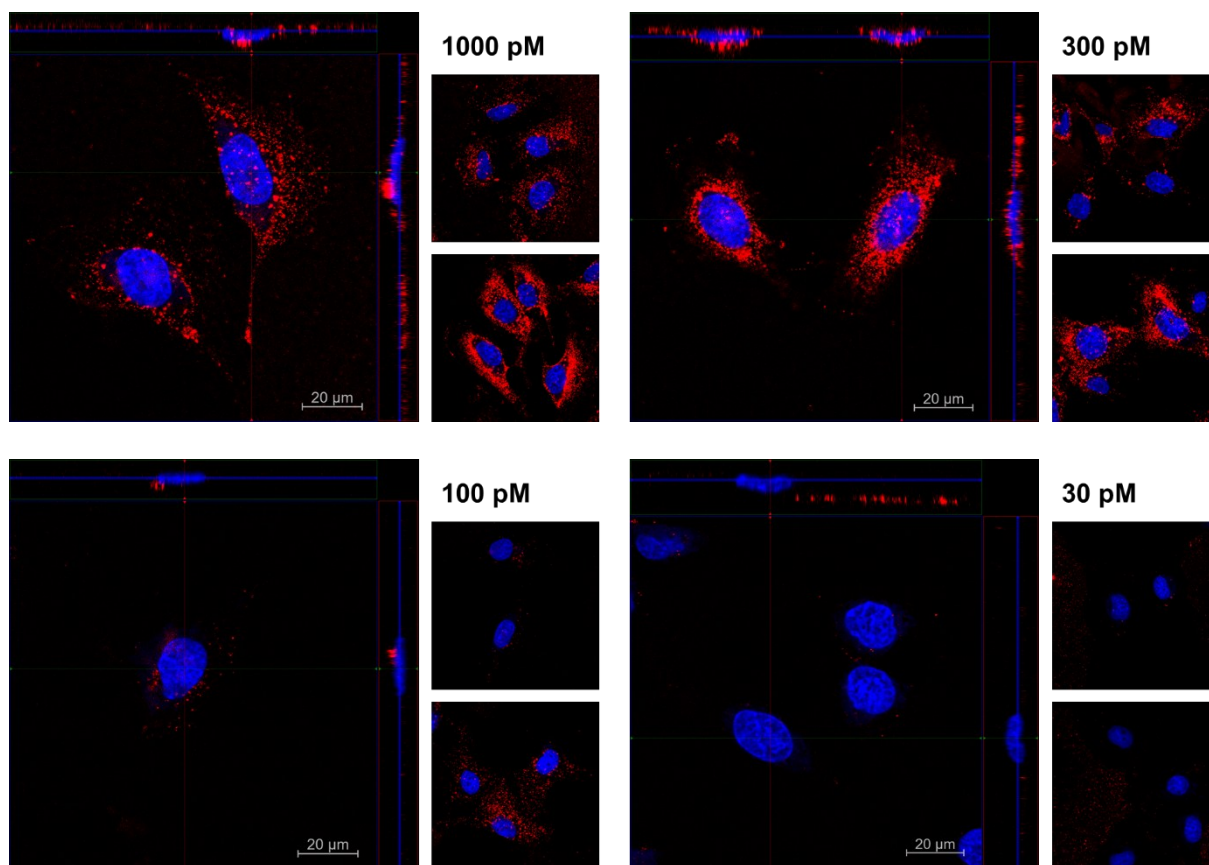
Since it was not evident from previous protocols whether EXP3174 was present only during the pre-incubation or also during the incubation with the NPs, both treatments were compared. NP-Ang-II were consistently taken up to a higher extent in EXP-pretreated cells than in untreated rMCs. This result is somewhat surprising, as EXP3174, being an AT1R antagonist, should block AT1 receptor-mediated endocytosis, leading to lower uptake of Ang-II functionalized NPs. As discussed in the main part of the paper, NP-Ang-II likely do not undergo receptor-mediated uptake. Therefore, the uptake should be the same with and without EXP3174 pre-incubation. When EXP3174 was present not only during the pre-incubation but also during the incubation of the NPs with the cells, an increased uptake of NP-Ang-II was also observed. The increase in uptake compared to untreated cells was even more pronounced in this case (see **SI Figure 8**). It seems that EXP3174 facilitates NP uptake, with a more pronounced effect when it remains on the cells for a longer duration. Overall, no significant differences between the two treatments could be identified, which is probably due to the fact that the particles are not internalized via AT1R.

Supplementary Information - Switchable NP Uptake



SI Figure 8. Comparison of cell association of NP-Ang-II with only pre-incubation with EXP3174 or pre-incubation and additional NP incubation with EXP3174. NP-derived cell-associated fluorescence for the particles with COOH filler polymer shown as (A) binding curve and (B) bar graph. The NPs were incubated for 1h with the rMCs as target cells before being processed for flow cytometry measurement. Results are presented as mean \pm SD of n=3 measurements.

X. Appropriate concentration for investigating NP uptake using CLSM



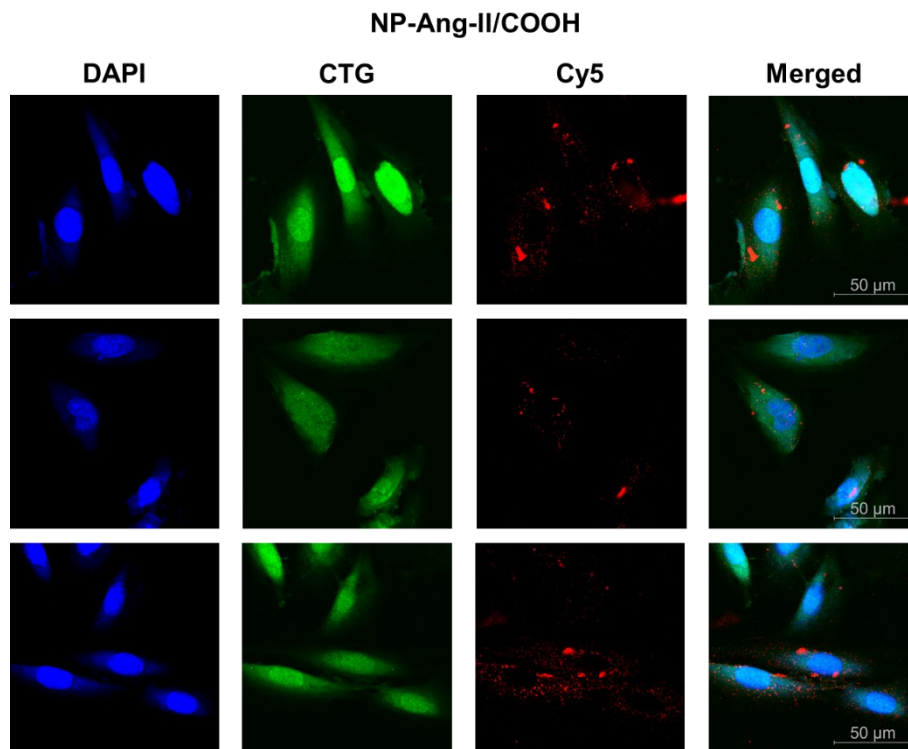
SI Figure 9. NP uptake for a dilution series of NP-Ang-II analyzed using CLSM. Cy-5 labeled NPs are shown in red and DAPI cell nuclear staining in blue. The large image represents a typical Z-stack, while the two smaller images show additional sections. NP-Ang-II were functionalized with 20% Ang-II on extended PEG5k arms, with carboxy-terminated PLA10k-PEG2k-COOH serving as the filler polymer. All NPs (final concentrations ranging from 1000 pM diluted down to 30 pM) were incubated with rMCs as target cells in Leibovitz medium with 0.1% BSA for 1 hour.

To determine an appropriate concentration for investigating NP uptake using CLSM, a dilution series of Ang-II functionalized NPs was imaged. The particles were expected to exhibit specific receptor-mediated internalization due to the immediate availability of Angiotensin-II for binding to the AT1 receptor. Consequently, in addition to particles adsorbed on the cell membrane or bound to the AT1 receptor within the membrane, punctate fluorescence corresponding to NPs trapped in endosomes or lysosomes should also be observed within the cells. At 1000 pM NP-Ang-II, the NP-derived fluorescence in and on the cells is relatively pronounced, and punctate fluorescence can be observed within the cells. At 300 pM, slightly reduced fluorescence of the Cy-5 labeled NPs is observed, whereas

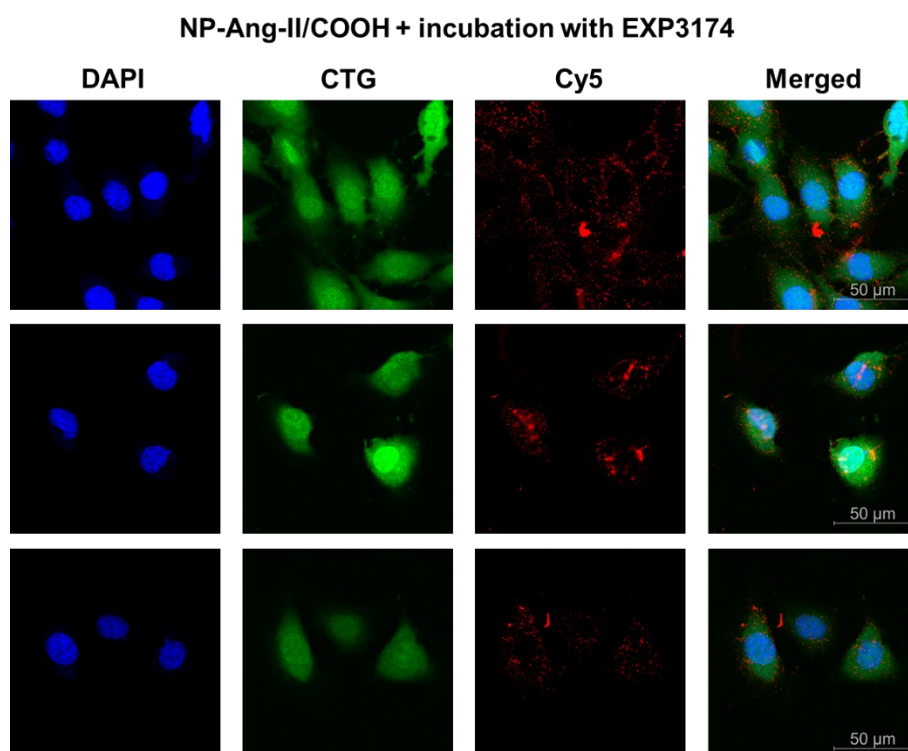
Supplementary Information - Switchable NP Uptake

at 100 pM and 30 pM, the fluorescence is very weak, and only a few NPs can be detected. Since at 300 pM the distribution of NPs on or within the cells can be clearly observed without the cells appearing overloaded with particles, 300 pM was chosen as an appropriate concentration for further investigations.

XI. Uptake of NP-Ang-II with and without EXP3174 as an inhibitor of the AT1 receptor



Chapter 5 – Supplementary Information



SI Figure 10. Comparison of the cellular localization of NP-Ang-II with and without pre-incubation of rMCs with EXP3174 as inhibitor analyzed by CLSM. Cell nuclei were stained with DAPI (blue), the whole cell itself was localized by cell tracker green (green) and NPs were core-labeled with Cy-5 dye (red). The NPs were incubated at a final concentration of 300 pM in Leibovitz medium with 0.1% BSA for 1 hour.

The uptake of NP-Ang-II with and without pre-incubation of rMCs with EXP3174, an AT1 receptor inhibitor, was investigated. The Ang-II functionalized NPs were expected to bind to the AT1 receptors on the target cells, leading to receptor-mediated endocytosis of the NPs through agonistic binding. [13] After pre-incubation of rMCs with the AT1R antagonist, losartan carboxylic acid (EXP3174), the NP-Ang-II should no longer bind to the target receptor, and only nonspecific uptake should be observed. However, as shown in **SI Figure 10**, there was no apparent difference with and without EXP3174. The cell-associated fluorescence from the NPs was more or less the same in both cases, and no different localization of the particles on or within the cells could be identified. This leads to the following conclusions: either NP-Ang-II were not endocytosed via receptor mediation as expected, or the pre-incubation with EXP3174 did not result in the anticipated receptor blockade.

References

1. Corbett JCW, Connah MT, Mattison K (2011) Advances in the measurement of protein mobility using laser Doppler electrophoresis - the diffusion barrier technique. *Electrophoresis* 32(14), 1787–1794. 10.1002/elps.201100108.
2. Filippov AV, Starov V (2023) Interaction of Nanoparticles in Electrolyte Solutions. *The journal of physical chemistry. B* 127(29), 6562–6572. 10.1021/acs.jpcb.3c01220.
3. Liu S, Yang W, Li Y, Sun C (2023) Fetal bovine serum, an important factor affecting the reproducibility of cell experiments. *Sci Rep* 13(1), 1942. 10.1038/s41598-023-29060-7.
4. Zhang X, Poniewierski A, Hou S, Sozański K, Wisniewska A, Wieczorek SA, Kalwarczyk T, Sun L, Hołyst R (2015) Tracking structural transitions of bovine serum albumin in surfactant solutions by fluorescence correlation spectroscopy and fluorescence lifetime analysis. *Soft Matter* 11(12), 2512–2518. 10.1039/C5SM00101C.
5. Malvern Panalytical (2019) NanoSight NS300 User Guide.
6. Bannon MS, López Ruiz A, Corrotea Reyes K, Marquez M, Wallizadeh Z, Savarmand M, LaPres CA, Lahann J, McEnnis K (2021) Nanoparticle Tracking Analysis of Polymer Nanoparticles in Blood Plasma. *Part & Part Syst Charact* 38(6), 2100016. 10.1002/ppsc.202100016.
7. Carmona AK, Schwager SL, Juliano MA, Juliano L, Sturrock ED (2006) A continuous fluorescence resonance energy transfer angiotensin I-converting enzyme assay. *Nat Protoc* 1(4), 1971–1976. 10.1038/nprot.2006.306.
8. Sigma-Aldrich (2011) QuantiPro BCA Assay Kit - Technical Bulletin. St. Louis, MO, USA.
9. Araujo MC, Melo RL, Cesari MH, Juliano MA, Juliano L, Carmona AK (2000) Peptidase specificity characterization of C- and N-terminal catalytic sites of angiotensin I-converting enzyme. *Biochemistry* 39(29), 8519–8525. 10.1021/bi9928905.
10. Sigma-Aldrich (1998) Enzymatic Assay of Angiotensin Converting Enzyme - Sigma Quality Control Test Procedure. St. Louis, MO, USA.
11. FitzGerald LI, Johnston APR (2021) It's what's on the inside that counts: Techniques for investigating the uptake and recycling of nanoparticles and proteins in cells. *Journal of Colloid and Interface Science* 587, 64–78. 10.1016/j.jcis.2020.11.076.
12. Åberg C (2021) Kinetics of nanoparticle uptake into and distribution in human cells. *Nanoscale Adv.* 3(8), 2196–2212. 10.1039/D0NA00716A.
13. Maslanka Figueroa S, Veser A, Abstiens K, Fleischmann D, Beck S, Goepferich A (2019) Influenza A virus mimetic nanoparticles trigger selective cell uptake. *Proceedings of the National Academy of Sciences of the United States of America* 116(20), 9831–9836. 10.1073/pnas.1902563116.

Chapter 5 – Supplementary Information

Chapter 6

Summary and Conclusion

Chapter 6

Summary

In modern pharmaceutical research, numerous drug candidates with high therapeutic potential have been identified. Nevertheless, the clinical efficacy of many compounds falls short of expectations, frequently due to unfavorable biodistribution that prevents the establishment of therapeutically relevant concentrations at the target site. In this context, nanoparticles (NPs) have attracted considerable attention. [1] By encapsulating pharmacologically active agents, NPs can protect them from enzymatic degradation and enable targeted delivery to specific tissues or cell types. In particular, the possibility of equipping NPs with ligands for active targeting raised high hopes of overcoming the limitations of conventional drug delivery. In theory, this strategy allows for enhanced accumulation at the site of action, reduced systemic side effects, and improved therapeutic efficacy. [2] However, in practice, NPs encounter a multitude of biological barriers. The spontaneous formation of a protein corona upon administration can obscure intended targeting properties, while the mononuclear phagocyte system (MPS) leads to rapid clearance from circulation. Further hurdles arise from processes such as extravasation, cellular internalization, and subsequent intracellular trafficking, each imposing distinct and often conflicting requirements on particle design. [3] To address these challenges, increasingly complex stimuli-responsive NPs have been developed that adapt their properties in response to endogenous or exogenous triggers. Most of these concepts rely on preconfigured architectures, where adaptability results from cleavage or rearrangement of existing functional moieties. [4]

A complementary approach would be the additive functionalization of NPs within the biological environment, equipping particles with functional moieties only upon demand. Such a strategy poses challenges, since NP and reactive moiety must first meet each other *in vivo*, and the subsequent coupling reaction must proceed selectively in the presence of a multitude of competing functional groups. Here, bioorthogonal chemistry provides a promising solution. In particular, the inverse electron-demand Diels–Alder (iEDDA) reaction combines exceptional selectivity with fast kinetics under physiological conditions, enabling efficient coupling even at low concentrations. [5] In **Chapter 3**, the principal suitability of the iEDDA reaction for the functionalization of polymeric NPs was investigated. NPs with variable TCO densities were prepared from core-forming PLGA and PLA-PEG block copolymers. A fluorogenic tetrazine-coumarin probe enabled real-time monitoring of iEDDA kinetics, revealing that the reaction proceeded significantly faster on NP surfaces than in solution, likely due to hydrophobic effects. Importantly, the reaction remained efficient in complex biological media, and stability studies confirmed sufficient robustness of the reactive partners, thereby laying the foundation for potential *in vivo* applications.

Building on this, **Chapter 4** established a concept for switchable target cell recognition. Unlike established approaches for ligand-switchable NPs such as temporary ligand blocking by covalent bonds or electrostatic interactions, the strategy pursued here relied on the *de novo* installation of ligands in the

Summary and Conclusion

biological environment. This design enables NPs to initially circulate in a “stealth” state and become activated only upon demand through a precisely triggered chemical reaction. As a proof of concept, angiotensin I (Ang-I) was conjugated to NPs via iEDDA as an inactive pro-ligand. Enzymatic conversion by angiotensin-converting enzyme (ACE) subsequently generated the active Ang-II ligand on the NP, capable of binding the AT1 receptor on mesangial cells. This enabled the establishment of a two-stage activation system consisting of chemical activation by iEDDA and biological activation by an ectoenzyme. At the same time, this two-stage activation system also corresponds to a two-stage recognition system. The target cell is checked for the presence of ectoenzyme ACE as well as the AT1 receptor, thereby conferring an additional level of specificity. Overall, the combination of bioorthogonal iEDDA chemistry with ectoenzyme-mediated ligand processing enabled the creation of NPs with switchable avidity for a target cell receptor.

Finally, **Chapter 5** examined whether switchable receptor recognition also translated into switchable cellular uptake. The hypothesis was that ACE-mediated activation of Ang-I to Ang-II would promote AT1R-driven internalization. However, the results of flow cytometry and confocal microscopy revealed that directly Ang-II-functionalized NPs did not exhibit increased uptake. Unexpectedly, unmodified particles showed the highest cellular association. These findings suggest that additional parameters such as incubation time, medium composition, or cell density may strongly influence uptake experiments. For realizing NPs with switchable cellular internalization, future studies should therefore consider alternative and more robust model ligand-receptor systems.

Conclusion

This thesis demonstrated that the iEDDA reaction represents a highly versatile tool for the development of switchable NPs. The production of modular, TCO-functionalized particles and real-time analysis of reaction kinetics using a fluorogenic probe demonstrated the unique potential of iEDDA chemistry for NP functionalization in a biological context. Moreover, by combining iEDDA-mediated ligand conjugation with enzymatic pro-ligand activation, an innovative two-step switching concept was established. This design integrates the advantages of stealth-like circulation with a temporally and spatially precise activation at the target site. In this way, unspecific ligand interactions might be reduced, while the specificity of NP systems is enhanced. The study on switchable cellular uptake, however, also showed the limitations of this approach. Under the investigated conditions, an increase in receptor-mediated internalization could not be demonstrated. Instead, the findings suggest that additional parameters must be considered to achieve efficient uptake.

Taken together, this work establishes iEDDA chemistry as a promising strategy for engineering dynamically controllable NPs. Future studies should extend the concept to preclinical models and systematically assess its applicability *in vivo*. In the long term, the combination of chemical precision and biological adaptability may open new perspectives for advanced nanomedicines that unite stability during circulation, selective activation, and controlled functionality at the site of action.

References

1. Mitchell MJ, Billingsley MM, Haley RM, Wechsler ME, Peppas NA, Langer R (2021) Engineering precision nanoparticles for drug delivery. *Nat Rev Drug Discov* 20(2), 101–124. 10.1038/s41573-020-0090-8.
2. Tietjen GT, Bracaglia LG, Saltzman WM, Pober JS (2018) Focus on Fundamentals: Achieving Effective Nanoparticle Targeting. *Trends in Molecular Medicine* 24(7), 598–606. 10.1016/j.molmed.2018.05.003.
3. Blanco E, Shen H, Ferrari M (2015) Principles of nanoparticle design for overcoming biological barriers to drug delivery. *Nat Biotechnol* 33(9), 941–951. 10.1038/nbt.3330.
4. Lu Q, Yu H, Zhao T, Zhu G, Li X (2023) Nanoparticles with transformable physicochemical properties for overcoming biological barriers. *Nanoscale* 15(32), 13202–13223. 10.1039/D3NR01332D.
5. Oliveira BL, Guo Z, Bernardes GJL (2017) Inverse electron demand Diels-Alder reactions in chemical biology. *Chem. Soc. Rev.* 46(16), 4895–4950. 10.1039/C7CS00184C.

Chapter 6

Appendix

Appendix

Abbreviations

^1H NMR	Proton nuclear magnetic resonance
ACE	Angiotensin converting enzyme
ALP	Alkaline phosphatase
Ang-I	Angiotensin I
Ang-II	Angiotensin II
AT1R	Angiotensin II receptor type 1
ATP	Adenosine triphosphate
BARAC	Biarylazacyclooctynone
BBB	Blood-brain barrier
BCA	Bicinchoninic acid
BCN	Bicyclo[6.1.0]non-4-yne
BDP	Boron-dipyromethene
BOND	Bioorthogonal nanoparticle detection
BSA	Bovine serum albumin
CA inhibition	Carbonic anhydrase inhibition
CCPs	Clathrin-coated pits
CDCl_3	Deuterated chloroform
CLSM	Confocal laser scanning microscopy
COOH	Carboxy
CRISPR	Clustered regularly interspaced short palindromic repeats
CTG	CellTracker™ green

CuAAC	Cu(I)-catalyzed [3+2] azide–alkyne cycloaddition
Cy-5	Cyanine5 fluorophore
DAPI	4',6-Diamidino-2-phenylindole
DBCO	Dibenzocyclooctyne
DBU	1,8-Diazabicyclo[5.4.0]undec-7-ene
DIPEA	N,N-Diisopropylethylamine
DLS	Dynamic light scattering
DMF	Dimethylformamide
DMSO	Dimethyl sulfoxide
Dox	Doxorubicin
DPBS	Dulbecco's phosphate buffered saline
DSPE	1,2-Distearoyl-sn-glycero-3-phosphorylethanolamine
EC ₅₀	Half maximal effective concentration
EDC	1-Ethyl-3-(3-dimethylaminopropyl)carbodiimide
EDG	Electron-donating group
EGFR	Epidermal growth factor receptor
EGTA	Ethylene glycol-bis(β-aminoethyl ether)-N,N,N',N'-tetraacetic acid
EPR effect	Enhanced permeability and retention effect
EWG	Electron-withdrawing group
EXP3174	Losartan carboxylic acid
FBS	Fetal bovine serum
FCS	Fluorescence correlation spectroscopy

Appendix

FDA	U.S. food and drug administration
FMO	Frontier molecular orbital
FSC	Forward scattered light signals
GFP	Green fluorescent protein
GPCR	G protein-coupled receptor
HBTU	Hexafluorophosphate benzotriazole tetramethyl uranium
HELIOS	Hypermissive ligation-initiated orthogonal sensing
HOMO	Highest occupied molecular orbital
HPLC	High-performance liquid chromatography
HSA	Human serum albumin
IC ₅₀	Half maximal inhibitory concentration
ICG	Indocyanine green
iEDDA	Inverse electron-demand Diels–Alder reaction
iMCs	Immature myeloid cells
LAF box	Laminar flow box
LDL	Low-density lipoprotein
LUMO	Lowest unoccupied molecular orbital
MALDI-TOF	Matrix assisted laser desorption ionization - time of flight
MeCN	Acetonitrile
MeO	Methoxy
MFNPs	Magneto-fluorescent nanoparticles
MMP-2	Matrix metalloproteinase 2

MPS	Mononuclear phagocyte system
MRI	Magnetic resonance imaging
MS	Mass spectrometry
MSNs	Mesoporous silica nanoparticles
MWCO	Molecular weight cutoff
NBS	N-Bromosuccinimide
NHS	N-Hydroxysuccinimide
NIR dye	Near-infrared dye
NP	Nanoparticle
NTA	Nanoparticle tracking analysis
OAT	Organic anion transporter
PAC-1	First procaspase activating compound
PBS	Phosphate buffered saline
PDI	Polydispersity index
PDT	Photodynamic therapy
PEG	Polyethylene glycol
PET	Positron emission tomography
PFA	Paraformaldehyde
pHLIP	pH low insertion peptide
PLA	Poly lactide
PLGA	Poly(lactic-co-glycolic acid)
QD	Quantum dot

Appendix

RAFT	Reversible addition fragmentation chain transfer
rcf	Relative centrifugal force
RES	Reticuloendothelial system
RISC	RNA interference specificity complex
rMCs	Rat mesangial cells
ROI	Region of interest
ROS	Reactive oxygen species
rpm	Revolutions per minute
RT	Room temperature
s.c.	Subcutaneous injection
SD	Standard deviation
SEC	Size-exclusion chromatography
SPAAC	Strain-promoted [3+2] azide–alkyne cycloaddition
SPECT	Single-photon emission computed tomography
SSC	Side scattered light signals
SWCNTs	Single-walled carbon nanotubes
TAMRA	Tetramethylrhodamine fluorophore
TAMs	Tumor-associated macrophages
TCO	Trans-cyclooctene
TEA	Triethylamine
TFA	Trifluoroacetic acid
Tz	Tetrazine

Curriculum Vitae

Personal Information

Name: Johannes Lang
Date of birth: April 13, 1996
Place of birth: Würzburg
Nationality: German

Scientific Education

02/2021 – 01/2025 **PhD Candidate/Research Assistant**, Department of Pharmaceutical Technology, Universität Regensburg
10/2018 – 11/2020 **Master of Science (M.Sc.) in Chemistry**, Universität Regensburg
10/2014 – 02/2018 **Bachelor of Science (B.Sc.) in Chemistry**, Julius-Maximilians-Universität Würzburg

School Education

09/2006 – 06/2014 **Grammar School**, Dietrich-Bonhoeffer-Gymnasium Wertheim
09/2003 – 07/2006 **Primary School**, Grundschule Reicholzheim
09/2002 – 07/2003 **Primary School**, Grundschule Höchberg

Appendix

List of Publications

Peer-reviewed publications

1. Lang, Johannes; Schorr, Kathrin; Goepferich, Achim. Towards a Switchable Nanoparticle Behavior Using Inverse Electron-demand Diels-Alder Chemistry and Ectoenzyme-based Ligand Activation. *European Journal of Pharmaceutical Sciences* 2025, 204, 106944. DOI: 10.1016/j.ejps.2024.106944. Published Online: Oct. 24, 2024.
2. Schorr, Kathrin; Chen, Xinyu; Sasaki, Takanori; Arias-Loza, Anahi Paula; Lang, Johannes; Higuchi, Takahiro; Goepferich, Achim. Rethinking Thin-Layer Chromatography for Screening Technetium-99m Radiolabeled Polymer Nanoparticles. *ACS pharmacology & translational science* 2024, 7 (9), 2604–2611. DOI: 10.1021/acsptsci.4c00383. Published Online: Aug. 30, 2024.

Conference abstracts

1. Lang, Johannes; Goepferich, Achim. iEDDA Reactions for the Subsequent Modification of Nanoparticles. *13th PBP World Meeting on Pharmaceutics, Biopharmaceutics and Pharmaceutical Technology*, Rotterdam, the Netherlands, 2022.
2. Lang, Johannes; Goepferich, Achim. Switchable Nanoparticles using iEDDA Chemistry and Ectoenzymes for Ligand Activation. *CRS Germany Local Chapter Meeting*, Bad Dürkheim, Germany, 2024.

Acknowledgements

I would like to express my deepest gratitude to Prof. Dr. Achim Göpferich for giving me the opportunity to be part of his research group. I thank him for the trust he has placed in me and for the liberty he has granted me in planning and executing the research projects. I am grateful for his enthusiastic and friendly way of guiding me and for the numerous inspiring scientific conversations. This atmosphere has greatly contributed to the successful completion of this work and to my personal and academic development. For this, I am sincerely grateful.

I would also like to express my special thanks to Prof. Dr. Miriam Breunig for her scientific advice and valuable discussions. Her expertise and feedback notably enhanced the overall outcome of this dissertation.

Further, I would like to thank all my colleagues at the Department of Pharmaceutical Technology in Regensburg for their support and the pleasant working atmosphere. In particular, I wish to thank:

My lab colleague Andreas Schreiber for the many engaging conversations, both scientific and personal. Thank you, Andi, for creating a great atmosphere in the lab, for the laughter we shared, and for graciously subjecting me to “Stubenmusik” only on rare occasions.

Dr. Melanie Bresinsky, with whom I share the experience of starting a PhD during the COVID-19 pandemic. Thank you, Melli, for being there from day one, for your scientific support, and for the good times playing beach volleyball and spikeball.

Felix Baumann, who always had an open ear for the challenges I faced. Thank you, Felix, for your numerous scientific insights, for the many fruitful discussions, for your steady supply of sweets and for your infectious scientific curiosity.

Dr. Kathrin Schorr, for her valuable scientific advice, excellent collaboration, and for sharing experiences with the Fura-2 Ca^{2+} assay. Thank you, Kathrin, for your thoughtful input whenever challenges arose and, more generally, for the many pleasant conversations beyond work.

Jan Birringer and Stephan Melchner, for their support within the lab and for the kilometers run together. I greatly appreciated your company in both cases! Thank you, Stephan, for the exchange of ideas on tetrazine–coumarin fluorophores and for accompanying me to the CLSM.

Dr. Clara Barbey, for your caring nature, our enjoyable conversations, and your incredibly delicious cinnamon buns.

Appendix

Dr. Oliver Zimmer and Dr. Jonas Groner, for the evenings at the boulder gym and together with Melli and Clara for the unforgettable time in Rotterdam.

Marius Remmert, Carsten Damm, Johannes Konrad, and Felix Hauswirth for participating in countless rounds of “Schafkopf” during lunch breaks. You all greatly enriched my time in the department, and I will always look back on it fondly!

I would also like to extend my sincere thanks to the technical staff of the department. In particular, I wish to acknowledge Grace Faltermeier for her valuable assistance with the synthesis of the block copolymers and their modification, as well as Renate Liebl for her excellent support in cell culture. My heartfelt thanks to both of you! Furthermore, I am grateful to Eva Wrobel for her outstanding assistance with organizational and administrative matters.

I would also like to thank the Department of Pharmaceutical and Medicinal Chemistry II for the access to the preparative HPLC, and in particular to Beate Hoffelner for her support in this regard.

A very special thanks goes to my parents for their unconditional trust and support throughout my entire studies and now also during the years of my doctoral research. Finally, and most importantly, I would like to express my heartfelt gratitude to my wife, Sarah Karishma. Thank you for always being there for me – for your patience, your encouragement, and your unwavering support. Your understanding and confidence in me have been a constant source of strength and motivation throughout this journey.

Declaration in Lieu of an Oath

I hereby declare that I have completed the dissertation presented without the impermissible help of third parties, without the use of resources other than those indicated, and that any data and concepts stemming directly or indirectly from other sources are indicated with citations to the literature.

No further persons were involved with the creation of the contents of the dissertation presented. In particular, I have not made use of the assistance of a doctoral consultant or other person in return for payment. No-one has received payment in kind either directly or indirectly for work which is associated with the content of the dissertation submitted.

The dissertation has not been submitted in the same or similar form to another examining authority, neither in Germany nor abroad.

Regensburg, 01.12.2025

Johannes Lang